UNIVERSITY OF SOUTHAMPTON

Faculty of Engineering and Physical Sciences

School of Engineering

Steps towards mixed energy optimisation of Uncrewed Aerial Vehicles

by

Laminn McLay

MEng

ORCiD: 0000-0003-3484-006X

A thesis for the degree of

Doctor of Philosophy

April 2024

University of Southampton

Abstract

Faculty of Engineering and Physical Sciences

School of Engineering

Doctor of Philosophy

Steps towards mixed energy optimisation of Uncrewed Aerial Vehicles

by Laminn McLay

The long-range uncrewed aerial vehicle (UAV) is expected to utilise a combination of power sources, including photovoltaic modules, fuel cells, or direct combustion with hydrogen, lithium compound batteries, and hydrocarbon fuels. Hybrid powertrains are becoming more common, highlighting the need for automated powertrain topological exploration to identify the optimal design for mission performance. In this thesis, we develop tools to identify such optimal designs.

The first building block of such an optimiser is a scheme capable of the flexible, future-proof, yet economical encoding of powertrain topologies, and we propose such a scheme in this thesis. This scheme is adaptable for analysis and can be applied to any UAV powertrain topology, providing a means to compare and analyse different powertrains.

The second building block of the optimisation process is determining the optimal energy architecture. To achieve this, we use a point mass model to represent the aircraft performance, the energy components are modelled and the different powertrain topologies are evaluated through dynamically generated strings, based on the proposed encoding scheme. The point mass model can be used to evaluate different powertrain topologies for fixed-wing UAVs through the initial value problem (IVP) by simulating the dynamics of the UAV's motion over time. By simulating the UAV's motion over time, the model can provide insights into the energy consumption and other performance metrics of different powertrain topologies.

We compare two different fixed wing UAV models: a 5 kg maximum take-off mass with a 2 m wing span and a 25 kg maximum take-off mass with a 4 m wing span UAV; for set missions with different powertrains. Overall, we demonstrate that the framework proposed here delivers the lightest feasible powertrain topologies, describing the power supply as well as the preliminary flight profile for a specific platform for a given operation whilst developing a scheme that is suitable for embedding various topology strings with capability for a wide variety of multi-source and multi sink power systems. The proposed framework allows for refining the mission profile, minimising powertrain sizing, and finding an optimal energy split for hybrid powertrain topologies through novel powertrain topology parameterisation.

Contents

List of Figures **ix**

List of Tables **xv**

Declaration of Authorship **xvii**

Acknowledgements **xix**

Definitions and Abbreviations **xxi**

1 Introduction **1**
1.1 Series hybrid configuration . . . 1
1.2 Parallel hybrid configuration . . . 2
1.3 Motivation . . . 4
1.3.1 Requirements . . . 4
1.4 Research tasks . . . 5
1.4.1 Scope . . . 7
1.4.2 Limitations and assumptions . . . 8
1.4.3 Contributions . . . 10
1.5 Organisation of thesis . . . 13

2 Literature review **15**
2.1 Hybrid powertrain topologies and design considerations . . . 15
2.1.1 Current hybrid powertrains topologies for UAVs . . . 18
2.1.2 Powertrain architecture encoding – background . . . 20
2.1.3 String based encoding scheme . . . 22
2.1.3.1 Graph theory approach - background . . . 25
2.1.3.2 Graph theory approach - application to powertrains . . . 26
2.2 On-board powertrain components and the model choices . . . 29
2.2.1 Internal combustion engines . . . 32
2.2.1.1 Internal combustion engine - model choice . . . 33
2.2.2 Solar cells . . . 34
2.2.2.1 Solar cells - model choices . . . 37
2.2.3 Fuel cells . . . 38
2.2.3.1 PEMFC - model choices . . . 42
2.2.4 Batteries . . . 45
2.2.4.1 Lithium battery - model choices . . . 49
2.2.5 Electric motors . . . 50

2.2.5.1 Electric motor - model choices . . . 51
2.2.6 Propellers . . . 52
2.2.6.1 Propeller - model choices . . . 53
2.2.7 Propeller-electric motor matching . . . 53
2.2.7.1 Well-matched systems vs ill-matched systems . . . 54
2.3 Applications of modelling and simulations methods for UAV hybrid powertrains . . . 56
2.3.1 Forward-facing model . . . 59
2.3.2 Backward-facing models . . . 61
2.3.3 Initial value problem . . . 63
2.4 Summary . . . 64

3 Proposed powertrain topology encoding scheme 67
3.1 Introducing the PoETS approach . . . 68
3.2 Contribution one - Application of PoETS for representing existing powertrains . . . 71
3.3 Summary . . . 74

4 Generating and modelling powertrain topologies through PoETS 75
4.1 Contribution two – the automatic generation of feasible powertrains . . . 76
4.2 Modelling and simulation . . . 79
4.2.1 Implementation of the component models . . . 80
4.2.2 Curating component data . . . 82
4.2.3 Refining the component data . . . 83
4.3 Contribution three – evaluating the feasibility and performance of a powertrain . . . 86
4.4 Summary . . . 87

5 Optimising and evaluating PoETS topologies 89
5.1 Formulation of problem and component sizing . . . 89
5.2 Overview of initial sizing methodology . . . 91
5.2.1 Calculating efficiency of the modelled system . . . 92
5.3 Objective function formulation and rationale . . . 93
5.4 Contribution four – optimising powertrains . . . 99
5.4.1 Optimisation convergence check . . . 99
5.4.2 Mission 1 . . . 101
5.4.3 Component output results comparisons . . . 108
5.5 Powertrain outcome of each mission . . . 111
5.6 FliTePlat vs PEREGRIN - comparisons . . . 113
5.7 Summary and outlook . . . 115

6 Discussion and conclusions 117
6.1 Discussion summary . . . 117
6.2 Summary of chapters . . . 119
6.3 Summary of research contributions . . . 120
6.4 Future work recommendations . . . 122
6.4.1 Generating new topologies through genetic programming . . . 122
6.4.1.1 Encoding powertrain topologies . . . 122

6.4.1.2 Component selection 126
6.4.1.3 Objective function 126

Appendix A Test platforms **127**
Appendix A.1 FliTePlat 127
Appendix A.1.1 Aerodynamic coefficient calculations – experimental set-up 128
Appendix A.2 PEREGRIN 130
Appendix A.2.1 Aerodynamic coefficient calculations – experimental set-up 130
Appendix A.3 UAV model – basic equation of motion 133
Appendix A.3.1 Smoothing functions for change in flight segments . . 135
Appendix A.4 Case study missions 136

Appendix B Modelling the components of a UAV powertrain **137**
Appendix B.1 Propeller model 137
Appendix B.2 Internal combustion (piston) engine model 139
Appendix B.2.1 Scaling the engine maps 141
Appendix B.3 Electric motor model 144
Appendix B.4 Battery model 150
Appendix B.5 Solar cell model 151
Appendix B.6 Fuel cell model 155
Appendix B.7 Multi-energy component class 158
Appendix B.7.1 Matching propeller-electric motor process 160
Appendix B.7.2 Verification of the propeller model 160
Appendix B.7.3 Verification of electric motor and battery model 164
Appendix B.7.3.1 Case study one – static case 164
Appendix B.7.3.2 Case study two - dynamic case 166
Appendix B.7.4 Internal combustion engine mapping 169
Appendix B.7.4.1 Scaling of the engines 172
Appendix B.7.5 Verification of solar cell models 177
Appendix B.7.6 Verification of fuel cell model 178
Appendix B.8 Summary 179

Appendix C Powertrain Optimisation Results **181**
Appendix C.1 Mission 2 181
Appendix C.2 Mission 3 187
Appendix C.3 Mission 4 192
Appendix C.4 Mission 5 197
Appendix C.5 Mission 6 202

References **207**

List of Figures

1.1 Series hybrid configuration: *yellow* line represents moving mass (chemical connection), *blue* line represents mechanical connection, *green* line represents electrical connection. 2
1.2 Parallel hybrid configuration: *yellow* line represents moving mass (chemical connection), *blue* line represents mechanical connection, *green* line represents electrical connection. 3
1.3 Proposed optimisation strategy. 8
1.4 Components considered in this study for modelling and simulation. . . 9
1.5 The two test platforms employed in this study. 9
1.6 Example mission profiles for powertrain comparison in this study. . . . 11

2.1 Hybrid electric architecture design space proposed by Harish et al. [63] for gas-turbine and battery hybrid. 17
2.2 AIAA pictorial representation of energy architecture components [7]. . . 21
2.3 Methanol molecular structure as a valence scheme approach [7]. 23
2.4 The use of lower case letters, upper case letters, parentheses, and numbers in SMILES [161]. 24
2.5 Total number of connected graphs with 3 nodes. 25
2.6 Total number of graphs with 3 nodes. 26
2.7 Internal combustion engine scaling process. 34
2.8 PHASA-35 [15]. The aircraft has a wingspan of 35 m and a gross take-off mass of approximately 150 kg. 35
2.9 SAT_i [153]. It has a wingspan of 7.3 m and MTOM of 6.3 kg. 35
2.10 APUS DUO 15 [153]. The aircraft has a wingspan of 15 m and a gross take-off mass of 43 kg. 36
2.11 High Altitude Pseudo-Satellite (HAPS) Zephyr in preparation before take-off [5]. This UAV has a wingspan of 25 m and weighs less than 75 kg. . . 38
2.12 Helios in flight [111]. This UAV has a wingspan of 75 m and a gross mass of up to 929 kg. 38
2.13 A fuel cell stack [9] summarising the proton exchange membrane fuel cell. 39
2.14 PEMFC general schematic [9]. 40
2.15 Results of AEROPACK Fuel Cell Tests: hydrogen flow rate plotted against the electrical power [44]. 43
2.16 Results of Aeropack Fuel Cell Tests: A) Voltage vs Current - PEMFC stack, B) Power vs Current - battery and PEM stack hybrid system, C) Power vs Current - PEMFC stack and D) Power vs Current - battery pack [44]. 44
2.17 Losses in fuel cells [103]. 44

2.18 Efficiency chains with typical component efficiencies for battery-powered drive trains [69]. . . . 48
2.19 Efficiency chains with typical component efficiencies for wet fuel powered drive trains [69]. . . . 48
2.20 Efficiency chains with typical component efficiencies for fuel cell powered drive trains [69]. . . . 48
2.21 Take-off gross weight for various battery specific energies and cruise ranges [66]. 7000 lb is the limit that Hascaryo and Merret [66] imposed when doing the sizing calculations. . . . 49
2.22 Equivalent Circuit for an electric motor [43]. . . . 51
2.23 Features extracted from the datasheet identifying the correlations between the dependent and independent variables for electric motors. . . . 52
2.24 Comparison plots of a well-matched propeller motor against an ill-matched propeller motor. The component sizes are found in Table 2.5. . . . 55
2.25 Forward facing model [13]. . . . 60
2.26 Backward facing model [13]. . . . 61

3.1 Powertrain as a graph – example of the simplest possible combustion engine powertrain. . . . 69
3.2 Series hybrid configuration: *yellow* line represents moving mass (chemical connection), *blue* line represents mechanical connection, *green* line represents electrical connection. . . . 70
3.3 Same number of nodes in parallel branch example - PoETS equivalent would be p[em | {gn[en(HC + {pc{fc(HY |. . . . 70
3.4 Powertrain as a graph – example of branched connections, with a single energy source and two propulsors. . . . 71
3.5 Examples of real life UAV - Top: NASA Greased Lightning GL-10 UAV [17], Bottom left: Eagle Plus UAV [141], Bottom right: Hybrid Tiger UAV [117]. . . . 72
3.6 Examples of real life UAV powertrains - Top: NASA Greased Lightning GL-10 UAV [17], Bottom left: Eagle Plus UAV [141], Bottom right: Hybrid Tiger UAV [117]. . . . 72
3.7 EAV-2 UAV powertrain. . . . 73

4.1 Examples of topologies generated based on the powertrain topology connection input-output edge types - Linear. . . . 78
4.2 Examples of topologies generated based on powertrain topology connection input-output edge types - Branched. . . . 78
4.3 The structure for the mission profile simulation. . . . 80
4.4 Self modifying python script process for a single timestep. . . . 81
4.5 Web scraping process for curating component data. . . . 82
4.6 Example constraint analysis output for mission 1. . . . 84
4.7 Initial process of refining the components down based on estimated efficiency and PoETS string. . . . 85

4.8 A comparison of three mission profile simulations in above ground level versus time space: a target mission (red +), a profile resulting from a simulation of the operation of a battery electric UAV flown to match the target profile as closely as possible (green +), and a similar simulation of a UAV powered by a photovoltaic powertrain (yellow +). The latter clearly fails to get close to the target mission. 87

5.1 Penalty function outputs for the cost function with respect to a maximum take-off mass of 5.5 kg. 96
5.2 Genetic algorithm convergence of the objective function demonstrator for Mission 1. 100
5.3 Mission 1 - profile. 101
5.4 Mission 1 - mass optimisation results. 103
5.5 Mission 1 - energy source split and efficiency results. 104
5.6 Mission 1 - time taken to complete the mission. 105

6.1 Example of the parent strings. 124
6.2 Example of the children produced by one point crossover. 125
6.3 Example results produced by one point crossover. 125
6.4 Example of the children produced by multi points crossover. 125
6.5 Example results produced by multi points crossover using the same parent strings in Figure 6.1. 126

Appendix A.1 Instrumentation onboard the test platform. 128
Appendix A.2 FliTePlat UAV in RJ Mitchell wind tunnel. 129
Appendix A.3 FliTePlat lift and drag coefficients based on experimental data obtained in the wind tunnel. 130
Appendix A.4 PEREGRIN UAV. 131
Appendix A.5 Manual flight in X-Plane 11 to obtain aerodynamics parameters.The take-off has been removed from the data. 132
Appendix A.6 Kinematic axis: i_f (incidence angle) is the offset angle of the wings in relation to the fuselage, α_f is the angle of attack with respect to the fuselage axis and free stream velocity, V_∞ is the free stream velocity, γ is the climb angle (the angle between V_∞ and the horizontal earth's axis), θ is the pitch angle (the angle between the horizontal fuselage axis and horizontal earth's axis). 134
Appendix A.7 Examples of control inputs for flight segment changes. 136

Appendix B.1 Comparison of different propellers: Speed [RPM] against Thrust [N] at 0 ms^{-1}, the data is collected from APC Propellers [11]. 138
Appendix B.2 Relational analysis of the commercial off-the-shelf brushless direct current motors. 145
Appendix B.3 Relations between no-load current and K_V rating with length and diameter of the electric motors. 147
Appendix B.4 Relations between internal resistance and K_V rating with length and diameter of the electric motors. 148
Appendix B.5 Approach used to predict photovoltaic power output. 152
Appendix B.6 A visual example of how the multi-energy component class is set up. 159

Appendix B.7 Propeller interpolation function test case based on 12″ x 6″ APC two-bladed propeller. . . . 161
Appendix B.8 IR sensor set up. . . . 163
Appendix B.9 Motor speed model based on experiment against the interpolated data from the propeller. . . . 163
Appendix B.10 Case study set up - battery, electronic speed controller and electric motor connections. . . . 165
Appendix B.11 Validation case study process - for δt - battery, electronic speed controller and electric motor connections. Assuming that the electronic speed controller's efficiency is 0.95 and is constant. This process is repeated until the final time step is reached. . . . 165
Appendix B.13 Sensitivity analysis to obtain electronic speed controller efficiency. . . . 165
Appendix B.12 Battery validation case study - comparison of the model and the experiment - for statics case. . . . 166
Appendix B.14 Electric motor efficiency - comparison of the model and the experiment - static case. . . . 167
Appendix B.15 Battery validation case study - comparison of the model and the experiment during flight testing. . . . 168
Appendix B.16 Power [W] v Engine rotation speed [RPM] relations at different throttle settings (%) for the OS GF 40 engine. The solid line shows the interpolated data whereas the dashed line is extrapolated. . . . 170
Appendix B.17 Power [W], Speed [RPM], and Torque [Nmm] relations at 100% throttle setting. . . . 171
Appendix B.18 Power [W], Speed [RPM] and Torque [Nmm] relations at 25 % throttle setting. . . . 171
Appendix B.19 Fuel flow [g s^{-1}] at 70% throttle setting, showing the nonlinear relations between fuel flow and power. . . . 172
Appendix B.20 The baseline engine maps used in this study for scaling of the engines through the Willans approximation [127, 140, 177]. . . . 173
Appendix B.21 Comparison of the Willans approximation and the experimental result. The red surface is the approximation from the Willans line calculations whereas the blue surface is the experimental data. . . . 174
Appendix B.22 Example scaling of the engine using Willans approximation. . . 176
Appendix B.23 Sunpower C-60 single solar cell - comparison of the model and the open data given by the manufacturer. . . . 178
Appendix B.24 Solar irradiance model at high altitude ($>$ 2.5 km) and low altitude ($<=$ 2.5 km) at the latitude of 50.9105 deg. . . . 179
Appendix B.25 Protium-25 PEM fuel cell model vs data comparison with data based on [51]. . . . 180

Appendix C.1 Mission 2 - profile. . . . 182
Appendix C.2 Mission 2 - mass optimisation results. . . . 183
Appendix C.3 Mission 2 - energy source split and efficiency results. . . . 184
Appendix C.4 Mission 3 - profile. . . . 187
Appendix C.5 Mission 3 - mass optimisation results. . . . 188
Appendix C.6 Mission 3 - energy source split and efficiency results. . . . 189
Appendix C.7 Mission 4 - profile. . . . 192

Appendix C.8 Mission 4 - mass optimisation results. 193
Appendix C.9 Mission 4 - energy source split and efficiency results. 194
Appendix C.10 Mission 5 - profile. 197
Appendix C.11 Mission 5 - mass optimisation results. 198
Appendix C.12 Mission 5 - energy source split and efficiency results. 199
Appendix C.13 Mission 6 - profile. 202
Appendix C.14 Mission 6 - mass optimisation results. 203
Appendix C.15 Mission 6 - energy source split and efficiency results. 204

List of Tables

2.1 Examples of current hybrid energy architectures 19
2.2 Bonds representations in SMILES [161]. 24
2.3 Comparison of fuel cell energy sources against internal combustion engines (three s.f.) based on [107, 119, 151]. 41
2.4 Propeller motor combinations for the test platforms after conducting a feasibility study. 54
2.5 Propeller motor combinations - component sizes for propeller and electric motor. 54

3.1 Proposed encoding scheme - symbols and their representations. 68

4.1 Powertrain topology connection input-output edge type. 76
4.2 Generated topologies based on powertrain topology connection input-output edge type. 77
4.3 Coverage of the components database used for the optimisation experiments described in Chapter 5. 83
4.4 Estimated parameters used in the constraint analysis. 84

5.1 Fixed powertrain topology case studies for the genetic algorithm to search the catalogues for the best components. 93
5.2 Design variables for Equation 5.6. 98
5.3 Design constraints for Equation 5.6. 99
5.4 Mission 1 - FliTePlat output - optimal thrust and climb angle. 106
5.5 Mission 1 - PEREGRIN output - optimal thrust and climb angle. 107
5.6 Test case 1 - p[em{B - component output results. 109
5.7 Test case 13 - p[em|{PV+{fc(HY| - component output results example. . 110

Appendix A.1 FliTePlat key parameters. 128
Appendix A.2 Coefficients generated through the wind tunnel data. 130
Appendix A.3 The PEREGRIN test UAV: a selection of key parameters. . . . 131
Appendix A.4 Coefficients generated through the software in the loop data. 131

Appendix B.1 Internal combustion engine's key parameter. 139
Appendix B.2 Constants values based on Schomann [133]. 148
Appendix B.3 Input parameter values for PEMFC based on the open literature [40, 157]. 157
Appendix B.4 Components during the static propeller test. 164
Appendix B.5 Components used in the dynamic propeller test. 167

Appendix B.6 Coefficients obtained from Willans approximation of the baseline engines engine. 175
Appendix B.7 Engine error metrics due to Willans approximation for the baseline engines. 175
Appendix B.8 Willans approximation - engine scaling. 175
Appendix B.9 Sunpower C-60 parameters. 177
Appendix B.10 PEMFC - Protium 25 specification. 179

Appendix C.1 Mission 2 - FliTePlat output - optimal thrust and climb angle. 185
Appendix C.2 Mission 2 - PEREGRIN output - optimal thrust and climb angle. 186
Appendix C.3 Mission 3 - FliTePlat output - optimal thrust and climb angle. 190
Appendix C.4 Mission 3 - PEREGRIN output - optimal thrust and climb angle. 191
Appendix C.5 Mission 4 - FliTePlat output - optimal thrust and climb angle. 195
Appendix C.6 Mission 4 - PEREGRIN output - optimal thrust and climb angle. 196
Appendix C.7 Mission 5 - FliTePlat output - optimal thrust and climb angle. 200
Appendix C.8 Mission 5 - PEREGRIN output - optimal thrust and climb angle. 201
Appendix C.9 Mission 6 - FliTePlat output - optimal thrust and climb angle. 205
Appendix C.10 Mission 6 - PEREGRIN output - optimal thrust and climb angle. 206

Declaration of Authorship

I declare that this thesis and the work presented in it is my own and has been generated by me as the result of my own original research.

I confirm that:

1. This work was done wholly or mainly while in candidature for a research degree at this University;
2. Where any part of this thesis has previously been submitted for a degree or any other qualification at this University or any other institution, this has been clearly stated;
3. Where I have consulted the published work of others, this is always clearly attributed;
4. Where I have quoted from the work of others, the source is always given. With the exception of such quotations, this thesis is entirely my own work;
5. I have acknowledged all main sources of help;
6. Where the thesis is based on work done by myself jointly with others, I have made clear exactly what was done by others and what I have contributed myself;

7. Parts of this work have been published as: L. McLay, J. Scanlan, and A. Sobester. PoETS: A Proposed Powertrain Topology Encoding Scheme. In *AIAA SCITECH 2023 Forum*, Reston, Virginia, jan 2023. American Institute of Aeronautics and Astronautics. DOI: 10.2514/6.2023-1363. ISBN: 978-1-62410-699-6

   A. Weishäupl, L. McLay, and A. Sóbester. Experimental evaluation of the drag curves of small fixed wing UAVs. *The Aeronautical Journal*, pages 1–30, jul 2023. DOI: 10.1017/aer.2023.61. ISSN: 0001-9240

Signed:..... Date:.....

Acknowledgements

I would like to extend my gratitude to my primary supervisor, Dr. András Sóbester for the continued guidance throughout the Ph.D. and the extraordinary support throughout the pandemic and beyond, be it in terms of cake or intellectual contribution. My thank also goes to Dr.Jim Scanlan, my secondary supervisor for his advice. A graceful appreciation goes to my partner, Dr.Adrian Weishäupl, for providing me with encouragement, without whom, none of this could have happened. I would also like to extend my thanks to my parents, who are always looking out for me. Finally, I would like to acknowledge the support of this work by the Engineering and Physical Sciences Research Council through grant EP/R009953/1.

Definitions and Abbreviations

η_f	fuel efficiency
η_p	propeller efficiency
η_{th}	thermal efficiency
δ	change in (typically timestep)
ρ	density [kg m^3]
μ	friction coefficient
Ω	motor speed [RPM]
AC	Alternating current
BLDC	Brushless direct current (motor)
bsfc	brake specific fuel consumption [g (Wh)$^{-1}$]
COTS	Commercial off the shelf
C_D	Drag coefficient
C_{nom}	Nominal capacity (of a battery) [Ah]
C_{rate}	Discharge rate (of a battery) [C]
DC	Direct current
DoH_E	Degree of energy hybridisation
DoH_{P_p}	Degree of power hybridisation for parallel configuration
DoH_{P_s}	Degree of power hybridisation for series configuration
E	Energy [Wh]
FliTePlat	Flight Test Platform
FF	Fill factor
I	Current [A]
I_{SC}	Short circuit current [A]

K_V	Motor speed constant [RPM V^{-1}]
K_Q	Motor torque constant [Nm A^{-1}]
Li-ion	Lithium ion
LiPo	Lithium polymer
m	mass [kg]
$\dot{m}_f$	fuel mass flow rate [kg s^{-1}]
MEP	Mean effective pressure [Pa]
MPPT	Maximum powerpoint tracker
MTOM	Maximum take off mass [kg]
P	Power [W]
P_{in}	Power in due to solar irradiance [W]
PEMFC	Proton exchange membrane fuel cell
PEREGRIN	Platform for Environmental Research in Extreme Geographic Regions using Integrated Navigation
PoETS	Powertrain Energy Topology Scheme
Q	Torque [Nm]
Q_{batt}	Battery charge capacity [C]
Q_{LHV}	Lower heating value of fuel [Wh g^{-1}]
R	Internal resistance [ohms]
SMC	Self Modifying Code
SMILES	Simplified Molecular Input Line Entry System
T	Thrust [N]
U	Motor terminal voltage [V]
UAV	Uncrewed Aerial Vehicle
V_{OC}	Open circuit voltage [V]
V_{TA}	True airspeed [ms^{-1}]
SOC	State of charge (of a battery)

Chapter 1

Introduction

Hybrid powertrains for Uncrewed Aerial Vehicles (UAV) are feasible solutions now more than ever, due to the increase in the availability of commercial off-the-shelf UAVs as well as advances in technology. Systems that seemed novel previously, such as those based on a fuel cell power system for UAV (for example *Ion Tiger* [144], *Scan Eagle* [75]) and crewed aircraft prototypes (for example *HY4* [62], *Airbus ZEROe* [6]), or those based on solar cell power systems (for example *Helios* [111], *Zephyr-S* [5]), have proven to be viable and valuable systems. A hybrid powertrain is a powertrain in which two or more types of energy storage devices, sources, or converters, provide the propulsion energy of a vehicle [50] [65]. For simplicity, the explanation of the configurations for hybrid powertrain in the following section are given in context of the electric motor and internal combustion engines.

1.1 Series hybrid configuration

In a series hybrid configuration, the propulsion system is driven by an electric motor powered by an electrical generator driven by a fuel-powered engine [73]. The engine is typically a gasoline or diesel engine, although other fuel sources such as natural gas or hydrogen can also be used. An example of the series hybrid configuration is shown in Figure 1.1. In this series hybrid configuration, the engine does not directly drive

the propeller or rotor, but rather drives the generator to provide electrical power to the motor. The motor drives the propeller or rotor, providing the necessary thrust for flight. The mechanical drive train is powered by an electric motor, allowing the internal combustion engine to operate in a maximum torque and speed range [73], which is one of the advantages of the series configuration, aside from the configuration being the simplest out of all the configurations. Therefore, if energy efficiency is a primary concern: series hybrid powertrains typically have higher energy efficiency than parallel hybrid powertrains due to their ability to operate the engine at a constant RPM at lower fuel consumption.

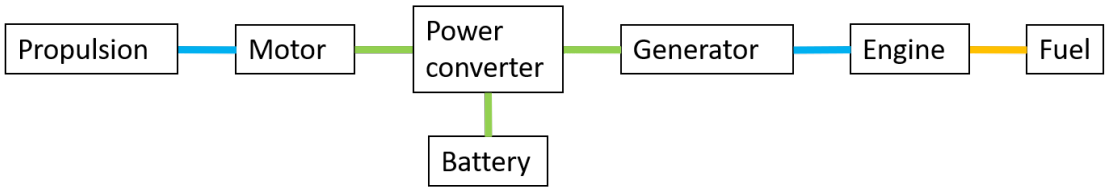

FIGURE 1.1: Series hybrid configuration: *yellow* line represents moving mass (chemical connection), *blue* line represents mechanical connection, *green* line represents electrical connection.

1.2 Parallel hybrid configuration

Powertrains laid out in a parallel hybrid configuration, shown in Figure 1.2, enable the use of either the internal combustion engine alone, the electric motor alone, or a combination of both through the use of a mechanical system, in this case, a clutch [73]. Harmon et al. [65] estimates that compared to the series hybrid configuration, the parallel configuration is lighter by around 1.1 kg for a 13.6 kg UAV. The reason is that the torque of the electric motor can supplement the torque required by the system, therefore the mass of the internal combustion engine and electric motor can be lower than in a series hybrid configuration. Moreover, the electric motor can become a generator if the battery needs charging.

There is some evidence that, for certain missions, more complex energy mixes yield better performance. For example:

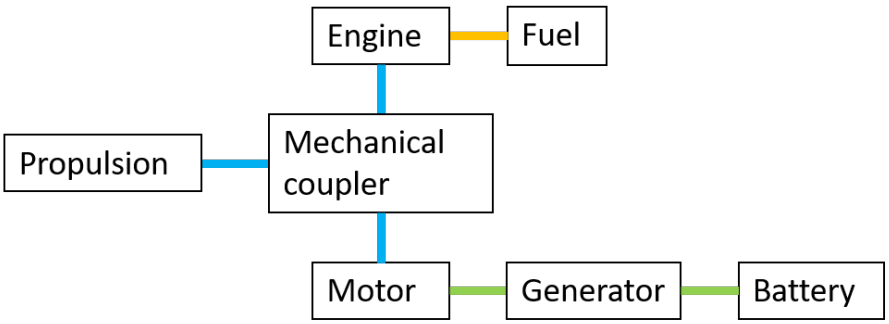

FIGURE 1.2: Parallel hybrid configuration: *yellow* line represents moving mass (chemical connection), *blue* line represents mechanical connection, *green* line represents electrical connection.

1. Yezeguelian and Isikveren [170] compared a baseline aircraft with two two-stroke piston engines, finding that a parallel hybrid configuration with a high-end battery would produce an 11% increase in endurance without increasing the maximum total take-off weight beyond +10%.

2. Thauvin et al. [147] assessed that a hybrid power generation system could largely help reduce the energy consumption during descent (by 60% for a 10 min descent compared to engines alone).

3. Hung and Gonzalez [73] found that a parallel hybrid architecture saves 6.5% more fuel compared to their simulation of an internal combustion engine-only powertrain configuration.

4. Eqbal et al. [46] highlights that a series hybrid configuration improved endurance to 23.7 hr in cruise, compared to 15.1 hr using a spark ignition combustion engine, and in a parallel hybrid configuration, the efficiency increased by 6.5 % compared to the engine only configuration.

Such results raise the question of how to: a) parameterise the architectures and b) identify the optimal architecture. By devising an encoding scheme which parameterises energy systems, especially in mixed energy or hybrid energy systems, a potential new energy architecture for an existing UAV can be found and refined to optimise the energy systems appropriately for each mission.

The aim here is to design an energy architecture encoding scheme that can be applied to any UAV energy system so that the rules of the scheme can provide a unique identification for any energy architecture. Therefore, it is increasingly important to devise a distinctive nomenclature for the energy system, not only to differentiate between two similar energy architectures but also to be able to create, analyse, and compare the different powertrain topologies appropriate to each mission. Powertrain topology refers to the components involved in the propulsion system of the UAV and their order.

1.3 Motivation

Aircraft missions involve multiple functional flight phases, such as take-off, climb, cruise, and descent. Among these, take-off and climb require high power, while cruise and descent demand lower power. Consequently, powertrain requirements differ depending not only on the type of vehicle but also on the kind of mission, making some missions more suitable for hybrid powertrains than others. The challenge with hybrid powertrains lies in balancing the increased mass resulting from the addition of energy sources (and hence the associated system) with the increased efficiency. Hybrid powertrain configurations can be optimised to reduce maximum take-off mass by selecting the optimal mix of power sources and by improving the overall efficiency of the powertrain.

The key hypothesis this thesis sets out to test is as follows. *The optimisation of the energy mix and the deployment schedule of this energy mix yields a fixed-wing UAV design that is lighter than a single energy source aircraft optimally sized for the same mission.*

1.3.1 Requirements

This work aims to satisfy the following set of requirements:

1. Identify and uniquely represent different powertrain topologies in a simplified manner.

2. Generate feasible powertrain topologies based on component availability.

3. Optimise powertrain topologies based on specific mission requirements.

1.4 Research tasks

Based on the motivation above, it is important to be able to create, analyse and compare different powertrain topologies appropriate for each mission for several reasons. Firstly, different missions have different requirements, and an optimal powertrain design for one mission may not suit another. Therefore, it is necessary to create different powertrain topologies that meet the specific requirements of each mission. Second, analysing and comparing the different powertrain topologies allows for determining the best solution for a particular mission. This can help optimise performance, increase efficiency, and reduce costs. Thirdly, the development of a distinctive nomenclature for the energy system is essential to differentiate between similar energy architectures and powertrain topologies. This will facilitate communication and enable researchers, designers, and manufacturers to collaborate effectively and share knowledge, ultimately leading to more efficient and effective powertrain designs for UAVs.

Therefore, the following tasks were established:

1. Determine the mission requirements: The first step is to identify mission requirements, such as maximum take-off mass, distance, altitude, and operating environment.

2. Define the design space: The next step is to define the design space of the powertrain, including the different components and their possible configurations. This involves selecting the types of power sources (such as batteries, fuel cells, or solar panels), motors, or hybrid systems that can meet mission requirements. This follows by analysing the power sources, including energy and power density, efficiency, and weight.

3. Develop an encoding scheme: An encoding scheme is necessary to represent the different configurations of the powertrain. This runs in parallel with defining the

design space described above in order to inform a systematic search of the space of propulsion system architectures. This task is broken down into the following sections:

   (a) Develop a scheme representing the different powertrain topologies - human readable/computer readable.

   (b) Develop a scheme that allows the analysis of the powertrains for a given mission.

   (c) Develop a scheme that allows for optimal powertrain topology and component sizes for a given mission.

4. Develop a UAV model suitable for mission analysis: A simulation model is needed to predict the performance of the powertrain under different operating conditions. This involves developing a mathematical model that describes the behaviour of the powertrain components, such as energy storage and conversion systems. The simulation model can be used to predict the performance of the powertrain in terms of efficiency, power output, and weight.

   (a) Develop models of the energy components that can be integrated into the UAV model.

   (b) Validate the components of the model where possible.

5. Define the objective function: This would allow for evaluating the powertrain configurations, including single or hybrid power sources, electric or combustion engines, and determining which configurations best meet the mission requirements. In the case of reducing maximum take-off mass, the objective function could be the total weight of the powertrain or the maximum power output per unit weight. Here we focus on the maximum take off mass reduction.

6. Implement an optimisation algorithm: An optimisation algorithm is used to search the design space for the optimal powertrain configuration that minimises the objective function. There are several optimisation algorithms that can be used, such as genetic algorithms.

By following these steps, it is possible to model and encode powertrain topologies for efficient optimisation of UAV performance with particular attention to reducing maximum take-off mass. This can help in the design of lightweight and efficient powertrains that meet the mission requirements of UAVs. It is important to note that the optimal powertrain design may vary depending on the specific requirements of each mission, and the process may require iteration and refinement to achieve the best results.

1.4.1 Scope

With the aforementioned points in mind, we developed a rapid optimisation capability for the design of UAV powertrain architectures. This is achieved by creating an energy architecture encoding scheme: PoETS, that can be used to generate many powertrain architecture configurations. The generated energy architectures should be suitable for a given mission for a fixed-wing UAV, with components chosen from a finite number of real commercial components. Component libraries are developed to contain the parameters required to create models, which are evaluated through rapid-performance modelling.

This is a two-level optimisation problem where the higher level defines the mix of energy sources while the lower level search optimises the deployment schedule of the given energy sources during the mission. The optimal solution returns a UAV energy architecture that minimises the energy consumption and UAV mass for a given mission. Figure 1.3 summarises the optimisation strategy.

- Powertrain topology generation: This section is based on the encoding scheme developed in this study (Chapter 3).
- Powertrain sizing and selection: This section is based on the powertrain models developed based on the literature search (Chapter 2) and commercial off-the-shelves components (Appendix B) - applied to Chapter 4 and Chapter 5.
- Powertrain evaluation: This section bridges the generation and selection by using the methodology described in Chapter 5 to obtain the optimal configuration and

mission profile for a given mission, described in Figures 1.6a - 1.6f for the chosen platforms (Appendix A).

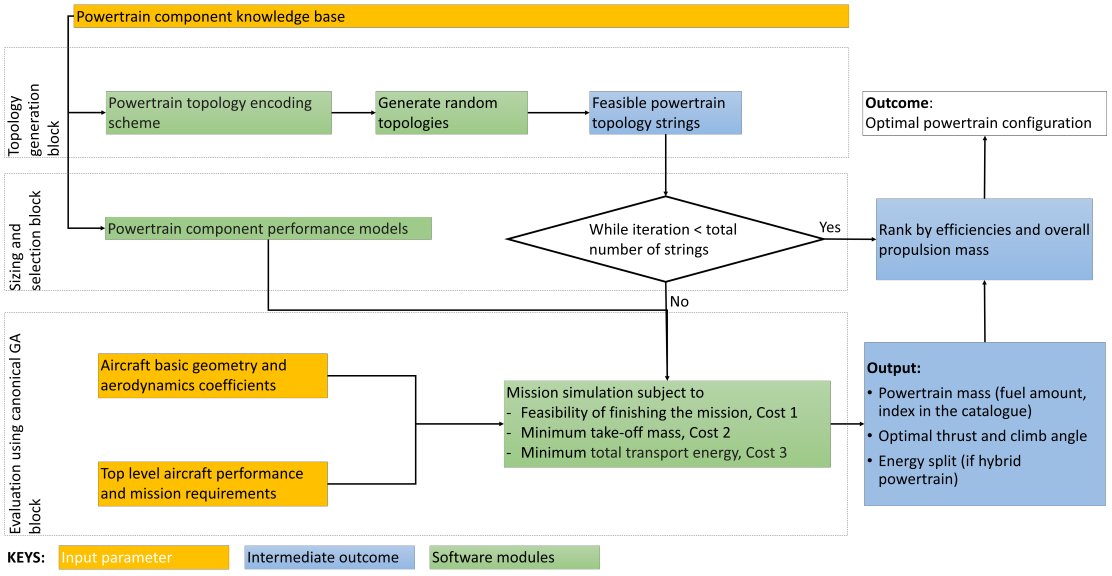

FIGURE 1.3: Proposed optimisation strategy.

1.4.2 Limitations and assumptions

The scope of this research is limited to fixed wing UAV using several assumptions. These assumptions are covered in this section.

We only consider the components shown in Figure 1.4. Furthermore, the components used for modelling are limited to discrete commercially off the shelf components. This, in general, limits the components used to the hobby market. This means that the mass of the components is also based on the specification given by the manufacturer.

For the case study, only two fixed-wing UAV (Figure 1.5a and 1.5b) are considered. These two platforms are chosen in order to develop a method for selecting propulsion for small ($\leq$ 25 kg) UAV by populating the powertrain topologies from potential available components. One has a maximum take-off mass of 5.5 kg and the other has 25 kg, to investigate the effect of the maximum allowable take-off mass on the feasible powertrain for the same missions. More information on these platforms can be found in Appendix A.

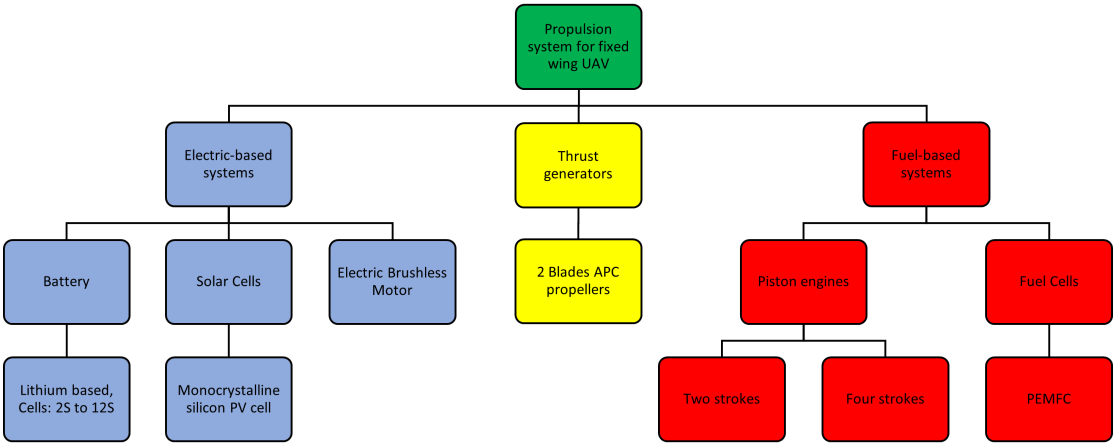

FIGURE 1.4: Components considered in this study for modelling and simulation.

(A) Test platform 1: FliTePlat.

(B) Test platform 2: PEREGRIN.

FIGURE 1.5: The two test platforms employed in this study.

The case study is also limited to simulate the following six types of missions, with the level of complexity increasing with each mission. One caveat here is that a single mission is mapped to a single powertrain topology. In reality, we would choose the powertrain topology performance which is "good" over a range of mission profiles.

1. Mission 1 - Figure 1.6a is a simple take-off combined with a climb to test for high power demands.

2. Mission 2 - Figure 1.6b is a simple take-off combined with a short climb followed by a long cruise to test endurance.

3. Mission 3 - Figure 1.6c is a simple take-off combined with a short climb followed by a long cruise and a second climb to test for high power demand as well as endurance.

4. Mission 4 - Figure 1.6d is a simple take-off combined with a longer initial climb followed by a long cruise and a second climb to test for high power demand as well as endurance similar to mission 3.

5. Mission 5 - Figure 1.6e represents a simple mission with a simple take-off combined with climb, cruise and descent.

6. Mission 6 - Figure 1.6f is a simple take-off combined with a longer initial climb followed by a long cruise and a second climb to test for high power demand as well as endurance. The main difference between the Mission 3, 4, and 6 are that 3 and 4 have different level cruises and 3 and 6 have different minimum allowable climb angles.

A point mass model is used for the mission simulation. Some of the current limitations due to the use of a point mass model include:

1. The aerodynamic consideration due to the prop-wash over the wings due to the placement of the propellers is not considered.

2. The geometry constraint, which would impact the centre of gravity calculations and the volume constraints, is neglected.

1.4.3 Contributions

Taken together, the framework developed in this thesis allows for the following:

1. Representing existing powertrain architectures for storing and comparing different powertrains using the encoding scheme (see Chapter 3). By providing a standard way of encoding powertrain topologies, the Powertrain Energy Topology

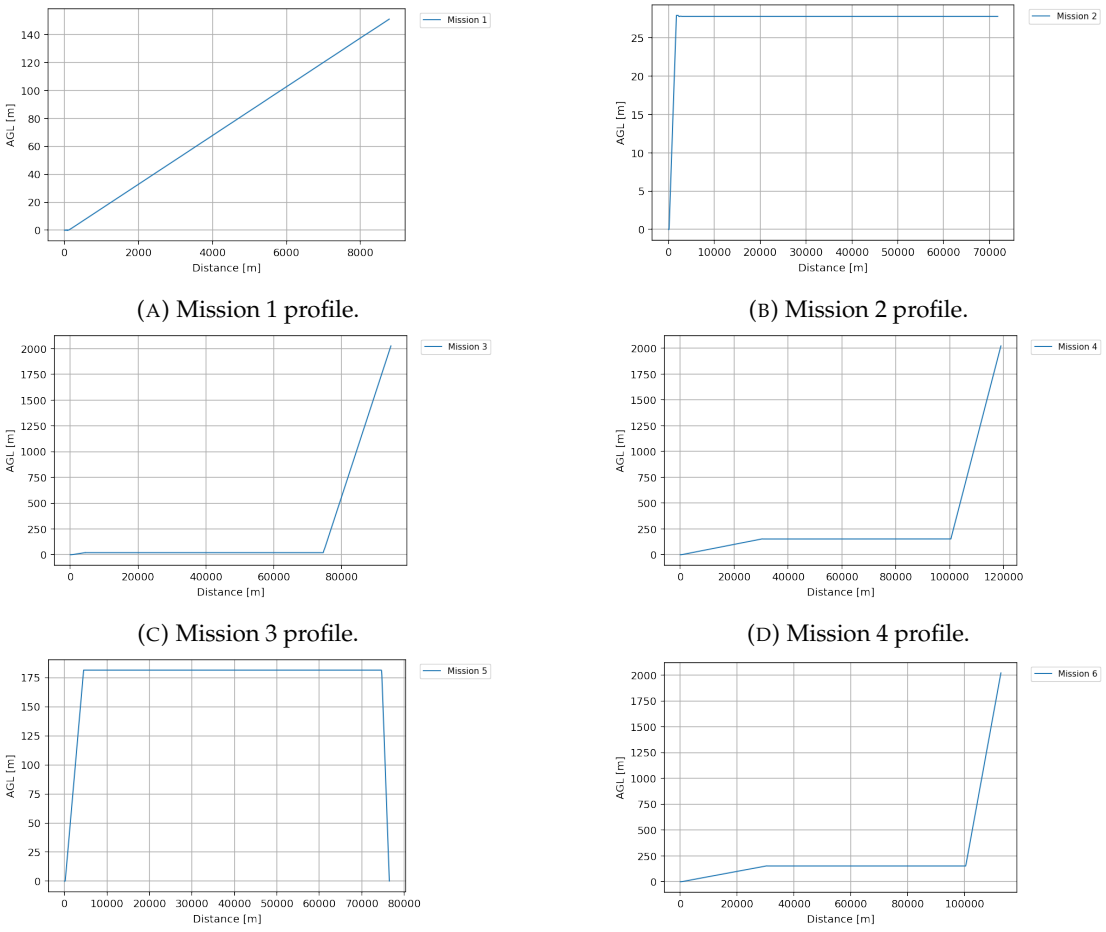

(A) Mission 1 profile.

(B) Mission 2 profile.

(C) Mission 3 profile.

(D) Mission 4 profile.

(E) Mission 5 profile.

(F) Mission 6 profile.

FIGURE 1.6: Example mission profiles for powertrain comparison in this study.

Scheme (PoETS) could help standardise the development and documentation of powertrain systems in different industries and applications (see more here McLay et al. [105]).

2. Generalisation of the powertrain topologies within the encoding scheme allowing the ability to create a powertrain topology based on the available components (see Chapter 4). This is useful for rapid generation of various topologies based on feasible connections and available components, leading to more flexibility in powertrain design and rapid exploration of different topologies and configurations, enabling the engineers to quickly evaluate the performance of different design options and select the most appropriate topology for a given application.

3. Determining the optimum size of the powertrain components (i.e. propeller, electric motor, battery, etc.) based on the energy consumption and minimum mass

proposed for any feasible system for a predefined mission. PoETS, therefore, can be used as a tool to aid optimisation algorithms to automatically generate powertrain topologies that meet specific performance or efficiency targets (see Chapter 5). This could enable the development of more efficient and cost-effective powertrain systems as well as finding the optimum energy split for such hybridised storage designs for a required mission.

4. Analysing the feasibility of the predefined powertrain for the known mission. PoETS could be used as part of a design automation process to automate the creation of powertrain topologies based on design requirements and constraints, leading to faster and more efficient design processes.

In order to explore the large design space, the methods developed here remain suitably generic. For performance estimation, the developed design method is composed of models based on state variables. For example, in the mechanical domains, the state variables are torque and rotational velocity, while in the electrical domains, they are current and voltage, and in the chemical domains, they are mass flow and lower heating values. These state variables are integrated into the performance estimation model of the given mission and are used to analyse the different powertrains and their feasibility to complete the mission.

Out of this thesis:

1. PoETS: A Proposed Powertrain Topology Encoding Scheme:McLay et al. [105], which proposed the novel encoding scheme.

2. Experimental evaluation of the drag curves of small fixed wing UAVs: Weishäupl et al. [164], which explores the power-on and power-off flight testing methods to obtain lift and drag coefficients of an electric-powered UAV.

3. McLay [104] for the open-source code repository for PoETS and its analysis.

are published.

1.5 Organisation of thesis

Chapter 2 summarises the fundamentals of the powertrain components and their limitations, with the current states of the hybrid electric propulsion systems and the existing platforms introduced. Existing methods of selecting and optimising hybrid powertrain topologies are also discussed in this chapter. This chapter also covers the choice of models to be used in modelling and simulation for the test platforms shown in Appendix A and Appendix B shows the verification taken for these models.

Chapter 3 delves into the inspiration behind the core concept. An encoding scheme capable of the flexible, future-proof, yet economical encoding of powertrain topologies. We propose PoETS: the Powertrain Energy Topology Scheme [105]. The encoding scheme proposed here (section 3.1) explains the representation of energy architectures using PoETS and the inspiration behind it. PoETS is developed to help inform a rapid, systematic search of the configuration space of multi-energy UAVs. Using this encoding scheme in conjunction with mathematical methods such as graph theory and evolutionary algorithms, shown in Chapter 4, new architectures can be developed for a pre-existing fixed-wing UAV platform. This work was presented at the AIAA SciTech 2023 forum [105].

Chapter 4 are a methodology for generating, evaluating and optimising the PoETS strings from Chapter 3 that ties with the modelling from Chapter 2 and Appendix B. Chapter 4 and Chapter 5 explore using low fidelity computational models to compare propulsion architectures for UAVs based on objective functions like mass, energy usage, and hybridisation whilst discussing the outcome of the study as well as key findings and shortcomings. Chapter 6 concludes the thesis, discussing the findings and presents any further recommendations.

Chapter 2

Literature review

The objectives of this chapter are to survey the current hybrid powertrain topologies and related design considerations - such as approaches to and need for an encoding scheme; the different hybrid and electric propulsion architectures; the technological level assumed for the components that make up the propulsion system for fixed wing UAV; the onboard energy sources, energy storage devices, and energy systems considered in the study; the investigation of the current modelling for the powertrain components; the modelling and simulation techniques suitable to our problem and the models to be used in the mission simulation. Detailed component models and verification are found in Appendix B.

2.1 Hybrid powertrain topologies and design considerations

Regardless of the configuration, be it series configuration or parallel configuration, the main parameters governing the powertrain according to Glassock et al. [55] are the mass and efficiency of all the components, energy and power density for the energy sources, torque and power curves for the power converters, and thrust and power coefficients for the propulsive devices.

Finger et al. [48] added that for hybrid powertrains, the degree of hybridisation of power and the degree of hybridisation of energy are also important. Finger et al. [48]

defined that the degree of hybridisation (DoH) of power for internal combustion engine and electric hybrid is the ratio of the installed propulsion power of all electric motors to the total installed propulsion power at the propeller shaft. The degree of hybridisation of the power of parallel hybrid systems can be calculated as the proportion of the electric power to the total power: $\mathrm{DoH_{P,p}} = \frac{P_{\mathrm{em,max}}}{P_{\mathrm{total,max}}}$. For series hybrid systems, the same metric can be calculated as the proportion of the electric power to the combustion engine power: $\mathrm{DoH_{P,s}} = \frac{P_{\mathrm{em,max}}}{P_{\mathrm{ice,max}}}$. The difference between the two equations is that for the parallel hybrid, the power can come directly from an individual power component, a combination of the power components or all of the power components (i.e. internal combustion engine, electric motor or both). Therefore the ratio can vary from 0 to 1. At 0 degrees of hybridisation of power, a power split does not occur and the power only comes from the internal combustion engine. A degree of hybridisation of power of 1 is where the electric motor supplies the full power required and no internal combustion engine power is needed. However, for the series hybrid system, the lowest value of $\mathrm{DoH_{P,s}}$ is 1, where the internal combustion engine is supporting the electric motor fully, therefore the battery power is not required to complete the mission.

Similarly, the degree of hybridisation of the energy is the ratio of the energy delivered by the battery (E_{batt}) to the energy delivered by the fuel (E_{f}): $\mathrm{DoH_E} = \frac{E_{\mathrm{batt}}}{E_{\mathrm{f}}}$. The degree of hybridisation of power is important as this determines the mass of the required power components, whereas the degree of hybridisation of energy would determine the energy source mass required.

Based on the parameters described above, Harish et al. [63] created a framework for the exploration of the design space for novel propulsion systems to allow for the evaluation and comparison of architectures on the same platform. Harish et al. [63] set out the multi-energy aircraft design space as a three-dimensional plot by leveraging the degree of hybridisation of power by way of distribution-of-power ($\mathrm{D_{p,1}}$ and $\mathrm{D_{p,2}}$), degree of hybridisation of energy by way of distribution-of-energy ($\mathrm{D_{E,1}}$ and $\mathrm{D_{E,2}}$), and transmission of power ($\mathrm{T_{p,1-1}}$ and $\mathrm{T_{p,2-1}}$). By this definition, different hybrid-electric

propulsion system architectures can be mapped onto different regions within the design space, as seen in Figure 2.1. The framework proposed by Harish et al. [63] enables designers to explore a wide range of design alternatives and eventually select the optimal propulsion system architecture for their specific requirements. Although the design space representation is meant to be able to represent a hybrid propulsion, it fell short on two points. First, the representation of the design space (see Figure 2.1) can be complicated, especially when representing hybrids due to the nature of the representing three-dimensional plots on paper. Secondly, when there are more than two energy sources and/or power sources, the representation diagram would have to expand accordingly, making it even more challenging for visualisation. Finally, the choice of powertrain ultimately depends on the specific needs and requirements of the vehicle and the intended use case. Therefore, a better system is required for the visualisation of the powertrain topologies, one which does not rely upon three-dimensional plots, whilst still able to represent optimal powertrain topologies.

Since many powertrain topologies are possible, we require a way of systematic, automated exploration of the space of powertrain topologies, with the goal of identifying the layout that optimises mission performance. Here, we discuss the inspiration based on graph theory, specifically the molecular graph encoding found in chemistry and how it could apply to the encoding of a UAV hybrid powertrain.

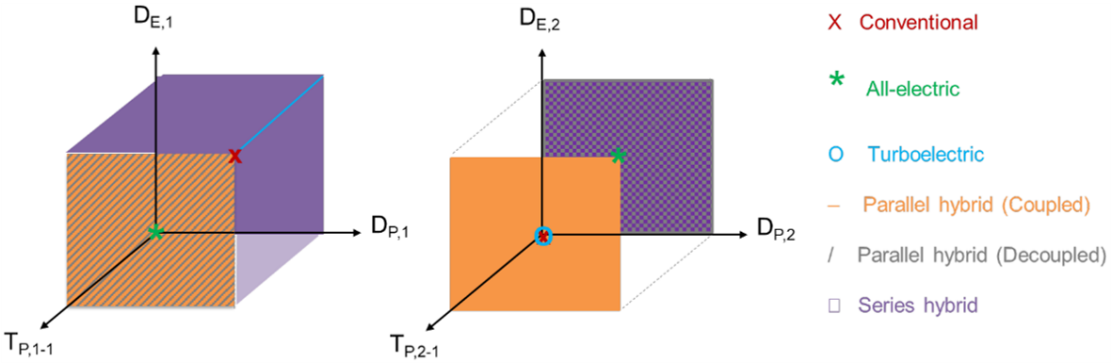

FIGURE 2.1: Hybrid electric architecture design space proposed by Harish et al. [63] for gas-turbine and battery hybrid.

2.1.1 Current hybrid powertrains topologies for UAVs

The ideal case for the UAV power system is to have a high energy density (for high energy storage) and a high power density (for high power response). For example, fuel cells have a higher energy density [110 - 1000 Wh kg^{-1}] but a lower power density [10 - 140 W kg^{-1}] compared to lithium-ion batteries which have a lower energy density [80 - 120 Wh kg^{-1}] but a higher power density [115 - 1100 W kg^{-1}][175].

A hybrid energy system can, to some extent, overcome the above problem by using more than one energy source. For example, wet-fuel powered UAVs can be coupled with battery packs or fuel cells in a hybrid system to increase the fuel efficiency of the UAV. Electric motor propulsion systems in battery powered UAVs have an operating efficiency close to 80% [165], an advantage compared to internal combustion engines, which have a thermal efficiency of nearly 40%. As a result of the low energy density of batteries (compared to that of hydrocarbon fuels), this often results in the largest component by weight in battery-powered UAVs being the battery itself. The use of a hybrid system can overcome some of the shortcomings of both conventional internal combustion engine propulsion and electric motor propulsion systems. Xie et al. [167] found that the use of hybrid propulsion systems can offer lower fuel consumption by 7% compared to using an internal combustion engine-powered aircraft. Another parameter to consider is the specific energy against overall efficiency [10]. This is because the weight of the UAV depends on the range and specific energy of the energy sources, however, the overall efficiency of the propulsion system remains relatively constant regardless of the range.

Currently, electric propulsion architectures can be divided into four main categories: full electric, turbo-electric, series hybrid electric and parallel hybrid electric [38]. As seen from the sections above, better energy storage and sources are needed for large electric transport aircraft to become feasible, and small and medium uncrewed aircraft are already feasible with electric propulsion. Some examples of current hybrid energy architectures are shown in Table 2.1.

TABLE 2.1: Examples of current hybrid energy architectures

Powertrain Topology	UAV	Purpose	Capabilities
Combustion engine Battery	*ScanEagle* [75]	Intelligence, surveillance and reconnaissance	20 hr endurance, 1,500 km range
	GL-10 [17]	Fixed-wing/multirotor hybrid	Distributed propulsion (10 motors), VTOL
	E-Fan X [4]	Passenger aircraft	Increased climb power with the gas turbines sized for cruise
Combustion engine Fuel cell	*HyFish* [72, 82]	Maritime surveillance	Fuel cell used for extended range, engine for high power demand situations
Battery Fuel cell	*Ion Tiger* [144]	Reconnaissance, surveillance and environmental monitoring	24 hr endurance
	HY4 [12, 108]	General aviation aircraft	80 kW fuel cell power output + batteries
	Phantom Eye [18]	Long-duration intelligence, surveillance, and reconnaissance	19,800 m operating altitude for up to four days
Battery Solar cell	*Pathfinder* [110]	Atmospheric research and environmental monitoring	24,000 m and a maximum endurance of over 12 hours
	Helios [111]	Atmospheric satellite	30,000 m, 14 electric motors and a maximum endurance of over 36 hours
	Zephyr-S [5]	Atmospheric satellite	21,000 meters, continuous flight for up to 30 days
Battery, Fuel cell and Solar cell	*EAV-2* [93]	Long endurance	Solar powered during the day, fuel cell powered during the night

2.1.2 Powertrain architecture encoding – background

Although one of the driving factors for hybridisation and electrification is to reduce the environmental impact [23, 27, 103], hybrid electric propulsion can also increase endurance [28, 115, 170] compared to vehicles operating with a single energy source. The available types of energy sources, storage and systems coupled with the ability to use more than one energy source to power a UAV mean that a UAV may have various energy architectures.

Donateo et al. [38] categorise electric aircraft propulsion into the following categories: full electric, series hybrid electric, parallel hybrid electric, and turbo electric. Classification for energy converters such as engines and EMs has also been done by Adamski [3] and Lieh et al. [96]. However, these are not comprehensive, do not portray the whole energy architecture and do not allow for the comparison of two similar architectures.

The American Institute of Aeronautics and Astronautics (AIAA) produced a set of recommended standard components. In their report [7], a pictorial representation (Figure 2.2) is used for the architectural representation of the energy system. It is a human-oriented pictorial representation and thus it is thus not suited for computational automation.

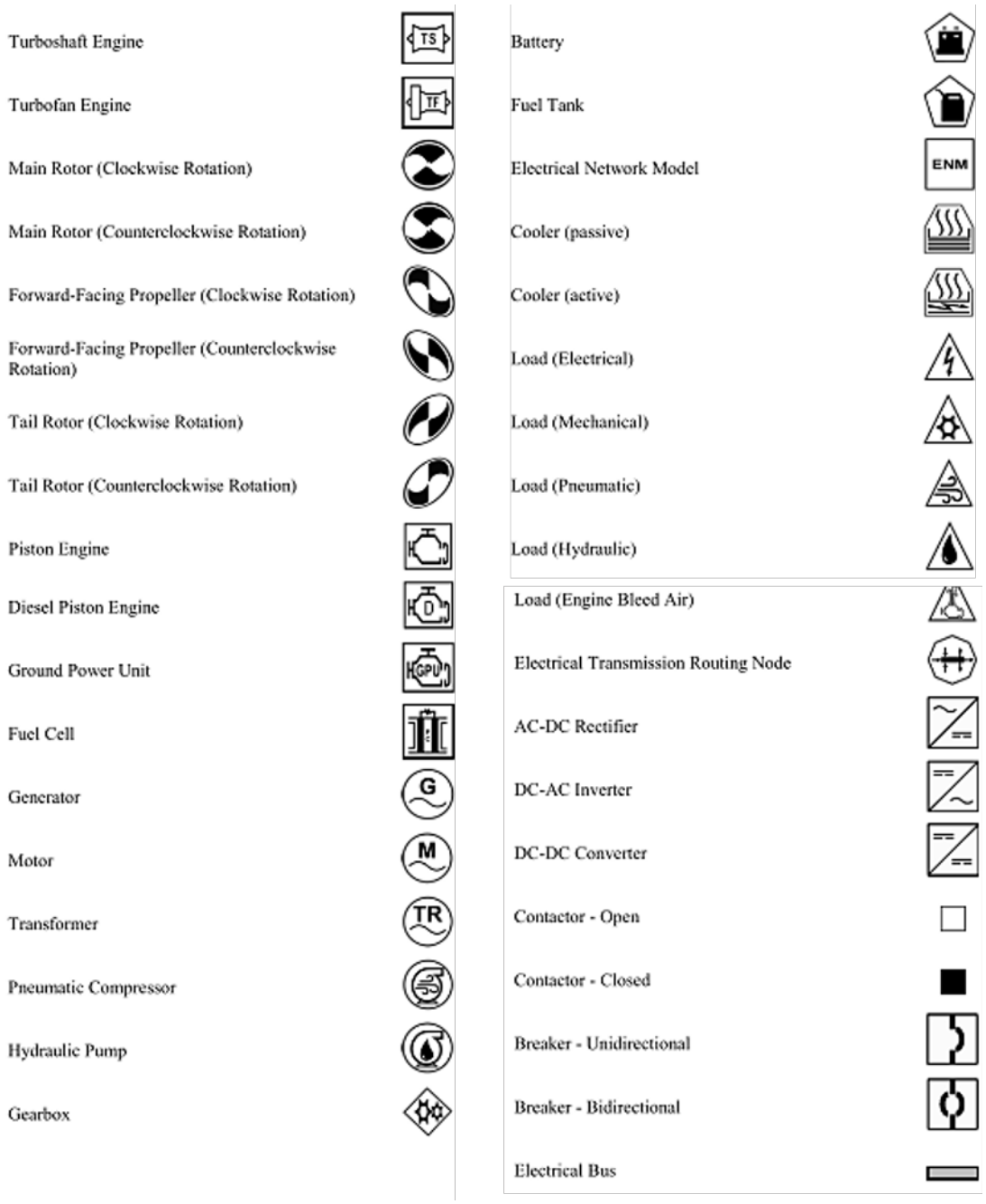

FIGURE 2.2: AIAA pictorial representation of energy architecture components [7].

A classification system by González-Espasandín et al. [59] has energy sources, energy storage and energy converters making up the propulsion system. Typical energy sources in the classification system include hydrocarbon fuels, solar energy and hydrogen. Similarly, a typical energy storage would include fuel tanks and batteries (including capacitors and super-capacitors). González-Espasandín et al. [59] further break down the energy converters into two types: mechanical energy converters such as IC

engines, fuel cells, and electric motors and lift and/or thrust converters such as propellers, jet engines and rotors. The encoding scheme we propose draws ideas from both of these classifications and expand upon to be suitable for specific topologies.

Read [125] proposed several rules of encoding, some of which include: the structure is to be uniquely described to avoid any ambiguity; user-friendly structure specifications are needed for ease of use, therefore the process should be simple enough to be done by hand for simple structures; and a machine-friendly and the machine-independent system is needed for interpretation and generation of a unique notation, therefore, the symbols should be familiar to the majority of users. This raises a few questions regarding the encoding of energy sources such as

- How to future-proof it for future energy sources?
- How to uniquely graph single or multiple energy architectures without raising ambiguity such as the same encoding mapping to two possible architectures or the architecture being encoded in more than one way?
- Would the machine encoding have to be human-readable? Do we need human-readable encoding?

2.1.3 String based encoding scheme

With the aforementioned requirements in mind, we have decided to take a broader look at string-based encoding of architectures in other fields, especially when representing molecular structures. A particularly compelling such approach is Simplified Molecular Input Line Entry System (SMILES) [161, 162, 163], a valence scheme approach based on the principles of molecular graph theory (Figure 2.3) by Weininger [161].

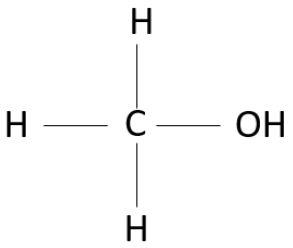

FIGURE 2.3: Methanol molecular structure as a valence scheme approach [7].

The SMILES method by Weininger [161] is both human-readable and relatively easy to implement computationally due to its compactness and only requiring a minimal number of rules. Similarly, as SMILES converts the pictorial structure (chemical) to a machine-readable structure (line notation), this can be applied to a UAV energy architecture encoding. One of the disadvantages of the SMILES scheme is that a molecule can be represented by multiple strings, therefore, just using SMILES string-like encoding would result in ambiguities when analysing energy architectures. To alleviate this problem in SMILES, a canonical labelling procedure was later produced [163]. Canonical labelling, as discussed by O'Boyle [113] is needed to generate a unique representation of the structure. For example, in [113], canonical labelling rules that, when reaching a branch point, multiple bonds are favoured over single bonds and using a depth-first search to start the graph traversal is employed.

In the SMILES algorithm, atoms are represented by their atomic symbols (such as C for carbon, and O for oxygen). In a UAV energy architecture encoding, the place of atoms could be taken by energy sources and other components.

The neighbouring atoms are represented next to each other. In the case of the example shown in Figure 2.3, the SMILES string would be `CO`. Similar techniques can be used in encoding a UAV energy architecture, for example, `prop en` can represent a propeller attached to an engine. SMILES utilises lower case letters to differentiate the atoms which are in aromatic rings and upper case letters for the atoms which are not (Figure 2.4). The use of numbers in Figure 2.4 signifies the connection between the two atoms in a cyclic structure. Parentheses are used to specify that the atom inside the parentheses is in the branch.

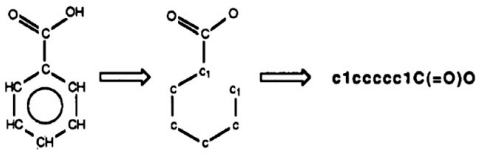

FIGURE 2.4: The use of lower case letters, upper case letters, parentheses, and numbers in SMILES [161].

Finally, in SMILES, the bonds are represented by symbols (Table 2.2). Bonds in the case of the UAV energy architecture as an example could be the mechanical connection output from the engine. This can, of course, only connect to a mechanical connection input (e.g. to a propeller).

TABLE 2.2: Bonds representations in SMILES [161].

Bond	Symbol
Single bond (usually omitted)	-
Double bond	=
Triple bond	#
Aromatic bond	:

Similar to SMILES, Sóbester [139] discussed parameterising aircraft geometric topology in a novel way through the use of hierarchical trees. This scheme includes splitting the aircraft components into classes such as 'L' for lifting surfaces, 'E' for enclosure such as payload or subsystem, and 'P' for propulsion. Components can be easily modified and reused in different contexts and are thought of as building blocks that can be assembled to create more complex geometries. These can then be used to speed up the design process and improve consistency.

From this classification, a broad range of UAV configurations can be obtained and evaluated, resulting in 34 basic aircraft geometries [116]. However, hierarchical trees are not particularly suitable for energy architectures as unlike aircraft topologies, cyclic connections can occur.

2.1.3.1 Graph theory approach - background

Graphs can generalise many abstract ideas, including energy architectures. A graph is a common data structure that has a collection of points (vertices or nodes), V, and lines joint some of these points (edges), E. The edges can be connected from any node to any other node, creating topologies.

Attributes are associated values for either the nodes or edges. These can also be embedded into the graph. When the set of nodes belongs to the specific graph, G, (syntax $V(G)$), the node element can be denoted using the index $v \in V(G)$. Similarly, for the edges belonging to the specific graph G (syntax $E(G)$), the edge element can be denoted using the index $e \in E(G)$ [76].

Graphs are a practical way to describe relationships amongst the object or to describe the topological properties [150]. However, exhaustive searches are impractical. From Sloane [138], the number of connected label graphs with n nodes is:

$$1,\ 1,\ 1,\ 4,\ 38,\ 728,\ 26704,\ 1866256,\ 251548592,\ 66296291072 \text{ for } n = 0, 1, ..., 9 \quad (2.1)$$

For example, a connected graph with three nodes would produce four connected graphs as seen in (Figure 2.5)

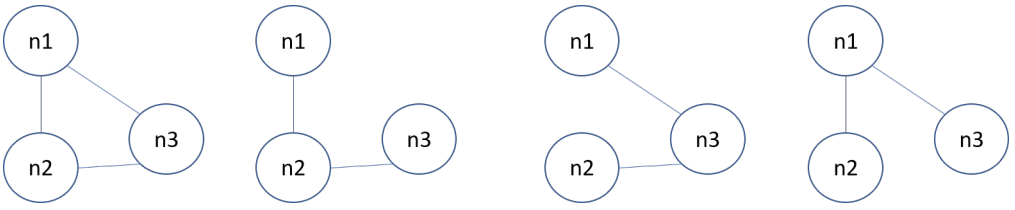

FIGURE 2.5: Total number of connected graphs with 3 nodes.

If unconnected graphs are considered [138], such as Figure 2.6, then the amount of graphs for n number of nodes increases dramatically

$$1,\ 1,\ 2,\ 8,\ 64,\ 1024,\ 32768,\ 2097152,\ 268435456,\ 68719476736 \text{ for } n = 0, 1, ..., 9 \quad (2.2)$$

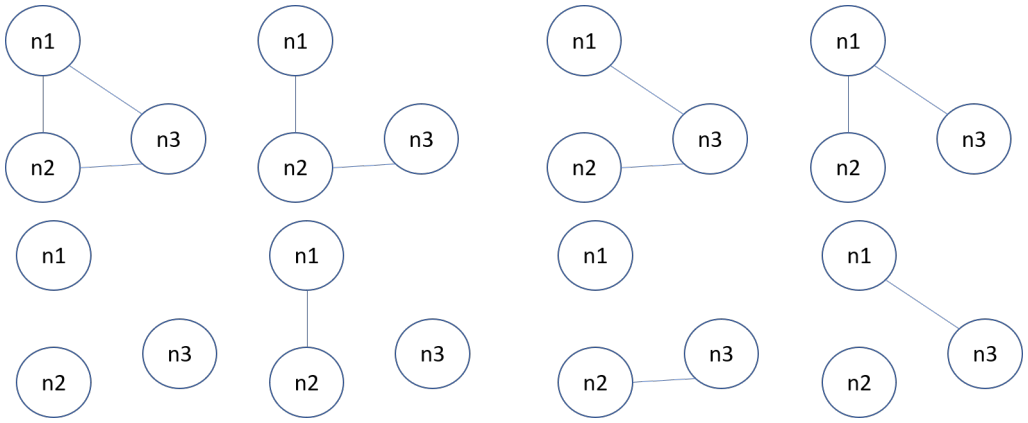

FIGURE 2.6: Total number of graphs with 3 nodes.

Taking into account the computation times, an exhaustive search would be costly. For example, if each graph takes one second to simulate, by having 10 nodes the simulation using a single core CPU, the search time would be around 2000 years without multiprocessing and assuming there are no infeasible topologies, no isomorphic graphs and the direction of the graphs is undefined. Therefore, heuristic search methods like evolutionary algorithms need to be explored.

2.1.3.2 Graph theory approach - application to powertrains

Powertrains for UAV can be analysed using graph theory - a branch of mathematics that studies the properties of graphs (i.e. networks of interconnected nodes). In the context of hybrid powertrains, graphs can be used to represent the flow of energy between different components of the system. For example, a graph can be used to represent the power flow between the battery, engine and propeller, with each component represented as a node and the power flow represented as edges. This graph can then be used to analyse the efficiency and performance of the powertrain under different operating conditions and control strategies.

Lawhorn et al. [89] proposed a method that leverages graph theory to model and optimise the power system of electric aircraft. It highlights the potential benefits of electric aircraft, including reduced fuel consumption, lower emissions and quieter operation. However, Lawhorn et al. [89] also notes that optimising the power system of electric aircraft is a complex task, requiring the integration of multiple subsystems and components. Lawhorn et al. [89] argued that current optimisation methods are often limited by a large number of variables and constraints and a lack of scalability. The proposed method uses a scalable graph theory to model the power system of the aircraft, representing components as nodes and connections as edges. This allows for the use of graph algorithms to optimise the power system, such as finding the shortest path between components or identifying critical components. Lawhorn et al. [89] then applied the method to a conceptual electric aircraft design. Lawhorn et al. [89] describe how the graph theory approach is used to model the power system and optimise it by reducing weight, improving efficiency and increasing reliability. The results of the case study show that the proposed method was able to optimise the power system of the aircraft and improve its overall performance.

In [90], the methodology was improved to a network graph technique for designing electric aircraft power systems. The proposed technique allows for the modelling and optimisation of the power system as a network of interconnected components, taking into account the various design objectives and constraints. One such constraint is that from every possible combination of propulsor and energy source considered, feasible sub-graphs, which meet the power and energy input requirements from the user, are extracted. The results indicate that higher efficiency is achieved at the cost of mass in systems with battery energy storage and that the technique is effective in designing a power system that meets the required specifications and is efficient and reliable. Lawhorn et al. [91] expanded the work into distributed propulsion, where the results indicated that smaller propulsors have an overall favourable efficiency and prove to be more survivable, at the cost of an incurred mass.

However, one limitation of Lawhorn et al. [89, 90, 91] is that the proposed approach has only been applied to a conceptual electric aircraft design, and further research is

needed to validate its effectiveness on other electric aircraft designs. Additionally, the authors do not discuss the potential limitations and drawbacks of using graph theory to model and optimise power systems.

Docimo and Alleyne [36] proposes a new approach for modelling and controlling an electric vehicle's thermal and electrical dynamics based on the development of a graph-based model that represents the thermal and electrical subsystems of an electric vehicle. The graph-based model consists of nodes representing components such as batteries, motors, and heat exchangers. The edges represent the connections between these components. The paper presents a detailed description of the graph-based model, including the mathematical equations used to describe the thermal and electrical dynamics of each component. This graph-based model allows for a hierarchical control strategy that optimises the performance of the vehicle while ensuring safety and reliability. The approach is demonstrated through a case study of an electric vehicle, which shows that the proposed approach achieves better performance in terms of thermal management and energy efficiency compared to traditional model-based approaches.

To evaluate the effectiveness of the proposed approach, Docimo and Alleyne [36] apply it to a case study of an electric vehicle. The results of their approach are compared with those of a traditional model-based approach and demonstrate that their approach achieves better performance in terms of thermal management and energy efficiency. Overall, the paper presents a novel approach for modelling and controlling an electric vehicle's thermal and electrical dynamics. The graph-based model provides a flexible framework for hierarchical control, which can be adapted to different types of vehicles and control objectives. However, it is important to note that the approach has only been demonstrated in a single case study and further research is needed to evaluate its effectiveness on different types of electric vehicles and in different operating conditions.

In summary, graph-based approaches are often used for powertrain optimisation in uncrewed aerial vehicles because they provide a flexible and efficient way to model the complex interconnections between the different components of the powertrain. UAVs' powertrains typically consist of multiple subsystems, including the propulsion system, energy storage system, and control system, which all need to work together in

a coordinated manner to ensure efficient and reliable operation. The interactions between these subsystems can be highly complex, making it challenging to develop accurate and efficient models for powertrain optimisation. Graph-based approaches can simplify this complexity by representing the powertrain as a graph, where the nodes represent the components of the powertrain and the edges represent the connections between them. This graph-based representation allows for a modular and hierarchical approach to modelling and optimisation, where each component can be modelled independently and then integrated into the overall powertrain model. This is the key advantage, where a graph-based approach can capture the dependencies between different components of the powertrain system. For example, the power output of the motor depends on the battery voltage and current, the propeller speed, and the ambient air temperature. By representing these dependencies in a graph, it becomes easier to analyse the system and optimise its performance. This allows for the development of optimal control strategies that take into account the interactions between the different components of the powertrain. This can result in improved performance and efficiency of the UAV powertrain. Based on these findings, in Chapter 3 we propose a solution based on the SMILES approach for compactness and flexibility. The graph approach is an efficient way to model the powertrain topology that can also be applied in an optimisation problem.

2.2 On-board powertrain components and the model choices

Now that we have discussed how the overall modelling is approached, we now discuss how the individual components are modelled. Regardless of the propulsion architectures, one of the parameters that determines the capability of a UAV is the choice of the overall energy system [3]. The choice of energy storage and supply interlinks with the mission and shapes the structure of the UAV. A UAV has three main energy consumers: propulsion, avionics, and payload. An example of a propulsion system of a UAV can be divided into the following:

- Energy source (such as petrol) required for the mission.

- Energy storage which would store the required energy source (fuel tank which stores the petrol).
- Energy converters (engines and electric motors) which then convert the energy into *useful* energy.
- Energy transmitters which transmit the same form of energy from one component to the other.
- Energy sinks convert energy into a useful function such as propulsion.

For example, a long-endurance mission may use wet fuel such as petrol as an energy source which is stored in the fuel tank (energy storage). The internal combustion engine is an energy converter that converts chemical energy into useful mechanical output, and the gearbox is an energy transmitter that may be used in the connection between the internal combustion engine to the propeller. Finally, the propeller, which may be attached to energy converters, such as an internal combustion engine or an electric motor, serves as the energy sink and converts the mechanical energy into propulsive energy. In addition to transmitters such as gearboxes, components such as electronic speed controllers (ESCs), which control the electric motors and in some cases power the on-board avionics, can also be classified as energy transmitters. Maximum power point trackers (MPPT) for photovoltaic cells, which modify the voltage of the solar panels to extract maximum power, are also considered energy distributors. In this section, we will go through the energy sources and components considered in this research project.

The component models used here are chosen for their relative simplicity, sufficient accuracy and efficient enough to aid in the modelling and the optimisation process described in Chapter 5.

1. Propeller surface model - based on interpolation of empirical data from APC Propellers [11].
2. Electric motor model - based on Drela's work Drela [43].

3. Internal combustion surface model - based on empirical data from Hung and Gonzalez [73] as well as in-house experimentation and Willans approximation for extrapolation into other combustion engines.

4. Battery model - based on Zhang et al. [172] of Lithium Polymer batteries.

5. Fuel cell model - based on Saleh et al. [131] of proton exchange membrane fuel cell.

6. Solar cell model - based on Lee et al. [93] with aid of the manufacturer's data sheets.

It is important to note that we use commercial off-the-shelf data for the choice of components, and assumed that all commercial off-the-shelf data are correct. The mass models also comes from these data. While commercial off-the-shelf data can be a valuable resource for many applications, it is not always accurate, complete and consistent. Especially at the low end of commercial off-the-shelf component that we are interested in in this study, complete data required for the models are seldom given, leading to the use of regression (I_{max} regression section B.3), interpolation (section B.1), or the use of existing coefficients based on the literature (section B.4, B.6, B.5). Moreover, commercial off-the-shelf data suffer from inherent biases that can influence the analysis (such as exaggerating the maximum allowable power output). Therefore, it is important to evaluate and validate the quality, relevance, and applicability of commercial off-the-shelf data before relying on it for critical decisions. However, commercial off-the-shelf data provides a benchmark for comparative analysis which can aid in decision-making. One other advantage that commercial off-the-shelf offer is that we know the components exist, making it easier to integrate standardised components into the powertrain system.

Component modelling is important in parameterisation because it allows for an accurate and detailed representation of the system. By breaking down the system into its individual components, each component can be modelled and analysed separately, which can provide insight into how each component contributes to the overall system behaviour. For example, in the context of electric UAVs, modelling the battery, motor and propeller as separate components allows for a more precise determination of

the vehicle's performance characteristics, such as range, acceleration and top speed. This information can be used to optimise the vehicle's design, including selecting the appropriate components and determining their optimal parameters.

2.2.1 Internal combustion engines

In the work presented here, we will only consider spark ignition, two-stroke and four-stroke petrol-based internal combustion engines. For small UAVs, gas turbine engines are not considered due to their poor performance, as well as the lack of data available compared to the two and four strokes engines. Internal combustion engines combined with fossil fuels are typically used in long-endurance UAVs as they have a relatively high gravimetric energy density compared to other energy sources, 48 times higher when compared to off-the-shelf lithium polymer (lithium polymer) batteries [134]. According to Adamski [3], UAVs weighing more than 50 kg are mainly powered by four-stroke piston engines as they have better efficiency, efficient cooling, and a decrease in the production of exhaust emissions compared to two-stroke engines. However, compared to two-stroke engines, four-stroke engines contain more moving parts, which account for a higher power-specific mass. Two-stroke engines can achieve a high power-to-weight ratio by performing two-cycle processes in each stroke of the piston [31], but one of their shortcomings is that the engines need to operate at a higher temperature and produce more exhaust fumes compared to four-stroke engines. This makes four-stroke engines particularly favourable compared to two-stroke engines. However, successful two-stroke engines can also be used for larger UAVs, as shown by *AEROSONDE* [146], a fixed-wing UAV with a 3.7 m wing span and a mass of 36.4 kg which uses a two-stroke jet fuel SI engine [97]. The aircraft is capable of carrying a 9.1 kg payload and has an endurance of more than 14 hr.

The efficiency of the powertrain component is one of the important parameter during the design decision process. Regarding thermal efficiency (the ratio of actual work per cycle to the amount of chemical energy released during the combustion process [121]), even though internal combustion engines use high energy density liquid hydrocarbon fuel, for a small civilian UAV powered by internal combustion engines are at most 34%

to 40% due to mechanical losses such as piston and crankcase motion leading to high friction losses and heat loss during the conversion process [41, 73]. Furthermore, the performance data stated by the publishers, especially for small internal combustion engines, are overstated. To account for the incomplete combustion process, the fuel conversion efficiency, η_f (the ratio between the useful mechanical work produced by the engine and the theoretical energy content of the fuel mass) can be used, which is calculated as:

$$\eta_f = \frac{1}{\text{bsfc } Q_{LHV}} \tag{2.3}$$

$$\text{bsfc} = \frac{\dot{m}_f}{P}, \tag{2.4}$$

where η_f is the fuel conversion efficiency, P is engine power [W], $\dot{m}_f$ is the mass flow rate of fuel (kg s^{-1}), bsfc is the brake specific fuel consumption [g $(Wh)^{-1}$], and Q_{LHV} is the lower heating value of fuel [Wh g^{-1}].

2.2.1.1 Internal combustion engine - model choice

The performance of an engine is typically given by obtaining the engine torque and engine speed values, imposed with constant map contours bsfc(also known as engine maps). The area of the map with the low bsfc shows the area which the engine is at a low fuel consumption [57].

If a sizing process requires a combustion (piston) engine, the optimal size of the engine needs to be determined from the available engine maps. However, there are limited number of available engine maps as these maps cannot be found easily via open sourced.

One method for finding an optimal size, especially in the early stage of the design is to use a scaling method for the engine maps as the internal combustion engines are generally scalable [68, 127, 140, 177]. This allows the representation of combustion

engines belonging to the same category using the same basic model and ensures that the model is independent of the scale used based on the Willans line formulation. This is a widely used and verified quasi-static method, that predicts the performance of unknown-scaled engines of the same family. The scaling procedure is shown in Figure 2.7.

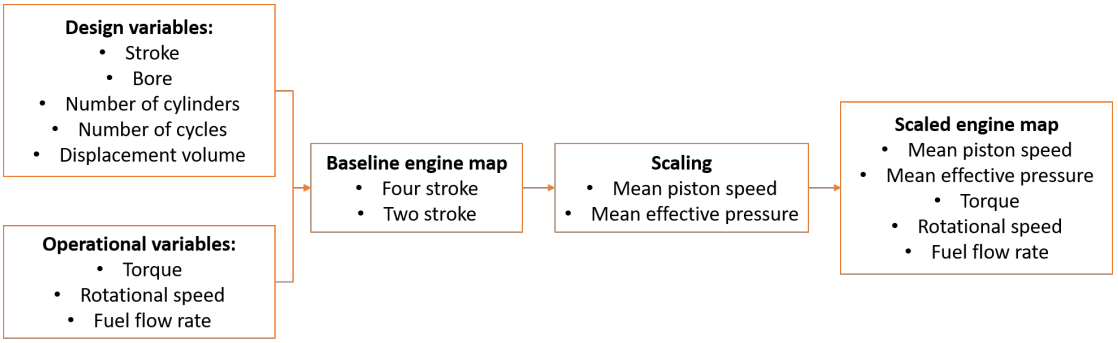

FIGURE 2.7: Internal combustion engine scaling process.

In Appendix B - Section B.2, the combustion baseline engine models, OS GF-40: a four-stroke internal combustion engine; acquired experimental data for the OS GF-40 as part of an undergraduate project [106] and the EL-005: a two-stroke internal combustion engine obtained from Hung and Gonzalez [73], are modelled, using the torque-speed-fuel consumptions relations, along with the detailed methods on how Willans approximation (detailed methodology given in Appendix B - section B.2.1) is applied to the two experimental engines and the limitations.

2.2.2 Solar cells

Solar cells (or photovoltaic cells) convert solar energy to electrical energy in the form of direct current. The cells are made of semiconductor materials. When solar energy hits the cells, the electrons from the semiconductor can escape from the atoms, creating electron-hole pairs [93]. The most attractive aspects of solar cells are that the energy source is free and practically unlimited. Annually, nearly 4×10^6 exajoules ($1\,\text{EJ} = 10^{18}\,\text{J}$) of solar energy reaches the Earth of which around 5×10^4 EJ is claimed to be harvestable [81].

Therefore, solar cells could allow for a theoretically perpetual flight, given that the aircraft is at a high enough altitude to glide down during night time and/or has a hybrid energy system where a battery or fuel cell activates at night time. Such an example is *PHASA-35* (Persistent High Altitude Solar Aircraft), (Figure 2.8), a 35 m wingspan and 150 kg maximum take-off mass solar electric UAV developed by BAe Systems and Prismatic, which successfully completed the flight test in February 2020 in South Australia. The test proved its potential to stay airborne for a year using solar power during the day and batteries during the night, operating in the stratosphere.

FIGURE 2.8: PHASA-35 [15]. The aircraft has a wingspan of 35 m and a gross take-off mass of approximately 150 kg.

Photovoltaics modules are suited to High Altitude Long Endurance (HALE) UAV to obtain as much sunlight as possible with a large wing surface area (Figure 2.9, Figure 2.10) to accommodate the photovoltaics panels, therefore, the power-to-area ratio is another important parameter to consider.

FIGURE 2.9: SAT_i [153]. It has a wingspan of 7.3 m and MTOM of 6.3 kg.

However, several factors such as location, climate, rotation of the Earth, and geography affect the intensity of the solar influx and the energy available. Careful considerations of the location of the initial and final destination need to be made. The system is also limited by the geometry of the platform (Figure 2.8, 2.9, 2.10) and low solar cell efficiency. The thickness of the solar cells is usually around 0.2 to 0.4 mm and the areas are around 100 cm^2 with the shape tending to be square, rectangular, or circular [154].

FIGURE 2.10: APUS DUO 15 [153]. The aircraft has a wingspan of 15 m and a gross take-off mass of 43 kg.

Moreover, since the airspeed and altitude of the flights are not always constant, the open circuit voltage (V_{OC}) and the maximum power of solar cells are also not constant [129]. To extract the maximum energy from the photovoltaics module, a maximum power point tracker (MPPT) system is used [28]. The maximum power point tracker optimises the power output of the solar cell by continuously adjusting the operating conditions of the photovoltaic cells to maintain the maximum power point, the point where the power generated by the cells is at its maximum point (in the voltage-current curve) and ensures that the solar panels operate at their highest efficiency.

Other important factors of solar cells noted by Chin [30] include the cell open circuit voltage (V_{OC}), short circuit current (I_{SC}), maximum power, fill factor (FF), and energy conversion efficiency. V_{OC} is independent of the cell size and is fairly constant with varying intensity. However, as the temperature rises, V_{OC} decreases at a rate of 2 mV C^{-1}. Short circuit current, on the other hand, is relatively constant at high temperatures, but it is directly proportional to the cell size and intensity. The maximum theoretical power is the product of V_{OC} and I_{SC}. The FF is the ratio of the actual power output to the theoretical power output.

Current conversion efficiency (Equation 2.5) is the most common parameter when comparing solar technologies. The efficiency parameter can be affected by multiple factors, such as wavelength, reflectance, and temperature [156]. The efficiency of a solar cell is the ratio of incident power (the power input from the sun to the module) which is converted to electricity (useful power output) [71] and is defined as:

$$\eta_{\text{PV}} = \frac{V_{\text{OC}}\, I_{\text{SC}}\, \text{FF}}{P_{\text{in}}}, \tag{2.5}$$

where η_{PV} is the current conversion efficiency, V_{OC} is open circuit voltage (V), I_{SC} is the short circuit current (A), FF is the fill factor and P_{in} is the input power of the efficiency. P_{in} is calculated using standard test conditions where solar irradiance is 1000 Wm^2 for the cell temperature of 25 $^{\text{o}}$C [137].

Typically, the solar cells used in UAVs have an overall efficiency of around 15 to 20% [129, 148] although US company Alta Devices (which has now ceased operations) claimed to have achieved 28.9% for a single p-n junction cell and 31.6% for dual p-n junction cells [156].

Finally, energy storage is an important part of solar-powered UAVs as solar-powered UAVs generally need some means of storing energy, for example, to ensure an uninterrupted energy supply at night. Solar cells are often used in combination with lithium-based batteries (E.g. *Zephyr 7* UAV (Figure 2.11)) and with fuel cells (e.g. *Helios* UAV (Figure 2.12)). The need for energy storage leads to around 30 to 50% of the total weight of the UAV being an energy storage system, considering the aerodynamics, overall geometry, and payload capacity. As for propulsion systems, direct current motors are preferred as the output of the solar energy system is direct current, thus, increasing the energy conversion efficiency as well as reducing the required conversion equipment and therefore directly reducing the aircraft's weight.

2.2.2.1 Solar cells - model choices

According to Lee et al. [93], for modelling a photovoltaic module, the equivalent electrical circuit can be divided into three models: the one-diode model, the two-diode model, and the empirical model. Since the parameters required for the empirical model are available from the manufacturer's data sheets, Lee et al. [93] employed the empirical method. More information regarding the three different models mentioned above can be found in Alrahim Shannan et al. [8], Dey et al. [34], Abounada et al. [1], Jervase

FIGURE 2.11: High Altitude Pseudo-Satellite (HAPS) Zephyr in preparation before take-off [5]. This UAV has a wingspan of 25 m and weighs less than 75 kg.

FIGURE 2.12: Helios in flight [111]. This UAV has a wingspan of 75 m and a gross mass of up to 929 kg.

et al. [80]. The models applied in this work and the relevant output are in Appendix B - Section B.5.

2.2.3 Fuel cells

Fuel cells are electrochemical conversion devices that convert reactants into electrical power. The by-products of the electrochemical reaction are water, heat, and low oxygen-containing exhaust air [103, 108]. The difference between a battery and a fuel cell is that the battery stores the electrochemical energy, whereas, in a fuel cell, the chemical energy is supplied to the fuel cell, which is then converted into electrical energy. There are six types of fuel cells available: proton exchange membrane fuel cell

(PEMFC), alkaline electrolyte fuel cell (AEFC), solid oxide fuel cell (SOFC), phosphoric acid fuel cell (PAFC), molten carbonate fuel cell (MCFC) and direct methanol fuel cell (DMFC) [45]. Among the six classes of fuel cells, PEMFC (Figure 2.14) has the highest efficiency between 40 to 60% in comparison to DMFC which has 20 to 30% efficiency and SOFC which has 30 to 50% efficiency [46, 58]. Figure 2.13 shows the reaction in the fuel cell stack in the PEMFC. Here, we limit ourselves to PEMFC due to the models and data available.

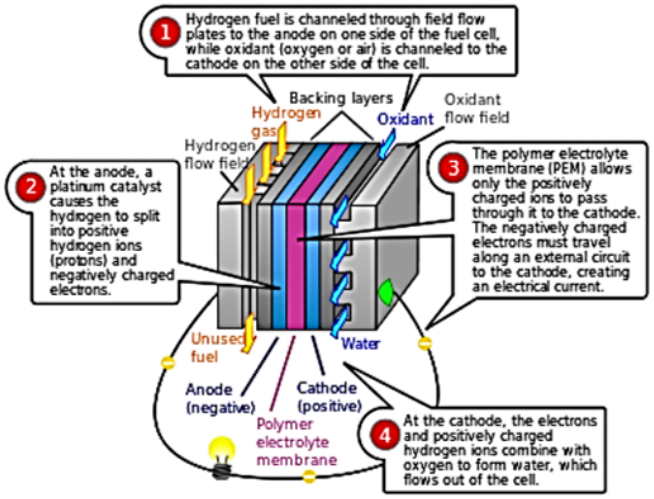

FIGURE 2.13: A fuel cell stack [9] summarising the proton exchange membrane fuel cell.

Hydrogen is the typical energy source of fuel cells and has the highest specific energy of all non-nuclear fuels [143]. Hydrogen is stored as high-pressure gas, typically 350 to 700 bar [69] using tanks and pressure regulators. The tanks and pressure regulator take up 95% of the storage system mass to accommodate the high-pressure requirements and therefore reduce the specific energy of the system [143]. If the pressure is reduced, tanks of larger volume are required, which leads to aerodynamic and weight penalties. The fuel cell system and hydrogen storage in the UAV typically use up 40% of the vehicle gross take-off weight [145].

The three basic subsystems of the fuel cell [9] are: the fuel source, an electro-active material delivered from the fuel tank which undergoes the electrochemical oxidation to produce ions and electrons; the cell stack, containing the anode, cathode, and electrolyte which converts the fuel to electricity; and finally a balance plant which is auxiliary equipment to provide the electricity to the load. A catalyst such as platinum is

used to coat the cathode and anode to increase the rate of the chemical reaction.

An additional complexity found by Saleh et al. [131] is that for the sufficient flow of air to the fuel cell, the fuel cell stack must be able to receive the flow of air through its intake directly, which is fed to the cathode as well as for sufficient cooling. Moreover, the difficulty of starting the fuel cell stack at subzero ambient temperature is a challenge as the water produced in the cathode can turn into ice, blocking the reactants from reaching the reaction interface as well as changing the conductive properties of the electrodes. Therefore, careful thermal and water management is needed for fuel cells to be operational at high altitudes and low ambient temperatures, such as a compressor, which also required a considerable amount of power and additional mass. The power output ranges between 100 W to several kW [46].

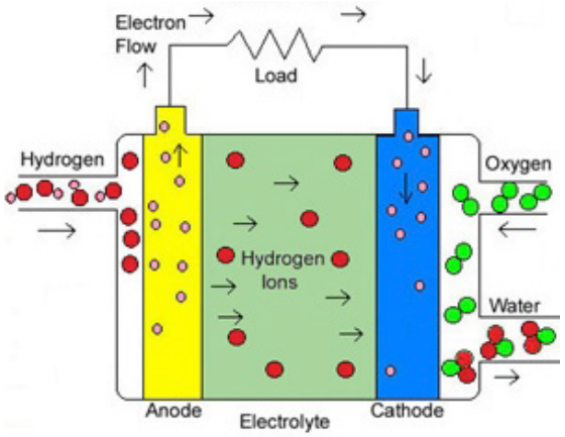

FIGURE 2.14: PEMFC general schematic [9].

Gaseous hydrogen (GH_2) energy density ($kWhm^{-3}$) is only 8% that of petrol due to its inferior volumetric efficiency at the lowest pressure storage (35 MPa) (Table 2.3). As opposed to GH_2, storing the liquid hydrogen LH_2) offers higher volumetric efficiency, as well as a lighter tank weight [58]. However, the main challenge of LH_2) storage is to match the rates of LH_2) to the consumption rate of GH_2 by the propulsion system. This requires a controlled heating element, while careful thermal management is also required for the safe operation of the LH_2).

TABLE 2.3: Comparison of fuel cell energy sources against internal combustion engines (three s.f.) based on [107, 119, 151].

Type of fuel	Petrol	Diesel	[20 C, 1 atm] Hydrogen	Methane	Propane	[20 C, 35 MPa] Hydrogen
Density [kg m3]	702	855	0.09	0.64	1.77	25.0
Specific energy [kWh kg^{-1}]	11.9	11.6	33.3	13.9	12.9	33.3
Energy density [kWh m^3]	8670	10100	2.79	9.06	22.6	776
Mass [kg] containing the same amount of energy as 1 kg of petrol	1.00	1.02	0.356	0.853	0.921	0.356
The volume required [m^3], with respect to 1 kg of petrol, excluding additional requirements, i.e. structure	1.42×10^{-3}	1.2×10^{-3}	3.96	1.33	5.21×10^{-1}	1.42×10^{-2}

As for energy conversion, compared to internal combustion engines, fuel cells do not need moving parts, which makes them more reliable, mechanically simpler to maintain, and result in little to no vibration effects. Fuel cells are 40 to 50% efficient (2 to 4 times more efficient compared to a combustion engine) due to the losses from the auxiliary system for fuel cell stack operation [20, 144]. Moreover, typically the exhaust from fuel cells is water vapour, making it more environmentally friendly [103]. The first documented fuel cell flight for Micro Air Vehicle (MAV), was the Hornet MAV AeroVironment in 2003 which had an endurance of 15 min. In 2009, with a 16 kg gross take-off weight and a wingspan of around 5.2 m, the Ion Tiger flew for 26 hours [143, 145] using GH_2. By 2013, the endurance increased to 48 hr, again by Ion Tiger using LH_2 [58, 94, 136], highlighting the advances of fuel cell technology.

2.2.3.1 PEMFC - model choices

The experiment of Dudek et al. [44] found that, although there is a linear relationship between power and hydrogen flow rate, there is a slight deviation (Figure 2.15) from the linear relationship due to Faraday losses. Faraday losses occur when the electrons are separated from the hydrogen at the anode and go directly to the cathode through an electrolyte, instead of passing through the load, which would contribute towards useful work. Mathematically, Faraday losses can be represented as a ratio between the actual current produced and the maximum theoretical current produced. This loss is the reason why the open circuit voltage (V_{OC}) is higher for theoretical purposes compared to experimental ones. Finally, the thermal efficiency, η_{th} estimated by Equation 2.6 is around 0.469. From this equation, the time it takes for the fuel to be used at a given power requirement can be calculated. In this experiment, it was found that 1.1 litres of LH_2 at 225 bar provided a constant power draw of 200 W for 93 min. The equation for the η_{th} can be written as

$$\eta_{\text{th}} = \frac{P}{\dot{m}\, Q_{\text{HHV}}\, 0.28} \tag{2.6}$$

where η_{th} is the thermal efficiency, P is the power of the PEMFC stack [W], $\dot{m}$ is the mass stream of H_2 [ml min^{-1}], Q_{HHV} is the higher heating value of H_2 [141.88 MJ kg^{-1}] and 0.28 is the conversion factor from MJ to kW.

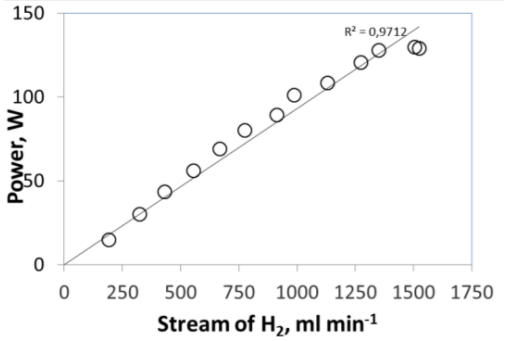

FIGURE 2.15: Results of AEROPACK Fuel Cell Tests: hydrogen flow rate plotted against the electrical power [44].

Dudek et al. [44] used a commercial AEROPACK PEMFC fuel cell stack in combination with a battery pack to observe the operational characteristics. The tests were conducted using a fixed-wing powered glider UAV with a 3 m wingspan, an MTOW of 5.5 kg and which required 200 W power for the cruise segment of the flight. The test revealed that after the maximum power is achieved at a certain current, the power supplied by the cell stack would fall beyond this point (Figure 2.16) which would create a power imbalance in the propulsion system. It was found that up to 5.5 to 6.0 A was withdrawn from the AEROPACK system and only at higher loading did the battery supplemented the additional power (Figure 2.16). Permitting that the current draw is low (up to 4 A), the voltage stays relatively stable for up to 120 minutes, however, with a higher current (above 6 A), the results show a gradual decrease in voltage, even with the help of a lithium polymer pack until, after at most 40 minutes, the voltage sharply decreased. This shows that when using the PEMFC, a high power demand needs to be avoided. Moreover, due to the overall lower system power density, high power density components such as batteries or capacitors are required to increase the performance, as seen in Figure 2.16, B. A final drawback of fuel cells is that their dynamic response is slow, making them unsuitable for abrupt power changes [94].

When calculating for the efficiency, some of the losses mentioned in Mazur and Domanski [103], Mench [107] as seen in Figure 2.17 include activation loss, mass transfer

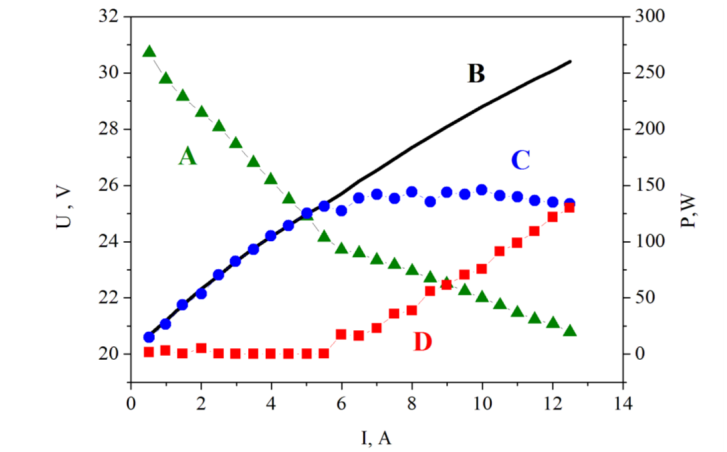

FIGURE 2.16: Results of Aeropack Fuel Cell Tests: A) Voltage vs Current - PEMFC stack, B) Power vs Current - battery and PEM stack hybrid system, C) Power vs Current - PEMFC stack and D) Power vs Current - battery pack [44].

losses, and ohmic loss. The activation losses induce voltage drops, which reduces the electromotive force during the direct current flow. The ohmic losses are due to the voltage drop caused by the internal resistance of the electrolyte because the ions and electrons flow through the cell. This loss increases linearly with the current increase. The loss of mass transfer occurs when the gas contacts the catalyst and the electrode consumption becomes faster, causing a sudden drop in the voltage.

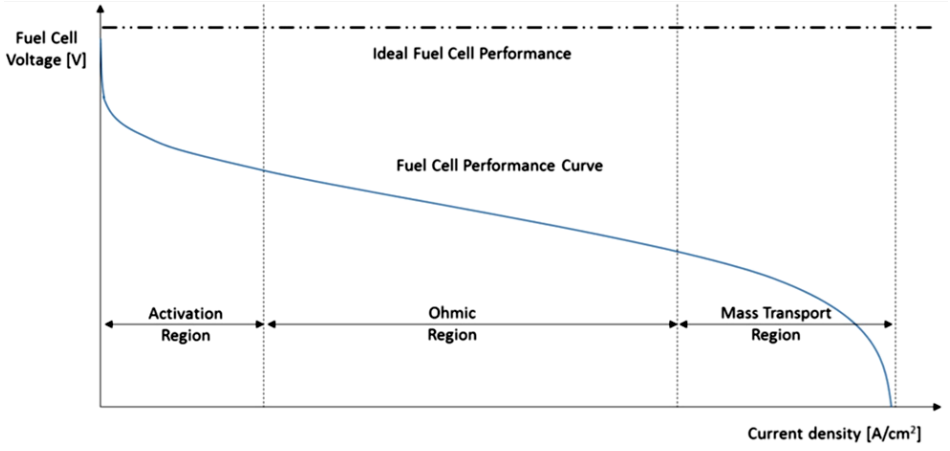

FIGURE 2.17: Losses in fuel cells [103].

Theoretically, a single fuel cell can generate an open circuit voltage (no load) between 1 and 1.2 V. However, with the load, due to the growing effects of irreversible processes in the cell, the voltage is reduced down to 0.4 0.5 V for DMFC, 0.65 0.7 V for PEMFC, and 0.75 0.85 V for SOFC [9]. Therefore, to increase the voltage, fuel cells need to be

stacked in series, where the total voltage is then the sum of the individual cell voltages [44].

Based on the information described above, we employed a semi-empirical equations with the assumption of the steady and adiabatic flow of ideal gas, uniform temperature of the gases inside the cathode and anode, and the temperature of the gasses being the same as the stack temperature. The models here are based on Saleh et al. [131]. The details of the models and its output are in Appendix B - Section B.6.

2.2.4 Batteries

Batteries are energy storage devices which store electrochemical energy with cells either connected in series or parallel inside the battery. The electrochemical cells convert the stored chemical energy to electrical energy due to oxidation-reduction (redox) reactions [23] by the cathode, anode, and electrolyte inside the cells. The choice of cathode and anode material determines the output voltage, capacity, and power.

The cathode, the positive electrode, consists of compounds such as lithium metal oxides in lithium ion batteries [168]. The choice of ion donor in the cathode material has an impact on the specific energy of the battery [176]. The anode, the negative electrode, consists of mostly carbon-based materials. Carbon-based materials, such as graphite, are used to increase the specific capacity of the cell [56]. The terminology of the battery comes from the cathode, for example, the lithium ion donator from the cathode results in the battery being called a lithium battery [176].

The battery module is made of cells either in series or in parallel, depending on their desired voltage output and capacity [41]. However, Donateo and Spedicato [41] mentioned that at least 30% of the final mass of the battery is due to the presence of control units such as the battery thermal management unit, the safety necessary for the fire hazard due to thermal runaway and other components, the final mass of the battery module is larger than the sum of cells. Moreover, the higher the discharge current is, the heavier the battery becomes.

Due to an agreeable size, low cost, and being the lightest metal in the periodic table, lithium-based batteries are the most common source for small UAVs [20]. Since lithium is highly reactive, for stability compound-based lithium is used [176] and this results in batteries having different characteristics. For example, for state of the art lithium ion with a graphite anodes and nickel, cobalt and manganese (NCM) cathodes, the nominal cell voltage is 3.7 V with specific energy of around 240 Wh kg^{-1} [47]. On the other hand, current commercial prototype cells such as lithium metal anode with an NCM cathode have a nominal cell voltage of 3.8 V and specific energy projected to be around 430 Wh kg^{-1} [47]. The light weight of the lithium metal, as well as a very low negative standard reduction potential, are added advantages of lithium-based batteries. Gallo et al. [53] discussed some of the attractive characteristics of lithium ion batteries which include high specific energy (150 to 250 Wh kg^{-1}); a high specific power (500 to 1000 W kg^{-1}); low self-discharge rate (0.1 to 0.3%) per day and good cycle life (2000 to 3000 cycles at 80% depth of discharge).

One of the downsides of lithium ion batteries is the thermal runaway condition where a battery is excessively heated through overcharging or short-circuiting, which can cause a fire hazard. Moreover, some of the electrodes and electrolytes are toxic, therefore safety measures need to be in place when recycling. Although at the cell level, state-of-the-art lithium ion have a specific energy around 250 Wh kg^{-1}, when taking into account of the thermal management system, battery management system and packaging, the specific energy can be reduced by 30 to 40% at the pack level, leaving to around 150 Wh kg^{-1} [47, 108].

Lithium polymer batteries, which have the polymer as the electrolyte, are the most widespread battery type used in UAVs. This is due to the minimal casing required and therefore leads to a low battery mass [133]. Schomann [133] notes that lithium polymer batteries have high specific energy (around 168 Wh kg^{-1}), high specific power (as high as 1 W kg^{-1}), and a high number of charge and discharge cycles with little to no memory effect (reduction of capacity due to incomplete discharge). Furthermore, the self-discharge rate of lithium polymer batteries is low, around 2 to 3% per month. However, excess charge or high operating temperature can cause a fire hazard due to

the decomposition of electrodes or electrolytes that release gas, expanding the casing, and inflammation [133]. Moreover, a good battery management system is required to ensure that all cells are charged equally to reduce the wear of the battery and to avoid the extraction of too much of the stored energy, leading to irreversible damage.

Compared to internal combustion engines, battery-powered propulsion systems are more reliable due to a lower number of moving parts [46]. However, the trade-off between batteries and conventional fuel is that batteries have a lower energy density compared to hydrocarbon fuels for internal combustion engines. lithium ion chemistry has a specific energy of around 220 - 240 Wh kg^{-1} at a cell level and around 200 Wh kg^{-1} at a pack level, whereas aviation fuel has a specific energy of around 11,100 Wh kg^{-1} [66]. Battery storage systems such as lithium polymer have significantly lower energy density and specific energy than wet fuel, such as petrol by roughly a factor of 48 in terms of specific energy and by roughly a factor of 30 in terms of gravimetric energy (energy density). As the energy required for flight must be stored on board, parameters such as the specific energy [Wh kg^{-1}] and the volumetric energy [Wh l^{-1} or Wh m^3] become important for quantifying and comparing batteries.

Volumetric energy is less critical in aircraft design if there is no limitation on the internal volume or space available. However, UAV design tends to impose geometry constraints. In a recent survey conducted on an existing electric aircraft by Hascaryo and Merret [66], batteries account for approximately 11% of the gross take-off weight for fixed-wing aircraft. They further mention that the lower specific energy of batteries means that even if the energy conversion of the battery is higher than that of internal combustion engines, for the aircraft to have a similar endurance, it would have to carry a heavier battery than its energy equivalent quantity of fuel. This highlights the current battery technology limit for electric aircraft. As a comparison for efficiency, Hepperle [69] calculated that for a fully battery-powered aircraft, the total powertrain efficiency can be calculated as 73% (Figure 2.18) when considering the efficiency chain, whereas for wet fuel energy sourced aircraft, the efficiency is around 39% (Figure 2.19) and for fuel cells around 44% (Figure 2.20).

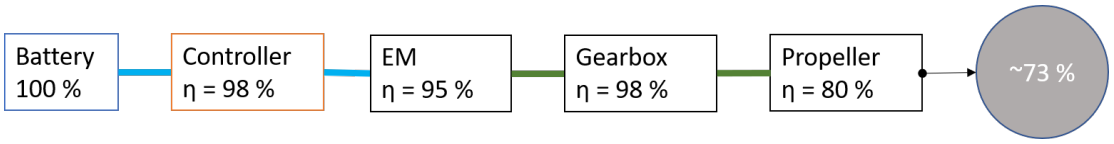

FIGURE 2.18: Efficiency chains with typical component efficiencies for battery-powered drive trains [69].

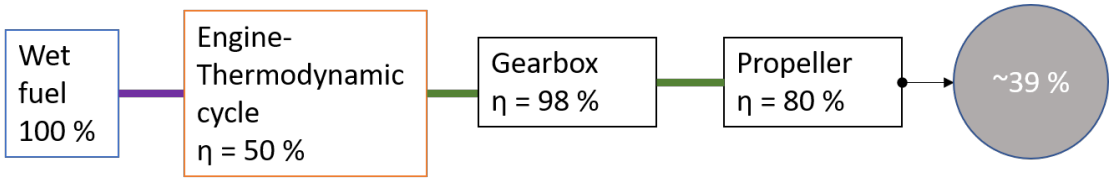

FIGURE 2.19: Efficiency chains with typical component efficiencies for wet fuel powered drive trains [69].

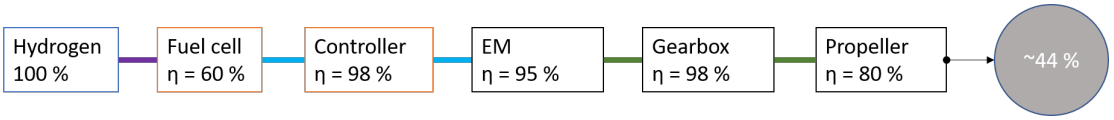

FIGURE 2.20: Efficiency chains with typical component efficiencies for fuel cell powered drive trains [69].

However, adding more batteries is generally not a solution. This is not only due to the space and weight constraints typical of aircraft design, but also due to diminishing returns. A sizing study by Hascaryo and Merret [66] found that the total maximum take of weight of the aircraft decreases with higher battery's specific energy (Figure 2.21) for a Cessna 172. At the same time, looking at the gradient in Figure 2.21, there is a diminishing decrease of specific energy. Therefore, at a given range, an improvement in the battery's specific energy will not be able to decrease the total weight significantly. Furthermore, adding larger wings, fuselages, or external energy pods to accommodate the energy storage would lead to losses in overall aircraft efficiency due to a larger wetted surface, adding cross-sectional area and mass.

Another important parameter of the battery is the capacity. The capacity of the battery is the amount of charge the battery can store and discharge. Typically, the nominal capacity is quoted for a battery. This assumes a constant discharge current. The C-rating quoted for a battery allows the user to calculate a maximum safe current draw through Equation 2.7:

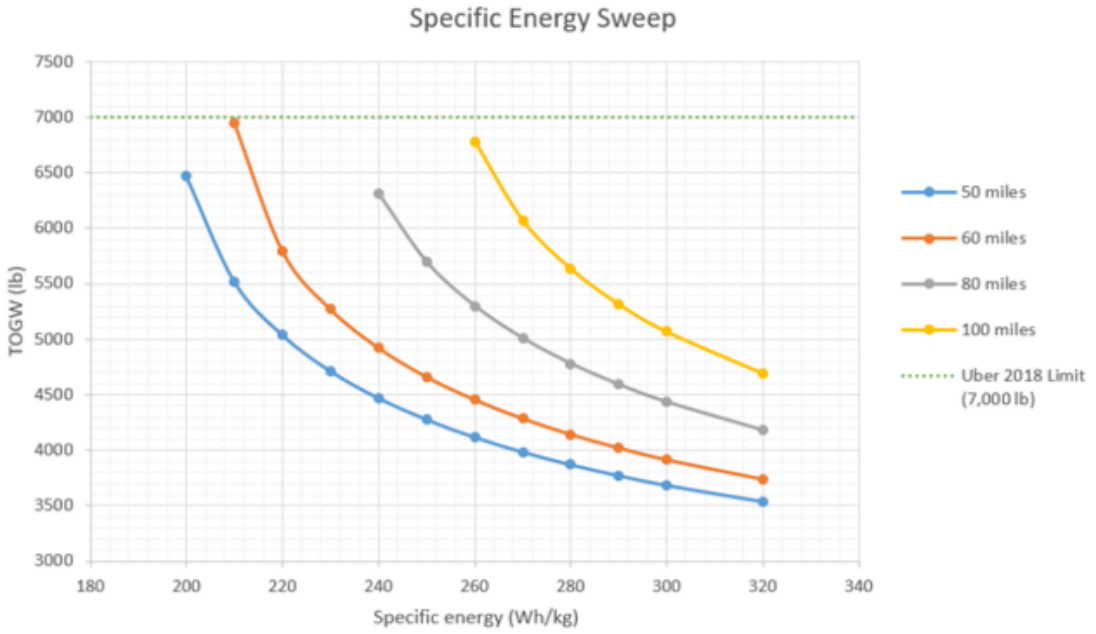

FIGURE 2.21: Take-off gross weight for various battery specific energies and cruise ranges [66]. 7000 lb is the limit that Hascaryo and Merret [66] imposed when doing the sizing calculations.

$$C_{\text{rate}}(t) = \frac{I(t)}{C_{\text{nom}}} \tag{2.7}$$

where I(t) is the charge or discharge current [A] and C_{nom} is the nominal charge capacity of the battery [Ah]. At a unity [1 C] discharge rate, the time taken for the nominal capacity to be fully discharged is 1 hr. A high C-rate allows for a faster discharge/recharge capability. Finally, another important parameter to know is the Peukert constant, due to the battery discharge rate affected by its effective capacity [74].

2.2.4.1 Lithium battery - model choices

To simulate the performance of a battery-powered energy architecture, a battery model approximating how the energy stored depletes is needed. Saldaña et al. [130] states that the complexity of the battery model should depend on the application. For example, the most detailed models are those that describe the electrochemical reactions that occur at the cell level such as [64]. However, they are complex to develop and may require

extensive computing resources. Equivalent circuit models are typically used to represent the entire battery by the equivalent characteristic behaviours which consist of the resistance and capacitance. These models have parameters estimated from empirical measurements and do not model the internal states of the battery. Although equivalent circuit models are simple with low model fidelity and computational cost, they are useful for systems with numerous components (such as hybrid energy systems) as they can provide relatively accurate state and transient behaviour of lithium ion batteries, therefore giving a rough approximation of system-level battery performance [168]. The details of the models, limitations and the model output are in Appendix B - Section B.4.

2.2.5 Electric motors

Electric motors are electro-mechanical energy converters that convert electrical energy into mechanical output to be used for propulsion. There are three types of electric motors: brushed DC or servo motors which have an efficiency of around 80%, induction motors with an efficiency of around 90%, and permanent magnet motors which have around 95% efficiency [95]. The losses are due to friction losses at the bearings, ohmic losses due to the heat dissipation occurring during the current drawn, iron losses such as hysteresis losses due to the alternating magnetisation of the iron core and eddy losses due to induced back-EMF [133].

Permanent magnet motors (a type of brushless direct current (BLDC) motor) are widely used in UAVs due to their lightweight, high efficiency, and low noise [112]. These are the only type of motors considered in this study. These motors are paired with electronic speed controllers to allow for speed control. Electronic speed controllers use electronic communication to change the direction of current going to the motor [67]. Therefore, although BLDC requires electronic speed controllers, the reduction in friction and heat dissipation compared to a brushed motor allows BLDC to accept a higher current draw and therefore higher specific power than brushed motors [133].

2.2.5.1 Electric motor - model choices

Relevant information such as mass, power, K_V ratings and current rating of 423 off the shelves brushless direct current (BLDC) motors are scraped from various commercial websites. Since K_V, I_0, and R tend to be given in the specification when buying commercial off the shelf motors, shaft power, torque and efficiency, following unit conversion, can be calculated. This is achieved using the equivalent brushed DC motor (Figure 2.22) equation developed by Drela [43]. These equations can be used to describe brushless DC motors. For simplicity, a first-order simplified model along with the following assumptions is applied when modelling electric motors.

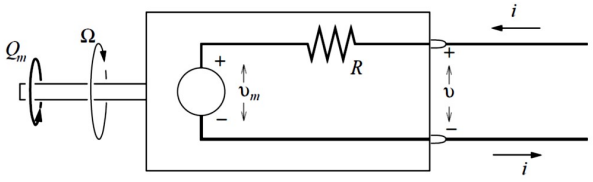

FIGURE 2.22: Equivalent Circuit for an electric motor [43].

In the case that I_0 [A], or R [ohm] or I_{max} [A] are not given by the manufacturer, the author's work is based on the regression models developed by Schomann [133]. This is useful as in some of the hobby electric motors, the maximum current data, internal resistance or the no-load current are not provided. However, it is important to know these parameters as an over-current causes the wires in the coil to heat up, which damages the coils and, therefore, should not be exceeded. This upper current limit is taken into account in the author's model.

The final parameter that is not required for the modelling but for refining the component list to a smaller subset is the peak power output from the electric motor, which sometimes is not provided by the manufacturer. To develop a regression model, the author first identified the features which are correlated to the power from the definite data given by the manufacturers (such as the geometry, mass and K_V rating). First, the correlations are extracted as seen in Figure 2.23 to observe the relations between each dependent variable and the independent variable (peak power output).

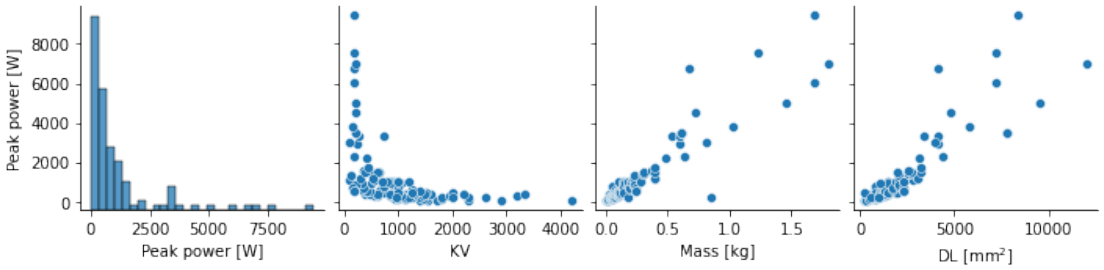

FIGURE 2.23: Features extracted from the datasheet identifying the correlations between the dependent and independent variables for electric motors.

In Appendix B - Section B.3, the use of Drela model, the details of the regression output, the formula derived from correlation and the output are discussed.

2.2.6 Propellers

Propellers for fixed wing UAVs convert the torque and rotational velocity into thrust which propels the UAV forwards. The propeller geometry and the relative wind at the blades are the main drivers of the generated thrust and the propeller efficiency. Propeller size is typically determined by the size and weight of the UAV. Larger UAVs require larger propellers with a greater diameter to generate enough thrust to overcome the drag. Propeller size is also influenced by the desired flight characteristics of the UAV, such as speed, range, and endurance. Propeller pitch refers to the distance that the propeller would travel in one revolution if it were moving through a solid medium. A higher-pitch propeller will move the aircraft faster, while a lower-pitch propeller will provide more thrust at low airspeeds. The pitch of the propeller is typically selected based on the UAV's weight and desired performance characteristics. Generally, the larger diameters coupled with low rotational velocity are more efficient than smaller diameter propellers rotating at high velocities. The number of blades on a propeller can also affect its performance. More blades typically provide greater efficiency and stability but they can also increase drag and weight, which can reduce the UAV's speed and endurance. The number of blades used is typically determined based on the size and weight of the UAV, as well as the desired flight characteristics. Another design

restriction for the propellers is their tip Mach number, which directly impacts the efficiency of the propeller, as well as increases noise. Finally, another constraint to consider is the ground clearance, which depends on the air-frame and the mode of take-off.

2.2.6.1 Propeller - model choices

Since propellers required their performance maps for modelling, in this work, we only consider the two-bladed propellers from APC [11]. Two-bladed propellers are generally more efficient than equivalent multi-bladed propellers because they produce less drag and have a simpler design, which can improve the overall efficiency of the UAV.

2.2.7 Propeller-electric motor matching

Matching a propeller to an electric motor is important to ensure optimal performance and efficiency of the system. If the propeller is too large or too small for the motor, it can result in inefficient power conversion, leading to wasted energy and reduced overall performance. Moreover, the propeller's size and pitch determine the amount of thrust it can generate, as shown in Figure B.1, matching the motor to the propeller ensures that the motor can provide enough power to spin the propeller and produce the required thrust for the intended application. If the propeller is too large or the motor is underpowered, it may struggle to produce enough thrust, leading to poor performance or even motor damage.

Electric motors have a rotations per minute (RPM) range at which they can operate and it can be given by the KV rating in the specifications typically. Matching the propeller to the electric motor helps ensure that the electric motor operates within its recommended RPM range. If the propeller is too large, it may require the electric motor to spin at a higher rotational speed than it's designed for, leading to excessive heat generation and potential motor failure. On the other hand, a propeller that is too small may not allow the electric motor to reach its optimal rotational speed range, resulting in reduced efficiency.

Therefore, propeller and electric motor matching is crucial to achieving optimal performance, power efficiency, thrust generation, and RPM range. Therefore, in this study, we also work on matching the propeller motor specific to the platform, decreasing the likelihood of mismatched propeller, as well as reducing the possible combinations.

TABLE 2.4: Propeller motor combinations for the test platforms after conducting a feasibility study.

Vehicle	Propeller	Electric motor	Number of combination
Peregrin	65 out of 521	94 out of 460	1381
Believer	145 out of 521	373 out of 460	7855

2.2.7.1 Well-matched systems vs ill-matched systems

As Drela [43] described, the propeller and electric motor are well matched if they are both operating close to their maximum efficiency. Figure 2.24a - 2.24f shows a coloured contour map of the torque, rotational speed, efficiency of propeller, electric motor and combined for a selected propeller motor combination - 'green' side show case the well-matched configuration and 'red' side for the ill-matched configuration based on the sizes of the components used in this study.

TABLE 2.5: Propeller motor combinations - component sizes for propeller and electric motor.

	Propeller	Electric Motor	Thrust [N]	True airspeed [ms^{-1}]
Well-matched	16.5x12	Hacker - A100-8 kv196	19-130	30-60
Ill-matched	11.5x6	SunnySky-kv 170	10-70	15-30

In a well-matched system, the efficiency of the propeller and electric motor are in a similar region, and the efficiency stays high for the larger range of thrust and airspeed required. This well-match system is shown in Figure 2.24a, 2.24c and 2.24e where propeller efficiency is high (0.7 minimum), electric motor efficiency is also high (0.82 minimum) for a large range of thrust from 19-130 N and a large range of true airspeed from 30-60 ms^{-1}. On the other hand, for the ill-matched propeller electric motor combination, not only are the high-efficiency regions for the propeller and electric motor opposite, see Figures 2.24d and 2.24b, the range of the high-efficiency regions are also lower than the well-matched propeller electric motor configurations. The process of propeller-motor matching is detailed in Appendix B - section B.7.1.

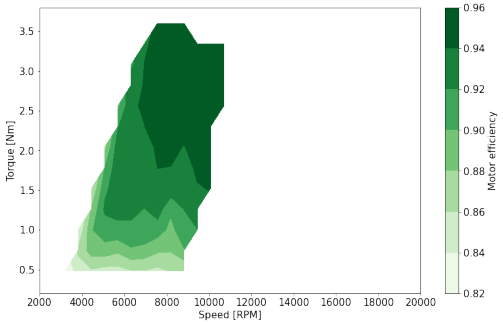

(A) Well-matched systems: torque against rotational speed with motor efficiency contour plot.

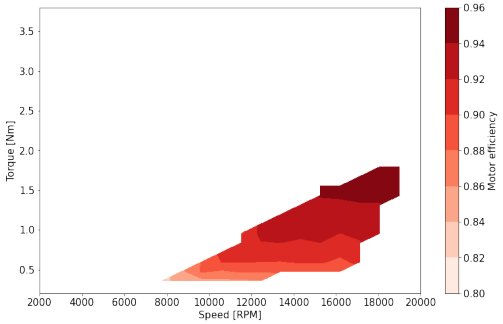

(B) Ill-matched systems: torque against rotational speed with motor efficiency contour plot.

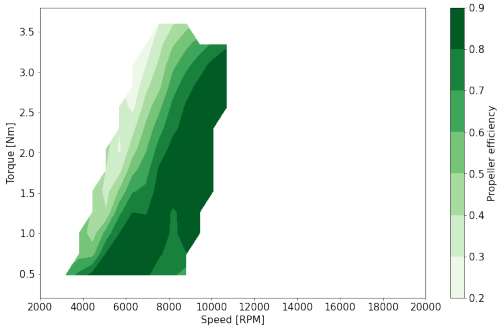

(C) Well-matched systems: torque against rotational speed with propeller efficiency contour plot.

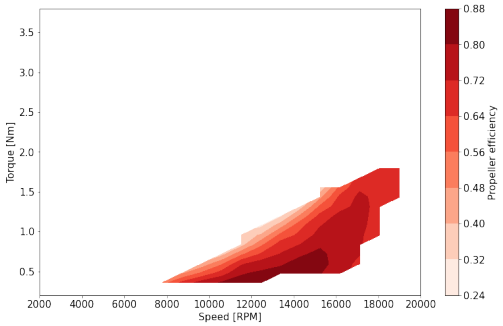

(D) Ill-matched systems: torque against rotational speed with propeller efficiency contour plot.

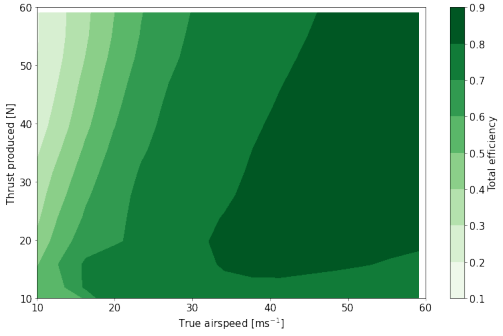

(E) Well-matched systems: thrust and airspeed range allowable with total system efficiency contour plot.

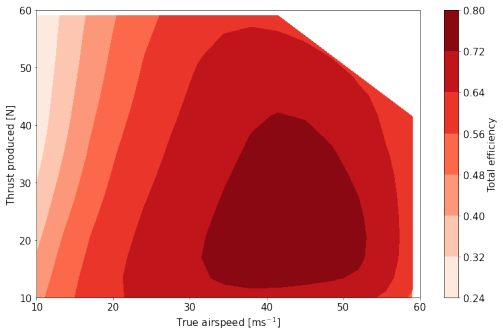

(F) Ill-matched systems: thrust and airspeed range allowable with total system efficiency contour plot.

FIGURE 2.24: Comparison plots of a well-matched propeller motor against an ill-matched propeller motor. The component sizes are found in Table 2.5.

2.3 Applications of modelling and simulations methods for UAV hybrid powertrains

The research on hybrid powertrain UAVs is focused on improving the performance, efficiency, and sustainability of UAVs for a range of applications such as surveillance, delivery, and agriculture [46] [147]. Some of the current research on hybrid powertrain UAVs includes:

- Modelling and optimisation of hybrid powertrain systems ([19], [21], [32], [77], [109]): Researchers are developing algorithms and optimisation techniques to improve the performance of hybrid powertrain systems. These techniques aim to minimise mass, minimise fuel consumption and emissions while maximising the UAV's endurance and payload capacity.
- Design of hybrid powertrain components ([2], [47], [70], [149]): researchers are developing new components such as batteries, electric motors, and generators to improve the efficiency of hybrid powertrain systems.
- Integration of hybrid powertrains with UAVs ([49], [68], [84], [128]): Researchers are exploring ways to integrate hybrid powertrains with different types of UAVs. This includes designing new airframes and propulsion systems that are optimised for hybrid powertrains.
- Flight testing and validation ([86], [93], [174]): Researchers are conducting flight tests to validate the performance of hybrid powertrain UAVs in real-world conditions. These tests aim to measure the endurance, payload capacity, and environmental impact of the hybrid powertrain systems.

In this study, we focus on the first point of research. Optimisation of hybrid powertrain systems for UAVs involves improving the overall efficiency and performance of the powertrain system. This can be achieved through various techniques, such as optimising the energy management strategy, improving component design, and reducing the weight of the system. Before going into optimisation methods, in this section, we

explore the various modelling and simulation methods present in the literature. The *MATLAB/Simulink* software tool has been used by several research groups as an environment for modelling and simulation to aid in performance analysis [13, 35, 102, 132], such as using the *AeroSim Blockset* to perform a closed-loop simulation platform which combined a hybrid power system model and the UAV model to simulate real flight conditions [173]; or simulating the hybrid photovoltaic panel in combination with a rechargeable fuel cell and a rechargeable energy storage system to provide a long-endurance flight-capable UAV [28]. These simulations are a useful indicator of how a specific powertrain behaves for specific cases. Since detailed setups are required, it is not suitable for sizing and comparing many different powertrains.

A fuzzy state machines are another technique use in research, for example, to decide the desired output of the fuel cell, depending upon the battery's maximum charge rate (if the battery charge rate was low and the photovoltaic module was already outputting its maximum power) [173]. Though the fuzzy state machine was validated to be superior to the controlled thermostat control strategy, it did not provide sufficient conditions for the controls to be optimal and proved to be insensitive to model uncertainties and noise.

In Harmon et al. [65], rule-based controller algorithms for a parallel hybrid configuration are used along with internal combustion engine and electric motor efficiency maps for specific points in the inputs (demand torque, rotational speed). Similarly, in Xie et al. [167]'s simplified version of the high-level parallel hybrid electric propulsion system, through the systematic approach of dividing the power train into two major models (the engine model and the generator/motor model), the mode of operation was determined. This was based on rules such as logical and conditional statements and assuming predefined criteria are known. The result includes the electric mode (power from the battery only), fuel mode (power from the engine only), charge mode (power from the engine also goes into the battery) and combined mode (engine and battery working together). Although the rule-based modelling approach has given satisfying results through validation with experimental data, the optimisation only gave rise to the minimum fuel consumption criterion. Xie et al. [167] does not detail the challenges

in the implementation of the physical system in the real world, nor the inefficiency of the overall system.

Wang et al. [160] presents an evaluation of the weight and power distribution of a small fixed-wing UAV using a PEM fuel cell and battery hybrid power system. The authors conducted a series of constraint and mission analyses to determine the optimal sizing and configuration of the hybrid power system for the drone, based on the mission requirements and physical constraints. The constraint analysis considered the weight, size, and power constraints of the drone, as well as the availability and cost of the fuel cell and battery technologies. The mission analysis considered a typical mission profile, including take-off, climb, cruise and descent, and calculated the energy requirements and performance parameters, such as range, endurance and speed. The authors compared the performance of the fuel cell and battery hybrid power system with a conventional battery-only system and evaluated the effects of different parameters, such as fuel cell size, battery capacity and fuel cell efficiency on the performance of the hybrid system. The results showed that the fuel cell and battery hybrid power system could achieve longer range and endurance than the battery-only system, and could operate at higher altitudes and temperatures.

From this study, we can infer that the optimal sizing and configuration of the hybrid system depended on the specific mission requirements and physical constraints, such as the weight and size of the fuel cell and battery, and the availability of hydrogen. The results show that 162.7 W of electrical power and 8.5 g hr^{-1} of hydrogen fuel are needed for 6.3 kg of maximum take-off mass with 6.8 hr of endurance. The fuel cell system takes up roughly 34% of the total take-off mass. The article contributes to the development of hybrid power systems for small UAVs by providing a systematic approach for evaluating the performance and constraints of different configurations, and by highlighting the benefits and challenges of using fuel cell technology in UAVs.

Overall, these studies demonstrate the potential benefits of hybrid powertrain designs for UAVs, and the importance of optimising the powertrain for maximum efficiency and minimum mass. The specific hybrid powertrain design and optimisation approach will depend on the specific goals of the analysis and the operating conditions of the

UAV. One common factor in all of the above is the lack of ability to compare the different powertrains available in one study. Therefore, in our current project, we proposed a method to parameterise the powertrain topology so that we can analyse different powertrain topologies in one framework.

Generally, the choice of model depends on the specific application and the available data. Forward-facing, backwards-facing, and initial value problem models can be used for the modelling and simulation of UAVs. In some cases, a combination of these models may be used to achieve the desired level of accuracy and computational efficiency. The following section explains some examples of how each model type might be used.

2.3.1 Forward-facing model

Forward-facing models (Figure 2.25) are dynamic models with the inputs being the driver's inputs (e.g. throttle commands) on the controls which then give vehicle responses as outputs. Here, the models refer to the type of simulation of the components in the powertrain, not the individual component models. This output is acquired from one or more proportional-integral (P-I) controllers with reference to the desired speed to meet the torque demand of the engine [13]. Forward-facing models are particularly useful for hardware development, as well as detailed control simulations [102] and understanding the physical limits of the powertrain. The actual speed is calculated through multiple-state integration, which means that the simulation needs to run in small time steps. Similarly, Schomann [133] states that in forward-facing modelling, the procedure follows the energy source to obtain the propulsive performance of the propeller, with the initial efficiency of the power converters needed to correctly size the components. This means that the inputs also need to be tuned again if the power train is resized, making the model simulation time longer than for backward-facing models. The models also require a significant amount of data and a generally complex model for the performance results to be reliable [35].

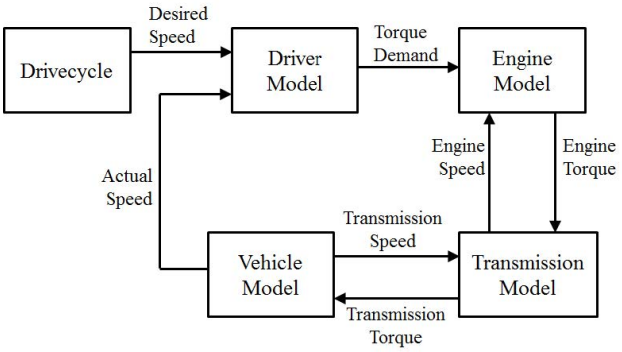

FIGURE 2.25: Forward facing model [13].

Schouten et al. [134] also used a forward-facing model in conjunction with a rule-based approach using logical statements (if-then rules) and predefined criteria. Fuzzy logic is used as it is tolerant to imprecise measures and component variability, albeit it uses a collection of if-then rules which allows for the formulation of human knowledge and reasoning. Although their paper defines the advantages of hybrid systems in the automotive industry, the reasoning for the advantages is similar to that in UAV applications. The overall aim is to optimise the fuel economy through the optimisation of all four major components (internal combustion engine, electric motors, battery, and transmission). Here, the efficiency maps of the components were used to identify the optimal operating points with a power split strategy that was used to optimise the efficiency of operating all four components. Knowing the efficiency allows for different types of power split strategies and helps to determine which components should be activated and when. Once the power split has been optimised, the power generation/conversion of the individual components was optimised.

Therefore, in this model, the state variables of the system are predicted based on the current inputs and initial conditions. For example, we could use a forward-facing model to predict the position and velocity of a UAV based on its current acceleration, the wind conditions, and its initial position and velocity. A common approach to constructing a forward-facing model is to use differential equations to describe the dynamics of the system.

2.3.2 Backward-facing models

On the other hand, backward-facing models (Figure 2.26) assume that the vehicles meet the drive cycle (speed vs time graph) and work backward to determine how each component must perform [102]. This is equivalent to knowing the mission profile before the mission starts and then calculating the required components to fulfil the mission. The models rely on efficiency maps based on real data. This allows for, during the power train sizing optimisation routine, both speed and torque to be imposed on the components [13]. As the calculations are simpler than those that make up forward-facing models, faster simulations can be achieved. The backward-facing models do not include driver or engine/power-train models, so they can be used to make comparisons and perform sizing studies [35]. An example of this would be the study conducted by Donateo and Totaro [42] where the real-world flight data (94 flights) of a piston engine training aircraft were analysed for power demand. In this analysis, the required propulsive power of the propeller is known before the sizing of the components. The preliminary results showed a 5% reduction in fuel consumption compared to the original conventional power train. However, backward-facing models are not suited to cases where the vehicles may deviate from the set mission profiles. Moreover, the dynamic effects are not included in the efficiency maps, which makes the backward-facing models difficult for control system development and hardware-in-the-loop implementations [13, 102].

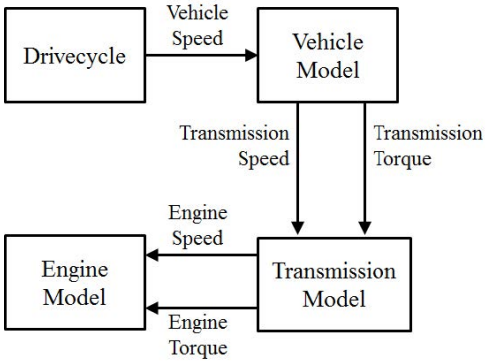

FIGURE 2.26: Backward facing model [13].

The Advanced Vehicle Simulator (ADVISOR), developed by the National Renewable

Energy Laboratory, is a widely used simulation tool [102] for hybrid electric vehicles. The component models (internal combustion engine, fuel cell, and battery pack models) are empirical models based on test data. The tool is a hybrid model using a combination of backward and forward-facing models. Quasistatic component models as well as taking vehicle speed as an input to determine torque make this tool closer to a backward-facing model.

Some of the current modelling and simulation software using backward-facing modelling for academic research include *PLA.N.E.S* [39] and *SUAVE* [19, 99]. These software are developed for aircraft performance and analysis and are covered in the following paragraphs.

PLA.N.E.S was developed and validated by Donateo et al. [37]. It uses a force-balance-based mission solver and a backward modelling approach, where the time histories of speed and altitude are known a priori, and then works out the forces required by the propulsion system and, therefore, the power to be delivered by the power train. The engine power and speed are then used to calculate the fuel consumption and the aircraft mass is updated for the next time step. Donateo et al. [39] states that for this type of simulation, correct sizing of the power train is required and therefore the software has been integrated with a numerical procedure for sizing of the power train. The user decides the specification of the aircraft and the type of power train required. An empirical optimisation tool is then used to size the components, which also looks into the performance of the aircraft on the selected power train. The fuel consumption and state of charge of the battery are then simulated followed by the mission profile, and then the energy management strategies are optimised. Finally, the results are used by a multi-objective optimisation tool to determine the optimal power train. The performance indices used in *PLA.N.E.S* to compare the new results with the initial results are explained as follows. *PLA.N.E.S* looks at the flight performance, such as the take-off, specifically the take-off distance required which affects the runway length, climb, and cruise. The program also compares range and endurance. If any additional mass and volume to the updated model is more than 10% higher than the initial mass, the structure of the aircraft needs to be upgraded while the wing loading is kept constant.

Finally, the program can also check the ability to perform the baseline mission and estimate fuel consumption.

SUAVE [19, 99] is an open-source environment written in *Python* and is a multi-fidelity conceptual design environment, which allows for incorporating future technologies. The code is flexible as the data structure is built upon dictionaries in *Python*, which allows for the objects to be mutable, meaning the objects can be appended, deleted, or modified easily by the user. *SUAVE* has capabilities to model propulsion and energy networks using gas turbines and ducted fans, powered by batteries, fuel-cells or solar [158]. *SUAVE* uses a force-balance-based mission solver, similar to *PLA.N.E.S*, along with user-input propulsion and initial aerodynamic modules. The program can either be treated as an analysis tool or for optimisation using additional external tools.

Both *PLA.N.E.S* and *SUAVE* are promising tools for analysing aircraft mission and flight performance. However, *PLA.N.E.S* is not an open-source tool and at the time of writing, *SUAVE* is still in the midst of development with the code development focus towards high fidelity on the aerodynamics aspect of the conceptual design, requiring high level and detailed geometry inputs of the aircraft.

To summarise backward-facing models, the inputs to the system are predicted based on the desired outputs and the initial conditions. For example, we could use a backward-facing model to determine the optimal thrust and control inputs needed to achieve the desired altitude and speed for a UAV. Backward-facing models can be useful for planning and controlling applications.

2.3.3 Initial value problem

An initial value problem is a mathematical problem that involves finding a function that satisfies a given differential equation using an initial condition that specifies the value of the function at a particular point in its domain. In the context of mission simulation for UAVs, an initial value problem can be used to simulate the UAV's flight trajectory and behaviour over time, given a set of initial conditions and flight parameters.

To solve an initial value problem for mission simulation in UAVs, one would typically begin by formulating a set of differential equations that describe the UAV's flight dynamics (such as its position, velocity, and acceleration, as well as its attitude and angular rates) over time, given the initial conditions of the system. For example: consider a UAV with mass m, a position given by the vector $r = [x, y]$, and velocity given by the vector $v = [vx, vy]$. Assuming the UAV is subject to a constant force F_x in the x direction and F_y in the y direction (these equations assumed that the UAV moves only in the $x - y$ plane (distance and altitude) and that its mass is concentrated at a single point).

Once the differential equations have been solved numerically, by iterating these equations forward in time, we can simulate the motion of the UAV over a desired time interval. The resulting solution can be used to simulate the UAV's flight trajectory as well as the behaviour over time, given a set of initial conditions, such as its initial position, velocity, and orientation, as well as its mission parameters, such as its desired altitude, airspeed and waypoints.

Overall, an initial value problem can be a powerful tool for simulating the mission performance of UAVs, and can help to optimise their design and control algorithms to achieve optimal performance in real-world flight scenarios.

To summarise, the initial value problem model can be used to solve a set of differential equations to determine the trajectory of a UAV given initial conditions. For example, we could use an initial value problem model to simulate the motion of a UAV in response to different input commands or disturbances. This type of model is commonly used in simulation and optimisation applications, and this study adopts the initial value problem approach.

2.4 Summary

In this chapter, we review the current state of the powertrain components for UAVs, their advantages and setback, along with real-life examples. We also discussed the current methodology available for modelling and simulations for hybrid powertrains in

UAVs and the gap in the market. While there are some software packages available that can simulate and analyse the hybrid powertrains, there is still a need for the ability to compare and analyse the different powertrains available in one study, the predominant number of studies focus on individual powertrain topologies. Comprehensive software tools that can assist engineers in the design and optimisation of hybrid powertrains are either in progress for open-source or are in-house tools. Moreover, the hybrid powertrain topology analysis for UAVs lacks standardised methods and tools for evaluating and comparing different hybrid powertrain configurations and a need for more sophisticated simulation and modelling software that can predict the performance of different powertrain configurations rapidly under varying operating conditions. As UAVs are often customised for specific missions, there may be a wide variety of powertrain configurations, making it challenging to compare and evaluate their performance without a framework which could handle the plethora of possible powertrain configurations.

Therefore, we propose a method to parameterise the powertrain topology and analysis so that we can analyse different powertrain topologies under one framework. Finally, we have identified that the initial value problem coupled with the backwards-facing model approach would be suitable for the mission simulations for sizing and optimisation as well as to identify the parameters, such as the battery state of charge and fuel mass consumption for engines. Appendix A discusses the fixed-wing platforms that are used to demonstrate the method, as well as the modelling of the platforms based on point mass models. Detailed modelling and verification of the models are found in Appendix B.

Chapter 3

Proposed powertrain topology encoding scheme

To solve the challenges stated in Chapter 1, we have developed PoETS (Powertrain Energy Topology Scheme). We presented this work at the AIAA SCITECH 2023 conference [105]. Since many powertrain topologies are possible, a system that allows for a systematic, automated exploration of the space of powertrain topologies is needed, with the goal of identifying the layout that optimises mission performance. In this chapter, we propose the building block of such an optimiser, a scheme capable of the flexible, future-proof, yet economical encoding of powertrain topologies.

The proposed UAV energy architecture encoding scheme is a string-based representation of the powertrain topology created from the traversal of a graph representation of a topology. The components (nodes) are divided into the energy source, storage, converter, transmitter and sink categories. The components are connected via connection types (edges). The connection types are divided into mechanical, electrical and fuel flow. The relevant symbols and examples are shown in Table 3.1. Note that although 'PV' cells convert solar energy to electrical energy in the form of direct current, solar irradiance is external to the UAV, and therefore in the PoETS notation, it is classified as a source.

TABLE 3.1: Proposed encoding scheme - symbols and their representations.

Component type	Examples	Symbols
Termination node in the topology	Hydrocarbon (HC), Battery (B) Solar cell (PV), Hydrogen (HY)	UPPER CASE letters
Any non termination nodes	Propeller (p), Electric motor (em), Engine (en), Fuel cell (fc), Generator (gn)	lower case letters
Source	Fuel - Hydrocarbon fuel	HC
	Fuel - Liquid or Gaseous hydrogen	HY
	Photovoltaic cell	PV
Storage	Battery	B
Converter	Engine	en
	Electric motor	em
	Fuel cell	fc
Transmitter	Mechanical couplers (such as gearbox, clutch, etc)	gb
	Electrical couplers (such as printed circuit boards, inverters, converters, electronic speed controllers)	pc
Sink	Propeller	p
Connection type	Examples	Symbols
Mechanical	Connection between an engine and a propeller	[
Electrical	Electric connection between an electronic speed controller and an electric motor	{
Moving mass	Fuel flow from a fuel tank into an engine	(
Branch system	p[en|(HC+(HC| , |p[em+p[em+p[em+p[em|{pc|{B+{PV|	|....+....|
Not within the scope of the work		
Duplicate systems in the branch	|p[em+p[em+p[em+p[em|{pc|{B+{PV| = |p[em|*4{pc|{B+{PV|	* with Numbering
Connecting cyclic systems	p[em|{B_1{fc{HY+{pc_1{PV	Numbering with _
Independent system inside the platform	p[en(HC; p[en(HY	;

3.1 Introducing the PoETS approach

The steps for encoding a powertrain topology utilising a graph theory approach are described in the following section. First, we create a graph representation of the topology, whose nodes are the components (engine ('en'), propeller ('p'), fuel cell ('fc'), etc.), its edges are the connections between them. The sink component(s) is(are) the initial

node(s) in the traversal of the powertrain topology graphs. From this, we work our way backwards towards the source(s).

At each node, the input and output connections are determined. For example, we begin encoding the graph shown in Figure 3.1, with the propeller ('p') as the first node. The input edge is a mechanical connection and there is no output edge (since the propeller, a sink component, does not have a output connection into another component). The encoding so far is 'p['.

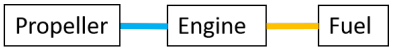

FIGURE 3.1: Powertrain as a graph – example of the simplest possible combustion engine powertrain.

The mechanical connection output from the engine requires a mechanical input into the next component. In the example, the input of the propeller and the output of the engine have a common edge type hence it is an acceptable connection.

It should be noted at this point that, aside from source nodes (energy sources), sink nodes (e.g. 'p') and batteries that are non-rechargeable during flight, all other nodes should have both input and output edges defined. 'Battery' components are an exception as they may be recharged in flight and hence can have both input and output edges; however they do not *require* an input edge.

In our example, the engine node thus takes in a fuel flow connection from a hydrocarbon storage ('HC') and generates an output to the propeller through a mechanical connection. The completed encoding thus becomes

p[en(HC

Since fuel will always need some form of containment, such as a fuel tank, the fuel tanks can be ignored and assumed to be incorporated into the 'Fuel' component.

At branch points, such as on the architecture shown in Figure 3.2 where there are multiple branches – in this case the power converter ('{pc{') connects both to a battery component ('{B') and generator component ('{gn[') – the branch with the lowest number of nodes is favoured first. If each branch has the same number of nodes, as in the

case seen in Figure 3.3, the branches will be ordered in ascending alphabetical order (for example, the electric motor ('gn') branch would be chosen before the engine ('pc') branch. This ensures that the powertrain topologies are not duplicated, allowing the comparison of almost identical graphical representations.

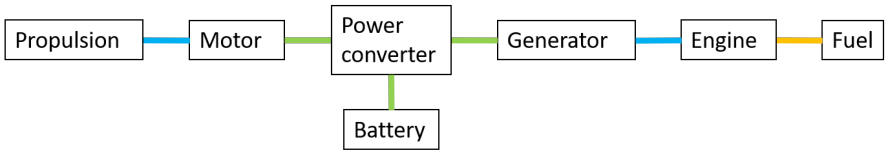

FIGURE 3.2: Series hybrid configuration: *yellow* line represents moving mass (chemical connection), *blue* line represents mechanical connection, *green* line represents electrical connection.

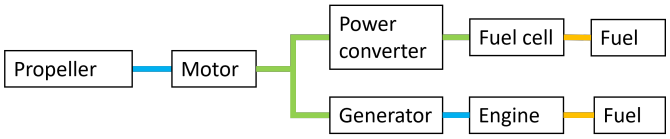

FIGURE 3.3: Same number of nodes in parallel branch example - PoETS equivalent would be p[em | {gn[en(HC + {pc{fc(HY |.

The encoding of branches requires additional symbols. For example, branches from the system shown in Figure 3.2 are represented by the string

$$\{pc|\{...+\{...|$$

with the first '|' symbolising the start of the branch leading out of the power converter and a '+' separating the branches. The second '|' represents the closing of the branch. The complete PoETS string of Figure 3.2 is

$$p[em\{pc|\{B+\{gn[en(HC|$$

Similarly, in the case of the example shown in Figure 3.4 the following notation is used:

$$|p[em+p[em|\{B$$

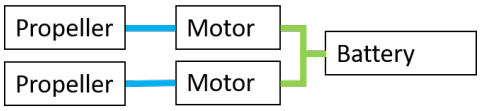

FIGURE 3.4: Powertrain as a graph – example of branched connections, with a single energy source and two propulsors.

Table 3.1 summarises the key elements of the scheme as discussed above. In this section we introduced these building blocks on a set of simple examples, illustrating the proposition that PoETS meets the four challenges outlined in the introduction; in particular, showing that the scheme allows relatively easy human readability and the ability to construct the string by hand to an extent.

3.2 Contribution one - Application of PoETS for representing existing powertrains

Let us now consider a series of examples of actual aircraft, with relatively complex powertrains to demonstrate the flexibility of PoETS. The graphical representations of the powertrains are created from the PoETS string via a decoder-script using `PyGraphviz` [122], an open-source graph visualisation software for Python. Each graph is built from a PoETS string, with the notation of 'NX_component', where N stands for node, X is the node number followed by the component name. The number follows the component's position in the string. Different connection types are represented by different colours: orange for fuel flow, green for electrical and blue for mechanical connections.

- NASAs Greased Lightning 10-Engine (GL-10) [17] (Figure 3.5, top) is a 28.1 kg, 3.0 m wing span, VTOL, hybrid electric propulsion UAV designed for long endurance (10 hr) missions. This UAV has 10 propellers, eight on the wings and two on the tail. The motors are powered by two 8 hp (6.0 kW) diesel prime movers, which are in a serial hybrid configuration. The powertrain architecture is visualised in Figure 3.6 (top). NASA's GL-10 powertrain topology can be encoded as:

|p[em+p[em+p[em+p[em+p[em+p[em+p[em+p[em+p[em+p[em|{pc{B{gn|[en+[en|(HC

FIGURE 3.5: Examples of real life UAV - Top: NASA Greased Lightning GL-10 UAV [17], Bottom left: Eagle Plus UAV [141], Bottom right: Hybrid Tiger UAV [117].

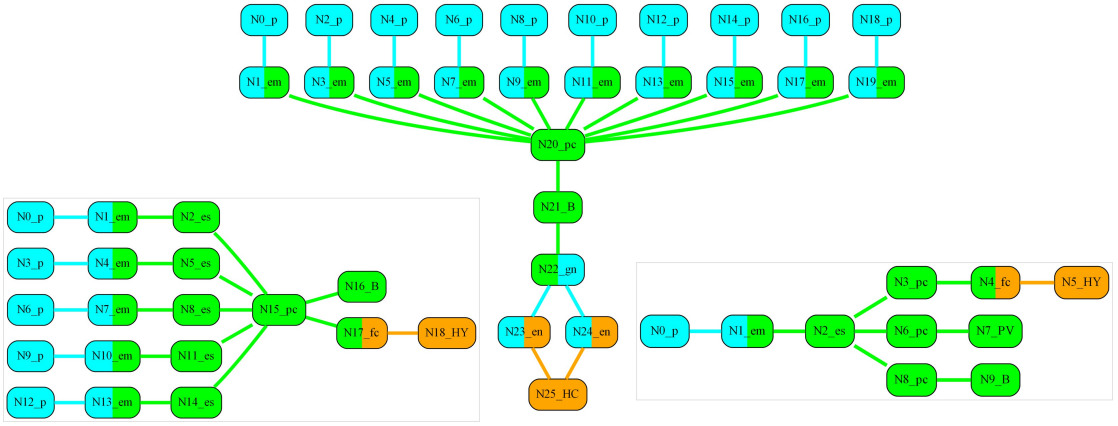

FIGURE 3.6: Examples of real life UAV powertrains - Top: NASA Greased Lightning GL-10 UAV [17], Bottom left: Eagle Plus UAV [141], Bottom right: Hybrid Tiger UAV [117].

In short form, this can also be written as

|p[em|*10_{pc{B{gn|[en+[en|(HC

- Sparkle Tech's Eagle Plus [141] (Figure 3.5, bottom left) is a small VTOL, UAV with a 3.5 m wing span and maximum take off mass of 21 kg, utilising a 500 W electric motor that is powered by a 9 litre liquid hydrogen fuel cell which can provide 500 W. This UAV is also equipped with a 10,000 mAh Lithium Polymer battery as a redundancy for flight safety. The powertrain architecture is visualised in Figure 3.6 (bottom left). The Eagle Plus UAV powertrain topolgy can be

encoded as:

$$|p[em\{es+p[em\{es+p[em\{es+p[em\{es+p[em\{es|\{pc|\{B+\{fc(HY|$$

- Hybrid Tiger [117] (Figure 3.5, bottom right) is a 25 kg, 7.3 m wing span fixed wing UAV developed by the US Naval Research Laboratory (NRL). It is a long endurance and long range UAV with a hybrid energy system: a 430 W solar cell array, a 53 litre liquid hydrogen fuel tank, and a 32 Wh Li-ion battery pack.

  The hybrid Tiger powertrain topology can be encoded as:

$$p[em\{es|\{pc\{fc(HY+\{pc\{PV+\{pc\{B|$$

  and is visualised in Figure 3.6 (bottom right).

- EAV-2 [92], developed by the Korea Aerospace Research Institute, is a 6.9 m wing span, 18 kg glider with a 200 W fuel cell, a 240 W solar cell array and a 1.3 kW Lithium Polymer battery pack with 4.3 Ah capacity. The powertrain architecture is visualised in Figure 3.7.

  The EAV-2 UAV powertrain topolgy can be encoded as:

$$p[em\{es\{B\{pc|\{PV+\{PV+\{PV+\{fc(HY+\{fc(HY|$$

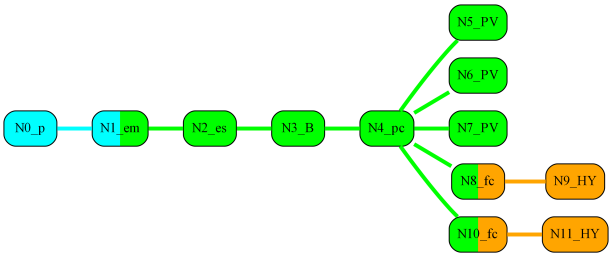

FIGURE 3.7: EAV-2 UAV powertrain.

Through the ability to standardise the different powertrain topologies (be it in physical or virtual realm) PoETS enables different powertrain topology from various existing literature to be use in documentation. PoETS also allows for the direct comparison of

existing designs, leading to more efficient development processes. Finally, PoETS provides a common language for describing powertrain configurations as the availability of the different configurations increases.

3.3 Summary

We propose a string-based approach for encoding conventional, hybrid, and electric propulsion systems in UAVs to serve as the basis of systematic searches of layouts. We described the encoding approach and provided a range of examples to demonstrate the applicability and suitability of the scheme. PoETS boasts the following advantages:

- By defining the input edges and output edges, physically feasible connections are guaranteed.
- By allowing the definition of any inputs and outputs, PoETS is future-proof, as engineers can easily define new components.
- ASCII-based string encoding allows for machine readability and, to an extent, human readability (aided by the intrinsically visual, graph-based definition).
- The construction of the scheme, stemming from a graph based definition of the topology, readily allows the application of existing algorithms design to search design spaces defined by graphs.

In the following chapters, we will look into the benefits of the proposed encoding scheme and how it can fit into optimising the powertrain sizes and mission simulations such that it can be used to automate the optimisation of powertrain designs. By encoding the topology of a powertrain system using PoETS, optimisation algorithms can be applied to identify the optimal configuration of components and interconnections that meet specific performance targets and design constraints. Overall, the encoding scheme developed here allows for the topology parameterisation, to aid in the optimisation process by way of embedding the component models (described in Appendix B).

Chapter 4

Generating and modelling powertrain topologies through PoETS

PoETS also has the capability to automatically generate feasible powertrains provided that the engineer knows the input and output requirements of the individual components. This chapter focuses on using the rules described in the previous chapter to generate physically meaningful architecture strings, given a set of component types. Table 4.1 shows each component considered and the allowable input and output power types. PoETS is set up based on the logic that the input of the current node has to be the same as the output of the previous node. After generating the powertrain topologies, modelling and simulations are required to evaluate the feasibility. Therefore, this chapter also delve into the implementation of the component modelling, described in Chapter 2 and Appendix B on the generated powertrain topologies.

TABLE 4.1: Powertrain topology connection input-output edge type.

Component	Symbol	Input edge	Output edge
Propeller	p	[	[
Electric motor	em	{	[
Electronic speed controller	es	{	{
Battery	B	{	{
Generator	gn	[	{
Combustion engine	en	(	[
Fuel cell	fc	(	{
Solar cell	PV	n/a	{
Hydrogen	HY	n/a	(
Hydrocarbon	HC	n/a	(

4.1 Contribution two – the automatic generation of feasible powertrains

Let us consider the example of a single propeller: "p[" as a starting point, which has an initial input into the next component of a mechanical connection: [. Feasible connections from here include p[em{, p[en(and | p+. Examples of infeasible connections from this point include p[gn, p[HC.

When using PoETS for generating new topology strings, the initial input is always the sink node: 'p', which is a propeller. Following on from this, the number of initial propellers is determined between one to n, where n is the user-defined maximum number of propellers, along with the number of parallel branches associated with these propellers. For example, if two propellers are chosen, | p[... + p[... | is the initial branch of the generated powertrain. For this case, where a branch exists, a branch termination edge is chosen at random (i.e. {, [or ( ). Feasible sub-strings for each branch can then be generated until such an output edge is reached. At this point, the branches are combined. For example, | p[em + p[em |{ if { is chosen as the branch termination edge. This will be the example from now on.

Following on from this, there are three options, either branch out again, add a single component or add a string that has a terminating source. This choice is randomly made again, subject to the component type based on the processing node. Expanding

the previous example to add a component: | p[em + p[em | {pc{. If the system is chosen to branch, another branch terminating edge is chosen and the feasible sub-strings are generated. For example, for a non-terminating branch, the system could result in | p[em + p[em || {pc + {gn[em | {. For a terminating branch, the decision is made on how many branches it splits into. In the case of two branches: | p[em + p[em || {B + {fc(HY.

Note that constraints on the strings should be imposed such as limiting the maximum number of branches, the maximum branch length, not allowing immediate repeated components and a limit to the quantity of any one component in the string. This is to prevent valid but impractical strings, such as repeated components ({pc{pc{pc{pc{pc{pc) or repeated loops ({em[gn{em[gn{em[gn{em[gn).

Using the method described above and based on Table 4.1, a total of 743,856 non-repeated strings (with the constraints of no repeated feasible components right after each other, i.e. p[em{B{B{B{B{B, and no more than 10 components in a single branch) can be rapidly generated for powertrains starting with up to two propellers (in approximately 100 minutes on a standard Intel i7-10700K CPU) - which can act as an initial design search during the preliminary design phase. This is a vast quantity of topology strings and it is infeasible to size and analyse each string for a mission. Some examples of the output of the topologies generated are shown in Table 4.2.

TABLE 4.2: Generated topologies based on powertrain topology connection input-output edge type.

Type	PoETS scheme	Definition and figure
Linear	p[em{es{pc{B	Non-rechargeable battery powered (Figure 4.1a)
Linear	p[em{B{pc{PV	Rechargeable battery / battery acting as a capacitor for photovoltaics module (Figure 4.1b)
Branch	|p[em{pc+p[em{es{B|{PV	Two propeller configuration with a battery and photovoltaics (Figure 4.2a)
Branch	|p+p|[gb[en(HC	Two propeller configuration with engine only (Figure 4.2b)
Branch	p|[gb[en+[gb[en|(HC	Single propeller configuration with dual engines (Figure 4.2c)
Branch	|p[em+p[em{B|{pc|{PV+{PV|	Two propeller configuration battery and dual photovoltaics modules (Figure 4.2d)

(A) PoETS powertrain generation - Linear string type A.

(B) PoETS powertrain generation - Linear string type B.

FIGURE 4.1: Examples of topologies generated based on the powertrain topology connection input-output edge types - Linear.

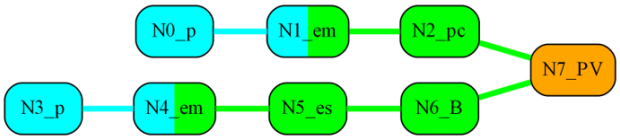

(A) PoETS powertrain generation - Branch string type A.

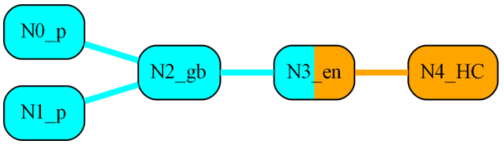

(B) PoETS powertrain generation - Branch string type B.

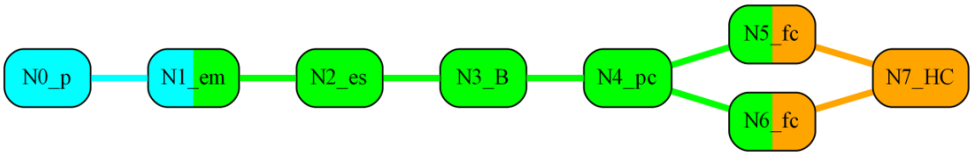

(C) PoETS powertrain generation - Branch string type C.

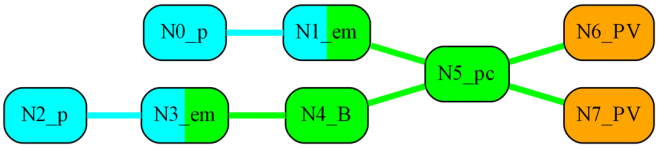

(D) PoETS powertrain generation - Branch string type D.

FIGURE 4.2: Examples of topologies generated based on powertrain topology connection input-output edge types - Branched.

A current limitation of PoETS encoding is the lack of a geometrical layout, such as the propellers being mounted on the wings, behind the wings, or elsewhere. However, this provides a unique starting point for the UAV design process as the powertrain can be chosen before a platform has been designed. For example, Figure 4.2a might work in a pusher tractor configuration, where p[em{pc is at the front of the aircraft, p[em{es{B is at the rear and the photovoltaics module supplies both the back propeller and the front propeller during the day. Alternatively, the rear propeller acts to supplement high power demands when required and is folded at other times. Similarly design ambiguity is available in Figure 4.2b, where the propeller configuration could be co-axial

or distributed. PoETS original intention is to identify the energy type available in the powertrain topologies, adding the geometrical layout within the encoding would increase the complexity in the encoding string. Therefore, the recommendation is to add an extra module within modelling and simulating to compare the outcome of the different configurations for the given powertrain topologies (i.e coaxial, pusher, puller, etc). The author also recognises that for detailed analysis, understanding the geometrical layout is an important factor to calculate the aerodynamic performances (such as the effect of the prop-wash over the wing) and center of gravity calculations. These can be considered in the detailed modelling in simulations, once we have identified feasible powertrain sizing in the future.

4.2 Modelling and simulation

Once the topologies have been generated, we need to evaluate the feasibility of the generated powertrain for the test UAVs for a given mission. For the initial part of the analysis, it is essential to classify the different hybridisation elements found within the hybrid powertrain topologies. This is because one of the objectives of the study is to optimise the performance of a hybrid powertrain system once the hybrid powertrain system is deemed feasible for the given mission (as in how a particular energy source is deployed). Hybridisation can occur on two levels of the overall power flow arrangement: the source level of hybridisation and the propulsion level, where power is converted to thrust. In this study, we focus on the source level to vary the hybridisation, with the power level maintained at an equal split when required from the thrust generators - i.e. propellers.

For the modelling and simulation method shown in Figure 4.3 - component models in Chapter 2 and Appendix B, we assume a point mass (detailed in Appendix A.3) that flies a predetermined flight path (initial value problem method described in section 2.3.3). The flight path is also optimised and is used to determine thrust, and therefore determine the power requirements for the powertrain. We are only solving the problem in the altitude versus distance flown domain.

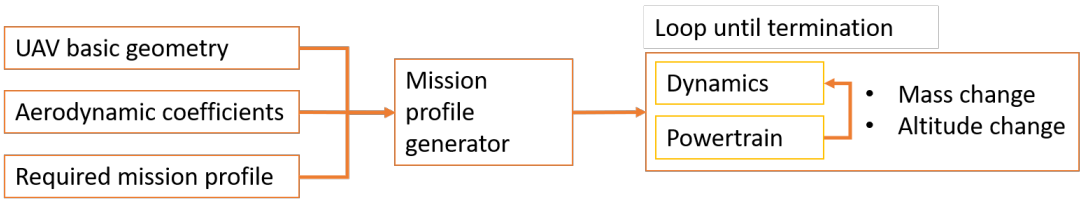

FIGURE 4.3: The structure for the mission profile simulation.

Initially, the mass, initial kinematic characteristics and hybridisation factor are known (through the genetic optimisation), and the dynamics module, in the form of an initial value problem, is solved for the desired profile using Newton's second law described in Appendix A.3.

The power flow is calculated from the values of the hybridisation factors and is cascaded backwards through each component until the final source nodes are reached. Through this, the fuel and energy consumption for a single time step is calculated, along with the necessary mass change due to wet fuel consumption, which directly impacts the forces. The outcome of the optimisation includes the distribution of stored energy, energy consumption, variation in mass, mission thrust and angles, as well as the characteristics of the components (such as rotational speed, torque, current, voltage, and efficiency).

4.2.1 Implementation of the component models

A computational tool is developed and employs object-oriented programming and a procedural programming language, in this case, *Python 3.8*, is utilised in this study for the following reasons. The object has properties and can contain methods and classes that act as a template to create new objects [123]. The energy component class starts from the class of `Energy System` in an aircraft. A top-down development approach is used, where the most generalised class is defined, and subsequent specialisation classes are built up. An object of the energy component class defines the energy in the aircraft in terms of `sources`, `storage`, `converters`, `transmitters`, `sinks`, and `additional` for the components considered in this study (Figure 1.4).

Given that UAV powertrains constitute a chain of components, a simplified powertrain model is required to link the propulsive power produced by the propellers to the power required from the individual powertrain components. Moreover, since the aim of the study is to analyse many different powertrain topologies, as opposed to a single powertrain type in one framework, we implemented a self-modifying code which is sensitive to different powertrain architectures. This is a python script that changes as it executes, leveraging object-oriented programming properties called polymorphism. A common function name exists in every single component class and is called by the self-modifying script. This function calculates the required power flow (backwards modelling) at each component given the previous component's inputs. The process of the self-modifying script is seen in Figure 4.4. The advantage of such a technique allows the linking of the definition of the architecture (as expressed by a PoETS string, described in Chapter 3) to a Python class structure representing models of physical components. The collection of the component models is then blended automatically into a vehicle object, which then enables evaluating the virtual 'flight' of any given PoETS string through a flight simulation framework. This method provides the information that the objective function requires to guide a design search through the space of PoETS configurations with a limited number of input variables.

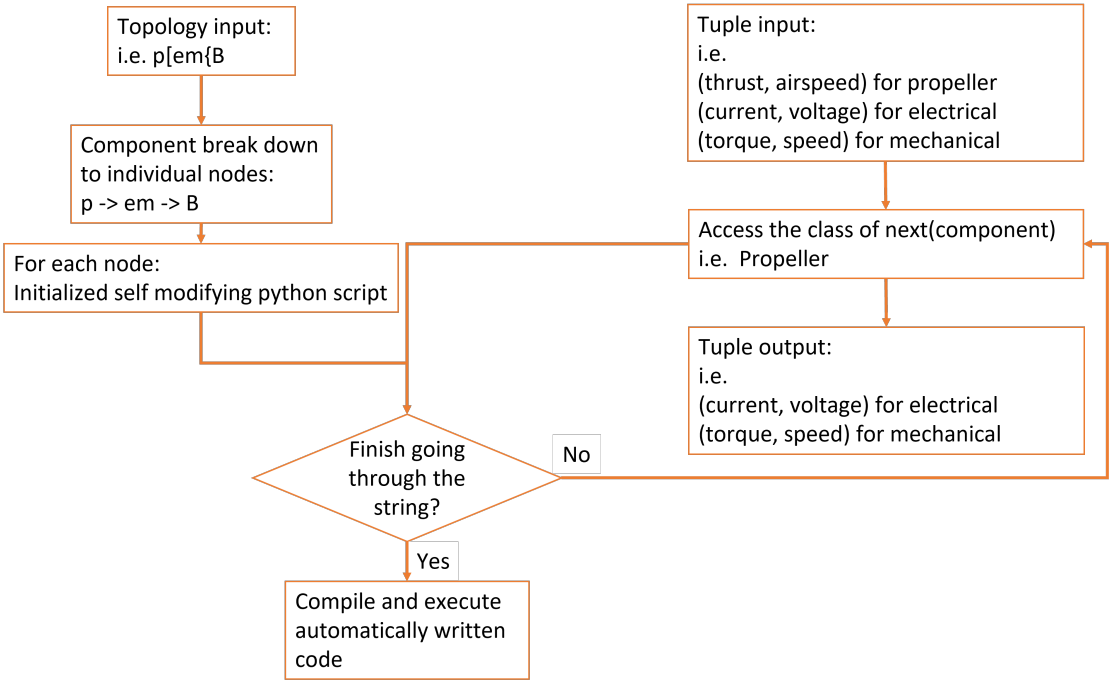

FIGURE 4.4: Self modifying python script process for a single timestep.

4.2.2 Curating component data

The starting point of architecture optimisation is a catalogue of components - see the models in Appendix B. Commercial off-the-shelf components are generally better to use in the optimisation of fixed-wing UAV powertrains. One of the reasons for this is that commercial off-the-shelf components are mass-produced and their specifications are relatively well-defined (though some manufacturers may exaggerate these), making these components consistent in terms of performance and characteristics. In contrast, when using the estimation of parameters, this can introduce variability in the optimisation process. Another source of variability is that estimation may result in sub-optimal designs if the models are created with inaccurate or incomplete data, which can lead to failures or reduced performance in a physical system. Commercial off-the-shelf components are widely available in the market, making them more accessible and cost-effective than the custom-designed components required to satisfy a powertrain generated through estimation sizing. This allows designers to choose from a range of components that best fit their requirements and optimise their design based on their availability and cost.

To obtain information on commercial off-the-shelf components, we employ web-scraping. Web scraping is the extraction of data from websites (e.g., e-commerce websites), using automated software (bots), which can be implemented using a *Python* tool such as the *requests* and *Beautiful Soup* libraries [126] or the *Scrapy* framework [87]. The data extracted can be stored in any form the user requires. In most cases, there is no single bot that can accommodate all the possible websites, due to the variety of front-end codes used across the industry. The process is shown in Figure 4.5.

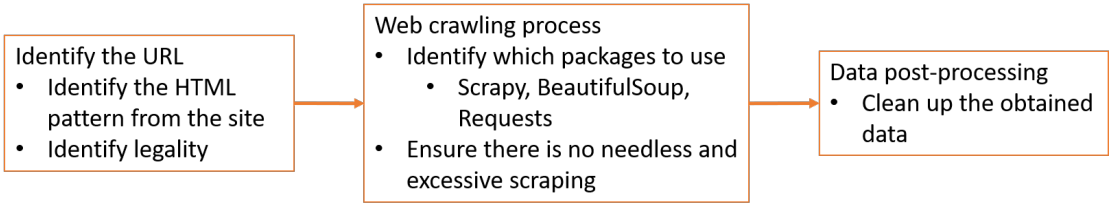

FIGURE 4.5: Web scraping process for curating component data.

Web scraping tools are particularly useful for repetitive tasks, such as going through web pages and extracting data for one component after another. To give an idea of its usefulness, to scrape the data from the *Genstattu* website [54] for batteries, the web scraping tool extracted the data of 232 batteries in 30 seconds and, of the 232 URLs, 213 URLs were extracted correctly. The remaining 19 URLs were not extracted due to non-standard formatting within the website. Web scraping to collect data on the components required for energy architectures, such as electric motors, batteries and fuel tanks, enables agile database creation that can be used in conjunction with the scheme described in Chapter 3. These databases serve along with the energy component models described in Appendix B to enable feasibility analyses of the generated powertrains.

4.2.3 Refining the component data

Table 4.3 shows the total number of commercial off-the-shelf components available for this study. As described in section 2.1.3, it is unlikely that all the combinations can be evaluated through brute force, nor that all of the components can provide the required power output. Therefore, a constraint analysis (for example, Figures 4.6a and 4.6b for mission 1 based on the values of Table 4.4) was used as a basis for the reduction of the commercial off-the-shelf component data.

TABLE 4.3: Coverage of the components database used for the optimisation experiments described in Chapter 5.

Component class	No. of components	Range
Propeller	525	4.1″ x 4.1″ - 28″ x 20.4″
Combustion Engine	46	30- 6000 W
Electric Motor	460	90 - 5300 KV, 5 - 250 A
Fuel Cell	10	25 - 1000 W
Solar Cell	96 cells FliTePlat 392 cells PEREGRIN	0.07 m x 0.07 m, 1.7 W
Battery	663	1 - 12 s, 120 - 30000 mAh, 10 - 130 C-rate

Since we used commercial off-the-shelf data, based on the power estimated at each component we can narrow the design space further by eliminating the components which are not within the range:

$$0.85\ P_{\text{estimate}} <= P_{\text{data, max}} <= 2\ P_{\text{estimate}}$$

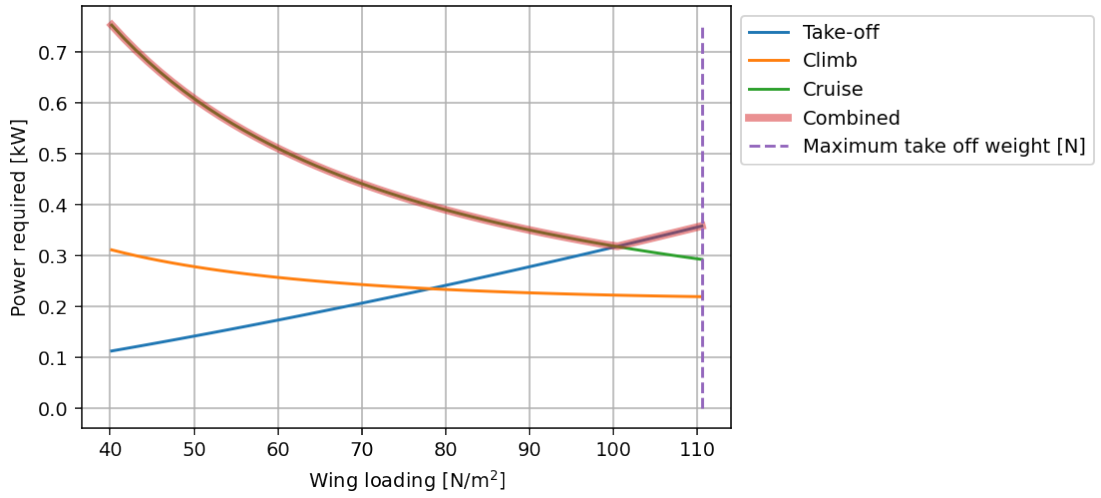

(A) Test platform FliTePlat – see Appendix A.1.

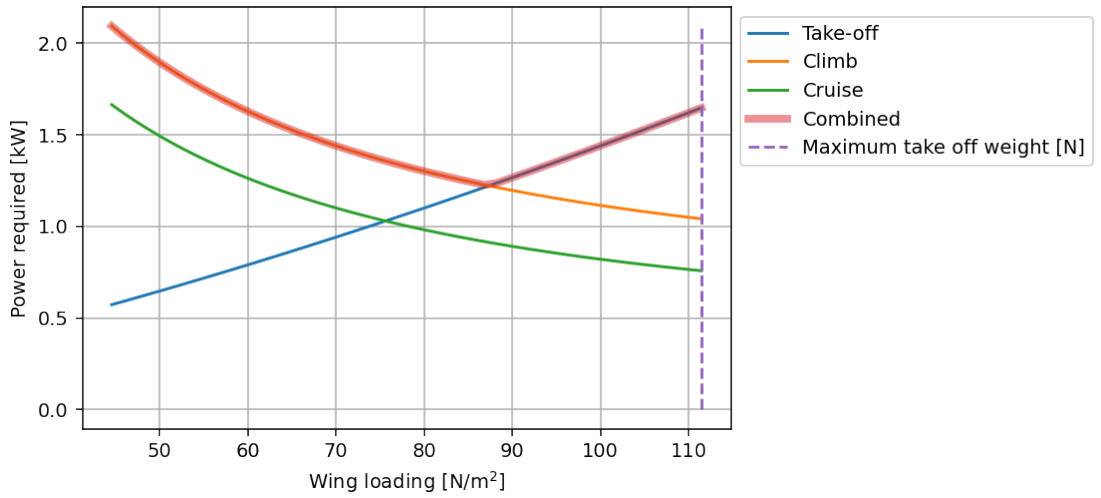

(B) Test platform PEREGRIN – see Appendix A.2.

FIGURE 4.6: Example constraint analysis output for mission 1.

TABLE 4.4: Estimated parameters used in the constraint analysis.

Parameter	Value
Climb altitude [m]	150 (depends on the mission)
Cruise altitude [m]	150 (depends on the mission)
Climb rate [feet per minute]	300
Cruise speed [ms^{-1}]	20
Climb speed [ms^{-1}]	15
Stall speed [ms^{-1}]	11
Ground run [m]	40

where P_{estimate} is based on the estimates following the process in shown in Figure 4.7 and $P_{\text{data,max}}$ is based on the commercial off-the-shelf data. Since the values of the estimated power are based on the constraint analysis applied at the start of each mission,

the power output values are also an estimate, only to aid in design space reduction, hence the range is erring on the side of caution here. Moreover, the value of the power here is only applied to the output power at the end of the propulsion side; therefore, for each component of the topology, we also use an estimated efficiency, shown in Figure 4.7.

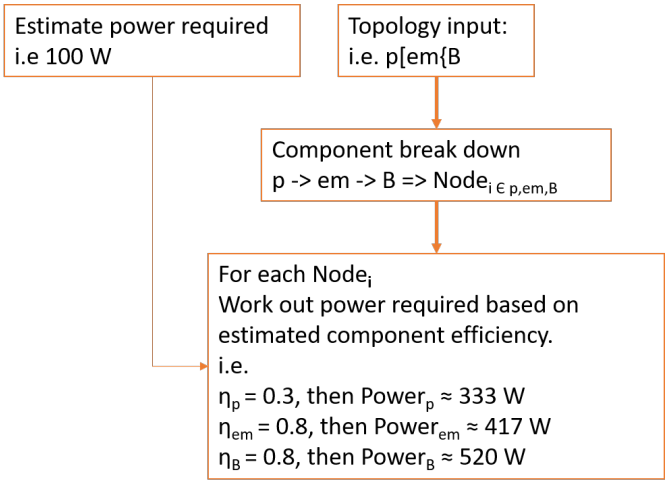

FIGURE 4.7: Initial process of refining the components down based on estimated efficiency and PoETS string.

For propeller refinement, we used the estimation found in Gudmundsson [60] based on the work by Stinton [142] to reduce the data:

$$D = 10^4 \left(\frac{T \; 1.34102 \; 10^{-3}}{\Omega^2 \; 53.5} \right)^{0.25}$$

where D is the diameter of the propeller [inch], Ω is the estimated propeller rotational speed [RPM] and T is the estimated thrust required [N], with the bounds calculated as

$$T_{\text{min}} = 0.2 \text{ MTOW}$$

$$T_{\text{max}} = \text{MTOW}$$

The component masses are based on off the shelf data, however, for fuel tanks, we used the following approaches.

Fuel tank for internal combustion based on the collected commercial off-the-shelf data: where $A = 1.704\,10^{-1}$, $B = 6.246\,10^{-1}$ and m_f is the mass of fuel [kg]

$$m = A\, m_f^B$$

Fuel tank for hydrogen: where m is the mass of hydrogen fuel [kg] based on Jarry et al. [77] where the author assumed that the weight of hydrogen fuel is proportional to the fuel tank

$$m = \frac{m}{0.14}$$

As a result, based on the estimated power required from the constraint analysis, for test case 14 – mission 1 – FliTePlat (Appendix A.1) the allowable engines are reduced to 2 components, batteries to 10, electric motors to 41, generators to 8 and propellers to 2.

4.3 Contribution three – evaluating the feasibility and performance of a powertrain

For a given powertrain topology and the details of its components, we can use the methodology shown in Figure 4.4 to establish its performance, in terms of meeting the requirements of a certain mission using the initial value problem (see Chapter 2 - section 2.3.3.

As an example, Figure 4.8 shows a battery powered architecture and a photovoltaic architecture performing the same mission. We can see that for a given powertrain configuration and component size, the battery powered architecture can complete the mission, whilst the photovoltaic cannot. For powertrains that are unable to complete the mission, this method is able to highlight the critical failing component and failure method (e.g. exceeding the maximum current on an electric motor).

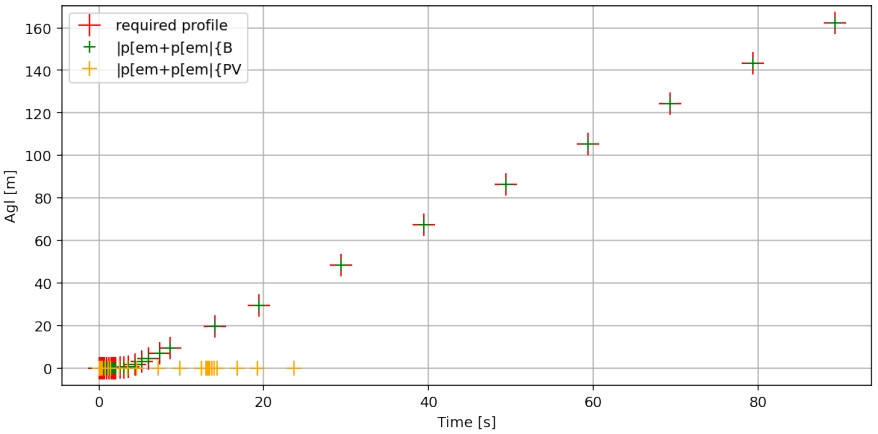

FIGURE 4.8: A comparison of three mission profile simulations in above ground level versus time space: a target mission (red +), a profile resulting from a simulation of the operation of a battery electric UAV flown to match the target profile as closely as possible (green +), and a similar simulation of a UAV powered by a photovoltaic powertrain (yellow +). The latter clearly fails to get close to the target mission.

4.4 Summary

In this chapter we demonstrated how the models discussed in Chapter 2 and in Appendix B and the novel encoding scheme (Chapter 3) are combined to create, analyse, and compare different powertrain topologies appropriate to each mission. By modelling the power flow and using the novel self-modifying script, engineers and researchers can gain insights into the behaviour of the system under different operating conditions and design more efficient and effective hybrid powertrains. This is demonstrated and discussed further in the following chapter.

Chapter 5

Optimising and evaluating PoETS topologies

In the previous chapter, we discussed how to model and simulate the given powertrain topologies to evaluate their feasibility for the required mission and the platform. In this chapter, we build upon this by applying a canonical genetic algorithm to size the powertrain and optimise the power flow for a thorough selection of single and hybrid energy source based powertrain topologies. The study begins with the representations of (potentially) hybrid electric propulsion systems in Chapter 3, using the models of energy components discussed in Appendix B.

5.1 Formulation of problem and component sizing

We use a canonical genetic algorithm as a search process for the design configuration that minimises a specific cost function - minimised the powertrain mass by the following design variables: the total transport energy (as a function of thrust and climb angle), energy splits in hybrid UAVs and the powertrain configuration. The initial value problem described in Chapter 2 is used to solve the mission simulation for the platform and the graph-based modelling (Sections 2.1.3.1 and 3.1) for powertrain modelling and

analysis is used as the basis for the fitness function that drives the genetic algorithm. We discuss the objective function further in section 5.3.

This combination of the methods provides a way to simulate the UAV's behaviour over time, given a set of initial conditions and mission parameters. This simulation can then be used to calculate various performance metrics, such as the UAV's mass, efficiency, mission success rate, or other performance metrics. The inclusion of the initial value problem in the performance model allows for a more accurate evaluation of the dynamic response of the UAV during the flight, especially changes in segments such as from climb to cruise.

To use the initial value problem introduced in section 2.3.3 and the methodology from Appendix A.3 in conjunction with a canonical genetic algorithm, the fitness function needs to be defined as a combination of these performance metrics (efficiency, mission success rate). The genetic algorithm can then be used to search the set of design variables in the design space of the hybrid powertrain, seeking an optimal solution that minimises the total weight or cost of the powertrain whilst satisfying the constraints imposed by the initial value problem, simulating the flight profile of the UAV and the desired mission performance. The genetic algorithm starts the initial population with a set of candidate designs, each defined by a vector of design parameters such as battery capacity, solar cell area, and fuel cell power density. Other design variables include parameters such as powertrain component's indices and the power split between different propulsion systems.

By searching for the optimal set of design variables using the genetic algorithm, the author determines the combination of component sizes, power splits, and other design parameters - such as thrust and climb angles required for the given powertrain components that maximise the UAV's performance for a given set of mission requirements. For each topology string, the indices identifying the available components are the chromosomes and each chromosome consists of genes, with each gene representing a parameter of the solution. For example:

p[em{B

where $\mathrm{p} \in \{0,\ i_{\mathrm{p}}\}$, $\mathrm{em} \in \{0,\ i_{\mathrm{em}}\}$, $\mathrm{B} \in \{0,\ i_{\mathrm{B}}\}$ where i is the index of the available component in the collection. Therefore, a chromosome of such topology may look like:

$$\mathrm{p}[\mathrm{em}\{\mathrm{B} = (0\ 0\ 0)$$

where each gene – all zeros in this example – is a catalogue index value. In the above chromosome, the value in the first position represents the catalogue number of the propeller selected, the second is the catalogue number of the electric motor and the third is that of the battery. For example: 'p' at index 0 could represent a 12" x 6" propeller, which is used to solve the mission simulation. Note that the topology is fixed for a particular GA encoding, that is, the GA searches the catalogues for the best components for a given topology, not the space of the topologies.

In general, the combination of an initial value problem for mission simulation and a genetic algorithm for optimisation can be a powerful tool for designing and optimising hybrid UAVs, allowing a wide range of design options to be explored and optimised for performance in real-world flight scenarios.

5.2 Overview of initial sizing methodology

To develop a simulation model that predicts the performance of the powertrain under different operating conditions, the following steps are taken:

1. Estimate the power requirements: Determine the required power output of the hybrid powertrain based on the maximum allowable mass of the UAV (i.e. 5.5 kg for the Believer and 25 kg for PEREGRIN) and desired flight performance of the UAV. In this study, this is achieved by determining the thrust requirements as well as the climb angles for each flight segment. This will depend on the aircraft's weight, airspeed and altitude.

2. Identify the different components that make up the powertrain, including the energy storage and conversion systems, motors and propellers as seen in - see Table 5.1.

3. Develop a mathematical model that describes the behaviour of the powertrain components. This involves considering the physical laws that govern the behaviour of these components. For example, for a battery, the model describes the battery's voltage and current as a function of the charge and discharge rates (Appendix B.4).

4. Integrate the models of the different powertrain components to create a comprehensive model of the entire powertrain system. This involves considering how the components interact with each other, such as how the motor's speed and torque impact the battery's output voltage.

5. Define the input variables to the model, such as flight conditions (e.g. altitude) (seen in Figures 1.6a - 1.6f) and the power demand of the UAV, found through a self-modifying code, visualised in Figure 4.4. The output of the model includes thrust, climb angle, true airspeed, climb rate, ground speed, accelerations in x and z, energy split, powertrain efficiency, power output and weight at each time step.

5.2.1 Calculating efficiency of the modelled system

Knowing the total efficiency of the system is important when comparing different powertrain topologies, as well as the powertrain efficiency at each flight segment. In order to obtain the total powertrain efficiency, the following method is applied.

For a single branch (i.e. linear), calculating the efficiency is straight forward. The individual component efficiencies are calculated based on the current demands and are multiplied to obtain the total efficiency of the branch. For example, if the system is p[em{B and each component is calculated to have 0.5 efficiency, then the total system efficiency would be 0.125 (p = 0.5, em = 0.5, B = 0.5). We treat the string as linear, until a branch is reached. In the example of | p[em{pc + p[em{B | {PV, the first branch

TABLE 5.1: Fixed powertrain topology case studies for the genetic algorithm to search the catalogues for the best components.

Case study number	PoETS String
Single energy source	Single propeller
1	p[em{B
2	p[en(HC
3	p[em{fc(HY
4	p[em{PV
Single energy source	Twin propellers
5	|p[em+p[em|{B
6	|p[en+p[en|(HC
7	|p[em+p[em|{fc(HY
8	|p[em+p[em|{PV
Multi energy source	Single propeller
9	p[em|{B+{gn[en(HC|
10	p[em|{B+{fc(HY|
11	p[em|{B+{PV|
12	p[em|{PV+{gn[en(HC|
13	p[em|{PV+{fc(HY|
Multi energy source	Twin propellers
14	|p[em+p[em|{pc|{B+{gn[en(HC|
15	|p[em+p[em|{pc|{B+{fc(HY|
16	|p[em+p[em|{pc|{B+{PV|
17	|p[em+p[em|{pc|{PV+{gn[en(HC|
18	|p[em+p[em|{pc|{PV+{fc(HY|

p[em{pc is first calculated, then the second branch p[em{B is calculated. Then, with the assumption that the two branches are providing equal weight, we add the output of the two branches and divide by two to obtain the efficiency of the branches. After that, the single branch way of calculating the efficiency is applied.

5.3 Objective function formulation and rationale

The optimisation problem is a problem with nonlinear constraints to determine the optimal powertrain sizing, energy split factor (if hybrid) and the mission profile (thrust and climb angles required). Therefore, the objective function is based on an energy-based sizing methodology for optimising the mission profile, minimising propulsion

mass and optimising the hybridisation factors of the powertrain. The complete optimisation problem is defined using a weighted sum approach, which incorporates constraint violations as penalty terms, to combine several objectives into a single cost function.

The energy flow optimisation method employs combinatorial optimisation using a canonical genetic algorithm optimiser to choose components for each mission and determine the energy management during the flights. This study aims to optimise the power and energy flow. The objective function is the combination of the total energy consumption and mass of the propulsion system, including with wet fuel. For the objective function based on the energy-based sizing, we used the total transport energy. This is the energy required to transport the UAV from one point to another; it is the sum of the potential energy, kinetic energy and energy required to overcome drag during flight, as well as the energy to overcome friction during the take-off segment. By minimising the total transport energy, we can improve the endurance and range of the UAV. To minimise the total transport energy, we need to find the combination of a feasible thrust and climb angle of the UAV. The thrust required to overcome drag during flight depends on the weight and aerodynamics of the UAV as well as the altitude and airspeed. With the thrust (and climb angle) variable corresponding to the minimum transport energy for the given powertrain configurations, we can reduce the drag and thus the energy required to overcome it. The climb angle, which affects the maximum power demand from the powertrain, also affects the potential energy required to lift the UAV off the ground and maintain it at a certain altitude. By optimising the climb angle, we can reduce the potential energy required and thus reduce the total transport energy. Therefore, we can improve the performance and efficiency of the UAV and fly better mission profiles. Minimising total transport energy can also help minimise the required power from the powertrain. By reducing the drag and climb power, we can reduce the power required from the energy source and components in the powertrain, thus enabling lighter components and saving weight. To achieve this, the mission is broken into a number of short segments: take off, climb, cruise, and descent. The flight (combination of segments) is then simulated to obtain the energy consumed in every time step of the flight phase using:

$$\Delta E = \left(\frac{m\ g\ V_{\text{TAS}}}{\frac{L}{D}} + \frac{m\ \Delta v^2}{2} + m\ g\ \text{RoC} + m\ g\ V_{\text{TAS}}\ \mu \right) \Delta t \tag{5.1}$$

where the first term corresponds to the energy demand arising from aerodynamic drag, the second to the kinetic energy (acceleration), the third to the potential energy (altitude change) and the fourth to the energy lost due to friction which is zero for all segments except take-off. To ensure that the energy objective is compatible with the mass objective, we normalise it by a reference total transport energy and scale it by the maximum take-off mass.

$$E_{\text{norm}} = \text{MTOM}_{\text{max}} \frac{\sum \Delta E}{E_{\text{ref}}}$$

In addition to minimising the total transport energy, we also minimise the powertrain sizing of the UAV. Minimising powertrain sizing typically involves reducing the weight and size of the propulsion system while still meeting the performance requirements of the UAV. This involves optimising the design of the motor, propeller and other components to reduce their weight and improve their efficiency. The total mass, m_{total}, is defined as:

$$m_{\text{total}} = m_{\text{propulsion}} + m_{\text{wet fuel}} \tag{5.2}$$

If the powertrain mass, $m_{\text{propulsion}} + m_{\text{wet fuel}} > 0.6\,\text{MTOM}_{\text{max}}$, the powertrain is deemed too heavy to be feasible and the following penalty, P_1, is added with $\lambda = 0.3$ (Figure 5.1a):

$$P_1 = \lambda\ (m_{\text{propulsion}} + m_{\text{wet fuel}} - 0.6\,\text{MTOM}_{\text{max}}) \tag{5.3}$$

One of the constraints is that the chosen propulsion should be able to complete the mission. Therefore, for each incomplete (unsuccessful) mission, the penalty P_2 is chosen as:

$$P_2 = \text{MTOM}_{\text{max}}\ (1 - p) \tag{5.4}$$

where p is the proportion of the mission failure to the mission success (Figure 5.1b) in times.

The final constraint is the component matching in the powertrain, such that if a component mismatch occurs (i.e. motor cannot handle above a certain current during the climb segment and it 'burns out' (virtually) or if the fuel runs out but the battery does not run out in a dual-energy source architecture) the penalty P_3 is chosen as

$$P_3 = \text{MTOM}_{\text{max}} \, (1 - p) \tag{5.5}$$

where p is the proportion of the success of the component to the success of the mission (Figure 5.1c).

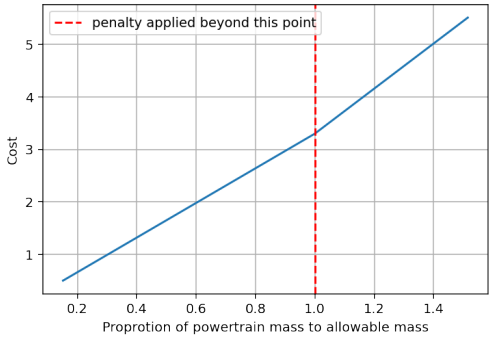

(A) Penalty applied on the mass constraint: Equation 5.3.

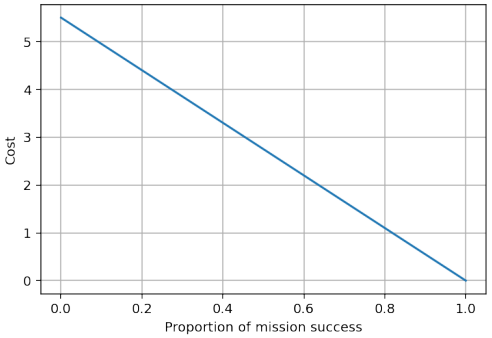

(B) Penalty applied on mission failure constraint: Equation 5.4.

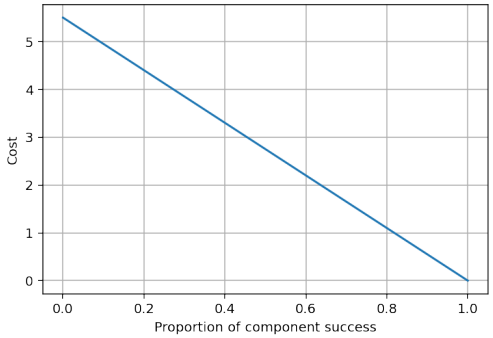

(C) Penalty applied on component failure constraint: Equation 5.5.

FIGURE 5.1: Penalty function outputs for the cost function with respect to a maximum take-off mass of 5.5 kg.

Therefore, the complete optimisation problem is defined using a weighted sum approach to combine the above objectives into a single cost function. The weights represent the relative importance of each objective and are heavily weighted toward minimising the final mass and less towards minimising the total transport energy. Weighting factors are used in multi-objective optimisation problems to combine different objectives into a single objective function. The weighting factors help to balance the contribution of each objective towards the overall objective function value.

For example,

$$\text{minimise } f(w_1\, m_{\text{total}} + w_2\, \Delta E) + P_1 + P_2 + P_3 \tag{5.6}$$

where w_1 is 0.65 and w_2 is 0.35. The penalties, P_1, P_2 and P_3, are zero if the powertrain is under the mass limit, the mission is completed successfully, there is no mismatch of the components and both energy sources last until the end for hybrid configurations. In the case of P_1, P_2 and P_3 being non-zero, their values outweigh the actual objectives (mass and total transport energy), hence heavily penalising the cost.

In order for the search process to be carried out, the following design variables (Table 5.2) and design constraints (Table 5.3) are employed. The design variables are the parameters determined by the engineer and in our study, the general case of the topology design of the powertrain is divided into three categories, as seen in Table 5.2.

The first category in Table 5.2 directly impacts the mission profile portion of the optimisation problem, which is applicable to Equation 5.6 as efficient thrust management can significantly affect transport energy. This can be achieved by using thrust at levels that provide adequate performance while minimising excessive energy consumption. Although a shallower climbing angle generally requires less thrust and therefore reduces energy consumption, it is important to balance the climb angle with factors such as altitude gain requirements, aircraft performance capabilities, and operational constraints. The nature of these design variables is continuous as these describe the state of the platform at each segment at a given time for the entire mission for the given

powertrain (i.e. power source, p, is generating x amount of power due to the thrust, T, required at timestep, s).

The second part of the optimisation is the sizing process which is driven by the commercial off-the-shelf data and includes parameters such as mass, propeller dimensions, maximum allowable rotation speed for the combustion engines and electric motors, maximum allowable current of the electric motors. These variables are embedded inside the indexes of each component data). Thirdly, for topology strings which have more than one energy source, the degree of energy hybridisation is applied here to obtain the optimal split of the energy sources, which is shown in the third part of Table 5.2. The nature of these design variables is discrete as we employ off-the-shelf components.

TABLE 5.2: Design variables for Equation 5.6.

Parameter	Range	Lower bound	Upper Bound
Applicable to	Equation 5.1 and 5.4		
T [N]	Thrust	0.2 MTOW	MTOW
γ [deg]	Climb angle - takeoff	1	5
	Climb angle - climb	5	20
	Climb angle - descent	-20	-1
V_r [ms^{-1}]	Takeoff rotate speed	13	18
Applicable to	Equation 5.2 and 5.4		
p_i	index of propeller	0	525
em_i	index of electric motor	0	460
en_i	index of engine	0	46
gn_i	index of generator	0	460
fc_i	index of fuel cell	0	10
PV_i	index of solar cell	0	19800
B_i	index of Battery	0	663
HY [kg]	mass of hydrogen fuel	0.001	2
HC [kg]	mass of gasoline fuel	0.5	3
Applicable to	Equation 5.1, 5.2 and 5.4		
DoH_e s.t $\sum DoH_e = 1$	degree of energy hybridisation	0	1

The onboard power components also need to satisfy constraints (shown in Table 5.3) in order to determine the feasibility of each topology string. Violation of these constraints leads to infeasible solutions as it would in a physical system. For example, violation of the maximum allowable current would lead to electric motor failure due to overheating, state of charge (SOC) of below 0.2 may lead to damage to the battery, or an angle of attack above a certain angle would lead to the stall of the aircraft.

TABLE 5.3: Design constraints for Equation 5.6.

Parameter where i = component	Definition	Value
I_i [A]	Current	<= maximum allowable current
ω_i [RPM]	Engine speed	<= KV V_i
P_i [W]	Power	<= Peak power
η_i	Efficiency	>= 0.3
SOC	>= Battery state of charge	0.2
α [deg]	Angle of attack	<= 20
Control parameter	Definition	Value
u_T [N s^{-1}]	Thrust control	10
u_θ [deg s^{-1}]	Angle control	1

5.4 Contribution four – optimising powertrains

Stepping up from contribution three, we can also design a powertrain such that it optimises a cost function for a given mission. Table 5.1 shows the test cases that were chosen from Mission 1 (Figure 1.6a) to 6 (Figure 1.6f) for both test platforms discussed in Appendix A. In this study, we look into two different-sized UAVs: one with no more than 5.5 kg (2 kg structural mass) maximum take-off mass and another which has no more than 25 kg (10 kg structural mass) maximum take-off mass. The same mission cases were presented to both UAVs for comparison purposes. Only the feasible powertrains are included in the results section (for example, if a component failed midway during the mission - such as the expected propeller performance is more than the limits of the experimental data, these are counted as infeasible powertrains).

5.4.1 Optimisation convergence check

To ensure that the design space is explored in a reasonable time, a convergence study is performed. The population of each generation (n_{pop}) was chosen such that

$$n_{\text{pop}} = 2\left(n_{\text{mission vars}} + n_{\text{max components}}\right)$$

where $n_{\text{mission vars}}$ is the number of thrust and climb angles required (i.e. up to two variables per segment) and $n_{\text{max components}}$ is the number of components in the topology string (i.e. p[em{B contains three). The sum of the variables is multiplied by a factor

of two to ensure that the initial population size is above 100. This is because genetic algorithms are stochastic and they are therefore dependent on their initial population. In the canonical genetic algorithm, when the initial population is too small, the genetic algorithm might not find a feasible solution. Whereas when the population is too large, there will be a computational time penalty.

The algorithm is terminated if the tolerance in the objective space on average is below 0.05 or if the maximum number of generations reaches 100. This is achieved by tracking the fitness value of the best solution found in each iteration. If the fitness value has not improved significantly for several iterations, the genetic algorithm is assumed to have converged. Examples using Mission 1 are shown in Figure 5.2a - a single propeller with a single energy source and Figure 5.2d which shows a relatively complex test case for this mission - multiple propellers with multiple energy sources - which demonstrates that the genetic algorithm is only terminated once the convergence is reached.

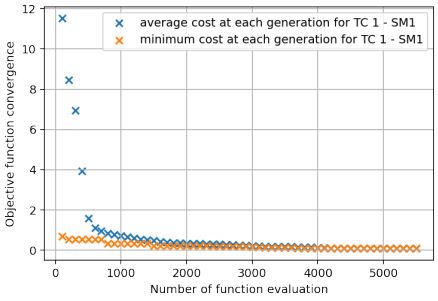

(A) Test case 1 (single prop, single source).

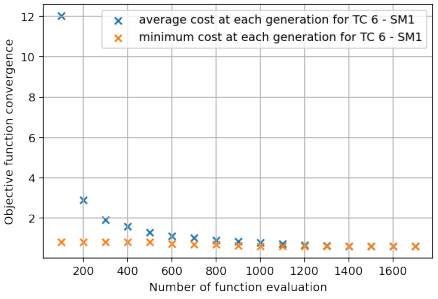

(B) Test case 6 (multi props, single source).

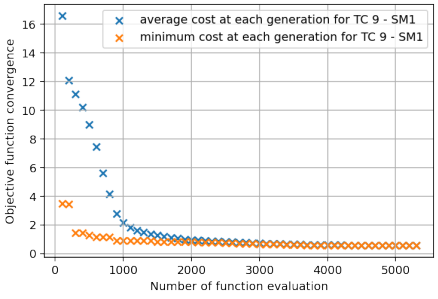

(C) Test case 9 (single prop, multi sources).

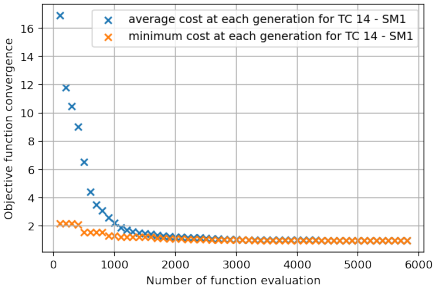

(D) Test case 14 (multi props, multi sources).

FIGURE 5.2: Genetic algorithm convergence of the objective function demonstrator for Mission 1.

5.4.2 Mission 1

In this section, we discuss the output of running a canonical genetic algorithm to find the optimum set of components for a given architecture and a target mission (for example: Figure 5.3), for the two test platforms. Note that the two test platforms (FliTePlat and PEREGRIN) described in Appendix A differ in their maximum allowable take-off mass (with different powertrain mass fractions) as well as their aerodynamic coefficients.

Figure 5.4 shows the feasible topology string outputs (x-axis) and their respective total take-off mass (y-axis, blue crosses), as well as the dry propulsion mass (as a label in black). Figure 5.4a represents the result of Mission 1 for FliTePlat which has a structural mass of 2 kg, whereas Figure 5.4b represents the result of Mission 1 for PEREGRIN which has a structural mass of 10 kg. On the left of the grey dashed vertical line in both figures are single energy source powertrains whereas the right are multi-energy source powertrains. The topology strings are then arranged following the number of propulsors follow by their respective total masses. From this, we can see that for both platforms, the best outcome is p[em{B.

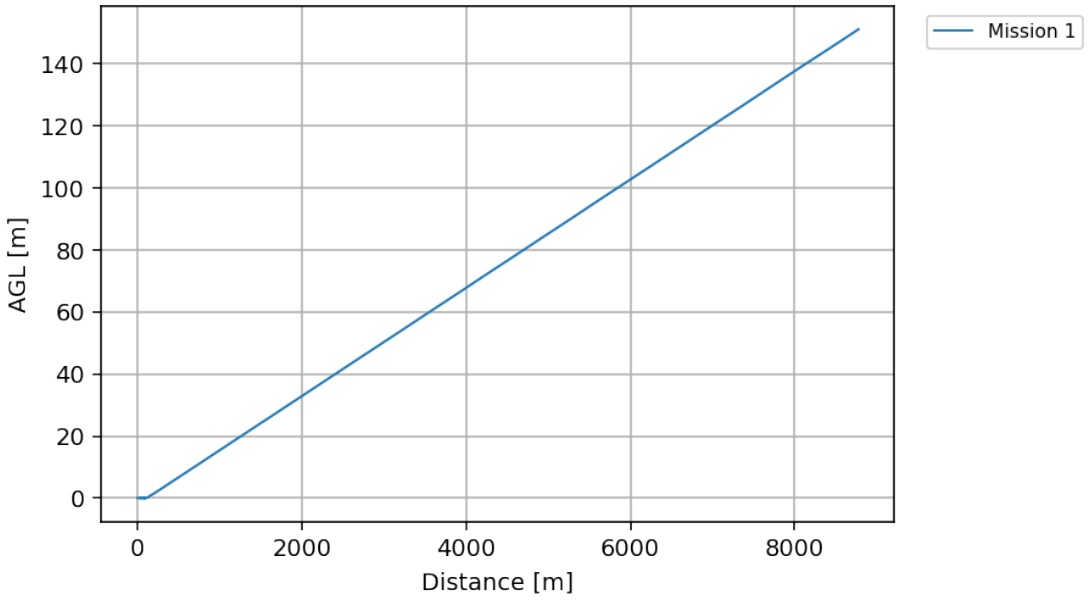

FIGURE 5.3: Mission 1 - profile.

Figure 5.5 shows the energy split for the hybrid powertrains as well as the average powertrain efficiency for Mission 1. For each topology string represented in x-axis, the energy sources are shown at the top and the bottom (for a single energy source, the same letter is shown at the top and the bottom, i.e. B). The bar represents the proportion of the energy source responsible for that segment. For example, in Figure 5.5a, for topology string: p[em | {B + {gn[en(HC |, the darker orange shows the proportion of the energy supplied by the battery (0.4) and the lighter orange from the petrol (0.6). The average powertrain efficiency for this powertrain is shown by the black marker ($\approx$ 0.2), with the maximum and minimum shown by the vertical component of the black marker.

Figure 5.6 shows the time taken for each topology string to complete Mission 1 in simulated time. Figure 5.6a shows the time taken for FliTePlat. Here we can see that the majority of the powertrains complete the mission in less than 50 seconds with three of the powertrains taking more than 200 seconds. The slow time is the result of the shallower climb angles (as seen in Tables 5.4 and Tables 5.5). On the heavier platform, PEREGRIN in Figure 5.6b, most of the powertrains, on average, take longer to complete the same mission than FliTePlat.

Tables 5.4 and Tables 5.5 show the design variables corresponding to the powertrain for Mission 1 shown in Figure 5.4. The total thrust demanded by the propeller(s) as well as the demanded climb angles at the initial timestep and the final timestep are shown here. As expected, the heavier platform (PEREGRIN) requires on average a higher thrust and a shallower final climb angle than FliTePlat.

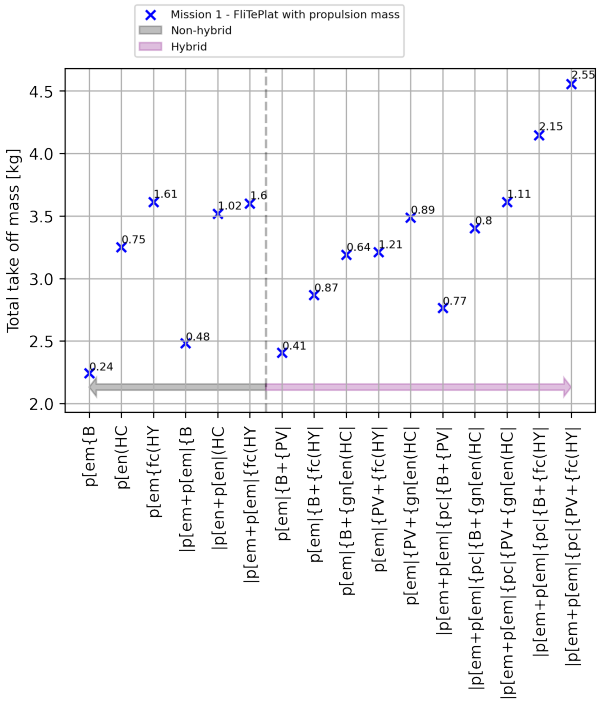

(A) Mission 1 - FliTePlat test case 1.5a.

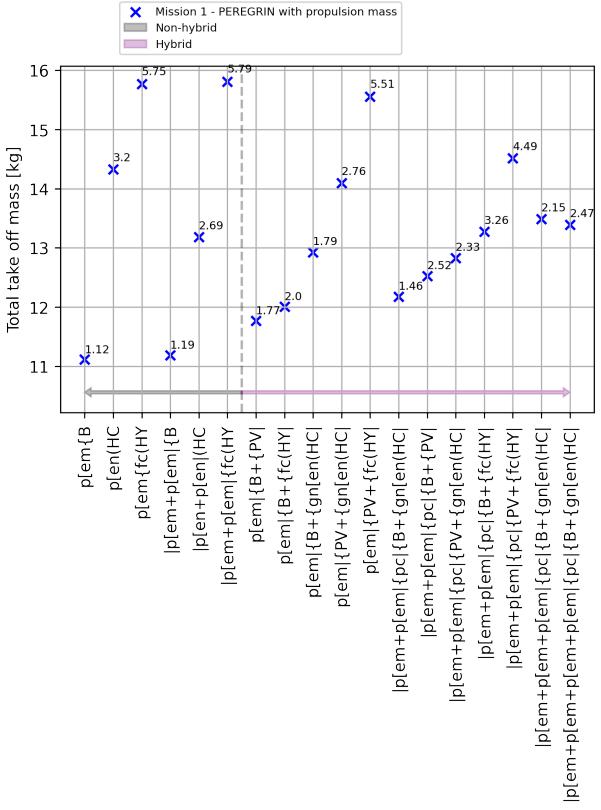

(B) Mission 1 - PEREGRIN test case 1.5b.

FIGURE 5.4: Mission 1 - mass optimisation results.

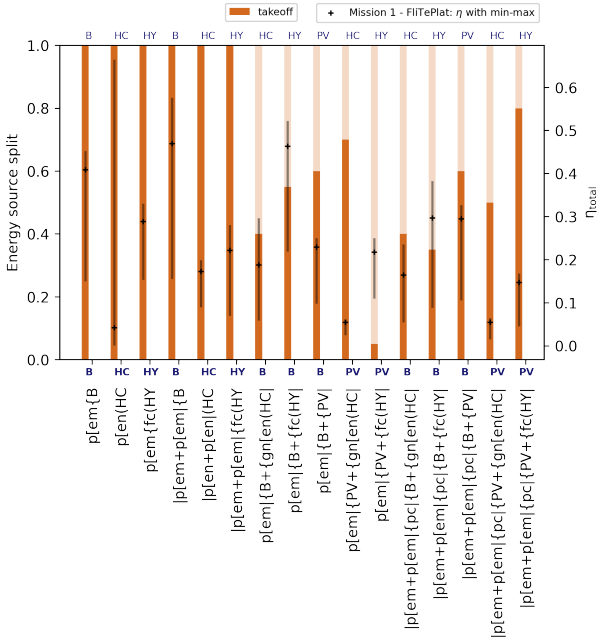

(A) Mission 1 - FliTePlat test case 1.5a.

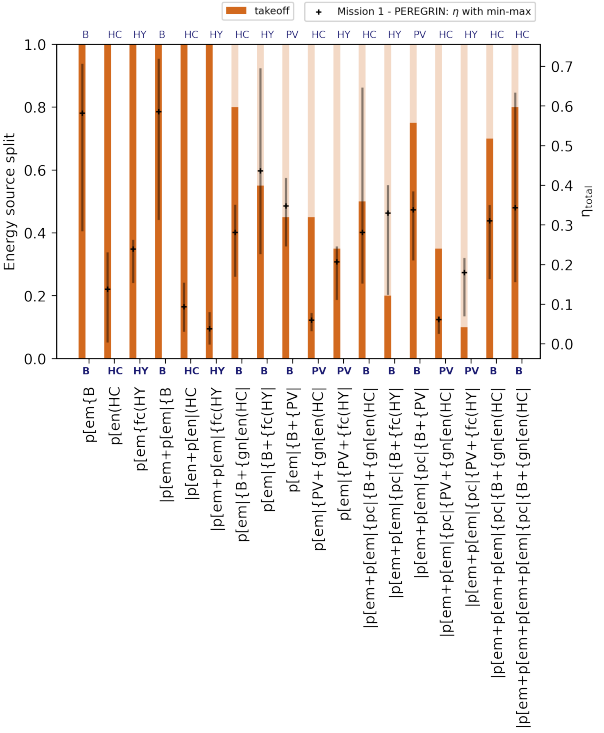

(B) Mission 1 - PEREGRIN test case 1.5b.

FIGURE 5.5: Mission 1 - energy source split and efficiency results.

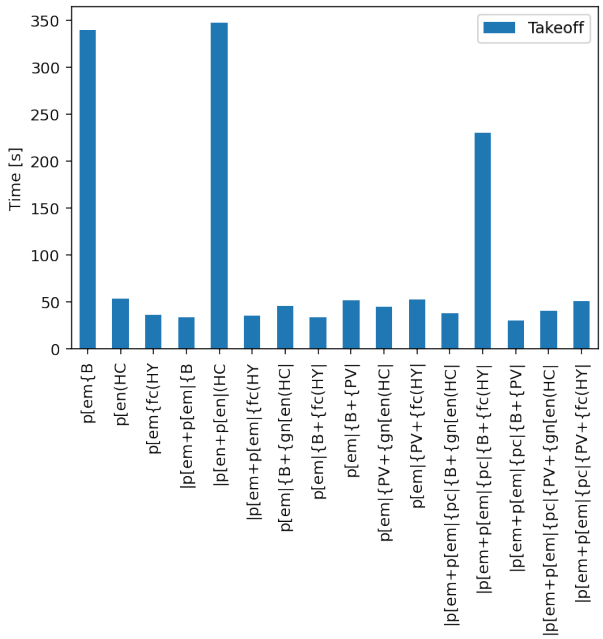

(A) Mission 1 - FliTePlat test case 1.5a.

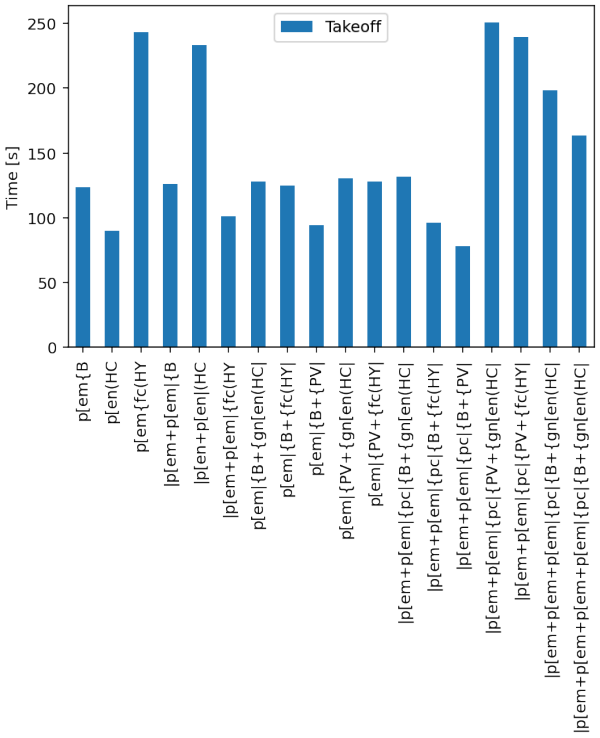

(B) Mission 1 - PEREGRIN test case 1.5b.

FIGURE 5.6: Mission 1 - time taken to complete the mission.

TABLE 5.4: Mission 1 - FliTePlat output - optimal thrust and climb angle.

Number	Test string - FliTePlat - Mission 1	Thrust [N] Takeoff		Climb angle - Takeoff [deg] Takeoff	
		Initial	Final	Initial	Final
1	p[em{B	15.10	10.79	0	1
11	p[em|{B+{PV|	28.05	19.42	0	5.75
5	|p[em+p[em|{B	23.73	23.73	0	12.4
16	|p[em+p[em|{pc|{B+{PV|	32.36	34.52	0	12.4
10	p[em|{B+{fc(HY|	36.68	38.83	0	9.55
9	p[em|{B+{gn[en(HC|	15.10	21.57	0	9.55
13	p[em|{PV+{fc(HY|	47.46	36.68	0	3.85
2	p[en(HC	15.10	19.42	0	7.65
14	|p[em+p[em|{pc|{B+{gn[en(HC|	17.26	30.20	0	7.65
12	p[em|{PV+{gn[en(HC|	45.31	34.52	0	5.75
6	|p[en+p[en|(HC	17.26	10.79	0	1
7	|p[em+p[em|{fc(HY	19.42	28.05	0	8.6
17	|p[em+p[em|{pc|{PV+{gn[en(HC|	19.42	17.26	0	11.45
3	p[em{fc(HY	53.94	40.99	0	7.65
15	|p[em+p[em|{pc|{B+{fc(HY|	15.10	23.73	0	1
18	|p[em+p[em|{pc|{PV+{fc(HY|	19.42	17.26	0	8.6

TABLE 5.5: Mission 1 - PEREGRIN output - optimal thrust and climb angle.

Number	Test string - PEREGRIN - Mission 1	Thrust [N] Takeoff		Climb angle - Takeoff [deg] Takeoff	
		Initial	Final	Initial	Final
1	p[em{B	117.68	49.03	0	1.95
5	|p[em+p[em|{B	58.84	49.03	0	1.95
11	p[em|{B+{PV|	68.65	49.03	0	2.9
10	p[em|{B+{fc(HY|	88.26	49.03	0	1.95
14	|p[em+p[em|{pc|{B+{gn[en(HC|	49.03	49.03	0	1
16	|p[em+p[em|{pc|{B+{PV|	58.84	49.03	0	3.85
17	|p[em+p[em|{pc|{PV+{gn[en(HC|	58.84	58.84	0	1
9	p[em|{B+{gn[en(HC|	68.65	49.03	0	1.95
6	|p[en+p[en|(HC	107.87	49.03	0	1
15	|p[em+p[em|{pc|{B+{fc(HY|	49.03	49.03	0	2.9
23	|p[em+p[em+p[em+p[em|{pc|{B+{gn[en(HC|	68.65	98.07	0	1
22	|p[em+p[em+p[em|{pc|{B+{gn[en(HC|	49.03	68.65	0	1
12	p[em|{PV+{gn[en(HC|	88.26	49.03	0	1.95
2	p[en(HC	68.65	49.03	0	3.85
18	|p[em+p[em|{pc|{PV+{fc(HY|	58.84	49.03	0	1
13	p[em|{PV+{fc(HY|	98.07	49.03	0	1.95
3	p[em{fc(HY	58.84	49.03	0	1
7	|p[em+p[em|{fc(HY	58.84	49.03	0	2.9

Since the format for the results are similar for Missions 2 - 6, detailed results for the remaining missions can be found in Appendix C.

5.4.3 Component output results comparisons

In Tables 5.6 - 5.7, some of the example outputs from the optimisation framework for both single (Table 5.6) and multi-energy sources (Table 5.7) are presented. The results from this powertrain optimisation process demonstrate the capabilities of the framework and demonstrate the ability to correctly size the optimal components for a given powertrain and mission. As component models are based on physical data, the designer can acquire the exact off-the-shelf components for their design.

TABLE 5.6: Test case 1 - p[em{B - component output results.

Mission		1	1
Vehicle		PEREGRIN	FliTePlat
Propeller	Type	18.1x10	13x14
Electric Motor - based on the specifications	KV [RPM/V]	90.0	1040.0
	Mass [kg]	0.815	0.129
	I max [A]	65.8	40.0
	P peak [W]	3000	630
Battery	Cells	5	3
	Capacity [mAh]	1550	550
	Mass [kg]	0.21	0.05
	Discharge rate [C]	120.0	95.0

TABLE 5.7: Test case 13 - p[em|{PV+{fc(HY| - component output results example.

Mission		1	2	4	5	6	1	2	3	4	5	6
Vehicle		PEREGRIN					FliTePlat					
Propeller	Type	22x12	18.1x12	18.1x11	18.1x11	18.1x11	13x14	13x14	13x14	13x14	13x10	13x14
Electric Motor	KV $[\frac{RPM}{V}]$	90.0	190.0	170.0	195.0	160.0	900.0	860.0	475.0	400.0	200.0	2095.0
	Mass [kg]	0.815	0.8556	0.67	0.6348	0.8599	0.108	0.143	0.108	0.138	0.232	0.23
	I_{max} [A]	65.8	90.0	149.1	75.0	85.0	40.0	65.0	22.1	25.0	40.0	51.0
Solar Cells	Series Parallel	6s32p	6s40p	11s21p	16s12p	11s17p	1s889	1s74p	1s81p	1s75p	6s12p	1s89p
	P_{peak} [W]	334	417	310	334	325	81	68	75	69	67	82
	G $[\frac{W}{m^2}]$	1765	1765	1360	1765	1765	945	945	945	945	945	945
	V_{mpp} [V]	5.60	5.60	10.42	14.93	10.26	0.94	0.94	0.94	0.94	5.61	0.94
	I_{mpp} [A]	59.60	74.50	29.71	22.35	31.66	86.95	73.12	80.04	74.11	11.86	87.94
	Mass [kg]	0.94	1.18	1.13	0.94	0.92	0.43	0.36	0.40	0.37	0.35	0.44
	Area $[m^2]$	0.94	1.18	1.13	0.94	0.92	0.43	0.36	0.40	0.37	0.35	0.44
	Cells	37	40	37	37	37	20	20	20	20	20	20
	P_{peak} [W]	300	300	300	300	300	60	60	60	60	60	60
	Mass [kg]	0.72	1.17	0.72	0.72	0.72	0.536	0.536	0.536	0.536	0.536	0.536

5.5 Powertrain outcome of each mission

Small UAVs require high power-to-weight ratios to achieve sufficient thrust for takeoff and climb. While hybrid systems can provide improved efficiency, the power output of small-scale combustion engines is often sufficient to meet the power requirements of these UAVs. In this section, we discuss the chosen powertrains for each mission for FliTePlat and PEREGRIN.

For FliTePlat, the battery powertrain is chosen to be optimal regardless of the mission type given here. One of the reasons is the maximum allowable mass (no more than 5.5 kg maximum take-off mass) imposed upon the platform, this favours the high discharge rate of the battery. This reason is also reflected in the hybrid propulsion architectures, where FliTePlat favours the battery and photovoltaics more than any other powertrain; other powertrains require a fuel tank. The heaviest propulsion systems are consistently hydrogen fuel cell systems, be it hybrid or single energy source. For both Mission 1 (Figure 5.4a) and Mission 3 (Figure C.5a), a single propeller battery powered and single engine powered system is better in terms of mass than the equivalent source systems with dual propellers. However, for Mission 2 and 4, there is a negligible difference in maximum take-off mass for the single propeller and dual propeller architectures for the battery system.

In general (Missions 1, 2, 4 and 5), single-propeller powertrains combining battery and photovoltaics as well as battery and fuel cell energy sources are lighter than the photovoltaic and fuel cell combination. This is due to the fact that the powertrain needs to be sized for the power output, especially during high power demand phases such as take-off. The battery is typically able to handle the high power demand instantaneously (especially if it has a high discharge rate). In contrast, either the fuel cell or photovoltaic cell (in this case the fuel cell) needs to be oversized to be able to handle such demand.

In Mission 1 for FliTePlat, the energy source split is linked to the climb angle for powertrains containing a battery. These powertrains prefer steeper climb angles - Figure 5.4a and Table 5.4. However, when a shallower climb angle is allowable, non-battery energy

sources, such as a solar cells (when there is enough solar irradiance) or energy-dense sources (such as hydrocarbon fuel or hydrogen fuel), are preferred to be used as the dominant energy source, thus reducing the battery size.

In Mission 2 for FliTePlat, the best hybrid powertrain (test case 11: p[em | {B + {PV |) favours heavily towards photovoltaics with 0.75 (75%) of the energy contribution for take-off and 0.85 energy contribution for the cruise. This is combined with the shallow climb angle, thus the power demand is within the photovoltaic capability. On the other hand, in Mission 3, for the same test case, the energy split favours the battery for all flight segments with the optimiser choosing steeper climb angles for the take-off and climb for this powertrain components configuration. This is a realistic outcome, where the steeper climb angle is enabled by the battery's ability to cope with power burst demand. Mission 6 combines these ideas in the optimal hybrid powertrain (test case 11). Here, the shallow climb angle at takeoff is predominantly powered with the photovoltaics but the steeper climb angle in the final segment utilises the battery more.

For a bigger UAV, such as PEREGRIN, energy-dense fuel types such as hydrocarbon and hydrogen are preferred (Figures C.2b, C.5b, C.8b, C.11b and C.14b), except Mission 1 (Figure 5.4b) which is relatively short compared to the other missions. One interesting observation is that, unlike in FliTePlat where the p[em{B powertrain performs well, in PEREGRIN, this does not seem feasible for long-duration missions. This is likely due to the limitation of the energy density of current commercial UAV batteries which is not high enough for a single battery powering bigger UAVs.

Similarly to FliTePlat, for Mission 1, 2 and 6, the battery and fuel cell powertrain are lighter and have a higher overall powertrain efficiency than that of photovoltaics and fuel cell powertrains. The exception is the case where very shallow climb angles are followed (Table C.6). In this case, the photovoltaic and fuel cell powertrain is lighter than the battery and fuel cell combination, though this is still not better for the overall efficiency.

In Mission 1 for PEREGRIN, when the energy source is fixed, (i.e. Battery or Hydrocarbon), the single propulsor (electric motor) is slightly lighter than dual propulsors for a battery energy source system (though only by 0.07 kg). For hydrocarbon fuel, on the

other hand, dual propulsors (engines) are lighter than a single propulsor (by 0.51 kg). This is because, by distributing the thrust, the power output required per engine is reduced, leading to reduced sizing of each combustion engine. The trend seen in the engines is also visible in Mission 6 (Figure C.14b).

In terms of the energy source split factors for the lightest hybrid powertrain, in Mission 1, the photovoltaic cells is preferred (0.55) to the battery (0.45). In Mission 2, where the battery and fuel cell are the energy components of the lightest system, for both take-off and cruise, the fuel cell is the dominant (~ 0.9). A fuel cell is also dominant for Mission 4, 5, and 6 compared to its counterpart: the battery. All of the climbs performed are as shallow as possible which is likely to reduce the peak power demand of the fuel cell and thus reduce the mass.

Mission 3 deviates from this trend with the battery supporting the take-off and being the dominant energy source due to the climb segment. The cruise is predominantly powered by the fuel cell. In this strategy, the steady power output from the fuel cell is used to minimise the weight required to carry the energy for the cruise, with shorter high bursts of power (as it has a lower altitude to reach for the take-off compared to Mission 4 and 6) supplied by the battery for the higher power demand required for the final climb. Therefore, it is likely that the battery was sized for the first segment of higher but shorter power demand (unlike for Mission 4, 5 and 6), thus leading to this outcome.

5.6 FliTePlat vs PEREGRIN - comparisons

Where the previous section compared the performance between different powertrains and missions for the same UAV, this section aims to compare the powertrains of the two UAVs with each other.

Generally, PEREGRIN, which has different aerodynamic properties and mass limitation compared to FliTePlat, produced fewer valid topology strings than FliTePlat. This is likely due to the fact that commercial UAV components (especially at the lower cost end) are catered towards the small UAV market - UAVs of FliTePlat's size rather than

that of PEREGRIN. This also results in powertrain such as p[em{B or | p[em + p[em | {B not being valid topology strings (a string populated with components able to complete the mission) for PEREGRIN, as well as PEREGRINE favouring the high energy density sources such as hydrogen or hydrocarbon. However, for FliTePlat (in Figures 5.4a, C.2a, C.5a, C.8a, C.11a and C.14a), the battery based powertrains are generally lighter than wet fuel based. One common result across both FliTePlat and PEREGRIN is that all missions favour as shallow a climb as possible for reduced powertrain mass. This is because the time taken to complete the mission is not an objective of the cost function, therefore the optimiser prioritises minimising the total transport energy.

It is no surprise that almost all of the test strings produced valid powertrains in the optimisation of Mission 1 as it is a short mission with only one segment (except the purely photovoltaic powertrain for both test platforms due to its incapability for high load demands). Focusing on Mission 1 (Figures 5.4a and 5.4b), for both single and dual propulsors, the battery is favoured as the main energy source. For hybrid energy sources, both platforms favour batteries with photovoltaics with both sources contributing to the mission in roughly equal proportions (Figures 5.5a and 5.5b). However, for dual propulsor strings, FliTePlat favours a battery and photovoltaics powertrain and PEREGRIN favours a battery and internal combustion powertrain. This could be due to the limits on the powertrain allowable mass (due to the platform size), where adding an internal combustion engine would violate the mass constraint in FliTePlat but not in PEREGRIN. It is also not surprising that the worse powertrains for both platforms are any powertrains containing fuel cells. This is due to the mass penalty from the fuel tanks required for storing the hydrogen fuel as well as the fuel cell system outweighing any benefit (i.e. high efficiency) when mass is the priority.

Regardless of the platform, since the propeller and electric motor are matched for high efficiency (see section 2.2.7), the total powertrain efficiencies are dictated by the rest of the components in each topology string. The results show that battery powertrains (specifically p[em{B) have the highest efficiency. As discussed in Chapter 2, a powertrain with photovoltaics and a combustion engine gives out a very low overall efficiency, regardless of the segment type (take-off, cruise or climb). This is reflected in the

results (Figures 5.5a, 5.5b, C.3a, C.6a, C.9a, C.9b, C.12a and C.15a).

5.7 Summary and outlook

In this chapter, we demonstrate the capability of the encoding scheme - described in Chapter 3. Using the component models described in Chapter 2 - with the models and the verification in the Appendix B, we formulated the component sizing and optimising of the powertrain, generated by methodology given in Chapter 4 using PoETS encoding scheme, to be suitable for creating, analysing, and comparing different powertrain topologies appropriate to each mission (see Figure 1.6a - 1.6f) on two fixed wing platforms - described in Appendix A. The optimisation problem has been formulated with the aim of minimising the powertrain mass, which enables us to evaluate the hypothesis. The methodology proposed here allows for a comparison of the various feasible topologies, whilst sizing and determining the degree of energy hybridisation and the optimal energy split for hybrid topologies. PoETS shows potential to be used to generate a range of powertrain topologies for exploration, allowing engineers to evaluate the performance of different designs before selecting the most appropriate one. This can be particularly useful when there are multiple design objectives to consider, such as fuel efficiency, power output and cost. Overall, utilising PoETS, a linear string approach, which can be represented as graphs with nodes and edges computationally (described in Chapter 3), provides a powerful tool for analysing and optimising hybrid powertrains for UAVs. By modelling the power flow and control strategy of the system as a graph, engineers and researchers can gain insights into the behaviour of the system under different operating conditions and design more efficient and effective hybrid powertrains. We also discussed the outcome of applying this scheme to practical problems by solving the problem outlined in this chapter through evaluating two test UAV of 5.5 kg and 25 kg maximum take-off mass for various mission types. Setting the vehicle's maximum take-off mass, geometry, and aerodynamic coefficients as inputs, both hybrid and non-hybrid powertrains are explored, allowing for a comparison between different topologies for the same mission and platform. Since this is a proof of concept stage, direct optimisation of the powertrain topologies is considered

out of scope; however, recommendation of potential methods are discussed in Chapter 6 - section 6.4. More importantly, the methodology provided here is not fully tested due to the limitations in the depth of the modelling used. NASAs Greased Lightning 10-Engine (GL-10) in Figure 3.5 at the start is a case in point. Whilst the encoding string can define it the model used to assess the aircraft itself would perhaps not show the advantages of such a configuration. Therefore, in the detailed analysis, a geometric analysis module is needed, along with more advanced aerodynamics analysis.

Chapter 6

Discussion and conclusions

6.1 Discussion summary

This thesis has developed modelling and simulations of powertrains for two UAVs in different mass categories. This was done by developing a single and multi-energy source optimisation capability based on a finite number of components (e.g. batteries, motors, propellers etc.) with the optimiser selecting the components from the database curated in Appendix B as well as choosing the optimal layout and sizing of components, determining deployment schedules and optimising the mission profile.

The models and mission simulations developed here allow us to determine both trajectories (in terms of thrust and climb angles) and the required energy split for the hybrid powertrains. The optimisation is a weighted blend of several objective functions which combines with the encoding scheme to output optimal energy architectures. From the optimal mission profile (the output of the performance model and models of the components discussed in Appendix B), energy split strategies in terms of maximising the efficiency region of the energy components are calculated to obtain the deployment schedules.

While it may be apparent that single energy sources are the most efficient and have the lowest mass for the missions investigated, as Chapter 2 indicates, this may not always be the case. The energy source also depends on the allowable weight of the UAV and

the components available, as shown in the comparison between the two platforms. This research demonstrated that the proposed automated optimisation process can identify such best-case compromises represented by generated architectures with various degrees of electrical energy storage and topology layouts, including multiple propulsors.

Overall, the decision to use a hybrid energy source powertrain versus a single energy source powertrain for a UAV depends on the specific requirements and mission of the UAV. It is important to carefully consider the benefits and drawbacks of each type of powertrain and weigh them against the specific mission requirements to determine which one is most appropriate for the task at hand. Moreover, hybrid powertrains offer greater flexibility and adaptability in various operating scenarios, such as power management optimisation based on specific mission requirements which could enable the UAV to adapt to different flight conditions and mission profiles.

Finally, the hybridisation factor does not just depend on the mission but also on the platforms and the available off-the-shelf components. The thesis illustrates that even though the components may be deemed to be feasible in the preliminary study (such as constraint analysis), once the mission simulation is considered, which involves the transition points and system dynamics, the previously feasible potentially become infeasible. This is because the timestep simulations provide detailed and accurate representations of system dynamics by accounting for time-dependent effects, capture complex behaviours and allow us to understand how different variables evolve over time. For example, when components such as electrical motors are under loaded conditions and violate constraints such as the maximum allowable current. This is evident especially more so in the heavier platform, PEREGRIN, where the number of feasible topology strings are significantly less than that of FliTePlat (Figures C.5b, C.11b). This does not diminish the value of the constraint analysis, as the analysis itself can be used to help identify the limits within which an individual component can operate, thereby reducing the design space for the genetic algorithm during the sizing process.

In summary, the results indicate that a hybrid powertrain may not be necessary or practical for a smaller UAV due to the high mass penalty of the hybrid powertrain which may be more than the UAV can handle. In these cases, a fully electric powertrain or

a traditional internal combustion powertrain may be more suitable. However, hybrid powertrains are more applicable for larger UAV, where this study showed that most of the surviving powertrain topology strings are hybrid for PEREGRIN.

6.2 Summary of chapters

In Chapter 2, we reviewed the current state of the powertrain components for UAVs, their advantages and limitations, along with real-life examples, the current methodology for modelling of the powertrain components and simulations for hybrid powertrain UAVs. We also concluded that whilst there are some in-house software packages not available in open-source (or the packages which are available in the open-source are still in testing phase) that can simulate and analyse the hybrid powertrains, there is still a need for the ability to compare and analyse the different powertrains available in one study. This is because most of the literature focuses predominantly on one type of powertrain as opposed to searching the topology space of widely different powertrain topologies, i.e. focusing on just engine-battery powertrain, or just solar-battery, or fuel cell-battery. There is no comparison of engine-battery powertrains against solar-battery and fuel-cell battery powertrains. In this thesis, we also approach searching the space of topologies through a brute force search, with the component space search being evolutionary. Appendix A introduced the test platforms available for this study as well as the attainment of the required aerodynamics parameters for mission simulations.

In Chapter 2 and in Chapter 4 we described how the database of electric motors, and batteries have been collected through web scraping and from the existing literature and how they are modelled as well as verified (verification is present in Appendix B). This serves as a step towards choosing the most suitable commercially existing components for the mission. Section 2.1.3 serves as the background for Chapter 3, where we introduced a linear string representation system, that was general enough to account for any given set of powertrain topologies. The proposed scheme is a flexible, future-proof,

yet economical encoding of powertrain topologies, which is used in a systematic, automated exploration of the space of powertrain topologies, with the goal of identifying the layout that optimises mission performance.

Chapter 3 and Chapter 4 described the mathematical formulations and the proposed solution strategies for the case where the topology strings were given. We also discussed refining the component data to reduce the design space. Overall, solving the equations of motion aided in finding the design variables to optimise the performance of a UAV for a given mission scenario through supplying the solver with an objective function value (section 5.3). By using two different sizes of fixed-wing UAVs subjected to the same mission criteria (as seen in Figure 1.6a - 1.6f), we compared the outcome of the optimal powertrain configurations including the component sizes, whether the powertrain topology completed the mission and the energy source split for hybrid powertrain topology. Chapter 5 demonstrated the output of the proposed framework.

6.3 Summary of research contributions

The main focus of the study has been about providing the steps toward a mixed energy optimisation framework for uncrewed aerial vehicles. The novel aspect of the study proposes a powertrain topology encoding scheme, called PoETS, for powertrain design optimisation, which aims to provide a systematic and efficient way of encoding the powertrain topology. The powertrain topology has a significant impact on the performance and efficiency of the platform as well as the mission, and optimising it is crucial for achieving the desired system-level objectives. The PoETS scheme uses a combination of letters and numbers to represent the powertrain topology, based on the types and arrangement of power sources, transmission components, and control strategies. We demonstrate the effectiveness of the scheme by applying it to the design optimisation of selected powertrain topologies, along with PoETS capability for further expansion in optimisation.

The results show that the PoETS scheme can efficiently encode the powertrain topology and enable the use of optimisation algorithms, such as genetic algorithms, to explore

the design space and identify the optimal powertrain configuration. The PoETS scheme could help accelerate the development of the powertrain topology by reducing the time and cost of the design process in a large design space. The scheme also provides a standardised and efficient way of representing the powertrain topology, which could facilitate the use of optimisation techniques for powertrain design, be it single or multi-energy sources.

The present study also proposes a versatile computation tool and method that can simulate the performance of hybrid systems while extracting the maximum available information. For future work, we can extend the framework to incorporate capabilities such as battery charging during the flight, the addition of future components and various flight profiles (given the computational resources available). The optimisation is based on the genetic algorithm optimiser but is open to genetic programming (as proposed in Chapter 3).

The design variables such as the power flow as well as thrust and climb angles required for the mission profile embedded in the cost function allow for the elimination of infeasible topologies, leading to the minimum mass of the propulsion system with the maximum efficiency of the powertrain. The thrust and climb angle obtained here ensures that a minimum amount of energy is consumed for the given segment of flight.

The investigation of the literature includes the current commercial off-the-shelf components for energy systems. Combustion engines, different battery types, fuel cell types, photovoltaic cells and electric motors along with their advantages and disadvantages have been discussed. A database of electric motors and batteries has been collected through web scraping and from the existing literature. This serves as a step towards choosing the most suitable commercially existing components for the mission, ensuring that the components chosen are already available. Current hybrid systems and electric propulsion systems along with methods for modelling and simulation have also been discussed.

In summary, we present techniques for the preliminary mass sizing of powertrains for fixed wing uncrewed aerial vehicles. This is achieved by using a novel way of representing the powertrain topologies using the author's encoding scheme, PoETS (Chapter

3). The scheme allows for the unique representation of powertrains with the capability to generate different topologies from the available component types. This enables populating a given powertrain string with the associated models based on off-the-shelf components. Once the powertrain has been modelled, the performance can be evaluated for a given mission. Since we focus on various topology strings with various energy sources, we developed a tool that can automatically generate component performance models, combine these into the given powertrain topologies and evaluate their feasibility for a given mission, based only on the given PoETS string. The next stage, as recommended in section 6.4.1, is to implement genetic programming, to enable the generation of an ideal topology for a given airframe and mission with minimal prior input.

6.4 Future work recommendations

We present the following ideas as a possible extension of the encoding scheme, acknowledging that this discussion falls beyond the scope of the current work.

6.4.1 Generating new topologies through genetic programming

In this section, we suggest how we can generate new topologies through evolutionary search, such as genetic programming.

6.4.1.1 Encoding powertrain topologies

PoETS can be used to encode the topology of a powertrain system, such as the arrangement of components and their interconnections, into a standardised format that can be used for genetic programming. This can be achieved by defining the genetic operators used in genetic programming, such as mutation and crossover, to ensure that the resulting topologies are valid and meaningful. For example, crossover can be defined to only occur between components that are compatible with each other. Detailed operator examples can be seen in McLay et al. [105] and are adapted from the work

of Brown et al. [24], who generate evolving novel molecular graphs by perturbing the graph-based chromosomes directly using both existing and novel graph-based genetic operators. Let us consider some examples of potential genetic programming operators adapted for use in a PoETS-encoded population of powertrain topologies.

1. **Append or Prune** - A single node is either added or removed at the end of the string. For example:

$$\text{p[em\{es}- > \text{p[em\{es\{PV} \tag{6.1}$$

2. **Insert** - The operator selects a single edge in the graph and cuts it in half (gets two hanging edges, referred to as a hanging edge set). A list of the possible fragment(s) which can accommodate the edge sets is generated from the list of all fragments in the library. One important thing to note is that in order to obtain sensible connections, the operators need to be able to ensure that the operations give out a connected graph. For example:

   Inserting single fragment after '{es':

$$\text{p[em\{es\{PV}- > \text{p[em\{es\{B\{PV}$$

   Inserting a list of fragments after '{es':

$$\text{p[em\{es\{PV}- > \text{p[em\{es\{pc\{B\{PV}$$

3. **Delete** - The operator identifies a single node at random and deletes it, leaving a number of hanging edges. An attempt is then made to reconnect the nodes with hanging edges with the intention of minimising the disruption to the chromosome.

$$\text{p[em\{es\{B\{PV}- > \text{p[em\{es\{PV}$$

   The deletion can be done to generate anything from one edge to the total number of edges in the chromosome. One edge is deleted, while the other is reconnected to it at that deletion point. In situations where the two edges are of different connection, either append or insert can be used for re-connection. For example:

p[em{es{B{PV− > p[{es{B{PV

Since ‘p[’ and ‘{es’ connections are not valid, ’insert component(s)’ is required:

p[gb[em{pc{es{B{PV

4. **Final node mutation** - The operator randomly selects a node to mutate and generates its connector profile. The list of available fragments that satisfy this connector profile (swapping an existing fragment node with a new fragment node, such that the connector profile of the new fragment is compatible with the existing one; the connector profile is simply the right connection type) is then calculated, with one of those fragments selected at random. The selected fragment then replaces the existing fragment, reconnecting the hanging edges as required. For example:

p[em{es{B{PV− > p[em{es|{pc{B+{pc{PV|

In a crossover operation, to ensure the validity of the resulting string, the connector edge type must be compatible. In other words, the crossover operator must ensure that the result is a connected graph [24, 79]. Edges are removed from each parent graph until each graph consists of at least two disconnected subgraphs, with minimal disruption to the overall topology, such that the crossover point for both parents is at the common edge. Let us consider an example, as shown in Figure 6.1.

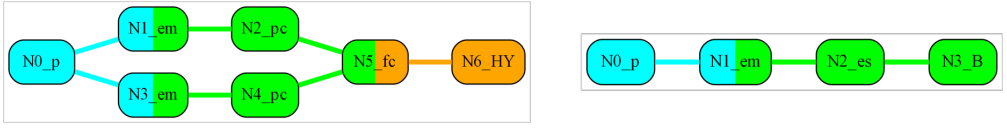

Parent 1 (left): p|[em{pc+[em{pc|{fc(HY
Parent 2 (right): p[em{es{B

FIGURE 6.1: Example of the parent strings.

In the case of one-point crossover, two-parent graphs are selected from the population and are cut/recombined at compatible points just as in conventional crossover operations. In this example, the cut point is at '{', as seen in Figure 6.2. The feasible results of one-point crossover can be seen in Figure 6.3.

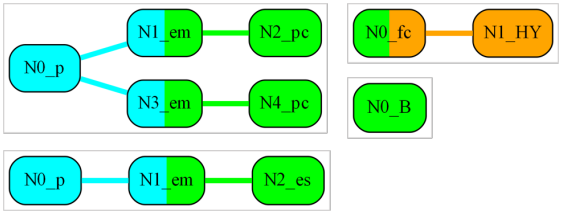

left column: p|[em{pc+[em{pc|, p[em{es
right column: {fc(HY, {B

FIGURE 6.2: Example of the children produced by one point crossover.

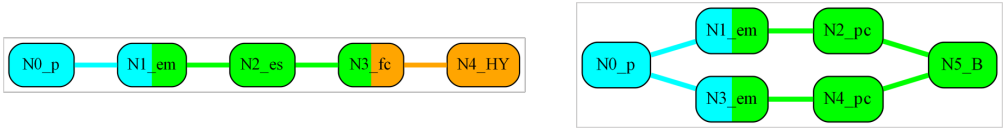

left: p[em{es{fc(HY
right: p|[em{pc+[em{pc|{B

FIGURE 6.3: Example results produced by one point crossover.

In the case of multi-point crossover, the strings inside the branch are broken into individual children as well as the branch is kept intact to preserve the branch integrity (Figure 6.4).

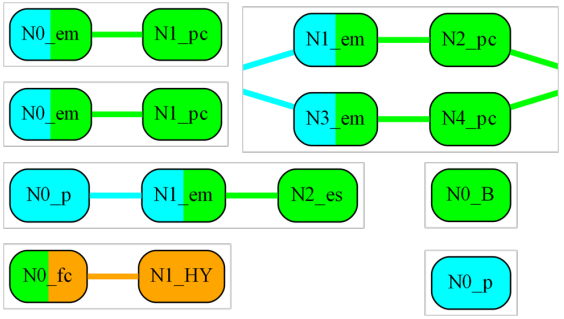

left column: [em{pc, [em{pc, p[em{es, {fc(HY
right column: |[em{pc+[em{pc|, {B, p

FIGURE 6.4: Example of the children produced by multi points crossover.

Some of the feasible results of the multi-points crossover are shown in Figure 6.5.

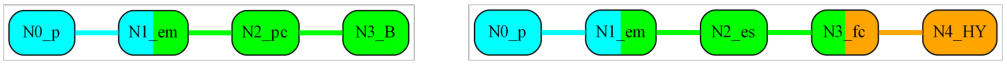

left: p[em{pc{B
right: p[em{es{fc(HY

FIGURE 6.5: Example results produced by multi points crossover using the same parent strings in Figure 6.1.

6.4.1.2 Component selection

PoETS can be used to optimise the selection of powertrain components that are suitable for the specific mission of the UAV. By encoding the components into the PoETS format, genetic programming can optimise the selection of components based on their suitability for the mission, while ensuring that the overall topology of the powertrain system is valid, based on the existing language introduced in Table 4.1 and 4.2, where the input and output connections are matched.

6.4.1.3 Objective function

Genetic programming is a search algorithm that iteratively evolves a population of candidate solutions towards an optimal solution by selecting the most promising individuals and combining them to produce new generations of individuals. PoETS can be used to define an objective function that considers both the performance of the powertrain system (e.g. mass, efficiency, power output) for a given mission requirements of the UAV (e.g. range, endurance), similar to the work presented in this thesis. To update the sizing as well as the new topology generation, we can use Lamarckian Genetic Programming (LGP) [166], such as the techiniques found in Kerstjens and De Winter [83] coupled with the work found in [14, 25, 169]. LGP differs from traditional genetic programming in that individuals are allowed to modify their genome during their lifetime, based on their interactions with the environment. This can be achieved by locally improving the powertrain topology, sizing, and energy management strategy based on the fitness evaluation and mission requirements.

Appendix A

Test platforms

In this appendix, we discuss the test platforms which served as the basis for the case studies we used to demonstrate the techniques put forward in this thesis, along with the various powertrain topologies discussed in Appendix B. Two fixed-wing airframes are chosen to determine the output of the optimisation problem – the FliTePlat and the PEREGRIN UAVs, with maximum take-off masses of 5 kg and 25 kg respectively.

A.1 FliTePlat

We used FliTePlat (Flight Test Platform) (Figure 1.5a) to represent small-scale UAVs. This UAV is based on a commercial-off-the-shelf airframe (MakeFlyEasy's 'Believer' airframe [100]). It is a low-cost, robust, and efficient UAV – see Table A.1 for its key parameters. It is of a foam construction with composite spars and the control surface layout consists of a pair of ailerons and a pair of ruddervators mounted on a V-tail with no undercarriage. It is hand-launched or deployed via a take-off trolley and recovered through belly-landing on grass. Its flight envelope is limited at high (positive and negative) load factors mostly by wing deformation causing loss of lift and by flutter at high speeds. The full instrumentation onboard for the flight testing in order to obtain the aerodynamics parameters is found in Figure A.1.

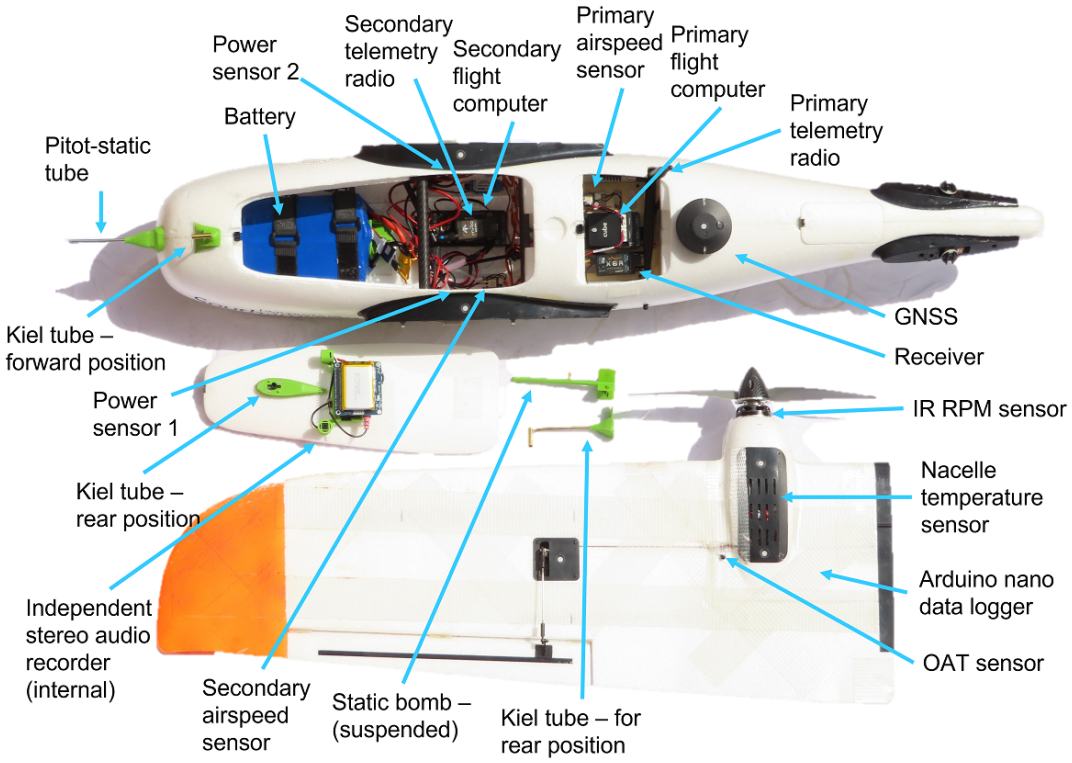

FIGURE A.1: Instrumentation onboard the test platform.

TABLE A.1: FliTePlat key parameters.

Description	Value
Wing span, b	1.96 m
Reference area, S	0.488 m^2
Mean aerodynamic chord, c	0.275 m
Empty mass, m	2.5 kg
Recommended propeller diameter	304.8 mm (12″)
Recommended propeller pitch	152.4 mm (6″)
Recommended propeller number of blades	2
Performance	
Maximum allowable take-off mass, m	5.5 kg
Manufacturer recommended cruise indicated airspeed	20 ms^{-1}
One g stall airspeed, V_S	11 ms^{-1}
Maximum dive airspeed	37 ms^{-1}

A.1.1 Aerodynamic coefficient calculations – experimental set-up

We conducted a wind tunnel test campaign at the *R.J. Mitchell* wind tunnel, to obtain the aerodynamics coefficient required for the mission simulations. The following results are based on: Weishäupl et al. [164]. Figure A.3 shows the data collected on FliTePlat . Each point represents data taken at a sampling rate of 1 kHz, averaged over 20 s. The tunnel has a test section 3.5 m wide and 2.4 m high, with a wind speed range

of 4.0 to 40.0 ms^{-1} and less than 0.2% turbulence [155]. In our experiments forces and moments were measured on a six-component overhead balance, with FliTePlat mounted in the centre of the test section (Figure A.2). The tail support was able to change the pitch electronically during wind tunnel operation, allowing for accurate positioning of FliTePlat.

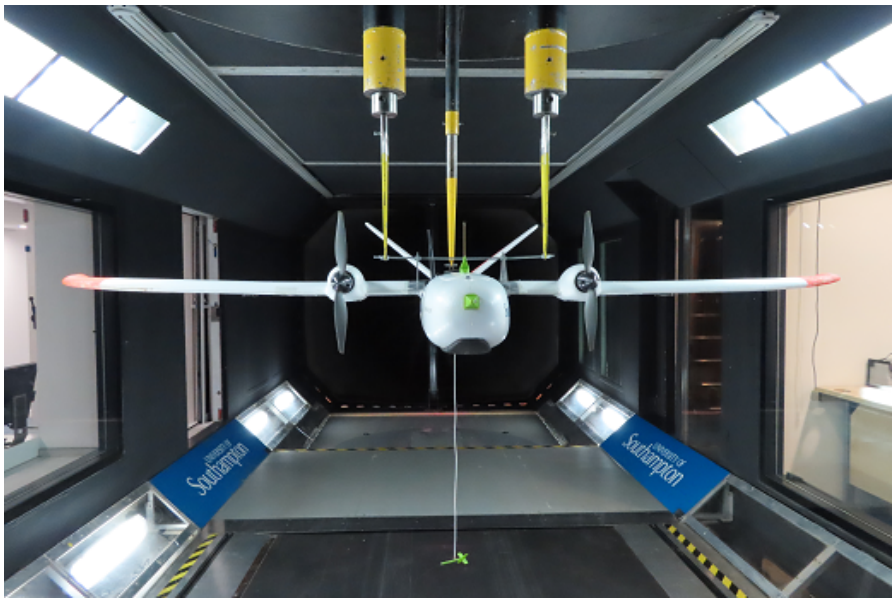

FIGURE A.2: FliTePlat UAV in RJ Mitchell wind tunnel.

The data was recorded from a multitude of sources, including the on-board sensors, load cell sensors, and the wind tunnel's own air data system. Data gathered by the wind tunnel's sensors included the three forces (lift, drag and side force), three moments (pitch, roll and yaw), the yaw and pitch angles, the wind speed and the ambient temperature and pressure. The wind tunnel's airspeed is calculated from a Pitot-static system located at the beginning of the test section and approximately 40 cm from the nearest wall, thus outside of the boundary layer.

The coefficients are extracted through linear regression through both the lift and drag data, with the intercept being the zero angle of attack lift coefficient and zero lift drag coefficient respectively, and the resulting gradients being the lift curve slope and the lift induced drag constant. As the wind tunnel data is collected in ideal test conditions, there is little noise present in the data. The coefficients are presented in Table A.2.

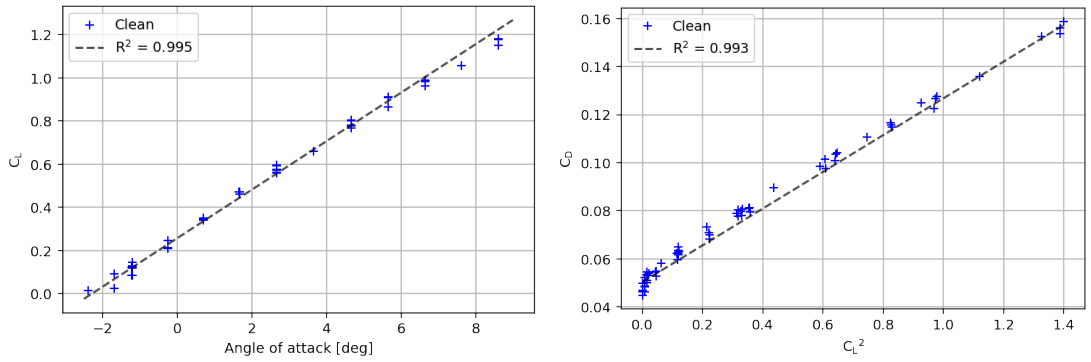

FIGURE A.3: FliTePlat lift and drag coefficients based on experimental data obtained in the wind tunnel.

TABLE A.2: Coefficients generated through the wind tunnel data.

Method	C_{D0}	K	C_{L0}	$C_{L\alpha}$ [1/deg]
Wind tunnel test	0.0503	0.0764	0.2570	0.1122

A.2 PEREGRIN

PEREGRIN (Platform for Environmental Research in Extreme Geographic Regions using Integrated Navigation) (Figure 1.5b and A.4), Table A.3) is a fixed-wing UAV and was developed by a team of master-level undergraduates in 2019. It is an ideal platform to use in modelling and simulation, due to its aerodynamic simplicity, with non-tapered, non-twisted, non-swept, and no dihedral rectangular wing and tail aerodynamic surfaces. The only deviation from this is the Hoerner wing-tips on the main wings. The main wings consist of a NACA-2415 aerofoil with the tail consisting of a symmetrical NACA-0012 aerofoil. Control surfaces have a plain hinge design. The fuselage and boom consist of constant cross-section structures (square and octagonal respectively. This platform serves to represent medium-sized UAV (compare to FliTePlat).

A.2.1 Aerodynamic coefficient calculations – experimental set-up

To estimate the aerodynamic coefficients, a model of the UAV was manually flown at a fixed altitude and varying airspeed in X-Plane 11 with a sampling rate of 10 Hz for 240 seconds with no high lift devices deployed. X-Plane 11 uses a blade element theory based physics solver and a drag build-up model to estimate the aerodynamic forces.

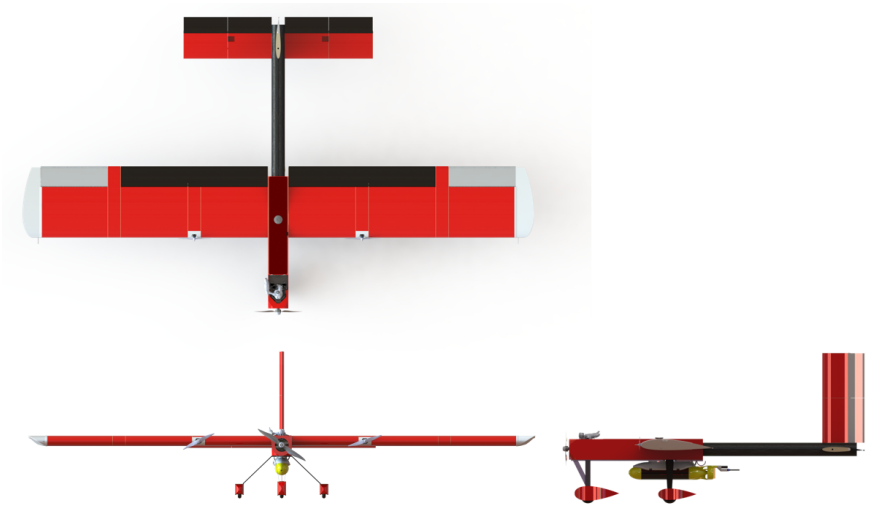

FIGURE A.4: PEREGRIN UAV.

TABLE A.3: The PEREGRIN test UAV: a selection of key parameters.

Wingspan, b	4.05 m
Mean aerodynamic chord, c	555 mm
Reference area, S	2.2 m
Empty mass	15.2 kg
Performance	
Maximum take off mass	25.0 kg
Take off distance	$<$20 m
Cruise speed	25 ms^{-1}
Rate of climb	1.524 ms^{-1}
Clean stall speed	10 ms^{-1}

The coefficients are recorded directly by X-Plane 11 along with the flight data (such as angle of attack, air speeds, etc.). The flight profile and the result can be seen in Figure A.5 and Table A.4.

TABLE A.4: Coefficients generated through the software in the loop data.

Method	C_{D0}	K	C_{L0}	$C_{L\alpha}$ [1/deg]
X-Plane 11	0.0236	0.0599	0.3054	0.0722

While X-plane 11 can provide aerodynamic coefficients, some of the limitations of using X-plane 11 to obtain the aerodynamic coefficients include:

- simplified aerodynamic models: X-plane 11 uses simplified aerodynamic models that do not accurately represent the full complexity of real-world aerodynamics. These models may not account for all the factors that affect aerodynamic performance, such as turbulence, compressibility, and viscous effects.

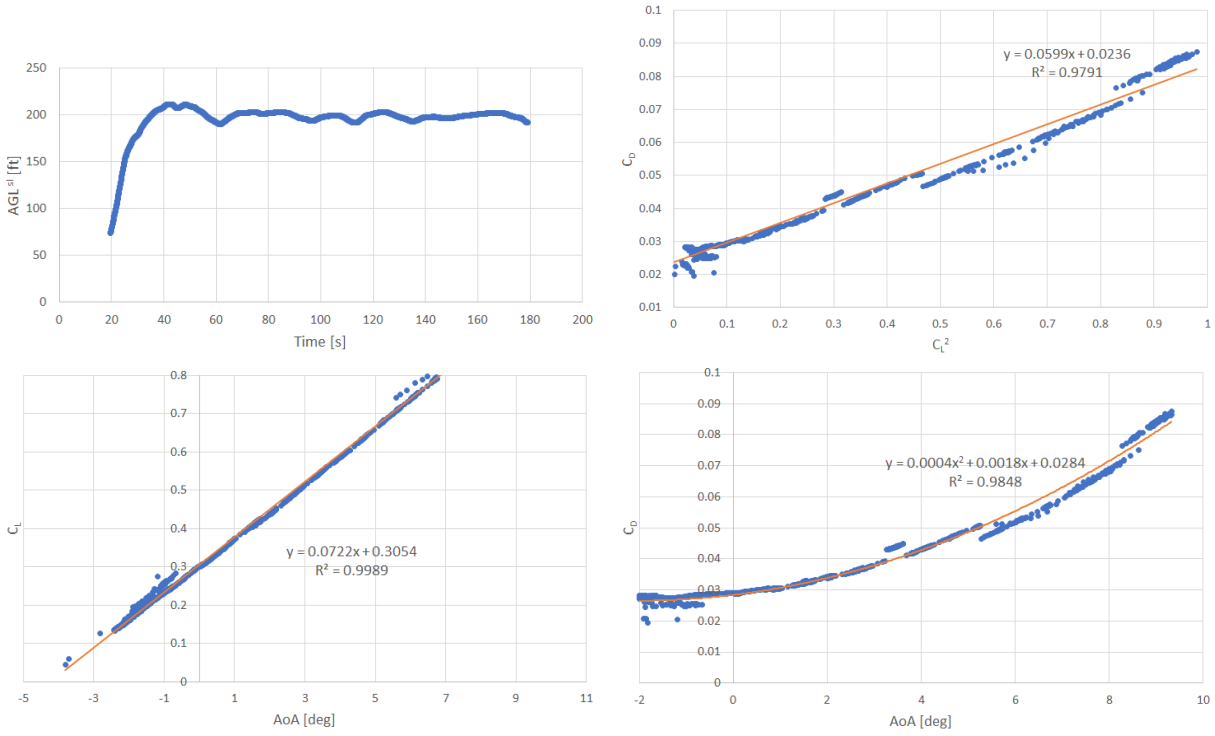

FIGURE A.5: Manual flight in X-Plane 11 to obtain aerodynamics parameters.The take-off has been removed from the data.

- simplified geometry: The aircraft models in X-plane 11 are often simplified versions of real-world aircraft designs. This simplification can affect the accuracy of the aerodynamic coefficients obtained from simulations.
- limited range of operating conditions: X-plane 11 has limitations on the range of operating conditions that can be simulated accurately. For example, it may not accurately simulate extreme flight conditions, such as high-speed flight or high-altitude flight.

Therefore, while X-plane 11 is a useful tool for aviation simulation, its simplified aerodynamic models, simplified geometry, limited range of operating conditions and lack of experimental verification make it less than ideal for obtaining accurate aerodynamic coefficients. If accurate coefficients are required, it may be necessary to use more sophisticated simulation tools or to perform wind tunnel testing or flight testing. However, since PEREGRIN was in the process of further development, we could not obtain flight test data to obtain said aerodynamics coefficients and full-scale wind tunnel testing is not feasible due to its large size. The coefficients estimated through X-plane 11

are sufficiently accurate to act as pseudo coefficients for the modelling and simulations to follow.

A.3 UAV model – basic equation of motion

To calculate the equations of motion introduced in section 2.3.3, a reference system is needed. The reference system is two dimensions and is divided into the following: the body coordinate system, the kinematic (wind) coordinate system and the earth coordinate system. The body coordinate system is relative to the fuselage's cross-section. The body coordinate system is rigidly fixed to the aircraft. The x-axis of the body coordinate system is aligned with the fuselage and the z-axis is set to point upward. The kinematic (wind) coordinate system (Figure A.6) is needed as the body coordinate system alone cannot take into account the variation of the direction of lift and drag with the angle of attack, α. The direction of lift and drag depend on the direction of the wind (this is noted as the kinematic coordinate system). The earth's coordinate system (Figure A.6) is the reference system for the distance travelled as well as the altitude above the ground level achieved by the UAV. The airspeed vector is tangent to the flight path and α is the angle between the airspeed vector and the x-axis of the aircraft. θ is the pitch angle and is the angle between the x-axis of the earth's axis and the x-axis of the aircraft's body axis. γ is the flight path angle and it is between the airspeed vector and the x-axis of the earth's axis. There is an assumption of no wind (calm) atmosphere, thus, the aerodynamic axis coincides with the kinematic axis.

The basic equations of motion, derived from Newton's Second Law, were decoupled into a horizontal and vertical axis. The reference axis for the equation of motion is derived from the kinematic axis (Figure A.6). The performance can be predicted using Equations A.1 - A.4. The equations are

$$F_{\mathrm{x}} = m\,\ddot{x} \tag{A.1}$$

$$\ddot{x} = \frac{dV_{\mathrm{TA}}}{dt} \tag{A.2}$$

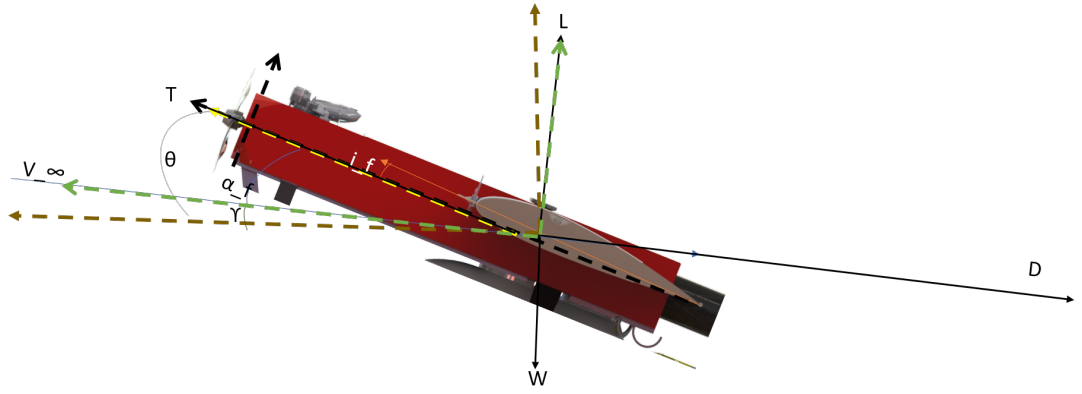

FIGURE A.6: Kinematic axis: i_f (incidence angle) is the offset angle of the wings in relation to the fuselage, α_f is the angle of attack with respect to the fuselage axis and free stream velocity, V_∞ is the free stream velocity, γ is the climb angle (the angle between V_∞ and the horizontal earth's axis), θ is the pitch angle (the angle between the horizontal fuselage axis and horizontal earth's axis).

$$F_z = m\,\ddot{z} \tag{A.3}$$

$$\ddot{z} = V_{\mathrm{TA}}\,\frac{d\gamma}{dt} \tag{A.4}$$

where F_i is the force in the i direction, $\ddot{i}$ is the acceleration in the i direction, m is the mass, V_{TA} is the true airspeed, t is time and γ is the flight path angle.

During flight, the forces acting on the aircraft are shown in Figure A.6. From the force diagram (Figure A.6) and from the equations of motion (Equation (A.1 - A.4)), the decoupled equations of motion are shown in Equation A.5 and Equation A.6, where $\rho(h)$ is the air density as a function of geopotential altitude, C_D is the drag coefficient and C_L is the lift coefficient. The rolling resistance needs to be taken into account during the ground run. The equations of the resultant forces in the kinematic coordinate system are

$$R_\mathrm{x} = T\cos(\theta) - 0.5\,\rho(h)\,V_{\mathrm{TA}}^2 S_\mathrm{w} C_\mathrm{D} - \mu_\mathrm{F}\,R_\mu - W\sin(\gamma) \tag{A.5}$$

$$R_\mathrm{z} = T\sin(\theta) + 0.5\,\rho(h)\,V_{\mathrm{TA}}^2 S_\mathrm{w} C_\mathrm{L} - W\cos(\gamma) \tag{A.6}$$

where R_x and R_z are the resultant forces (N), T is the thrust (N), $\rho(h)$ is the density at geopotential altitude ($\frac{\mathrm{kg}}{\mathrm{m}^3}$), V_{TA} is the true air speed ($\frac{\mathrm{m}}{\mathrm{s}}$), S_w is the wing area (m^2), C_D is the drag coefficient, μ_F is the rolling resistance coefficient during take-off, R_μ is the

reaction force, W is weight of aircraft (N), θ is pitch angle (radian) and γ is climb angle (radian).

The initial value problem for a UAV introduced in section 2.3.3 typically includes the equations of motion described above, which describe the UAV's position, velocity and acceleration as a function of time, as well as the other inputs. In this study, these inputs include the powertrain sizing and the power flow for the chosen topology. These should be set in order to achieve a desired trajectory.

By applying the force-balance equations to the initial value problem, the mission solver can determine the optimal trajectory and inputs that minimise powertrain mass and the energy required for steady flight. The solver may also need to consider other constraints, such as the UAV's maximum altitude, speed or payload capacity.

Once the optimal trajectory and inputs have been computed, the solver can then simulate the UAV's behaviour over time to ensure that the solution is physically feasible and meets the mission objectives. The solver may need to refine the solution through an iterative process of adjusting the initial conditions and inputs until a satisfactory solution is obtained.

A.3.1 Smoothing functions for change in flight segments

'*solve_ivp*' from '*scipy.integrate*' is the *Python* package utilised here to solve the initial value problem to approximate the solution of the ordinary differential equation over a given time interval. However, '*solve_ivp*' struggles with the sharp changes in the solution due to the numerical methods used here as it relies on the continuity of the solution and its derivatives. This is especially problematic during segment changes, i.e. 'climb' to 'cruise'- where the climb angle changes from positive to zero. For this continuity, we created a smooth blend between two levels of the signal (the initial point and the final point). As an example, if the initial climb angle is zero degrees, and final the climb angle ten degrees (as seen in Figure A.7a), the function returns the climb angle during the segment (until it reaches ten degrees) as a function of time elapsed

since the commencement of the rotation manoeuvre by assuming a sigmoid-shaped control input.

Therefore, our approach to deal with the sharp changes in the solution is to use smoothing parameters between the change in states such as angle control and thrust control as seen as Figure A.7a - A.7c.

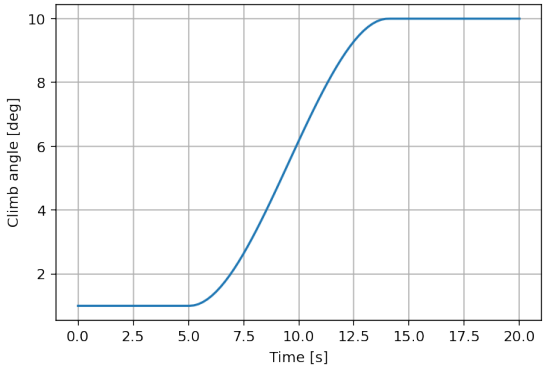

(A) Rotation rate control for climb angles.

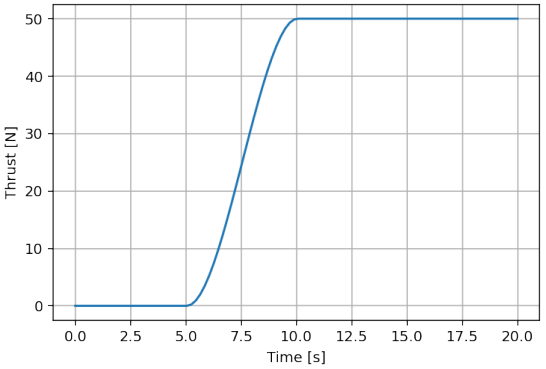

(B) Thrust rate control for FliTePlat.

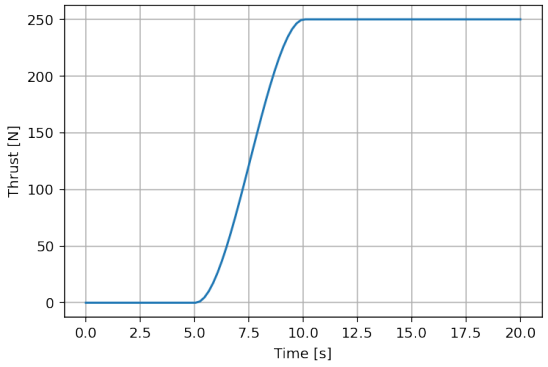

(C) Thrust rate control for Peregrin.

FIGURE A.7: Examples of control inputs for flight segment changes.

A.4 Case study missions

We used these two fixed-wing uncrewed vehicles to simulate the following six types of missions, with the level of complexity increasing with each mission. All of the cruise segments have a climb angle set to 0. Using the optimisation strategy (Figure 1.3) as a baseline, the following missions are used to compare the optimised powertrain topologies whilst only considering the components shown in Figure 1.4.

Appendix B

Modelling the components of a UAV powertrain

In this appendix, the components described in Chapter 2 and Figure 1.4 are discussed and models are created for each type of component. The models aid in the parameterisation of components for the optimisation introduced in section 2.1.3 and proposed in Chapter 3.

B.1 Propeller model

Fixed-pitch propellers have a fixed blade angle. Therefore, the operating parameter for the best efficiency, η_p, depends on the advance ratio, J, ($J = \frac{V_\infty}{n\,D}$) and hence, the propellers need to be sized for specific operating conditions, such as true airspeed, V_∞, the rotation speed, n and diameter of the propeller, D.

Diameter holds another importance when comparing the performance of fixed-pitch propellers. The thrust generated increases with the diameter of the propeller, but is less dependent on the pitch. Therefore, the power supplied to the propeller-based system depends on the diameter of the propeller. Although there is an increase in thrust as the pitch increases for a given diameter of the propeller, the increase in thrust is more so

with the increase in diameter. This can be seen in Figure B.1 which shows the experimental data obtained from the APC database [11] of a variety of different propellers. The reason is that as the diameter increases, the column of air approximately equal to the diameter of the air increases, hence the thrust. Although increasing the pitch primarily affects the amount of air moved by each blade element per revolution and does contribute to thrust by allowing the propeller to 'bite' into a larger mass of air, its effect is limited compared to the overall increase in diameter (as the diameter increases, the overall area increases with diameter squared), which influences a larger area and has a more significant impact on thrust production.

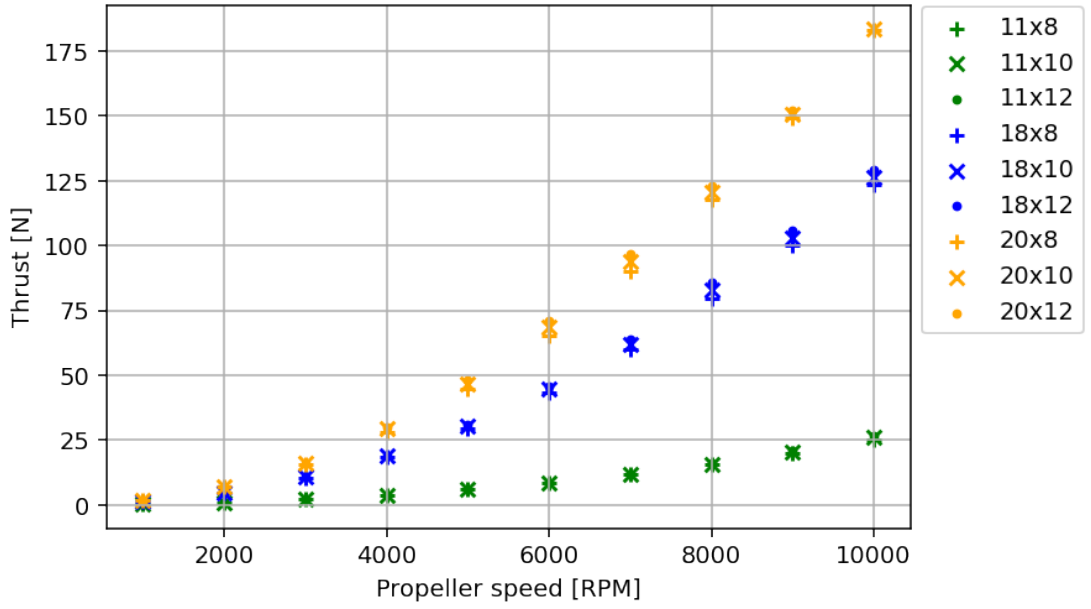

FIGURE B.1: Comparison of different propellers: Speed [RPM] against Thrust [N] at 0 ms^{-1}, the data is collected from APC Propellers [11].

η_p, along with torque, power, and rotation per minute (as the rotation per minute is fixed at an interval of 1000 for each data point), are given in the performance data available in manufacturers' data sets and generic databases such as the APC [11] and UIUC [22] databases. Although there are other propellers available, due to the experimental data availability, two-bladed fixed-pitch propellers are investigated. Two-bladed propeller data was obtained from the APC [11] propeller company as the company releases data ranging from three inches to 18 inches in diameter.

B.2 Internal combustion (piston) engine model

To simulate the engine performance used in the multi-energy component class, engine maps are required. An engine map is the map of the engine performance which shows the fuel consumption, speed and torque of the engines range, measured at the engine's primary output shaft [57]. The modelling we proposed is based on the OS GF-40, a four-stroke internal combustion engine and the EL-005, a two-stroke internal combustion engine. The geometry of the engines can be found in Table B.1. We acquired experimental data for the OS GF-40 as part of an undergraduate project [106], where the engine was tested on a dynamometer under sea-level conditions to map the fuel consumption and power output. Experimental data for the EL-005 is obtained from Hung and Gonzalez [73].

TABLE B.1: Internal combustion engine's key parameter.

Parameter	Variable	Value (OS GF-40)	Value (Lycoming EL-005)
Size of engine, cc	V_d	40	75
Bore, mm	b_r	40.0	49.0
Stroke, mm	s_t	31.8	40
IC Engine body mass, kg	m_{body}	1.38	6.25
Speed range, rpm	Ω	1800 9000	2200 5500
Output power, W	P	2050 at 8600 rpm	2980 at 5000 rpm

Before we dive into the details of the engine modelling, let us discuss the key parameters. Torque and power are the two most common figures of merit when it comes to individual engine performance as these parameters are crucial in ensuring that the engine can provide the demanded load. However, for an equivalent comparison between engines of varying sizes, the mean effective pressure and the specific fuel consumption of the engines are more suitable. The mean effective pressure, MEP [Pa], is defined as

$$\text{MEP} = \frac{W_c}{V_d} \tag{B.1}$$

where W_c is work per cycle per cylinder volume, V_d [m^3], and is directly related to the torque, Q [Nm], measured by dynamometer as

$$W_c = Q\, n_R\, 2\, \pi \tag{B.2}$$

where n_R is the number of crank revolutions for each power stroke.

Power, P [W], is calculated from torque and engine speed, N [RPM] by means of

$$P = 2\,\pi\,N\,Q \tag{B.3}$$

The specific fuel consumption, bsfc [g Wh^{-1}], shows how effective the engine is at converting the chemical energy stored in the fuel to useful work by

$$\text{bsfc} = \frac{\dot{m}_f}{P} \tag{B.4}$$

where $\dot{m}_f$ [kg s^{-1}] is the engine fuel flow rate. A dimensionless parameter that links the engine power output with the required fuel, η_f, assuming that the fuel energy supplied to the engine is entirely converted to thermal energy is defined as

$$\eta_f = \frac{1}{\text{bsfc}\;Q_{HV}} \tag{B.5}$$

where Q_{HV} is the lower heating value of the fuel.

Another important point to note is that when the UAV operates at a high altitude during the cruise phase of the flight, the density of the atmosphere is lower. In what follows we will assume the ISA model for ambient density decay with altitude. The decrease in air density decreases the flow of air mass into the engine and hence decreases the power, P and the torque output of the engine. The Gagg-Ferrar equation [52] used in Kimberlin [85] defines a power correction factor:

$$P_{alt} = \sigma - \frac{1-\sigma}{7.55}\,P_{sl} \tag{B.6}$$

where

$$\sigma = \frac{\rho}{\rho_{sl}} \tag{B.7}$$

P_{alt} is the brake power output at an altitude and P_{sl} is the brake power output at sea level. This power correction factor can be used to estimate the power output at various heights of an internal combustion engine. Based on these equations and the empirical models based on OS GF-40 and the EL-005, the baseline maps for the internal combustion engines are created and scaled accordingly.

B.2.1 Scaling the engine maps

As explained by Rizzoni et al. [127], Sorrentino et al. [140], Zuurendonk [177], the Willans line model describes an approximately linear relationship between the effective mean brake pressure (the engine's ability to fulfil mechanical work) and the fuel consumption of an internal combustion engine. When a chosen engine has either a different maximum power rating or different peak efficiency from the default values, its efficiency maps will be proportionally scaled with the efficiency ratio. The speed and torque indices of the efficiencies are also scaled based on the required maximum power of the engine. The calculations are based on the input-output power and the efficiency, η, of the engine. The intercept to the y-axis, P_{loss}, represents the global engine losses parameter.

$$P_{out} = \eta P_{in} - P_{loss} \tag{B.8}$$

η has been assumed as the product of thermodynamic and combustion efficiencies [140], and can be written as a function of speed and torque as:

$$Q_e = \eta \, \dot{m} \, Q_{LHV} \, \omega - P_{m,loss} \, \omega = \eta Q_a - Q_{loss} \tag{B.9}$$

where Q_a [Nm] is the available torque and Q_{loss} [Nm] represents the inner losses of the engine.

Another assumption is that the engines that need scaling belong to the same family (for example, the OS GF-40 can only represent four-stroke spark ignition engines). This

means that the coefficients of $P_{\mathrm{m,loss}}$ and $\eta(C_{\mathrm{m}})$ are typically the same for engines of the same family. Instead of the engine speed and power, normalised variables; mean piston speed and mean effective pressure, are used. The engine size parameters are introduced for making the Equation B.9 directly dependent on these size parameters, allowing for easier comparison and scaling of the engine performance. V $[\mathrm{m}^3]$, is the displacement of the engine, and s_{t} $[\mathrm{m}]$ is the stroke of the piston.

$$P_{\mathrm{me}} = \frac{4\pi Q_{\mathrm{e}}}{V} \tag{B.10}$$

$$C_{\mathrm{m}} = \frac{s_{\mathrm{t}}\omega}{\pi} \tag{B.11}$$

$$P_{\mathrm{ma}} = \frac{4\,\pi\,Q_{\mathrm{LHV}}\,\dot{m}}{V\omega} \tag{B.12}$$

where P_{me} [Pa], P_{ma} [Pa] and C_{m} $[\mathrm{ms}^{-1}]$ are the mean effective pressure (the engine's ability to produce mechanical work), the available mean effective pressure (the maximum mean effective pressure that could be produced if $\eta = 1$) and the mean piston speed (a measure of the operating speed of the engine) respectively.

Therefore, rewriting the equation of Q_{e} (Equation B.9) as:

$$P_{\mathrm{me}} = \eta P_{\mathrm{ma}} - P_{\mathrm{m,loss}} \tag{B.13}$$

where $P_{\mathrm{m,loss}}$ is:

$$P_{\mathrm{m,loss}} = \frac{4\pi Q_{\mathrm{loss}}}{V} \tag{B.14}$$

The following equation introduced the non-linearity necessary to capture the high load effects of the engines [127]:

$$P_{\mathrm{me}} = [\eta_0(C_{\mathrm{m}}) - \eta_1(C_{\mathrm{m}})P_{\mathrm{ma}}]P_{\mathrm{ma}} - P_{\mathrm{m,loss}}(C_{\mathrm{m}}) \tag{B.15}$$

where

$$\eta_0 = \eta_{00} + \eta_{01} C_{\mathrm{m}} + \eta_{02} C_{\mathrm{m}}^2 \tag{B.16}$$

$$\eta_1 = \eta_{10} + \eta_{11} C_{\mathrm{m}} \tag{B.17}$$

$$P_{\mathrm{m,loss}} = P_{\mathrm{m,loss0}} + P_{\mathrm{m,loss2}} C_{\mathrm{m}}^2 \tag{B.18}$$

And the least-squares fit on real data to acquire the introduced parameters is:

$$\begin{aligned} \epsilon \;=\; & \{\eta_{00},\ \eta_{01},\ \eta_{02},\ \eta_{10},\ \eta_{11},\ p_{\mathrm{m,loss0}},\ p_{\mathrm{m,loss2}}\} \\ & \min{}_{\epsilon} \sum_{i=1}^{n} ((\eta_0(C_{\mathrm{m,i}}) - \eta_1(C_{\mathrm{m,i}}) P_{\mathrm{ma,i}}) P_{\mathrm{ma,i}} - P_{\mathrm{m,loss}}(C_{\mathrm{m,i}}) - P_{\mathrm{me,i}}))^2 \end{aligned} \tag{B.19}$$

For scaling, the mean piston speed and available mean pressure are scaled with:

$$C_{\mathrm{m,scaled}} = C_{\mathrm{m,model}} \frac{s_{\mathrm{t,scaled}}}{s_{\mathrm{t,model}}} \tag{B.20}$$

$$P_{\mathrm{ma,scaled}} = P_{\mathrm{ma,model}} \frac{V_{\mathrm{model}}}{V_{\mathrm{scaled}}} \tag{B.21}$$

The mean effective pressure is scaled with the parameters that are obtained from the least square fit and is:

$$P_{\mathrm{me,scaled}} = [\eta_0(C_{\mathrm{m,scaled}}) - \eta_1(C_{\mathrm{m,scaled}}) P_{\mathrm{ma,scaled}}] P_{\mathrm{ma,scaled}} - P_{\mathrm{m,loss}}(C_{\mathrm{m,scaled}}) \tag{B.22}$$

The torque and speed of the scaled engine is:

$$Q_{\text{scaled}} = P_{\text{me,scaled}} \frac{V_{\text{scaled}}}{4\pi} \tag{B.23}$$

$$\omega_{\text{scaled}} = C_{\text{m,scaled}} \frac{\pi}{s_{\text{t,scaled}}} \tag{B.24}$$

The scaled fuel burn map is:

$$\dot{m} = P_{\text{ma,scaled}}\, \omega_{\text{scaled}} \frac{V_{\text{scaled}}}{4\pi Q_{\text{LHV}}} \tag{B.25}$$

B.3 Electric motor model

Similar to internal combustion engines, electric motors are rated in power rather than thrust. Therefore, to convert this power to thrust, assuming a propeller efficiency (as a function of airspeed), Equation B.26 can be used.

$$P = \frac{T\, V_{\text{TA}}}{\eta_{\text{p}} V_{\text{TA}}} \tag{B.26}$$

where P is power [W], T is thrust [N], V_{TA} is the velocity of the aircraft [m s^{-1}] and η_{p} is the efficiency of the propeller as a function of true airspeed.

The motor speed constant, K_{V} is directly related to the motor size in Figure B.2a. The reason for this is that the torque constant, which is the inverse of the speed constant, depends on the motor flux linkage and magnetic circuit. Therefore, the larger the motor, the larger the flux linkage and torque constant [61]. Figure B.2b shows the power output against the mass of motors with a variety of K_{V} ratings. The output of this regression can be used when the power ratings are unknown.

Unlike internal combustion engines, where the power output is a function of altitude, as long as the voltage and current supplied to the electric motor are constant, the motors can produce the rated power.

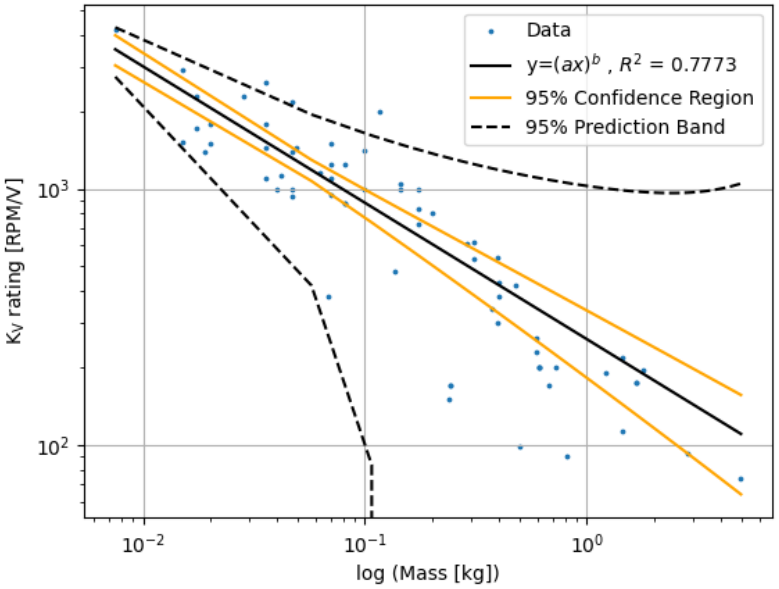

(A) Log-Log graph of K_V rating against mass for commercial off-the-shelf brushless direct current motors.

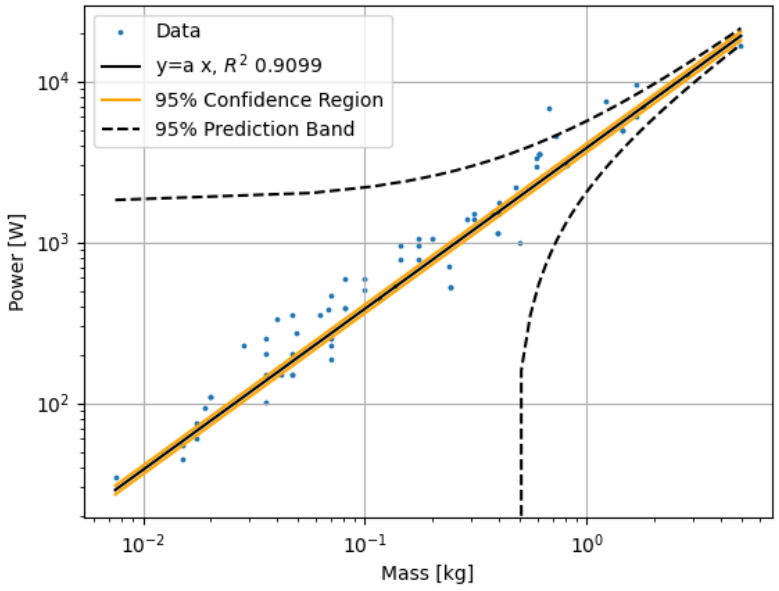

(B) Power [W] against mass [kg] for commercial off-the-shelf brushless direct current motors.

FIGURE B.2: Relational analysis of the commercial off-the-shelf brushless direct current motors.

For simplicity, a first-order simplified model along with the following assumptions is applied when modelling electric motors. Although in reality, the resistances vary with the temperature [120], the internal resistance, R, of the motor is assumed to be constant.

The shaft torque, Q_{m} is assumed to be proportional to the current, I, through the torque constant K_{Q}, minus the idle current, I_0. Therefore, friction-based losses can be taken into account in the torque, Q_{m} (Equation B.47). For internal back-EMF, V_{emf} is assumed proportional to the rotation rate, Ω, via K_{V}. Therefore, the terminal voltages, which include the voltage drop due to internal resistance, can be calculated via Equation B.29.

For simplicity, the torque of the motor shaft can be assumed as the torque of the propeller; as described in Equation B.47. The current, I, that the motor needs to draw from the power source can be calculated as follows.

$$I = (Q\, K_{\mathrm{Q}}) + I_0 \tag{B.27}$$

where Q is the torque [Nm], I is the current drawn by the motor [A], I_0 is no load current [A], and K_{Q} is the torque constant [NmA^{-1}]. K_{Q} and K_{V} are also related by the following equation:

$$K_{\mathrm{Q}} = \frac{60}{K_{\mathrm{V}}\, 2\, \pi} \tag{B.28}$$

From B.27, the voltage required by the motor to produce the necessary thrust can be calculated as:

$$U = \frac{\Omega}{K_{\mathrm{V}}} + IR \tag{B.29}$$

where U is the motor terminal voltage [V], Ω is the motor speed [RPM], K_{V} is the motor speed constant [$\mathrm{RPM\ V}^{-1}$], I is the current drawn by the motor [A] and R is the internal resistance of the motor [ohms].

For comparing different motors, a maximum efficiency comparison can be used (Equation B.30) [120].

$$\eta_{\mathrm{max}} = \left(1 - \sqrt{\frac{I_0 \times R}{U}}\right)^2 \tag{B.30}$$

As the motor dimension decreases in diameter (and length), the internal resistance increases, as decreasing the motor casing requires a decrease in the thickness of the wire gauges, which causes the higher resistance. For a constant supply voltage, according to ohms law ($V = IR$), if the resistance is higher, the current draw would be lower, which explains Figure B.4, where no load current decreases with decreasing length and diameter. No load current and internal resistance are values required for calculating the efficiency of the electric motor, throttle calculation, voltage calculation, and current calculation.

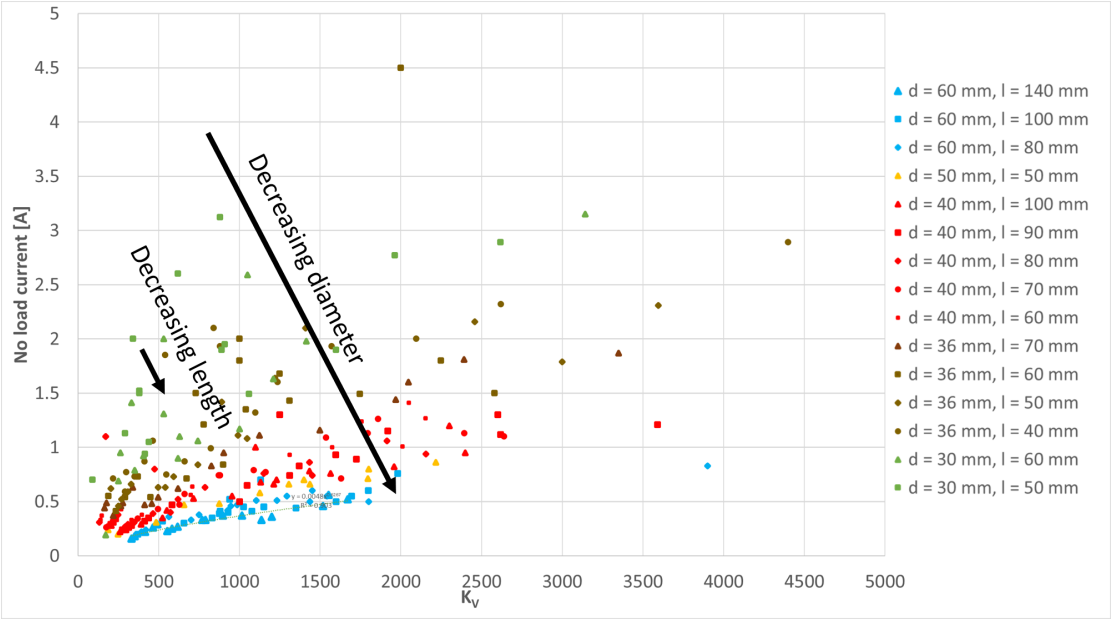

FIGURE B.3: Relations between no-load current and K_V rating with length and diameter of the electric motors.

The general relationship between the maximum current or resistance or no-load current and the geometry of the motor as well as K_V rating defined by Schomann [133] is

$$y = a\ \mathrm{dl}^b\ K_V^c + d\ \mathrm{dl}^e + f\ K_V^g + h\ \mathrm{dl} + i\ K_V + j\ \mathrm{dl}\ K_V + k$$

where $a, b, c, d, e, f, g, h, i, j, k$ are constants, dl is geometry of the motor (the product of the diameter and height) and K_V is the rating of the motor [RPM V^{-1}].

In the case that I_0 [A], or R [ohm] or I_{max} [A] are not given by the manufacturer, the author's work is based on the regression models developed by Schomann [133]. This is useful as in some of the hobby electric motors, the maximum current data, internal

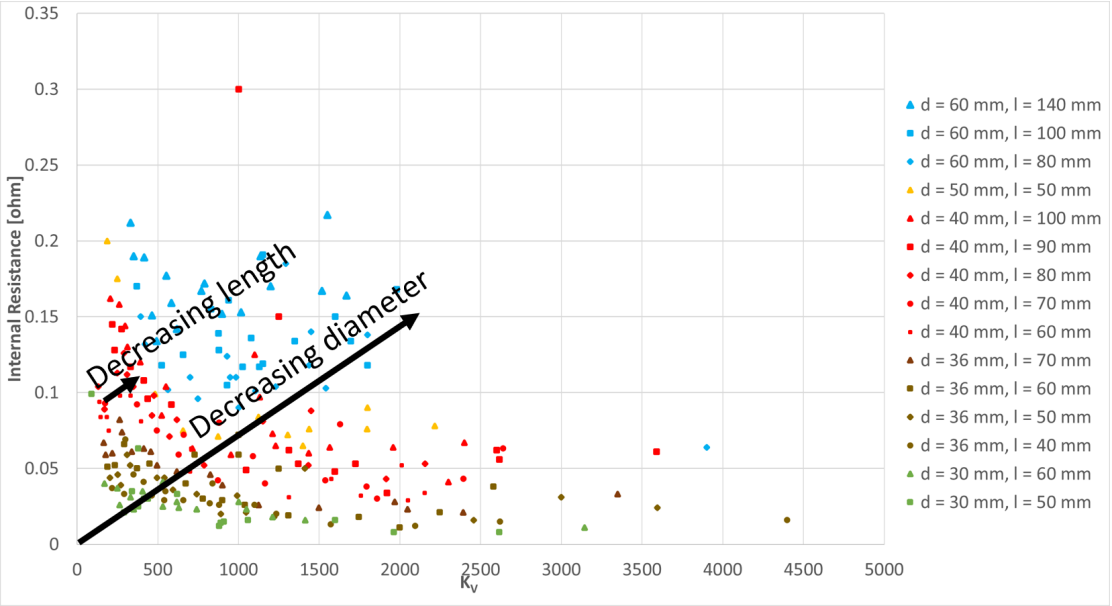

FIGURE B.4: Relations between internal resistance and K_V rating with length and diameter of the electric motors.

TABLE B.2: Constants values based on Schomann [133].

Schomann [133]	R [ohm]	I_0 [A]	I_{max} [A]
a	0.124	0.0420	$3.635\ 10^{-1}$
b	-0.436	-0.584	$-1.372\ 10^{-1}$
c	-0.0904	0.603	$1.931\ 10^{-1}$
d	0.271	-0.332	4.421
e	0.0541	0.599	$1.405\ 10^{1}$
f	-0.0912	0.0615	$6.380\ 10^{-4}$
g	0.0530	-0.437	-1.488
h	$0.136\ 10^{-6}$	0.140	$3.196\ 10^{-1}$
i	$-0.359\ 10^{-8}$	-0.356	$-7.237\ 10^{-1}$
j	$-0.651\ 10^{-8}$	11.33	8.812
k	0.158	-0.151	$-3.091\ 10^{-1}$
R^2	0.427	0.490	0.623
RMSE	0.059	26.95	23.18

resistance or the no-load current are not provided. However, it is important to know these parameters as an over-current causes the wires in the coil to heat up, which damages the coils and, therefore, should not be exceeded. This upper current limit is taken into account in the author's model.

The final parameter that is not required for the modelling but for refining the component list to a smaller subset is the peak power output from the electric motor, which sometimes is not provided by the manufacturer. To develop a regression model, the author first identified the features which are correlated to the power from the definite

data given by the manufacturers (such as the geometry, mass and K_V rating). First, the correlations are extracted as seen in Figure 2.23 to observe the relations between each dependent variable and the independent variable (peak power output).

From Figure 2.23, the relationship between the *K*V rating and the peak power output, mass and the peak power output, and the geometry (the product of diameter and height) and the peak power output are identified as

$$K_V = a\ P^b$$

$$m = c\ P + d$$

$$\mathrm{dl} = e\ P + f$$

where $a, b, c, d, e \text{and} f$ are constants to be determined.

To determine the coefficients, we minimise the sum of the squared error:

$$\text{minimise} \sum (\text{Data} - \text{Prediction})^2$$

where the prediction is

$$\text{Prediction} = K_V + m + \mathrm{dl}$$

The coefficients are as follows with an R^2 value of 0.88 and an RMSE of 636.8:

a	b	c	d	e	f
0.13308446	-0.01572676	0.78586029	-0.13651443	0.10698833	-0.00151319

B.4 Battery model

The state of charge (SOC) is the ratio of the amount of charge present in the battery relative to the total charge capacity and can be defined as [114, 41, 135]:

$$\mathrm{SOC}(t) = \frac{\int_{t_0}^{t_1} I(t)\mathrm{dt}}{Q_{\mathrm{batt}}} \tag{B.31}$$

where $\mathrm{Q_{batt}}$ is the charge capacity and $\int_{t_0}^{t_1} I(t)\mathrm{dt}$ is the amount of charge stored in the battery. For a very small time step, Equation B.32 is a valid replacement for Equation B.31 as it assumes the current is linear versus time.

$$\mathrm{SOC}(t) = \mathrm{SOC}(t-1) - I\,\eta\,\frac{t-(t-1)}{Q_{\mathrm{batt}}} \tag{B.32}$$

However, this equation assumes that the capacity is a known parameter (given as nominal capacity) and does not get affected by battery ageing.

To model the depletion of the charges in the battery, as well as to simulate the current and voltage draw and their effect on the state of charge, the following models are implemented. Zhang et al. [172] proposed an electrical model using open circuit voltage-based SOC estimation methods based on experimental results on lithium batteries. According to Zhang et al. [172], polynomial fitting is the most popular approach, with the highest number of polynomial fittings being seven which yielded a better fit. The relationship between the open circuit voltage and the SOC according to the experiment by Zhang et al. [172] is:

$$U_{\mathrm{OC}} = a_1\,\mathrm{SOC}(t)^n + a_2\,\mathrm{SOC}(t)^{n-1} + \cdots + a_{\mathrm{n}}\,\mathrm{SOC}(t) + a_{n+1} \tag{B.33}$$

where VOC is the open circuit voltage [V], SOC(t) is the current state of charge, and the coefficient values are:

a_1	a_2	a_3	a_4	a_5	a_6	a_7	a_8
-33.19	133.84	-212.24	165.57	-63.67	10.28	0.20	3.44

From the open circuit voltage calculation, the terminal voltage can be calculated using the model from Saldaña et al. [130]:

$$U_{\mathrm{T}} = U_{\mathrm{OC}} - R\ I \tag{B.34}$$

where U_{T} is terminal voltage [V], R is the internal resistance [Ω] and I is the current required from the battery [A]. This model imitates the instantaneous voltage drop when the load is applied and is directly proportional to the current draw.

To calculate the internal resistance, R, the model derived from the experimental model of Lithium based batteries by Chen and Rincón-Mora [29] is applied.

$$R = 0.1562\ e^{-24.37\ \mathrm{SOC}(t)} + 0.07446 \tag{B.35}$$

B.5 Solar cell model

The operation of photovoltaic cells is affected by altitude. The lower temperature at higher altitudes increases the power output of photovoltaic cells and the factor of increase depends on the temperature coefficient of the material. Between 15 to 24 km altitude, photovoltaics cells can obtain unobstructed solar irradiation, whilst being protected from ultraviolet radiation by the ozone layer [156].

According to Lee et al. [93], for modelling of a photovoltaic module, the equivalent electrical circuit can be divided into three models: the one-diode model, the two-diode model, and the empirical model. Since the parameters required for the empirical model are available from the manufacturer's data sheets, Lee et al. [93] employed the empirical method. More information regarding the three different models mentioned above can be found in Alrahim Shannan et al. [8], Dey et al. [34], Abounada et al. [1], Jervase et al. [80].

The methodology used to predict photovoltaics power output is found in Figure B.5.

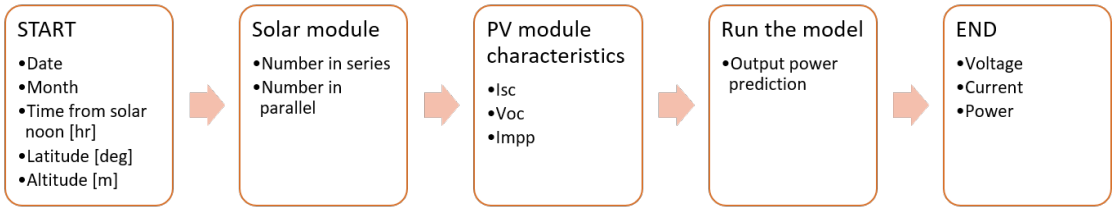

FIGURE B.5: Approach used to predict photovoltaic power output.

The equivalent circuit method which described the *I-V* characteristics and represents the non-linearity behaviour of the photovoltaics module is used here [16, 26, 33, 78, 88, 93, 98, 101, 124, 173]. The model takes in

- Open circuit voltage (U_{OC}), which is the maximum voltage that the cell can provide when there is no load connected.
- Short circuit current (I_{sc}), which is the maximum current provided by the cell when the output connectors are in a short circuit condition.
- Maximum power point (MPP), which is the maximum power that the cell can produce.
- Fill factor (FF), which is the ratio between the maximum power that the cell can provide under normal operating conditions and the product of the open-circuit voltage multiplied by the short-circuit current, typically between 0.7 to 0.8.
- The efficiency, which is the ratio between the maximum electrical power that the cell can produce to the amount of solar irradiance reaching the cell, typically around 10 to 20%.

I-V relations can be calculated as:

$$I_{pv} = I_{sc}\left(1 - K_1(e^{\frac{A}{U_{oc}^{B}}(U_{oc}\ B)-1})\right)$$

where

$$A = \log\left(\frac{1+K_1}{K_1}\right)$$

$$B = \frac{\log(\frac{C}{D})}{\log(\frac{U_{\text{mpp}}}{U_{\text{oc}}})}$$

$$C = \frac{\log(I_{\text{sc}}\ (1+K_1))}{K_1\ I_{\text{sc}}}$$

$$D = \log\left(\frac{1+K_1}{K_1}\right)$$

And since the *I-V* curve is dependent on the solar irradiance and the array temperature, the new I-V characteristics can be calculated as [88]:

$$\Delta T = T_{\text{c}} - T_{\text{ref}}$$

$$\Delta I_{\text{pv}} = \alpha_{\text{sc}}\ \left(\frac{G}{G_{\text{ref}}}\right)\ \Delta T + \left(\frac{G}{G_{\text{ref}}} - 1\right)\ I_{\text{sc}}$$

$$\Delta U_{\text{pv}} = -\beta_{\text{oc}}\ \Delta T - R_{\text{s}}\ \Delta I_{\text{pv}}$$

$$I_{\text{pv,new}} = I_{\text{pv}} + \Delta I_{\text{pv}}$$

$$U_{\text{pv,new}} = U_{\text{pv}} + \Delta U_{\text{pv}}$$

The monthly solar irradiance which is based on the time period of 1961-1990 collected by Burnett et al. [26] is used in the model for approximating the solar irradiance, G, for both low altitudes (less than 2,500 m) [26] and high altitude [16]. Rajendran and Smith

[124] identified that daylight duration which depends on latitude has an impact on the power output of the photovoltaics module. Therefore, the model which calculates the solar irradiance, G, is based on the following [78].

The angular position of the sun at solar noon with respect to the aircraft on the equator which is defined as the declination angle, δ, in degrees, calculated as

$$\delta = 23.45 \ \sin\left(\frac{360}{365}\right) \ (284 + n_{\mathrm{d}}) \tag{B.36}$$

where n_{d} is the day of the year (the day of the year (n) has to be specified as part of a numeric sequence that starts with 1 for January 1st and ends with 365 for December 31st). The hour angle of the sunset, h_{s} in degrees, which estimates the hour of sunlight in a given day is then calculated as

$$h_{\mathrm{s}} = \arccos\left(-\tan(\delta) \ \tan(\text{latitude})\right) \tag{B.37}$$

in which the latitude is in degrees. The solar altitude, a, in radians, can be calculated as:

$$a = \arcsin\left(cos(\delta) \ \cos(15 \ t_{\text{solarnoon}}) \ \cos(\text{latitude})\right) + \sin(\text{latitude}) \ \sin(\delta) \tag{B.38}$$

where $t_{\text{solar}_{\text{n}}\text{oon}}$ is the time from solar noon. Although local solar noon is different according to geography, here it is assumed to be at 12. Therefore, $t_{\text{solarnoon}} = 1$, means it is at 13:00, and $t_{\text{solarnoon}} = -1$, means it is at 11:00.

By combining Equations (B.36 - B.38), the hourly total surface irradiance can be calculated for the low altitude case as:

$$G = \bar{h} \ X \ Y \ Z$$

where $\bar{h}$ is average monthly solar irradiance from Burnett et al. [26],and

$$X = \frac{\pi}{24}\,[c + d\ \cos(15\ t_{\text{solarnoon}})]$$
$$c = 0.409 + 0.5016\ \sin\left[\left(h_{\text{s}}\frac{\pi}{180}\right) - 60\right]$$
$$d = 0.6609 - 0.4767\ \sin\left[\left(h_{\text{s}}\frac{\pi}{180}\right) - 60\right]$$
$$Y = \cos\left(h_{\text{s}}\frac{\pi}{180}\right) - \cos\left(h_{\text{s}}\frac{\pi}{180}\right)$$
$$Z = \sin\left(h_{\text{s}}\frac{\pi}{180}\right) - \left[h_{\text{s}}\frac{\pi}{180}\ \cos\left(h_{\text{s}}\frac{\pi}{180}\right)\right]$$

At high altitudes, the solar irradiance, G, is calculated as: $G = 0.5\ (e^{-0.65\ m_{\text{za}}} + e^{-0.095\ m_{\text{za}}})$ where m_{za} is the air mass at the given altitude calculated as

$$m_{\text{za}} = m_{\text{sla}}\ \frac{P_{\text{za}}}{P_{\text{sl}}}$$

where P_{za} and P_{sl} are the pressures at the given altitude and sea level respectively, and m_{sla} is the air mass at the sea level and calculated as

$$m_{\text{sla}} = \sqrt{1229 + (614\ \sin(a))^2} - 614\ \sin(a)$$

In series grouping, the voltage is calculated as $V_{\text{OCtot}} = N_{\text{s}}\ V_{\text{OC}}$ and the current are calculated as $I_{\text{SCtot}} = I_{\text{SC}}$. Whereas in parallel grouping, the voltage is calculated as $V_{\text{OCtot}} = V_{\text{OC}}$ and the current as $I_{\text{SCtot}} = N_{\text{p}}\ I_{\text{SC}}$.

where V_{OC} is the open circuit voltage, I_{SC} is the short circuit current, N_{s} is the number of solar cells in series and N_{p} is the number of solar cells in parallel.

B.6 Fuel cell model

Similar to internal combustion engines, the operation of normally aspirated fuel cells is affected by altitude. Saleh et al. [131] found that in the testing of the Ballard Nexa PEM fuel cell system on a Cessna Citation X, a net power drop of around 25% can be

observed from 1300 W at sea level to 970 W at 5000 ft. Moreover, it has been found that the power output of the fuel cell stack drops by 1.5% per 1000 ft., for a fuel cell using fresh air extracted directly from the atmosphere. This is only applicable for altitudes up to 10,000 ft, with more research needed for altitudes above this to determine the impact of high altitudes on the performance of the fuel cell stack and its power output.

The PEMFC model employs semi-empirical equations with the assumption of the steady and adiabatic flow of ideal gas, uniform temperature of the gases inside the cathode and anode, and the temperature of the gasses being the same as the stack temperature. The models here are based on Saleh et al. [131]. The voltage of the fuel cell output is:

$$U = U_{\text{oc}} - U_{\text{act}} - U_{\text{ohm}} - U_{\text{conc}} \tag{B.39}$$

where U is the actual voltage [V], U_{oc} is the open circuit voltage, U_{act} is the activation voltage, U_{ohm} is the ohmic loss voltage and U_{conc} is the concentration loss voltage. The equations are:

for open circuit voltage:

$$U_{\text{oc}} = E_0 + \frac{\Delta S}{n\,F}\,(T - T_{\text{ref}}) + \frac{R\,T}{n\,F}\,(\log(P_{\text{H}_2}) + 0.5\log\,(P_{\text{O}_2})) \tag{B.40}$$

for the activation voltage, U_{act}:

$$U_{\text{act}} = -(\xi_1 + \xi_2\,T + \xi_3 T\log(A) + \xi_4 T\log(i)) \tag{B.41}$$

where A is the oxygen concentration:

$$A = \frac{P_{\text{O}_2}}{5.08\;10^6 e^{-\frac{498}{T}}} \tag{B.42}$$

For the ohmic loss voltage, U_{ohm}:

$$U_{\text{ohm}} = I(R_{\text{m}} + R_{\text{c}}) \tag{B.43}$$

where the electrode resistance, R_{m}, is calculated by:

$$R_{\text{m}} = \frac{B\ L_{\text{meb}}}{S_{\text{meb}}} \tag{B.44}$$

where B is:

$$B = \frac{181.6\left(1 + \frac{0.03\ I}{S_{\text{meb}}} + \frac{0.062\ T}{303}\ (\frac{I}{S_{\text{meb}}})^{2.5}\right)}{(\lambda - 0.0634 - \frac{3\ I}{S_{\text{meb}}})\ e^{4.18\ \frac{T-303}{T}}} \tag{B.45}$$

For concentration loss voltage, U_{conc}:

$$U_{\text{conc}} = -b\left(1 - \frac{I}{I_{\text{max}}}\right) \tag{B.46}$$

The input parameter values used in the model can be found in the Table B.3.

TABLE B.3: Input parameter values for PEMFC based on the open literature [40, 157].

Symbol	Value
standard electrode potential, E_0	1.229
enthropy, ΔS	-164.025
universal gas constant, R	8.3145 J(molK)$^{-1}$
absolute partial pressure of hydrogen, P_{H2}	2 atm
absolute partial pressure of oxygen, P_{O2}	0.2094 atm
Faraday constant, F	96485 As(mol^{-1})
Model coefficient, ξ_1	-0.98
Model coefficient, ξ_2	$3.38 \times 10^{-}3$
Model coefficient, ξ_3	$10 \times 10^{-}5$
Model coefficient, ξ_4	$-2 \times 10^{-}4$
Model coefficient, b	0.028
intenal resistance of the model, R_c	0 ohm
Nafion membrance thickness, L_{meb}	0.018288 cm
area of the active part of the interelectrode unit, S_{meb}	83.22 cm^2
Model coefficient, λ	22.991
maximum current of the stack, I_{max}	25.7 A
operating temperature of the stack, T_{fc}	315.65 K

B.7 Multi-energy component class

To implement the powertrain components described above, we have created a multi-energy component classes in *Python 3.8*. The Python programming language is an object-oriented programming language. The object has properties and can contain methods and classes that act as a template to create new objects [123].

The class structure is as follows. The energy component class starts from the class called `Energy System` in an aircraft. A top-down development approach is used where the most generalised class is defined and subsequent specialisation classes are followed. An object of the energy component class defines the energy architecture in the aircraft in terms of `sources, storage, converters, transmitters, sinks, and additional` (Figure B.6a). The ultimate goal is to structure the class to have compatibility with the encoding scheme developed in this thesis (see Section 2.1.3 for the background and Chapter 3 for the scheme). The structure of the code acts as a housing for the necessary parameters of the components (i.e. mass models, current model for the power components, fuel flow for the energy components) individually, allowing for individual components to have the ability to compile a system from components - in other word, it does not matter if the powertrain is just electric, electric hybrid, internal combustion only, fuelcell-solar hybrid, the models for the individual components can be taken in from the class system for the modelling and simulation portion of the thesis. This further allow for the rapid generation of various topologies based on feasible connections and available components, leading to more flexibility in powertrain design and rapid exploration of different topologies and configurations. This could enable engineers to quickly evaluate the performance of different design options and select the most appropriate topology for a given application. All of the class structure is linked by one aspect: the developed design method is composed of models based on state variables. For example, in the mechanical domains, the state variables are torque and rotational velocity, in the electrical domains, current and voltage, and in the chemical domains, mass flow and lower heating values. These state variables link the individual components in the powertrain topology as well as ensure that the output of the powertrain component is matched up with the input of the following powertrain components.

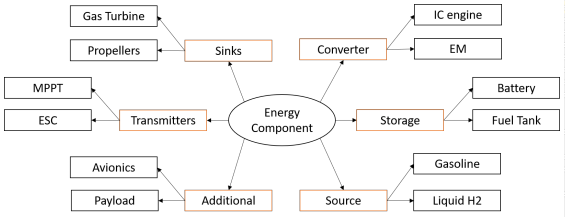

(A) Multi-energy component class example.

```python
class EnergyComponent:...
class Sink(EnergyComponent):...
class Source(EnergyComponent):...
class Converter(EnergyComponent):...
class Storage(EnergyComponent):...
class Transmitter(EnergyComponent):...
class Propeller(Sink):
    def __init__(self, name, thrust_n_required=None, true_airspeed_mps_required=None,
                 dataframe=None, mass_kg=None, file=None, sheet=None, class_name=None):...
    def calculate_mass_kg(self):...
    def _load_dataframe(self):...
    def power_flow_function(self, power_out, tuple_in):...
class Gasoline(Source):...
class H2(Source):...
class Battery(Storage):...
class ElectricMotor(Converter):...
class Generator(Converter):...
class CombustionEngine(Converter):...
class FuelCell(Converter):
    def __init__(self, product_name,max_power_w=None,mass_kg=None,
                 T_fc_K=None,i_max_A=None, v_max_v=None,
                 n_fc=None, specific_power_kwpkg=1.22, class_name=None):...

    def calculate_mass_kg(self):...
    def max_current_a_calculation(self):...
    def open_circuit_voltage_v_calculation(self, PH2_atm=2, PO2_atm=0.2094, delta_S=-164.025, n=2, R_JpmolK=8.3145,
                                           Faraday_const_Aspmol=96485):...
    def activation_voltage_calculation(self, PO2_atm=0.2094, ksi1=-0.98, ksi2=3.38 * 10 ** -3,
                                       ksi3=10 * 10 ** -5,
                                       ksi4=-2 * 10 ** -4):...
    def concentration_tension(self, b=-0.028):...
    def ohmic_loss_calculation(self, S_meb_cm2=83.22, L_meb_cm=0.018288, R_C_ohm=0, lambda_coeff=22.991):...
    def terminal_voltage_v_calculation(self):...
    def eta_fc_calculation(self, Faraday_constant_Cpmol=96485.4,
                           delta_h_Jpmol=284000):...
    def hydrogen_consumption_gps(self, k_kgpAs=1.0262 * 10 ** -8):...
    def power_flow_function(self, power_out, tuple_in):...
class PhotoVoltaics(Converter):...
class PC(Transmitter):...
```

(B) Multi-energy component class: code set up in `Python`.

FIGURE B.6: A visual example of how the multi-energy component class is set up.

The `sources` are components that are used up during the flight, such as wet fuel. `Storage` components store energy (such as batteries, fuel tanks). `Converters` convert one form of energy to another (such as internal combustion (IC) engines, which convert the chemical energy of fuel into mechanical energy). `Transmitters` transmits the same form of energy from one node to another (such as maximum power point trackers (MPPTs) in solar panels, DC/DC converters). `Sinks` are converters, but in the form of thrust creators, these end the flow of the energy network and are propulsive devices (such as propellers, jet engines, gas turbines). Finally, `Additional` does not contribute to the propulsion side of the aircraft, however, still requires power (such as avionics and payload). An example code can be seen in Figure B.6b. Here the `EnergyComponent` is the parent class, which contains general instances such as type of components and input-output connections. These are inherited by the sub-class, e.g. `Source`, which has its own instances. The class `Gasoline` is a subclass of `Sources`, which inherits the instances of the class and super-class. The classes include both attributes and methods. Attributes are data such as mass, length, width and height, whereas methods are calculated from the attributes, such as weight and density. Each class creates a functioning model based on the class's data - described in components modelling. These can be automatically generated with minimal input data, which can typically be found in the specification sheets.

B.7.1 Matching propeller-electric motor process

To find a well-matched propeller and electric motor configurations, we first select the propellers and electric motors seen in Table 4.3 for our chosen test platform (seen in Appendix A).

The process for the matching is as follows:

- First a propeller surface like the one shown in Figure 2.24c is created by the method described in section B.1 for the desired rotational speed, thrust, true airspeed, efficiency and torque.
- The next step is creating the electric motor surface (similar to Figure 2.24a), based on the allowable torque and rotational speed from the propeller. The model can be found in section B.3.
- Once the maps for the propeller and electric motors are created, we can compare the output of the two efficiency surface maps for the efficiency regions at the desired thrust and true airspeed ranges.
- To eliminate the infeasible matches, based on the equation (Equation B.28) as well as the maximum current limit of the electric motor, we can also determine whether the electric motor can handle the torque demanded by the propeller using

$$Q = \frac{I_{\max}}{K_Q}$$

B.7.2 Verification of the propeller model

Since the propeller data is obtained from APC [11] as a table with discrete steps for propeller speed, it is necessary to interpolate the data to be used in the simulation. In order to test whether the propeller data was interpolated properly, 70% of the data was taken to construct the interpolation function and the rest of the data was used to test the interpolation function. Figure B.7 shows the interpolation error (one standard deviation). The interpolation error is defined as the difference between the estimated value and the

true value at that point. The error is more prominent around the boundary, where there are not enough data points. However, in our region of interest where the airspeed is between 10 and 35 ms^{-1} and thrust of less than 60 N (for this specific propeller), the error is negligible.

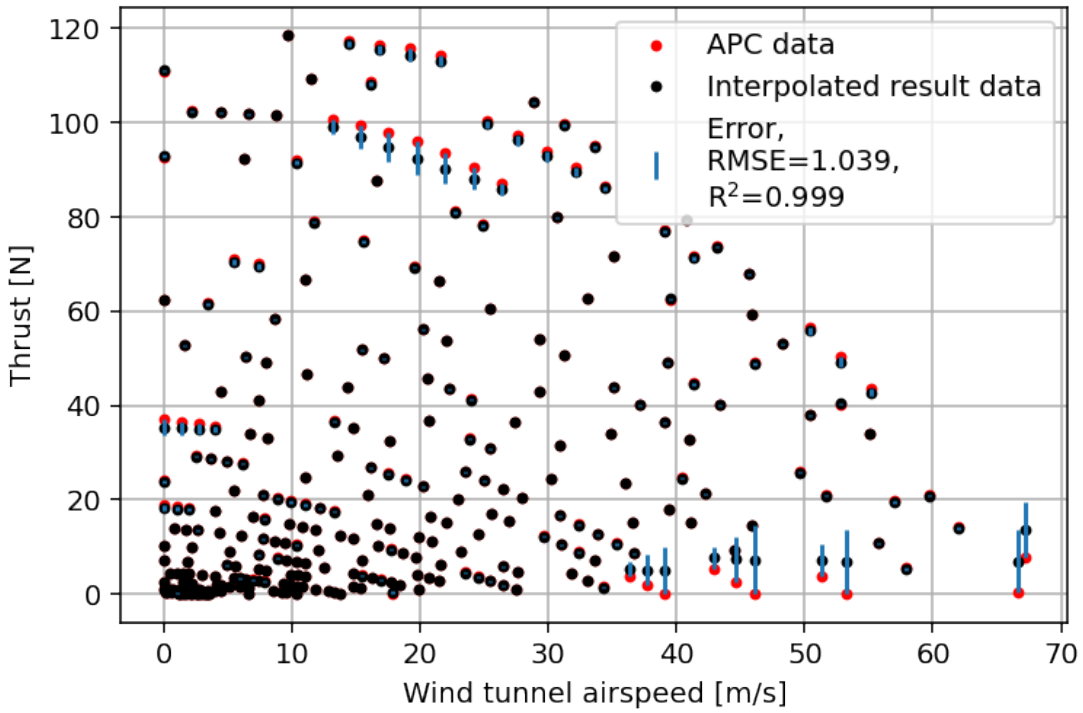

FIGURE B.7: Propeller interpolation function test case based on 12" x 6" APC two-bladed propeller.

Since the internal engine and propeller (or electric motor and propeller) are assumed to operate as a single combined system (no additional mechanical linkage such as gearbox), a torque equilibrium between the two components needs to be found. In the simple case where the propeller is mounted directly to the driveshaft and there are no linkages such as a gear or drive belt between the propeller and the drive shaft, the shaft speed is the same as the speed of the propeller. Assuming no losses, the torque must also be the same for both the propeller and the engine/motor.

For electric motors, the torque from the propeller can be balanced using Equation B.47 [43] for a specific flight speed, and the applied motor voltage (i.e., from the battery).

$$Q = \frac{(I - I_0)}{K_Q} \tag{B.47}$$

A well-balanced motor and propeller combination results in both components operating in their respective high-efficiency regions. The matching of the propeller with the motor is an important factor. If the propeller is too small for the motor, the mechanical friction in the motor lowers the efficiency and the aircraft would not reach its required performance. However, if the propeller is oversized for the electric motor, the electric motor would try to keep turning the propeller, leading to issues such as current draw exceeding the rated current and therefore risk damaging the electric motor. The method of propeller motor matching in this study is explained in section 2.2.7.

In order to test the interpolated propeller data, we conducted a wind tunnel test on the propeller-electric motor-battery combination [164]. If the propeller performance map is known, as in our case, obtained from APC database [11], the rotation speed of the propeller, along with the airspeed, can be used to derive a reasonably close estimate of the thrust generated by the propeller (with possible errors due to integration effects and propeller performance in-service degradation). If the propeller is directly attached to the motor shaft (as is the case with most small UAVs), the rotation speed of the propeller is the same as that of the rotor of the electric motor. Therefore, an optical tachometer based on an infrared (IR) sensor, a laser sensor, a Hall effect sensor, or photo-interrupter can be used to measure the rotation speed of the propeller.

The test platform used in the experiments described here (FliTePlat) is equipped with an IR sensor. It uses an LED, which emits IR waves toward the rotor of the electric motor. These get reflected by a reflective strip on the surface of the motor and are sensed by a photodiode. The sensor is paired with an onboard microcontroller, which reads the number of pulses that the photodiode detects, calculates the RPM, and stores the values on an SD card.

The author designed a relatively simple hardware setup (see Figure B.8 for an example implementation). The IR sensors are sensitive to daylight, they can be shielded from background IR radiation by embedding them inside the motor nacelle. Since the electric motor requires high current, the signal wires may require electromagnetic shielding in some installations.

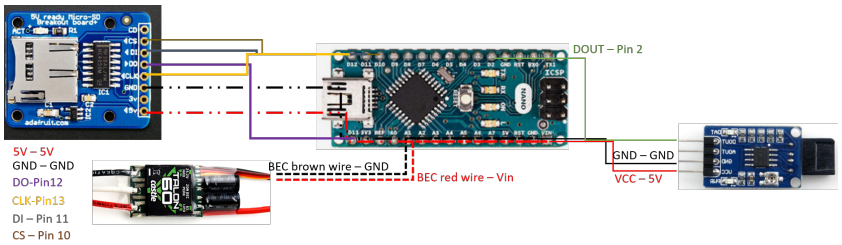

FIGURE B.8: IR sensor set up.

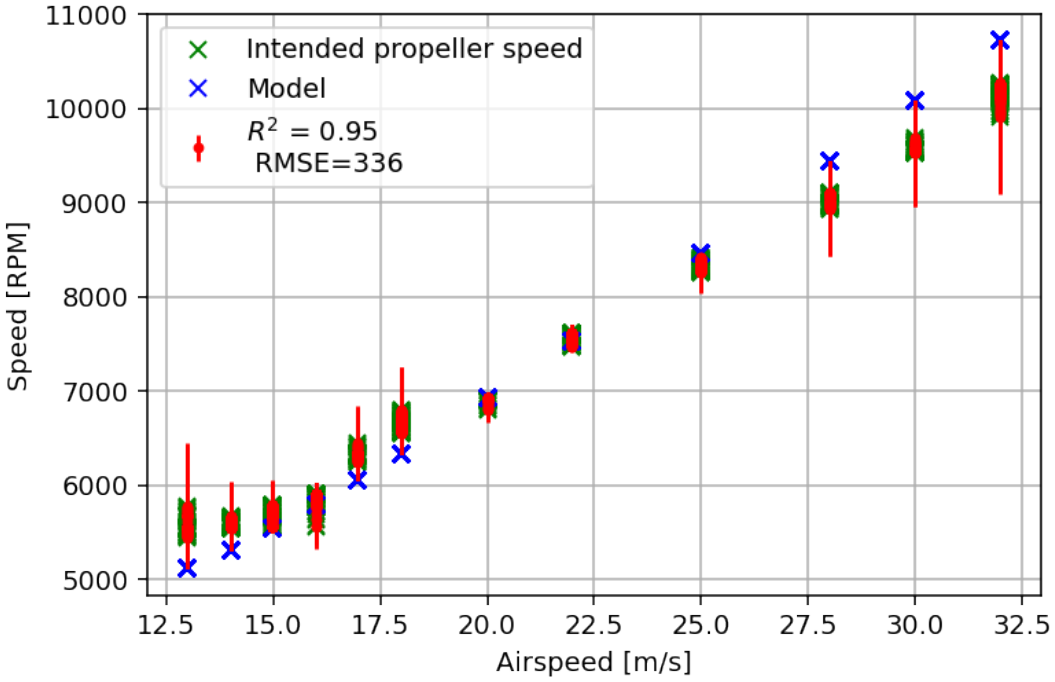

FIGURE B.9: Motor speed model based on experiment against the interpolated data from the propeller.

As can be seen in Figure B.9, the interpolated data and the experiment data collected by the setup (Figure B.8) match well. The R^2 value is a measure of how well the interpolated data fits the observed data. It represents the proportion of the variance in the dependent variable that can be explained by the independent variables in the model, with higher values indicating a better fit. It is supported by the relatively low Root Mean Squared Error (RMSE) value (the RMSE calculates the average magnitude of the errors in the predictions) compared to the magnitude (speed in the y-axis).

B.7.3 Verification of electric motor and battery model

Two case studies were conducted to verify the battery, electric motor and propeller models. One is the case where the propellers produce thrust in static conditions and the other in dynamic conditions.

B.7.3.1 Case study one – static case

The experimental data used in this case study is based on data collected by the author in 2018 for a group design project. The components used in the experiment are listed in Table B.4. The experiment is a static test conducted within a test rig, using two RCBenchmark Series 1780 (S1780) [152] load cell units for data acquisition. These contain three load cells per propeller and are able to determine the thrust [N], torque [Nm], angular velocity [RPM], voltage [V] and current [A] supplied to the setup. The experiment is used to validate the battery model described above during a static propeller test.

TABLE B.4: Components during the static propeller test.

Component	Type
Propeller	APC - 11" x 3.8"
Electric motor	T-motor MN4012 KV480
ESC	Castle Creations - Talon 60
Battery	Turnigy Nano-Tech Plus 3000mAh 6S 70C Lipo Pack w/XT90

The input parameters to the model are propeller torque, time step, propeller rotation speed, the type of battery, propeller, and electric motor of the experimental data. The assumption made here is that since there are no other mechanical connections, such as a gearbox, between the propeller and the electric motor, the torque and speed of the propeller are the same as the motor. Hence, the voltage and current required for the electric motor from the electronic speed controller were calculated by using the propeller speed and torque data as the primary input. The model combination can be seen in Figure B.10 with the detailed steps of the process shown in Figure B.11. Although, as described in Verstraete [159], the electronic speed controller's efficiency changed with the input voltage and the electronic speed controller's current during the

discharge of the battery, for the purposes of our study, we can assume it to be 0.95, as shown in the sensitivity study in Figure B.13.

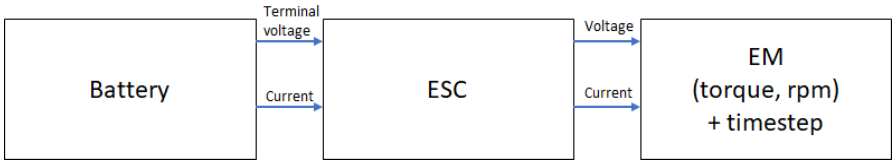

FIGURE B.10: Case study set up - battery, electronic speed controller and electric motor connections.

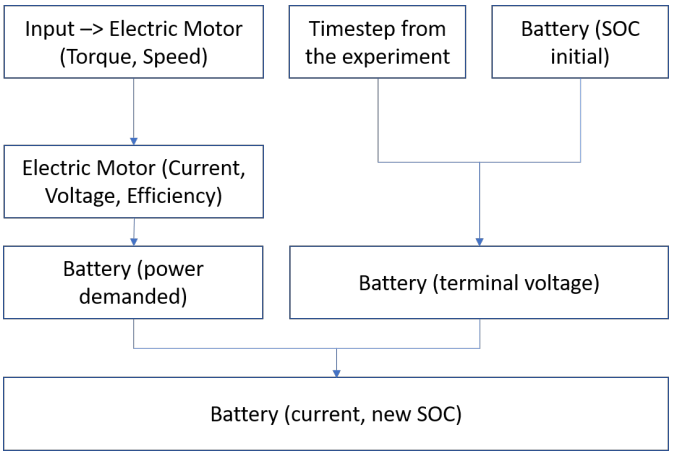

FIGURE B.11: Validation case study process - for δt - battery, electronic speed controller and electric motor connections. Assuming that the electronic speed controller's efficiency is 0.95 and is constant. This process is repeated until the final time step is reached.

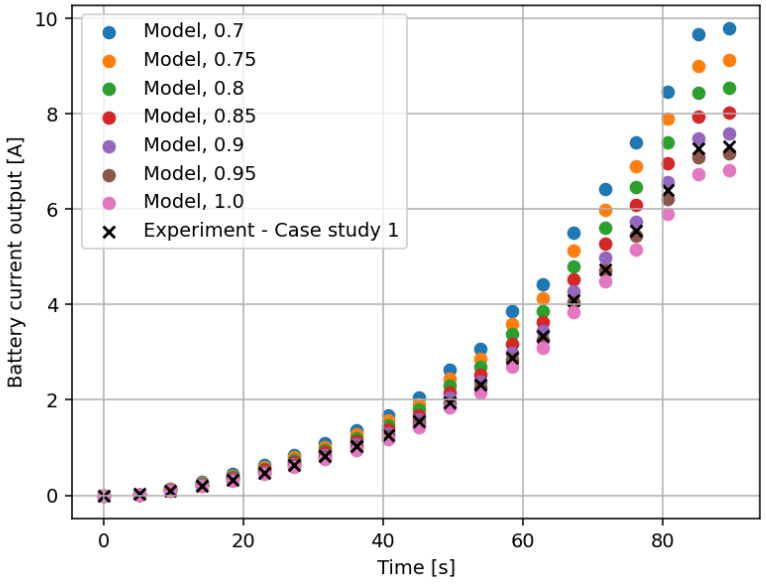

FIGURE B.13: Sensitivity analysis to obtain electronic speed controller efficiency.

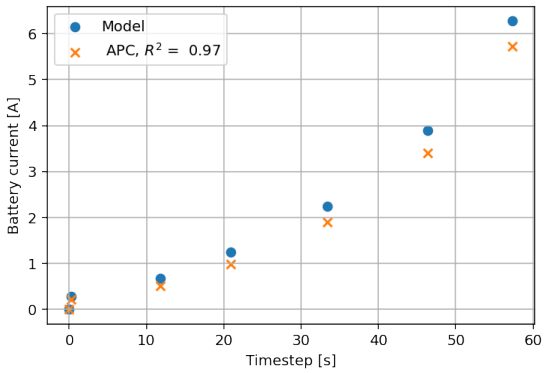

(A) Validation case study - current.

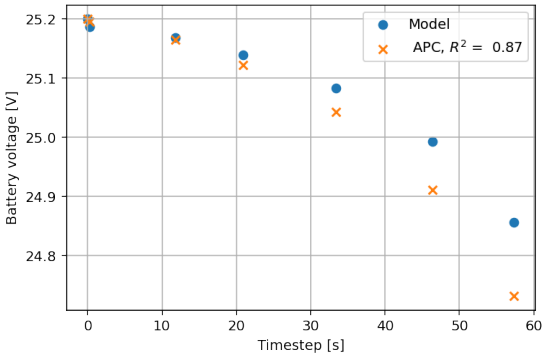

(B) Validation case study - voltage.

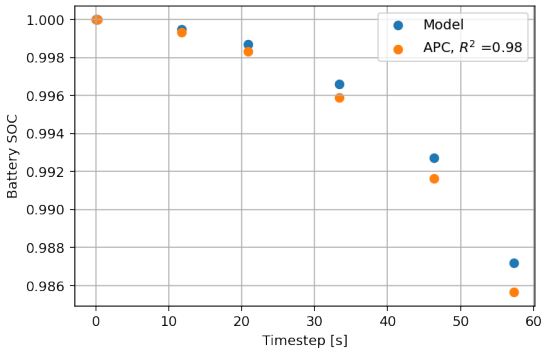

(C) Validation case study - state of charge.

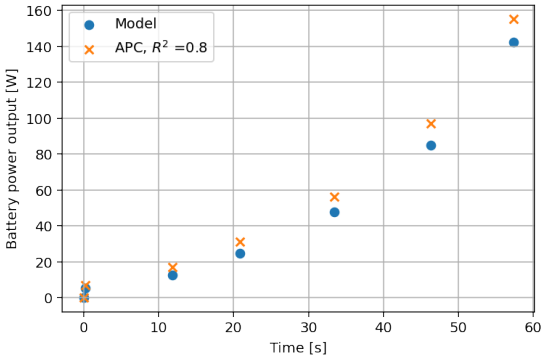

(D) Validation case study - power flow.

FIGURE B.12: Battery validation case study - comparison of the model and the experiment - for statics case.

The case study also indirectly validates the propeller and electric motor modelling as the powertrain is a single propeller, battery-powered electric powertrain. The input parameters are the measured propeller torque, time-step, measured propeller rotation speed, the type of battery, propeller, electronic speed controller and electric motor of the experimental data. The results (shown in Figure B.12a - B.12d, B.14) show a good agreement between the models and the experiment, with high R^2 values between the model and experiment results, demonstrating how well the model correlates to the data.

B.7.3.2 Case study two - dynamic case

While static propeller tests can be useful for some types of testing, they may not provide an accurate simulation of flight conditions. For example, propeller static tests typically

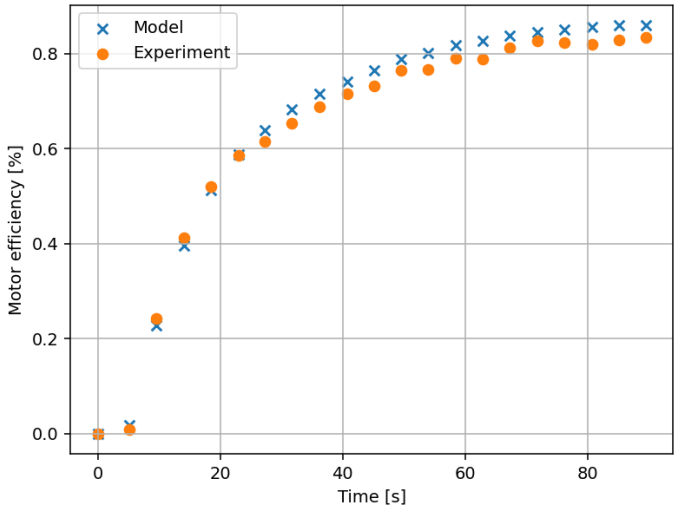

FIGURE B.14: Electric motor efficiency - comparison of the model and the experiment - static case.

involve the battery operating at a constant load, whereas flight conditions are more dynamic and variable. Additionally, propeller tests do not typically account for changes in temperature or other environmental factors. Therefore, we conducted a second case study during a flight testing campaign, which reflects the real-life situation better than the first case study. The results of this campaign are published in [164]. The data analysed here is from an extended cruise segment. Figure A.1 shows the onboard sensors available on the UAV.

The hardware setup for data collection is similar to the setup shown in Figure B.8, with the addition of voltage and current sensors, also called power sensor units (Mauch 100 A Hall sensor-based power module for Pixhawk). These can be seen in Figure A.1, situated inside the fuselage. The components used in the experiment are listed in Table B.5.

TABLE B.5: Components used in the dynamic propeller test.

Component	Type
Propeller	APC - 12″ x 6″
Electric motor	AT3520 KV 720 Electric motors
Electronic speed controller	Castle Creations - Talon 90
Battery	12500 mAh 22.2 V 6S2P 35 C Supersport XL LiPo Overlander Battery

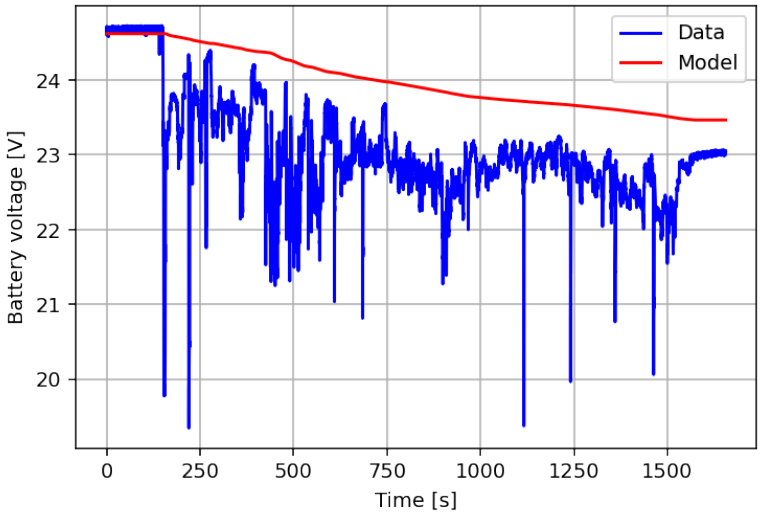

(A) Validation case study - voltage depletion.

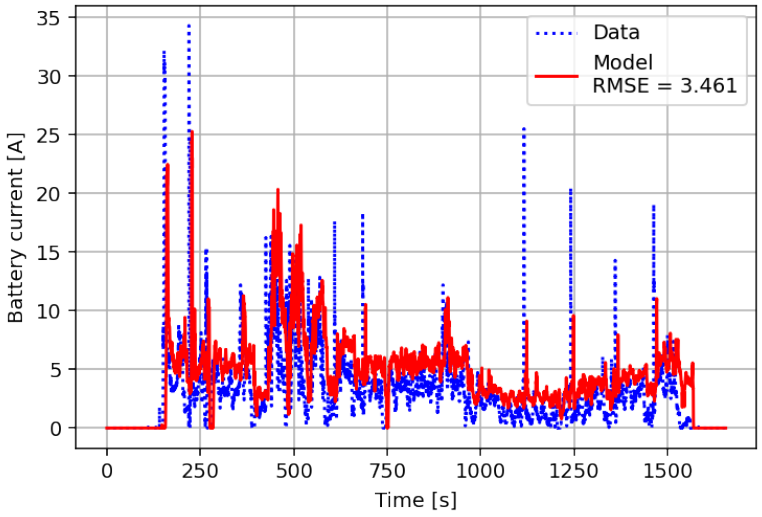

(B) Validation case study - current draw.

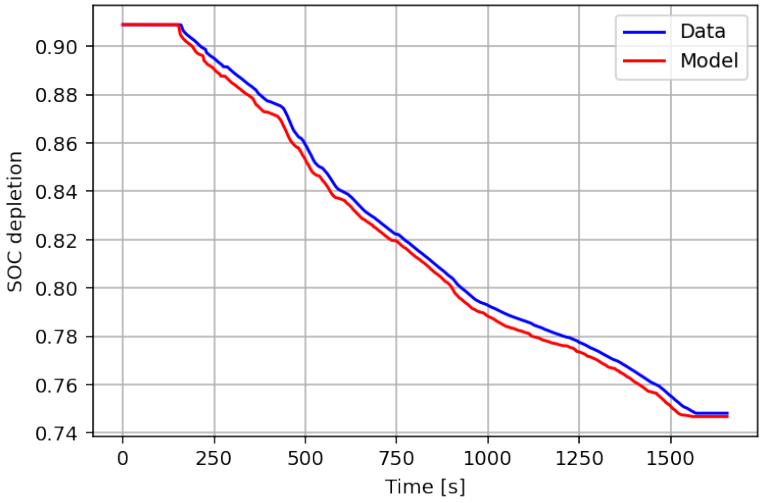

(C) Validation case study - state of charge depletion.

FIGURE B.15: Battery validation case study - comparison of the model and the experiment during flight testing.

Figures B.15a - B.15c show the result of the model compare to the output of the flight test data. The models are able to accurately predict the battery's depletion trend. One thing to note is that the model does not take into account the battery under load. Some other factors affecting the voltage draw include the model parameters (i.e. Equation B.33). The battery model depends on accurate parameters such as the capacity, internal resistance and open-circuit voltage. If these parameters are inaccurate, the model may not accurately predict the voltage draw. Moreover, the voltage of a battery can be affected by temperature changes. The battery model here does not account for temperature effects, it overestimates the voltage draw. Similarly, over time, batteries may degrade which can affect their voltage output. The battery model does not account for ageing effects. Lastly, the physical circuit and wiring losses are not taken into account, where voltage drops occur due to the resistance of the circuit and wiring. However, the model does follow the depletion trend nicely in Figure B.15a, given the correct start voltage. Figure B.15b and B.15c support the model's validity. In an ideal world, the individual batteries would be tested to form a better regression model for Equation B.33, however, at this stage, this current model is suitable for initial comparison between different topologies.

B.7.4 Internal combustion engine mapping

In this section, we discuss the results of the engine mapping, as discussed in section B.2.1, and how these are applied in the modelling and simulations. Due to the nature of the OS GF-40 engine, there exists excessive vibration. Therefore, the experimental data are required to be smoothed in order to apply to any optimisation. In general, at a specific throttle setting, torque and power are a function of engine speed. At the low engine speed region, the torque increases as the engine speed increases, up to the point where the torque reaches its maximum limit. One of the reasons for the decrease in torque is that the power loss due to friction losses increases with engine speed and, at a certain engine speed at each throttle setting, becomes a dominant factor Pulkrabek [121]. The power trends also hold similar to the torque trend. These relations between

power, torque and speed (an example of the OS GF-40 engine test can be seen in Figures B.16 - B.18).

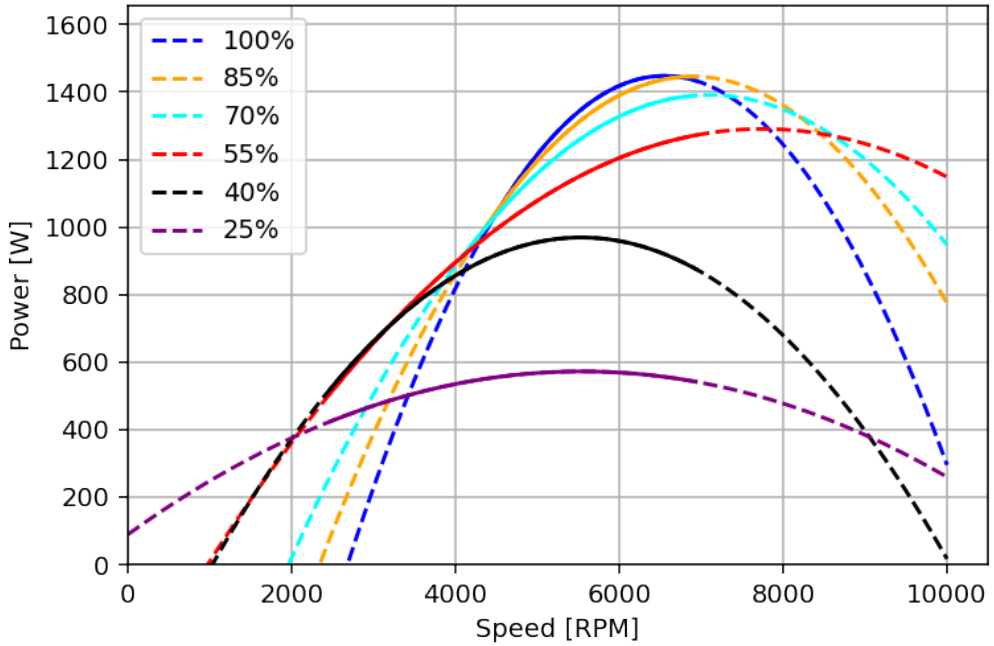

FIGURE B.16: Power [W] v Engine rotation speed [RPM] relations at different throttle settings (%) for the OS GF 40 engine. The solid line shows the interpolated data whereas the dashed line is extrapolated.

The figures (Figure B.18 - B.17) show the relationship between torque and power with respect to engine speed. Statistical methods have been applied to indicate the goodness of fit. The 95% confidence bound shows that the quadratic fit is well-fitted, especially for the higher end of the RPM region. From the prediction band, it can be seen that Figure B.18 shows the largest noise - as the experimental results lie outside of the confidence regions within the data and, therefore, indicates that there may be some unknown variability involved during the collection of this data, such as a low fuel flow rate. However, for the purpose of this work, the polynomial coefficients at each throttle setting are enough for the engine map.

Phlips [118] explains that for an internal combustion engine, the fuel burn increases proportionally with the power output, the offset on the y-axis, for example in Figure B.19, representing the losses in the engine, and the slope indicates efficiency. Therefore, for modelling the fuel flow, it can be assumed that the fuel flow and power output

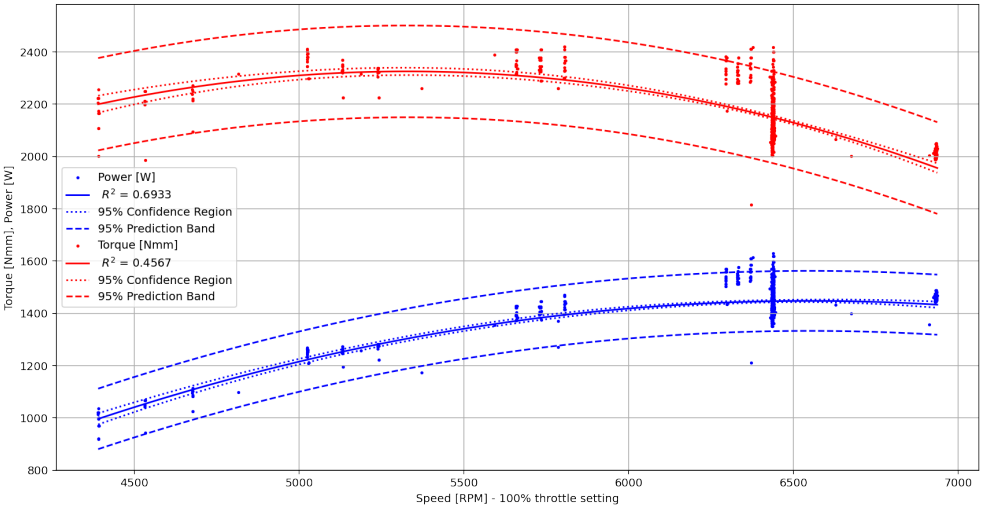

FIGURE B.17: Power [W], Speed [RPM], and Torque [Nmm] relations at 100% throttle setting.

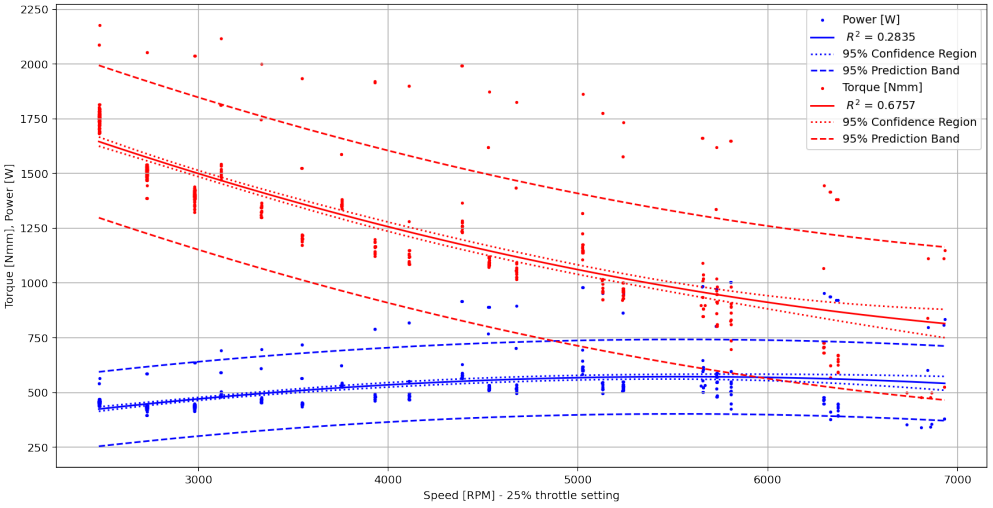

FIGURE B.18: Power [W], Speed [RPM] and Torque [Nmm] relations at 25 % throttle setting.

have a linear relationship. However, as can be seen in Figure B.19, when a regression model is fitted to the data. The root mean square error on this test set assesses how well my model performs in predictions for future observations, i.e. estimating accuracy on unseen observations. This root mean square error reveals that the quadratic fit is more suitable than the linear fit for this particular data set. The reason could be because, as Zhang et al. [171] discussed, fuel consumption depends on torque as well as engine speed. If the engine is operating at its highest efficiency, the fuel consumption

rate only depends on the engine power output. However, this particular engine was not operating at its peak efficiency. Generally, the expected behaviours of the engine characteristics are that the maximum performance at the wide open throttle is due to the largest amount of fuel injection in the cylinder, therefore, more power and torque are produced by stronger combustion. However, with the carburettor poorly fitted to the OS GF-40 (the attached carburettor was for an 80 cc engine as opposed to a 40 cc engine), there is a performance reduction in the wide open throttle setting due to a higher mass flow rate or volumetric efficiency, as well as affecting the fuel-to-air ratio. This is evident when comparing the power output at various throttle settings, which can be seen in Figure B.16.

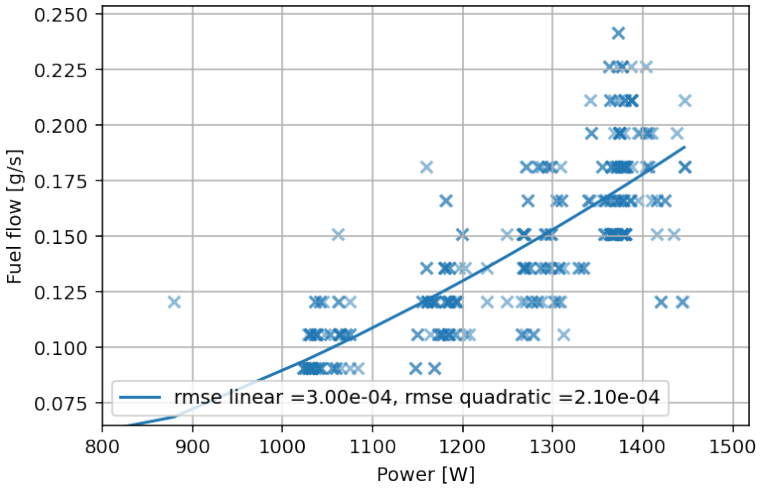

FIGURE B.19: Fuel flow [g s^{-1}] at 70% throttle setting, showing the nonlinear relations between fuel flow and power.

Based on the results of Figure B.16 - Figure B.19, an engine map (Figure B.20a is produced. This map also serves as a baseline four-stroke internal combustion engine map for scaling, which is described later.

B.7.4.1 Scaling of the engines

From the Willans line method, the coefficients for the baseline engines (to three significant figures) are shown in Table B.6.

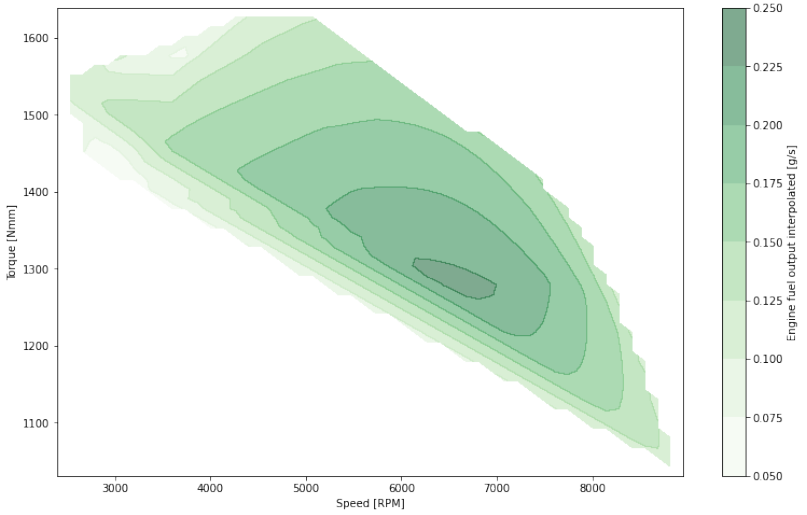

(A) OS GF-40 engine map.

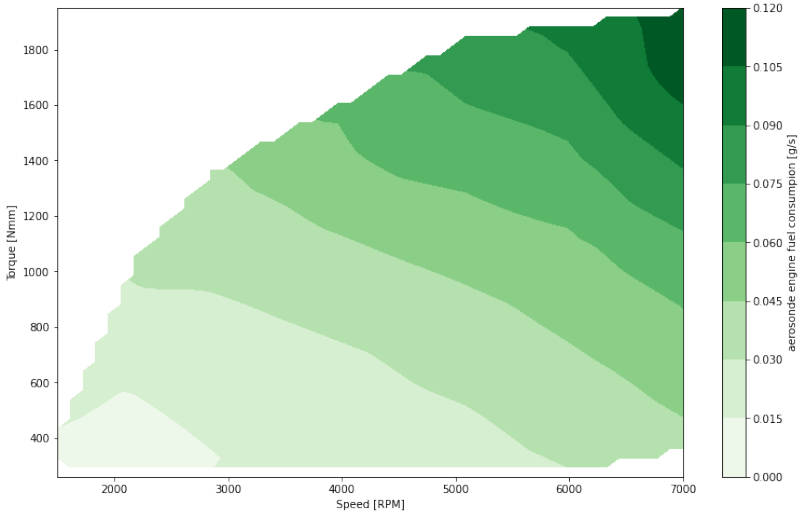

(B) EL-005 engine map based on Hung and Gonzalez [73].

FIGURE B.20: The baseline engine maps used in this study for scaling of the engines through the Willans approximation [127, 140, 177].

In order to compare the Willans approximation and actual data of the engine, Table B.7 shows the error metrics between the prediction and the actual values. The r^2 are relatively high (close to 1) for both power and torque approximation, indicating that the approximation fits the data well. This goodness of fit has been backed up by the low root mean square error and a low median absolute error, which is robust against the outliers. Both of these indicate a good measure of the approximation of the model accuracy, as it gives a lower value (relative to the actual value). This is also backed visually, seen in Figure B.21, that the Willans approximation overlaid on the experimental data, which shows that the approximation closely matches the data.

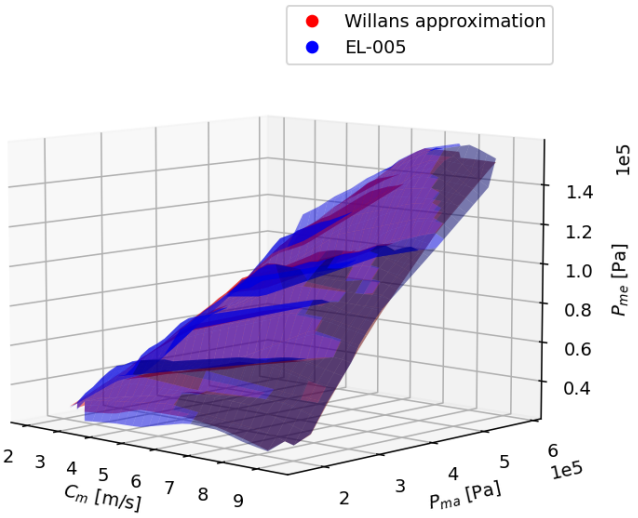

(A) Comparison of the Willans approximation and the experimental result - EL-005.

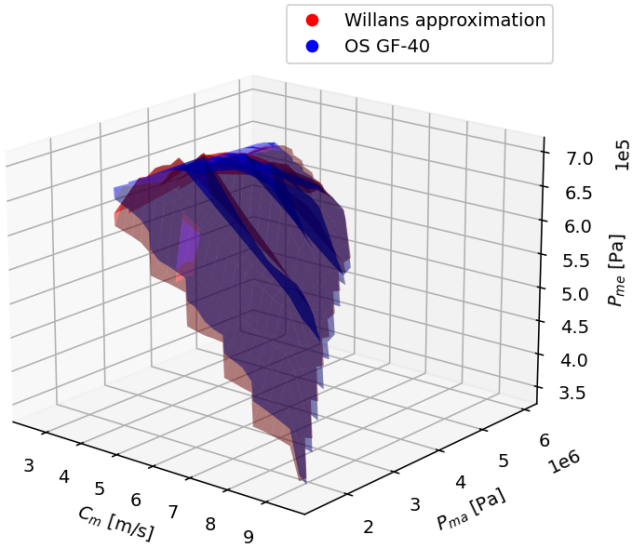

(B) Comparison of the Willans approximation and the experimental result - OS GF-40.

FIGURE B.21: Comparison of the Willans approximation and the experimental result. The red surface is the approximation from the Willans line calculations whereas the blue surface is the experimental data.

TABLE B.6: Coefficients obtained from Willans approximation of the baseline engines engine.

	OS GF-40	EL-005 [73]
η_{00}	-2.99×10^{-01}	-8.30×10^{-01}
η_{01}	2.22×10^{-01}	4.75×10^{-01}
η_{02}	-9.48×10^{-03}	-1.64×10^{-03}
η_{10}	-1.15×10^{-08}	-7.32×10^{-09}
$\eta 11$	1.80×10^{-08}	9.26×10^{-09}
$P_{\text{m,loss0}}$	-1.15×10^{06}	-6.11×10^{03}
$P_{\text{m,loss1}}$	3.96×10^{05}	4.91×10^{03}
$P_{\text{m,loss2}}$	-1.82×10^{04}	4.06×10^{02}

TABLE B.7: Engine error metrics due to Willans approximation for the baseline engines.

	Power [W]		Torque [Nmm]	
Error metrics	OS-GF40	EL-005	OS-GF40	EL-005
r^2	0.88	0.99	0.97	0.99
root mean square error	77.25	26.4	61.69	50.46
median absolute error	42.0	11.54	44.08	27.86

The method provides a simple and quick method for estimating the power output of an internal combustion engine based on its displacement or size. This can be helpful for engineers and designers who need to quickly assess the potential power output of different engine configurations. The Willans approximation is based on the assumption that the engine operates at a constant efficiency, which may not be entirely accurate in practice. However, because the approximation is relatively easy to use, it can provide a good starting point for estimating engine power output and comparing different engine designs. As an example, the scaled map of 'OS FSA-115' engine based on 'OS GF-40' is seen in Figure B.22 with Table B.8 give the physical parameters of the engines to be used in the approximations.

TABLE B.8: Willans approximation - engine scaling.

	OS GF-40	OS FSA-115
Total mass [kg]	1.378	0.9
Max power [W]	2800	1900
Number of cylinder	1	1
Piston stroke [m]	0.0318	0.0286
Piston bore [m]	0.04	0.0336
Displacement [cc]	40	25
Number of revolution per powerstroke	2	2

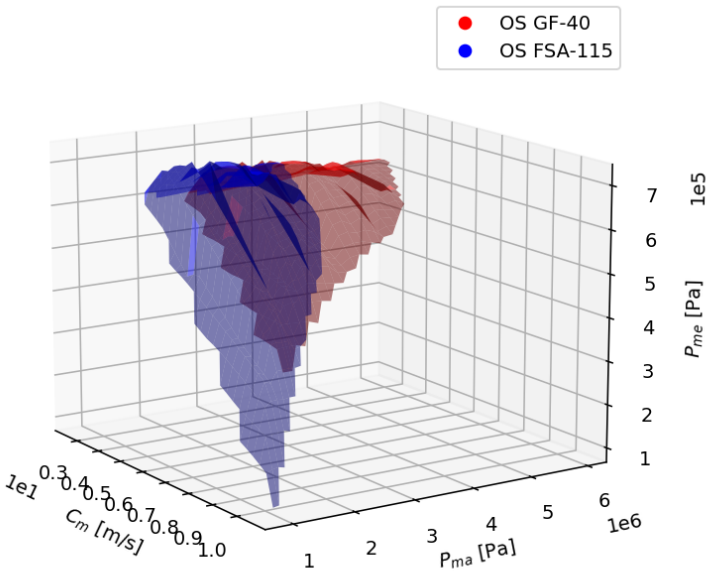

FIGURE B.22: Example scaling of the engine using Willans approximation.

The approximation can also be useful for estimating the fuel consumption of an engine since these are typically related to the engine's power output. This can be helpful in evaluating the overall efficiency of the engine. Overall, while the Willans approximation has its limitations, it remains a useful tool for quickly estimating the power output of an internal combustion engine and evaluating different engine designs; especially for commercial off-the-shelf engines, where the rapid evaluation of different engine options can be conducted. By using the Willans approximation to estimate engine power, designers can quickly compare different engine options and select the best one for their application based on mass, power output, cost, and other factors. The benefits outweigh the disadvantages at the early stages of design where testing all the possible engines is not feasible.

In summary, while the Willans approximation can provide a rough estimate of an engine's power output, it should be noted that actual engine performance can vary significantly depending on a range of factors, including the engine design, fuel quality, and operating conditions. Therefore, this approximation should be used as a guideline rather than a precise calculation.

B.7.5 Verification of solar cell models

For verification of the solar cell model described above, the Sunpower C-60 parameters shown in Table B.9 are used. The testing procedure follows the approach described in Figure B.5. Figure B.24 shows the average solar irradiance for different months at different times for high altitudes (above 2.5 km) and low altitude (below 2.5 km) at Southampton, UK, using the UK average solar irradiance given by Burnett et al. [26].

TABLE B.9: Sunpower C-60 parameters.

Sunpower C-60 parameters		
Number of cell in series	Ns	1
Number of cell in parallel	Np	1
Internal resistance	R [ohm]	0
Short circuit current	I_{sc} [A]	6.24
Maximum powerpoint current	I_{mpp} [A]	5.83
Maximum powerpoint voltage	V_{mpp} [V]	0.682
Current coefficient	KI [mA/C]	0
Voltage coefficient	KV [mV/C]	-1.7
Reference temperature	T ref [C]	25
Temperature on the day	T [C]	28
Solar irradiance reference	G ref $[W/m^2]$	1000
Solar irradiance on the day	G $[W/m^2]$	300, 500, 800, 1000

Based on this solar irradiance at low altitude, we model the voltage, current and power output from a single solar cell. Although the model predicts the maximum PowerPoint track point (voltage before the drop of the current) to be higher, therefore overpredict the maximum power output by roughly 5 W, Figures B.23a and B.23b. One of the reasons why the voltage output in Figure B.23a is underestimated could be that the accuracy of your solar cell model is highly dependent on the parameters used in the model, such as the efficiency, fill factor and series resistance. If these parameters are inaccurate, the model may not accurately predict the voltage output. However, at the early stage of the design process, and lack of experimental data available, this model is assumed to be correct, since up to the point of maximum allowable voltage and current output, the voltage and current output follows the model.

The combination of the result from Figure B.24 along with scaled values of Figure B.23a and Figure B.23b, suitable for the allowable wing area of the platform, are applied in the methodology described in Chapter 5.

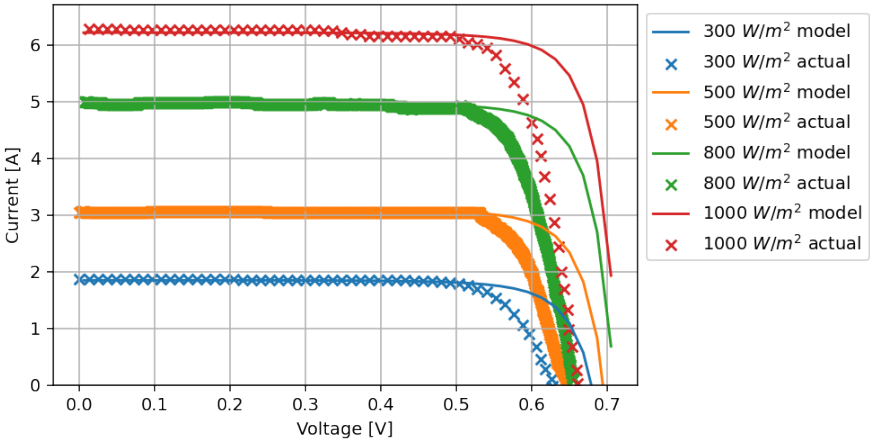

(A) Sunpower C-60 at 28 deg voltage-current relations at various solar irradiance.

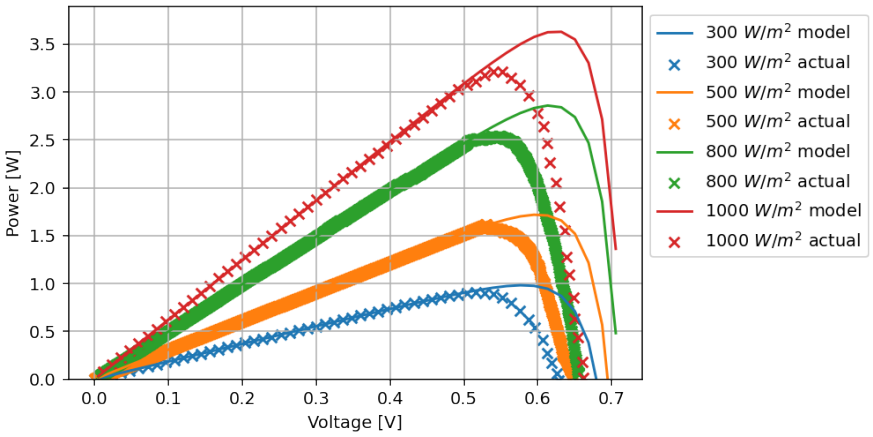

(B) Sunpower C-60 at 28 deg voltage-power relations at various solar irradiance.

FIGURE B.23: Sunpower C-60 single solar cell - comparison of the model and the open data given by the manufacturer.

B.7.6 Verification of fuel cell model

The parameters for the fuel cell can be seen in Table B.3 and the expected output can be seen in Figure B.10. From Figure B.25a, at low current, the model follows the data well with the results deviating from the data at higher current. We see the impact of this in Figure B.25b, where it is producing a maximum of 35 W at a maximum of 5 A current draw, over predicting by 5 W (as given by the specification found in Table B.10). PEM fuel cells rely on the transport of reactants and products to and from the catalyst layer to generate electricity. If the reactant transport is limited, the fuel cell performance will suffer, leading to a lower voltage output. This can happen at high current densities due to limitations in the diffusion of the reactants, such as hydrogen or oxygen, to the

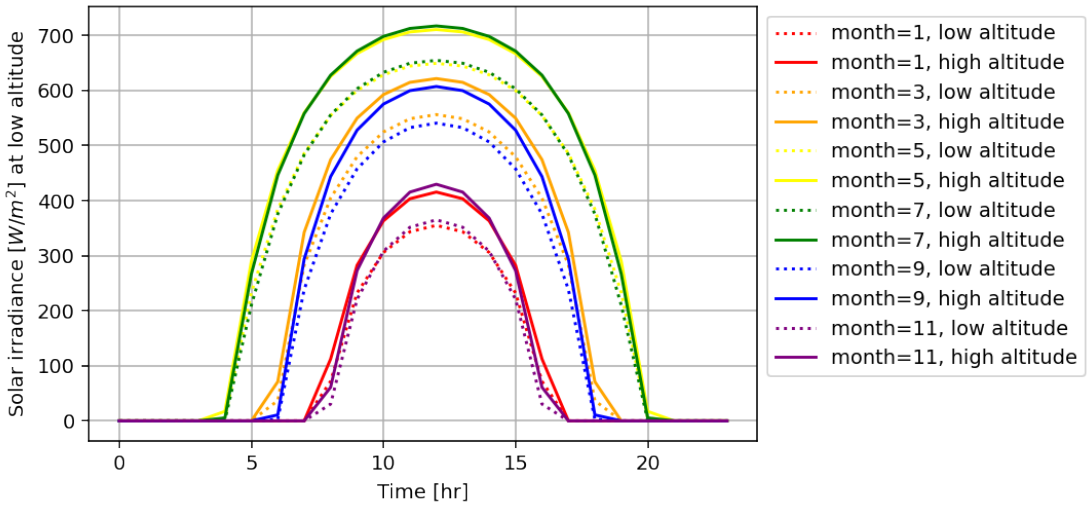

FIGURE B.24: Solar irradiance model at high altitude (> 2.5 km) and low altitude (<= 2.5 km) at the latitude of 50.9105 deg.

catalyst layer. Inadequate modelling of mass transport limitations could result in an over-prediction of the voltage output. Another reason is the lack of accurate modelling of the catalyst layer. This is crucial for predicting the fuel cell's performance accurately, leading to an over-prediction of the voltage output. Such discrepancies are expected as the model is based on an experimental result of a different PEMFC. However, for a proof of concept case, this model is deemed to be acceptable.

TABLE B.10: PEMFC - Protium 25 specification.

Parameter	Value
Rated power	30 W
Operating temperature	25 C
Mass	0.416 kg
Max hydrogen fuel consumption	0.3 L min^{-1}
Max voltage	9 V
Max current	5 A

B.8 Summary

In this appendix, we discussed the models for the components such as combustion engines, batteries, fuel cells, photovoltaic cells and electric motors along with their advantages and disadvantages. A database of the components to reduce the need for

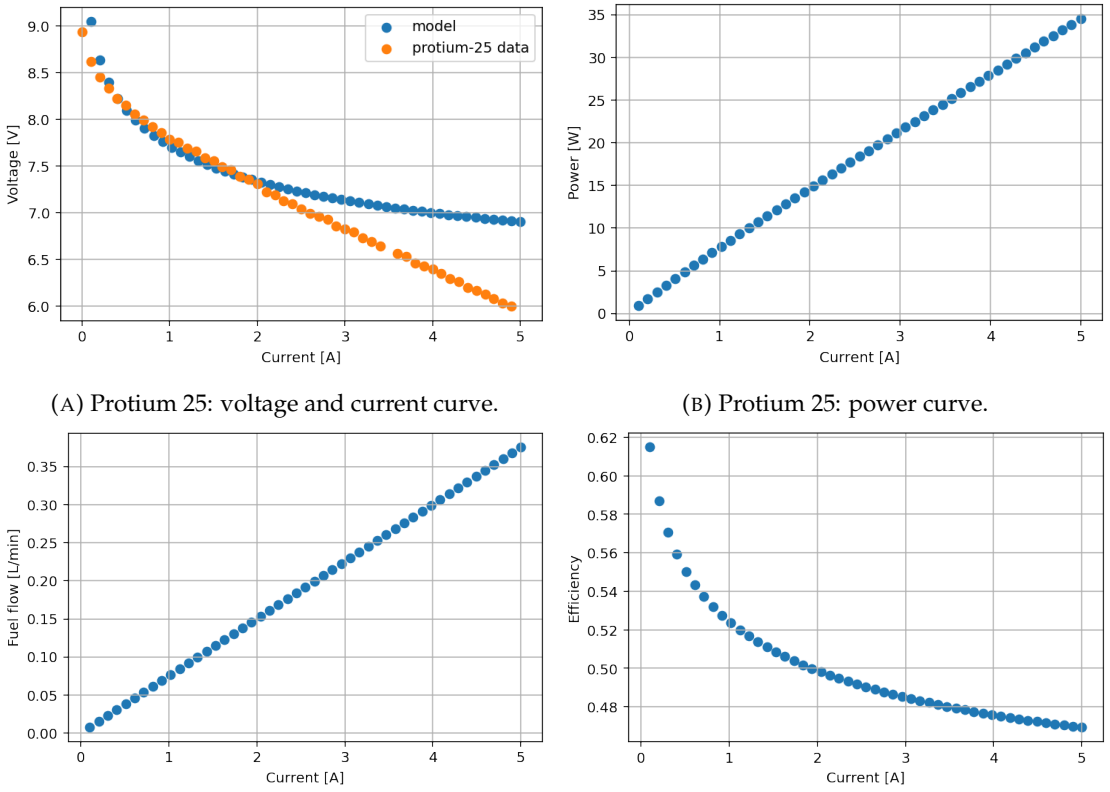

(A) Protium 25: voltage and current curve.

(B) Protium 25: power curve.

(C) Protium 25: fuel consumption curve.

(D) Protium 25: efficiency curve.

FIGURE B.25: Protium-25 PEM fuel cell model vs data comparison with data based on [51].

'rubber' sizing, has been collected through web scraping. This provides a key step towards modelling the entire powertrain and choosing the most suitable commercially existing components for a given mission.

We have also proposed simplified models for the powertrain topology and the setback that each model has. However, for the purpose of this study, the level of detail chosen for the powertrain modelling is compatible with the preliminary weight sizing phase of interest here. We verified the models where possible. In future work, the recommendation is to create reliable models based on experiments, implement improvements such as a better fuel sensor for the internal combustion engine model so that scaling of the engine model is more reliable, and to collect experimental data for fuel cells and solar cells.

Appendix C

Powertrain Optimisation Results

This Appendix includes additional mission cases and comparisons between FliTePlat and PEREGRIN powertrains.

C.1 Mission 2

The following section presents the results of Mission 2 and holds a similar structure as Mission 1 described above. For missions where there are more segments (i.e. here we now have two: take-off and cruise), there is one more variable (thrust at cruise) to consider. Figure C.1 shows the profile.

Similarly to Figure 5.4, Figure C.2 shows the final feasible topology strings and their corresponding masses. Note that in Figure C.2a, there are two powertrain topologies (above the red dotted horizontal line) that result in a higher than allowable maximum take-off mass. These are penalised as described in Equation 5.3 in section 5.3. There are also less feasible powertrain topologies produced for PEREGRIN (as seen in Figure C.2b).

Similar to Figure 5.5, Figure C.3 shows the energy source split and the average powertrain efficiency. Since there are different power demands for each segment, the energy source split and the average efficiency are also produced for each segment. Generally, for FliTePlat, the dominant energy source in the first segment is the same as the second,

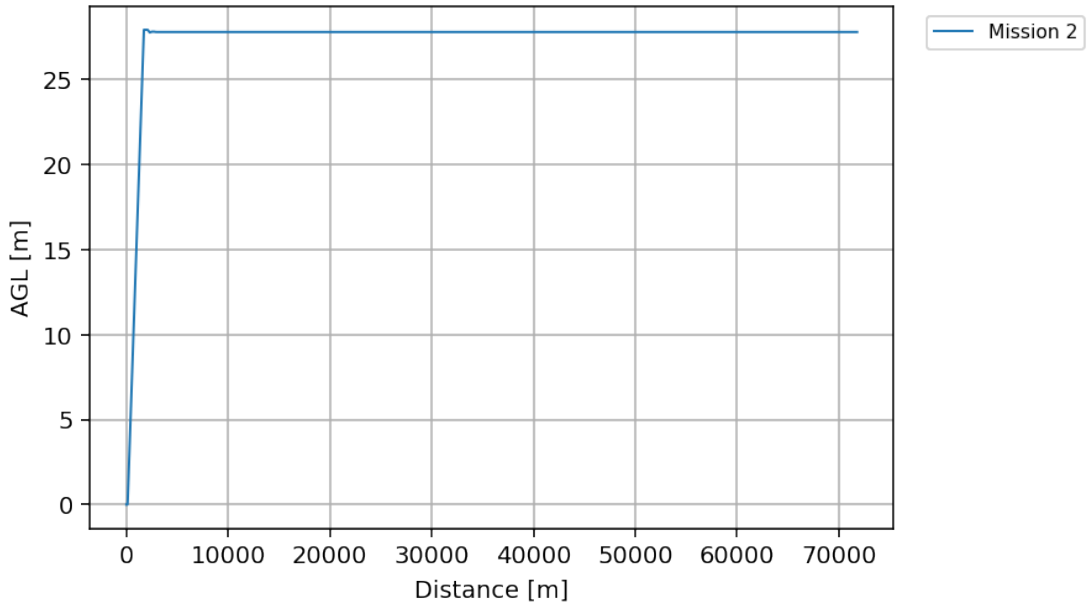

FIGURE C.1: Mission 2 - profile.

with the exception of p[em | {PV + {fc(HY | (which has the dominant energy source of 'HY' for the take-off and 'PV' for the cruise) and | p[em + p[em | {pc | {PV + {gn(en(HC | (which has the dominant energy source of 'PV' for the take-off and 'HC' for cruise). For hybrid powertrains of PEREGRIN in Figure C.3b, the dominant energy source in the first segment is the same as the second segment.

Tables C.1 and C.2 also show the design variables corresponding to the powertrain for Mission 2 shown in Figure C.2, with the addition of the cruise thrust variable compared to Mission 1. PEREGRIN requires on average a higher thrust and both platforms favour generally shallower climb angles.

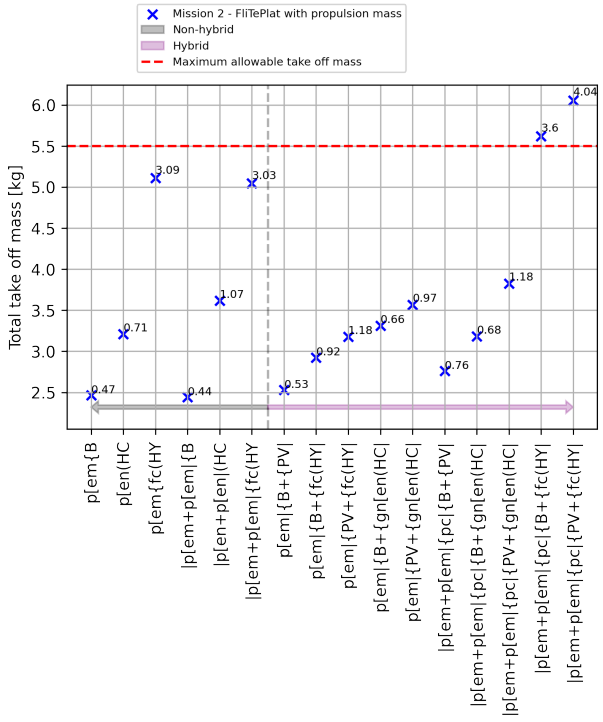

(A) Mission 2 - FliTePlat test case 1.5a.

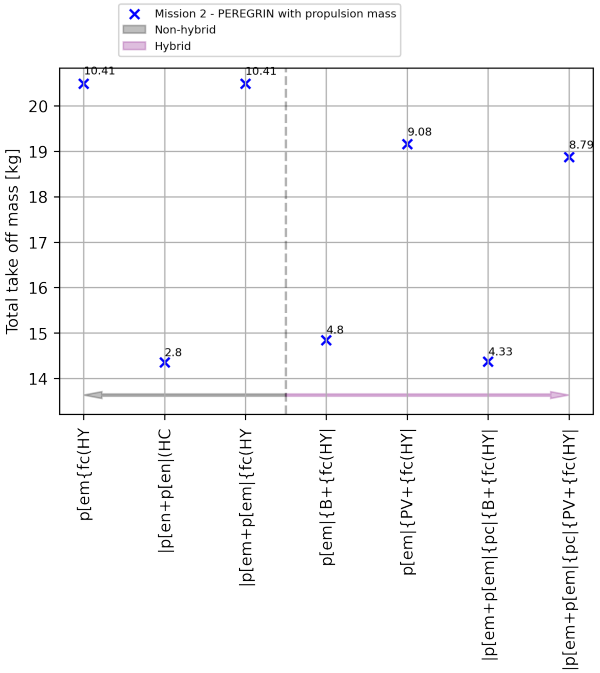

(B) Mission 2 - PEREGRIN test case 1.5b.

FIGURE C.2: Mission 2 - mass optimisation results.

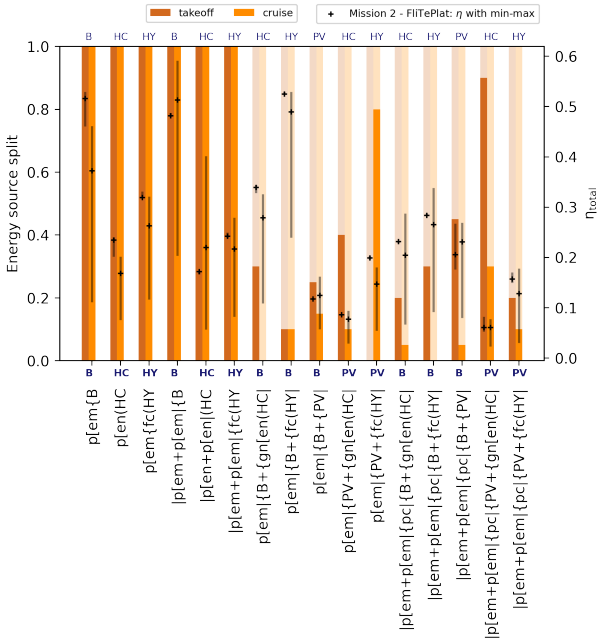

(A) Mission 2 - FliTePlat test case 1.5a.

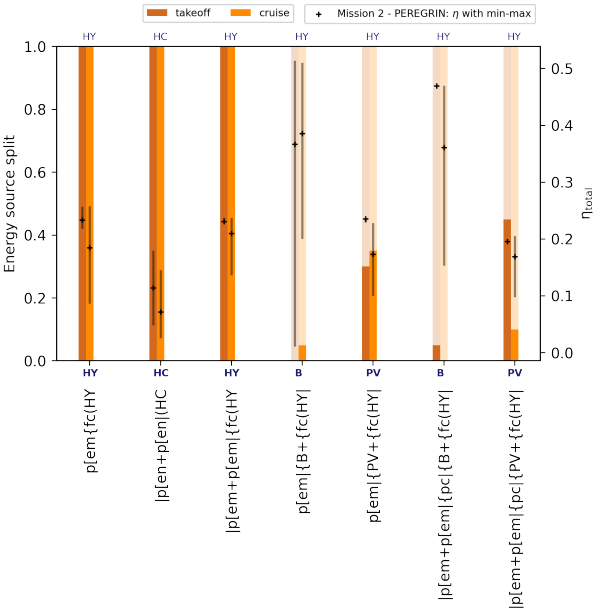

(B) Mission 2 - PEREGRIN test case 1.5b.

FIGURE C.3: Mission 2 - energy source split and efficiency results.

TABLE C.1: Mission 2 - FliTePlat output - optimal thrust and climb angle.

Number	Test string - FliTePlat - Mission 2	Thrust [N]			Climb angle - Takeoff [deg]		
		Takeoff		Cruise	Takeoff		Cruise
		Initial	Final	Final	Initial	Final	Final
5	|p[em+p[em|{B	36.68	15.10	15.10	0	1	0
1	p[em{B	10.79	12.94	21.57	0	1	0
11	p[em|{B+{PV|	23.73	10.79	10.79	0	1	0
16	|p[em+p[em|{pc|{B+{PV|	25.89	19.42	10.79	0	20	0
10	p[em|{B+{fc(HY|	45.31	28.05	25.89	0	1.95	0
13	p[em|{PV+{fc(HY|	15.10	12.94	15.10	0	1	0
14	|p[em+p[em|{pc|{B+{gn[en(HC|	15.10	10.79	10.79	0	1	0
2	p[en(HC	12.94	10.79	12.94	0	1	0
9	p[em|{B+{gn[en(HC|	15.10	10.79	12.94	0	1	0
12	p[em|{PV+{gn[en(HC|	17.26	10.79	10.79	0	1	0
6	|p[en+p[en|(HC	19.42	10.79	10.79	0	1	0
17	|p[em+p[em|{pc|{PV+{gn[en(HC|	40.99	19.42	28.05	0	1	0
7	|p[em+p[em|{fc(HY	28.05	17.26	15.10	0	1.95	0
3	p[em{fc(HY	25.89	19.42	10.79	0	1	0
15	|p[em+p[em|{pc|{B+{fc(HY|	21.57	15.10	15.10	0	1	0
18	|p[em+p[em|{pc|{PV+{fc(HY|	12.94	36.68	25.89	0	3.85	0

TABLE C.2: Mission 2 - PEREGRIN output - optimal thrust and climb angle.

Number	Test string - PEREGRIN - Mission 2	Thrust [N]			Climb angle - Takeoff [deg]		
		Takeoff		Cruise	Takeoff		Cruise
		Initial	Final	Final	Initial	Final	Final
6	|p[en+p[en|(HC	98.07	49.03	98.07	0	13.35	0
15	|p[em+p[em|{pc|{B+{fc(HY|	49.03	49.03	49.03	0	1	0
10	p[em|{B+{fc(HY|	147.10	49.03	58.84	0	1	0
18	|p[em+p[em|{pc|{PV+{fc(HY|	49.03	49.03	49.03	0	1	0
13	p[em|{PV+{fc(HY|	68.65	78.45	68.65	0	2.9	0
7	|p[em+p[em|{fc(HY	49.03	49.03	49.03	0	4.8	0
3	p[em{fc(HY	107.87	58.84	88.26	0	16.2	0

C.2 Mission 3

Figures C.5 and C.6 and Tables C.3 and C.4 show the powertrain results of Mission 3. Similar to the above mission for FliTePlat, the battery only powertrain still exhibits the least overall mass (Figure C.5a). On the other hand, only four powertrains with energy-dense sources, are shown to be feasible, with one violating the constraint of the maximum allowable mass (Figure C.5b). Figure C.4 shows the profile.

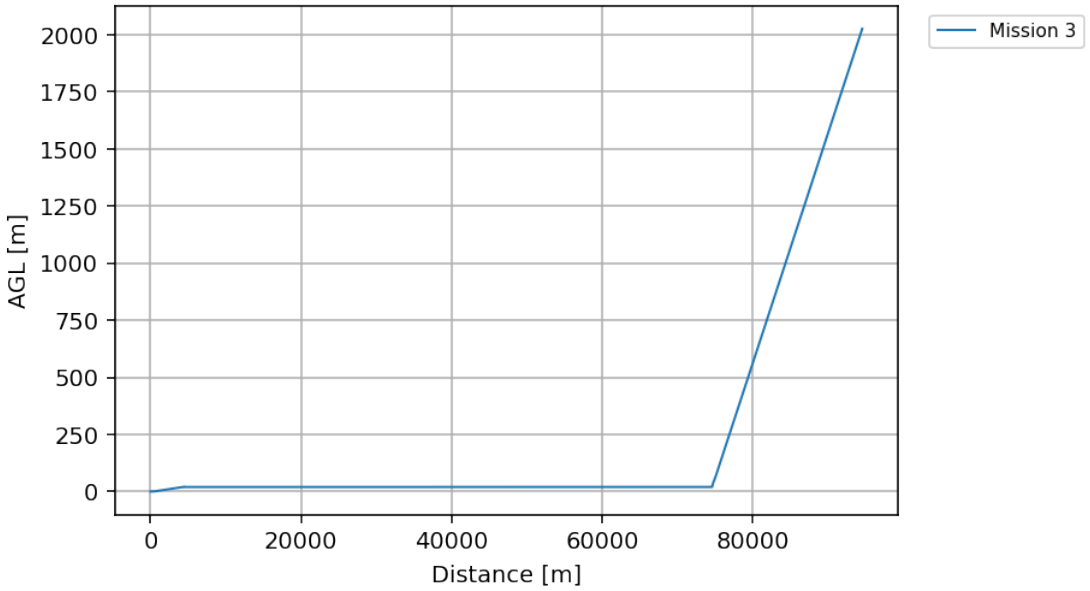

FIGURE C.4: Mission 3 - profile.

This mission added one more segment to the profile, making it more complex than the previous two missions (Figure C.6). As this is a long range mission, in hybrid powertrains for FliTePlat, the energy split favours the liquid fuel over the electric sources (Figure C.6a) during cruise. In these instances, the total powertrain efficiencies are less than 0.5 with the majority being less than 0.3. The efficiency is also similar for PEREGRIN (Figure C.6b). Note that only the powertrains containing the liquid fuel were feasible for PEREGRIN for this mission.

Tables C.3 and C.4 show the thrust and climb angle chosen by the optimiser each segment of the flight.

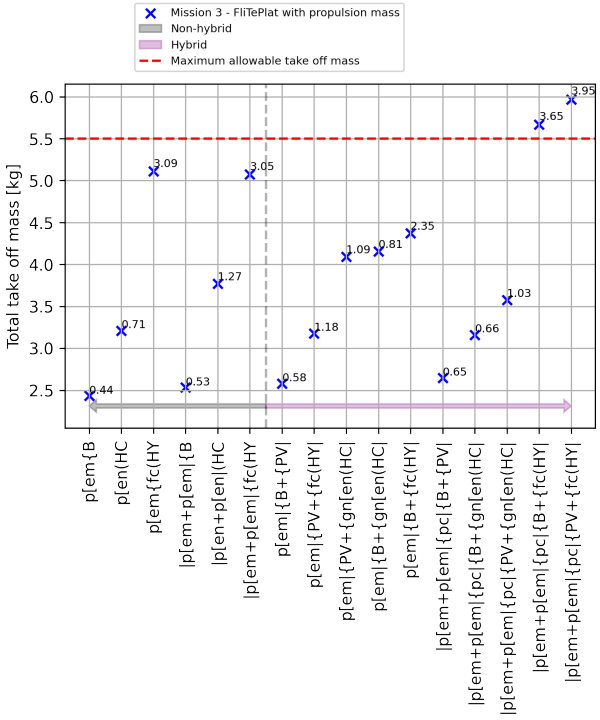

(A) Mission 3 - FliTePlat test case 1.5a.

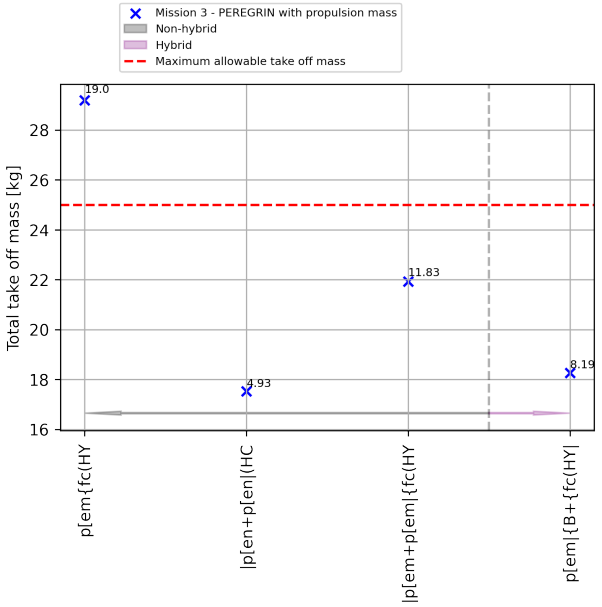

(B) Mission 3 - PEREGRIN test case 1.5b.

FIGURE C.5: Mission 3 - mass optimisation results.

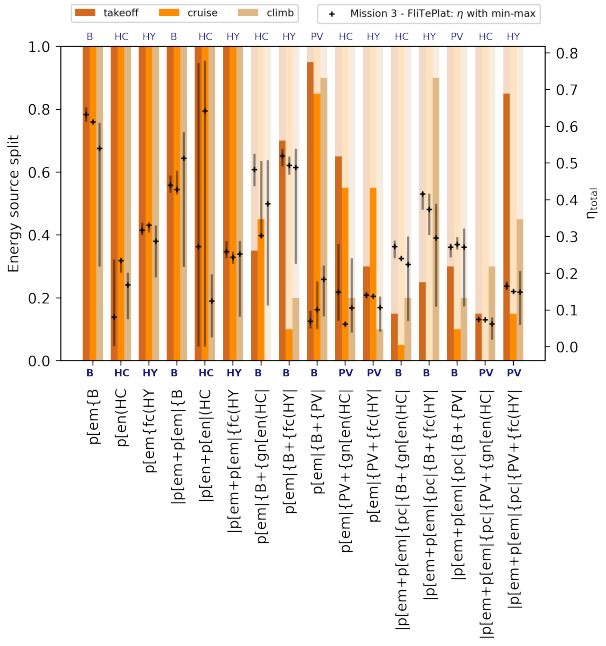

(A) Mission 3 - FliTePlat test case 1.5a.

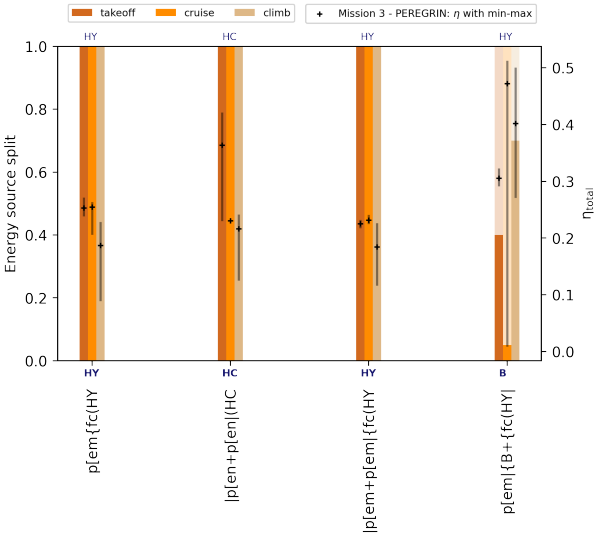

(B) Mission 3 - PEREGRIN test case 1.5b.

FIGURE C.6: Mission 3 - energy source split and efficiency results.

TABLE C.3: Mission 3 - FliTePlat output - optimal thrust and climb angle.

Number	Test string - FliTePlat- Mission 3	Thrust [N]				Climb angle [deg]			
		Takeoff		Cruise	Climb	Takeoff		Cruise	Climb
		Initial	Final	Final	Final	Initial	Final	Final	Final
1	p[em{B	17.26	10.79	10.79	19.42	0	1	0	3.85
5	|p[em+p[em|{B	49.62	23.73	15.10	21.57	0	10.5	0	8.6
11	p[em|{B+{PV|	36.68	19.42	15.10	49.62	0	15.25	0	10.5
16	|p[em+p[em|{pc|{B+{PV|	36.68	19.42	25.89	19.42	0	20	0	8.6
14	|p[em+p[em|{pc|{B+{gn[en(HC|	15.10	10.79	10.79	15.10	0	1	0	4.8
13	p[em|{PV+{fc(HY|	15.10	10.79	10.79	12.94	0	1	0	4.8
2	p[en(HC	12.94	10.79	12.94	17.26	0	1	0	3.85
17	|p[em+p[em|{pc|{PV+{gn[en(HC|	17.26	10.79	10.79	10.79	0	1	0	1.95
6	|p[en+p[en|(HC	15.10	10.79	19.42	34.52	0	1.95	0	3.85
12	p[em|{PV+{gn[en(HC|	38.83	47.46	28.05	12.94	0	19.05	0	7.65
9	p[em|{B+{gn[en(HC|	15.10	10.79	10.79	10.79	0	1	0	1
10	p[em|{B+{fc(HY|	32.36	23.73	10.79	32.36	0	2.9	0	4.8
7	|p[em+p[em|{fc(HY	25.89	25.89	17.26	40.99	0	1	0	1
3	p[em{fc(HY	23.73	10.79	23.73	10.79	0	1	0	4.8
15	|p[em+p[em|{pc|{B+{fc(HY|	23.73	12.94	49.62	34.52	0	19.05	0	13.35
18	|p[em+p[em|{pc|{PV+{fc(HY|	25.89	12.94	12.94	19.42	0	3.85	0	4.8

TABLE C.4: Mission 3 - PEREGRIN output - optimal thrust and climb angle.

Number	Test string - PEREGRIN - Mission 3	Thrust [N]				Climb angle [deg]			
		Takeoff		Cruise	Climb	Takeoff		Cruise	Climb
		Initial	Final	Final	Final	Initial	Final	Final	Final
6	|p[en+p[en|(HC	78.45	49.03	49.03	78.45	0	1	0	1.95
10	p[em|{B+{fc(HY|	58.84	49.03	49.03	88.26	0	2.9	0	2.9
7	|p[em+p[em|{fc(HY	88.26	58.84	49.03	58.84	0	4.8	0	4.8
3	p[em{fc(HY	107.87	78.45	88.26	68.65	0	13.35	0	7.65

C.3 Mission 4

Mission 4 has a take-off finishing around 150 m altitude (higher than Mission 3, where take-off finishes around 18 m). This section shows the results of Mission 4. Figure C.7 shows the profile.

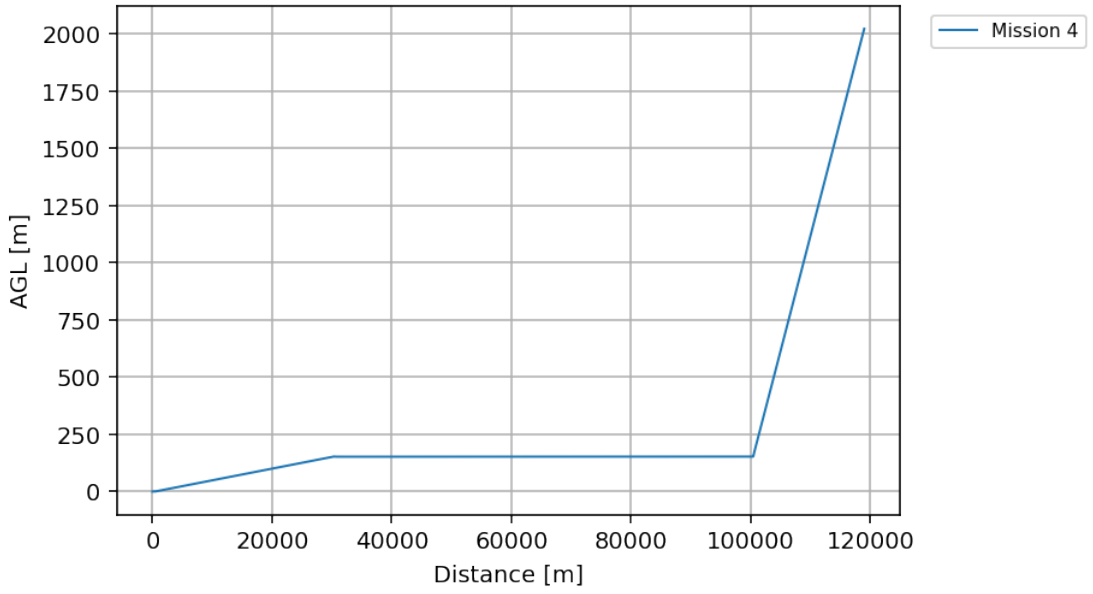

FIGURE C.7: Mission 4 - profile.

Figure C.8a shows that battery based powertrains are, once again, the lightest. Note that both in single motor and dual motor battery powertrain are equally light. This is one of the benefits of electrical propulsion where by splitting the thrust required per electric motor, the power and thereby the current demand reduces, effectively enabling the lighter electric motors. Unlike FliTePlat, for PEREGRIN, Figure C.8b shows that the two propeller-engine configurations is the lightest followed by the battery-fuel cell with two propellers powertrain.

Once again, Figure C.9 shows that PEREGRIN predominantly exploits liquid fuel powertrains. FliTePlat, on the other hand, predominantly favours electrical powertrains. This is due to the fact that FliTePlat does not have the capability to carry large amounts of fuel necessary for such exploitation. PEREGRIN also exhibits the highest total powertrain efficiency for the hybrid powertrain in this mission - p[em | {B + {fc(HY | with

an efficiency around 0.5. In comparison, the highest total efficiency for a hybrid powertrain for FliTePlat is only around 0.35. Tables C.5 and C.6 shows the detailed results of thrust and climb angles of each powertrain for both platforms.

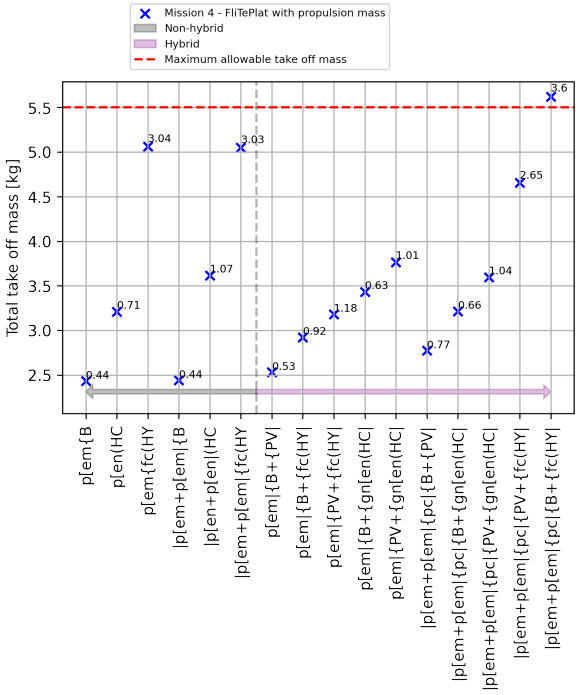

(A) Mission 4 - FliTePlat test case 1.5a.

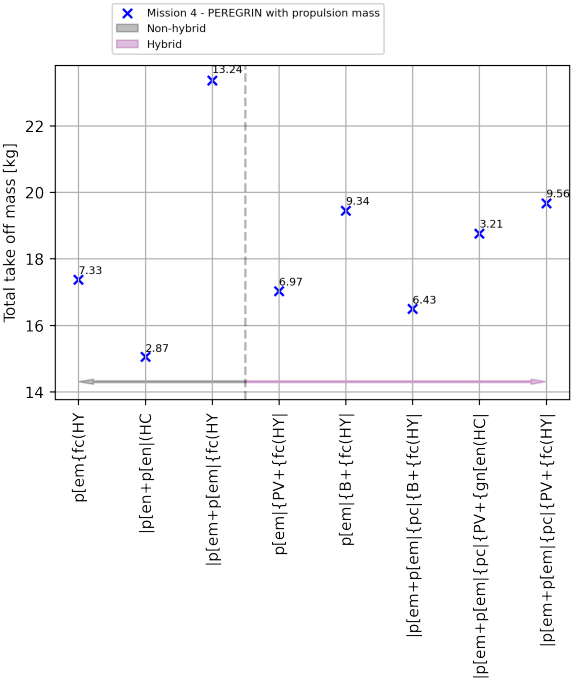

(B) Mission 4 - PEREGRIN test case 1.5b.

FIGURE C.8: Mission 4 - mass optimisation results.

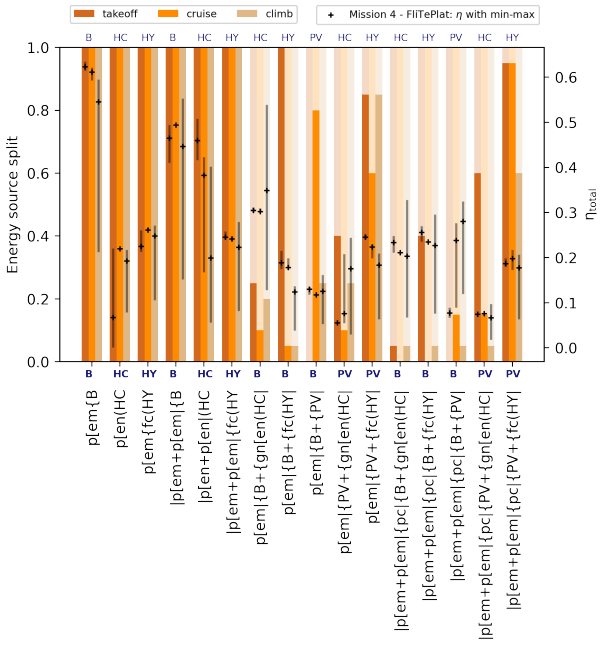

(A) Mission 4 - FliTePlat test case 1.5a.

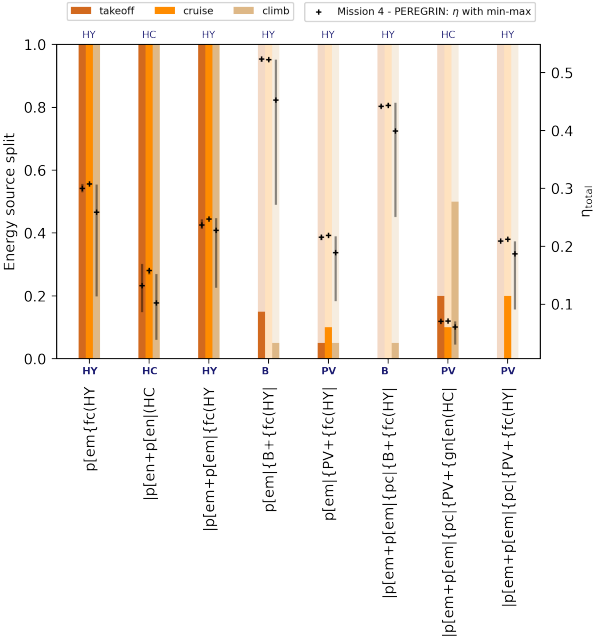

(B) Mission 4 - PEREGRIN test case 1.5b.

FIGURE C.9: Mission 4 - energy source split and efficiency results.

TABLE C.5: Mission 4 - FliTePlat output - optimal thrust and climb angle.

Number	Test string - FliTePlat- Mission 4	Thrust [N]				Climb angle [deg]			
		Takeoff		Cruise	Climb	Takeoff		Cruise	Climb
		Initial	Final	Final	Final	Initial	Final	Final	Final
1	p[em{B	17.26	10.79	12.94	19.42	0	1	0	7.65
5	|p[em+p[em|{B	17.26	12.94	12.94	12.94	0	1	0	17.15
11	p[em|{B+{PV|	21.57	10.79	10.79	12.94	0	1	0	2.9
16	|p[em+p[em|{pc|{B+{PV|	43.15	23.73	19.42	10.79	0	5.75	0	4.8
10	p[em|{B+{fc(HY|	15.10	12.94	10.79	15.10	0	1	0	14.3
13	p[em|{PV+{fc(HY|	15.10	12.94	23.73	28.05	0	1	0	6.7
2	p[en(HC	12.94	10.79	10.79	12.94	0	1	0	2.9
14	|p[em+p[em|{pc|{B+{gn[en(HC|	12.94	10.79	10.79	15.10	0	1	0	6.7
9	p[em|{B+{gn[en(HC|	25.89	25.89	21.57	25.89	0	7.65	0	6.7
17	|p[em+p[em|{pc|{PV+{gn[en(HC|	12.94	10.79	10.79	10.79	0	1	0	1.95
6	|p[en+p[en|(HC	19.42	10.79	15.10	17.26	0	1	0	4.8
12	p[em|{PV+{gn[en(HC|	21.57	12.94	19.42	21.57	0	1	0	10.5
18	|p[em+p[em|{pc|{PV+{fc(HY|	30.20	21.57	38.83	49.62	0	1	0	10.5
7	|p[em+p[em|{fc(HY	28.05	17.26	15.10	23.73	0	1.95	0	2.9
3	p[em{fc(HY	25.89	17.26	15.10	10.79	0	2.9	0	3.85
15	|p[em+p[em|{pc|{B+{fc(HY|	21.57	12.94	12.94	17.26	0	1	0	3.85

TABLE C.6: Mission 4 - PEREGRIN output - optimal thrust and climb angle.

Number	Test string - PEREGRIN- Mission 4	Thrust [N]				Climb angle [deg]			
		Takeoff		Cruise	Climb	Takeoff		Cruise	Climb
		Initial	Final	Final	Final	Initial	Final	Final	Final
6	|p[en+p[en|(HC	147.10	49.03	49.03	78.45	0	1	0	5.75
15	|p[em+p[em|{pc|{B+{fc(HY|	49.03	49.03	49.03	68.65	0	1.95	0	7.65
13	p[em|{PV+{fc(HY|	98.07	49.03	49.03	68.65	0	1	0	1.95
3	p[em{fc(HY	117.68	49.03	49.03	58.84	0	1.95	0	5.75
17	p[em|{B+{fc(HY|	58.84	49.03	49.03	58.84	0	1	0	1.95
10	|p[em+p[em|{pc|{PV+{fc(HY|	58.84	49.03	49.03	49.03	0	1	0	1
18	|p[em+p[em|{pc|{B+{gn[en(HC|	49.03	58.84	49.03	58.84	0	1.95	0	3.85
7	|p[em+p[em|{fc(HY	58.84	49.03	49.03	58.84	0	1	0	3.85

C.4 Mission 5

Unlike the previous missions, Mission 5 (see Figure C.10) explores the take-off, cruise followed by a descent - a typical mission profile. This section presents the data of such a profile. For FliTePlat in Figure C.11a, two of the hybrid powertrains, although these are feasible, break the maximum take-off mass constraint. Similarly in PEREGRIN in Figure C.11b, three of the six feasible powertrains break the mass constraint. In FliTePlat, electrical powertrains, with the single energy source using a battery powertrain, present the lowest mass. Interestingly, in hybrid powertrain, again for FliTePlat, three electric only powertrains also present a similar low maximum take-off masses. However, for PEREGRIN, the lightest maximum take-off mass is again a dual propeller-engine configuration with the second lightest being a distributed propulsion with four propeller-electric motor pairs battery-combustion engine powertrain.

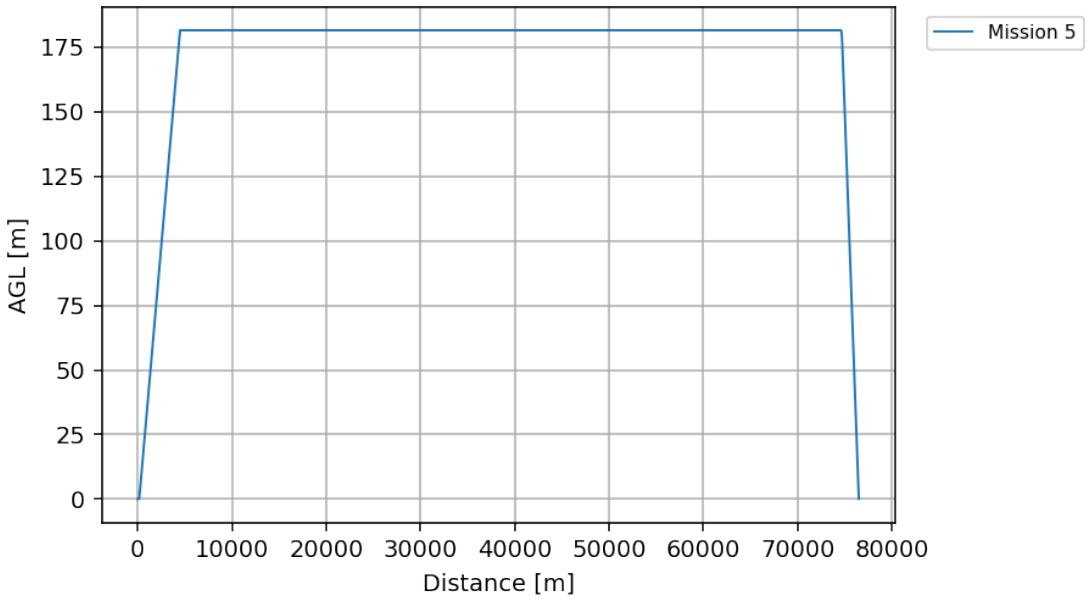

FIGURE C.10: Mission 5 - profile.

For PEREGRIN (Figure C.12b), not only the dual propeller-engine powertrains the lightest, it also has the highest average total efficiency. This is similar in FliTePlat (Figure C.12a), where the single propeller battery powertrain is the lightest with the highest overall total average powertrain efficiency. Again, Tables C.7 and C.8 describe the various thrust and climb angle required for the corresponding powertrain sizes.

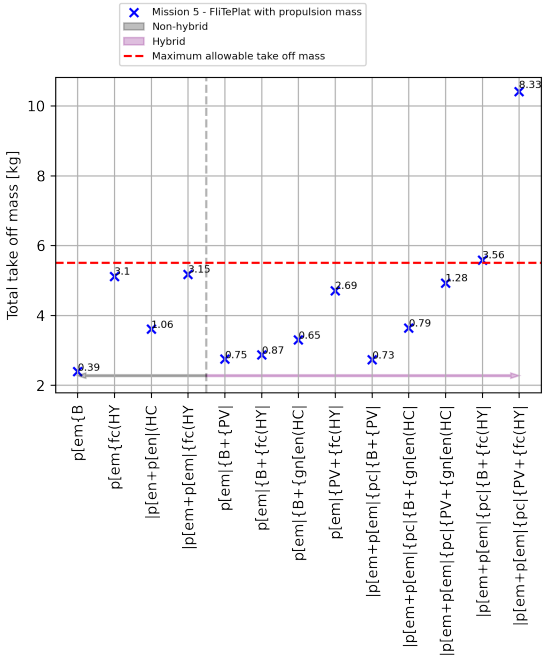

(A) Mission 5 - FliTePlat test case 1.5a.

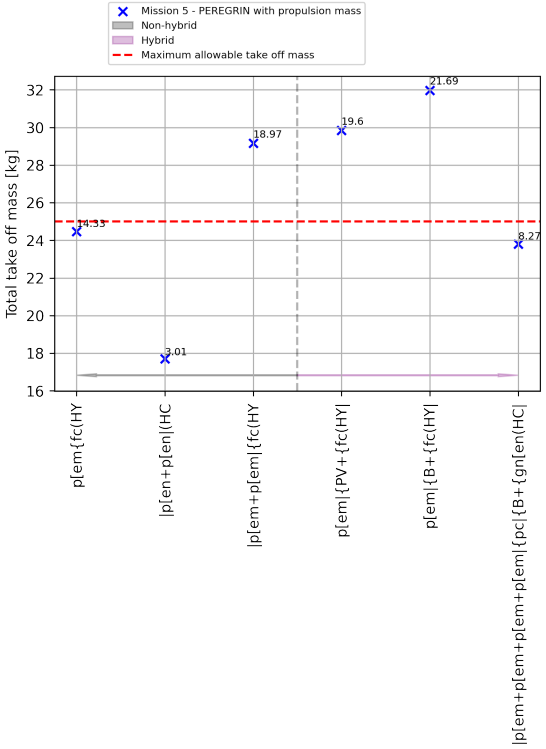

(B) Mission 5 - PEREGRIN test case 1.5b.

FIGURE C.11: Mission 5 - mass optimisation results.

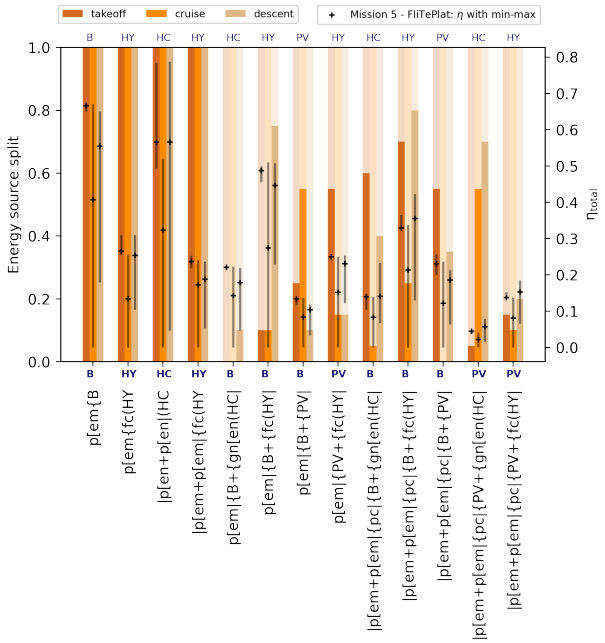

(A) Mission 5 - FliTePlat test case 1.5a.

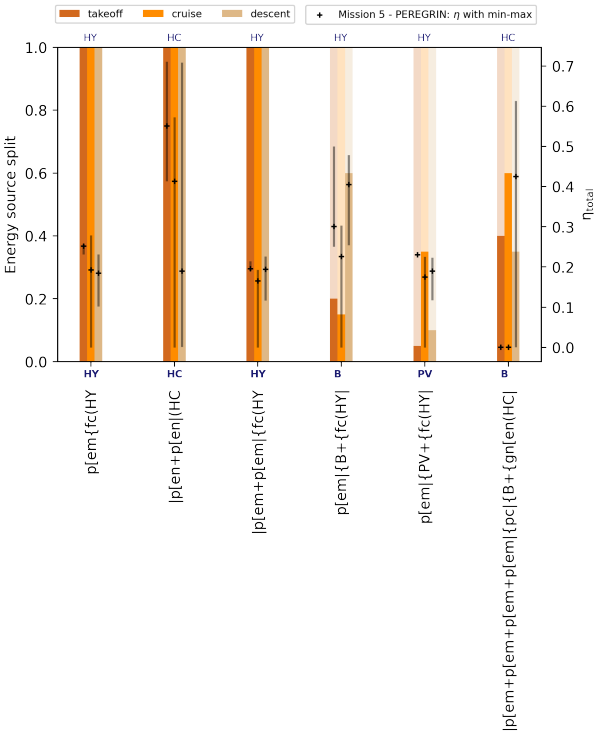

(B) Mission 5 - PEREGRIN test case 1.5b.

FIGURE C.12: Mission 5 - energy source split and efficiency results.

TABLE C.7: Mission 5 - FliTePlat output - optimal thrust and climb angle.

Number	Test string - FliTePlat- Mission 5	Thrust [N]				Climb angle [deg]			
		Takeoff		Cruise	Descent	Takeoff		Cruise	Descent
		Initial	Final	Final	Final	Initial	Final	Final	Final
1	p[em{B	12.94	28.05	38.83	0	0	10.5	0	-10.4
16	|p[em+p[em|{pc|{B+{PV|	21.57	12.94	23.73	0	0	3.85	0	-18
11	p[em|{B+{PV|	12.94	10.79	12.94	0	0	1	0	-5.65
10	p[em|{B+{fc(HY|	45.31	10.79	12.94	0	0	3.85	0	-5.65
9	p[em|{B+{gn[en(HC|	10.79	12.94	12.94	0	0	3.85	0	-5.65
14	|p[em+p[em|{pc|{B+{gn[en(HC|	38.83	10.79	12.94	0	0	10.5	0	-12.3
13	p[em|{PV+{fc(HY|	15.10	17.26	10.79	0	0	4.8	0	-5.65
17	|p[em+p[em|{pc|{PV+{gn[en(HC|	21.57	19.42	12.94	0	0	2.9	0	-7.55
3	p[em{fc(HY	36.68	49.62	25.89	0	0	9.55	0	-12.3
7	|p[em+p[em|{fc(HY	17.26	23.73	34.52	0	0	5.75	0	-12.3
15	|p[em+p[em|{pc|{B+{fc(HY|	32.36	17.26	12.94	0	0	4.8	0	-5.65
18	|p[em+p[em|{pc|{PV+{fc(HY|	38.83	19.42	12.94	0	0	18.1	0	-13.25

TABLE C.8: Mission 5 - PEREGRIN output - optimal thrust and climb angle.

Number	Test string - PEREGRIN- Mission 5	Thrust [N]				Climb angle [deg]			
		Takeoff		Cruise	Descent	Takeoff		Cruise	Descent
		Initial	Final	Final	Final	Initial	Final	Final	Final
6	|p[en+p[en|(HC	147.10	166.71	68.65	0	0	1.95	0	-17.05
20	|p[em+p[em+p[em+p[em|{pc|{B+{gn[en(HC|	88.26	58.84	88.26	0	0	1.95	0	-13.25
3	p[em{fc(HY	107.87	68.65	49.03	0	0	2.9	0	-13.25
7	|p[em+p[em|{fc(HY	88.26	58.84	68.65	0	0	1	0	-11.35
13	p[em|{PV+{fc(HY|	58.84	58.84	58.84	0	0	1	0	-4.7
10	p[em|{B+{fc(HY|	49.03	88.26	58.84	0	0	1	0	-7.55

C.5 Mission 6

Finally, Figures C.14 and C.15, as well as Tables C.9 and C.10 show the results of Mission 6. In this mission, the final climb angle is limited to the minimum of 8 degree (unlike in Mission 3 and 4). Figure C.13 shows the profile.

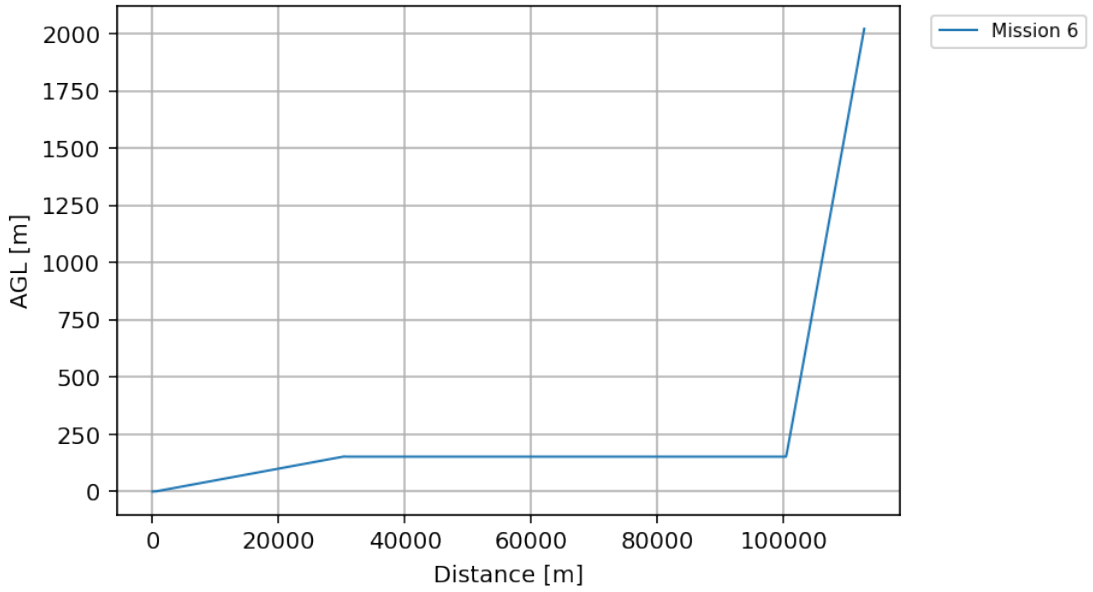

FIGURE C.13: Mission 6 - profile.

Figure C.14a shows that a single battery dual propeller-electric motor combination is the lightest. Note that the single propeller battery powered combination was not feasible for the steeper climb angle for FliTePlat. In PEREGRIN in Figure C.14b, the lightest powertrain is a hybrid powertrain. This is contrasting with the previous missions which consistently shows that single energy source were the lightest. Note that the previously lightest powertrain comes in close second in this mission.

Figures C.15a and C.15b show the energy split along with the efficiencies of the powertrains. Tables C.9 and C.10 describe the various thrust and climb angle required for the corresponding powertrain sizes.

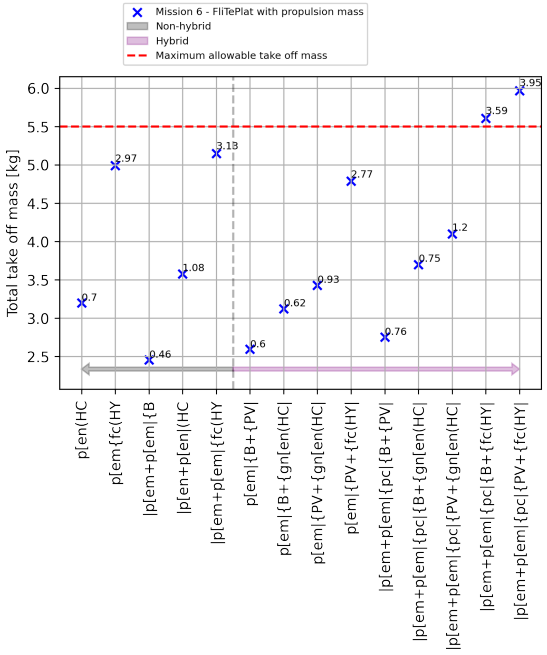

(A) Mission 6 - FliTePlat test case 1.5a.

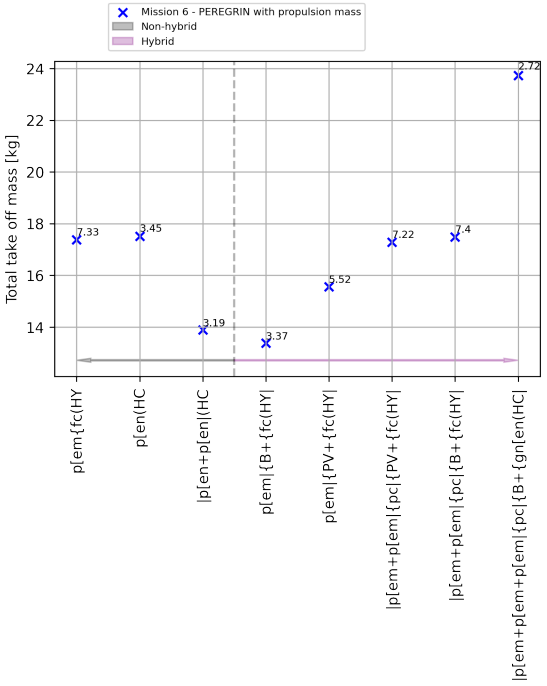

(B) Mission 6 - PEREGRIN test case 1.5b.

FIGURE C.14: Mission 6 - mass optimisation results.

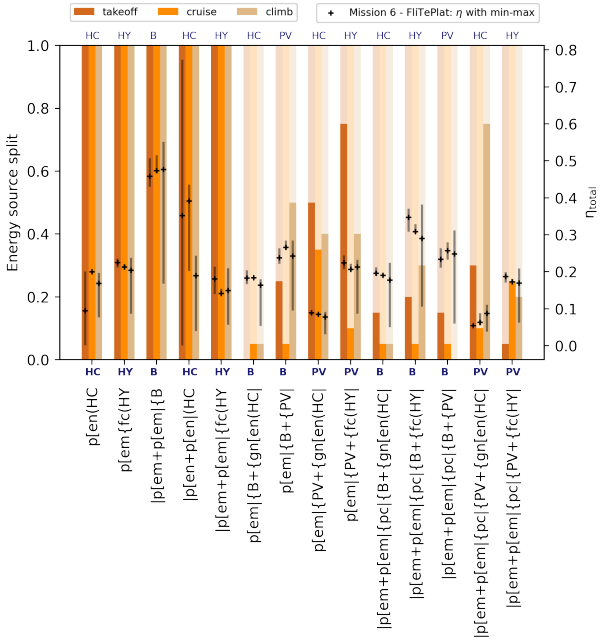

(A) Mission 6 - FliTePlat test case 1.5a.

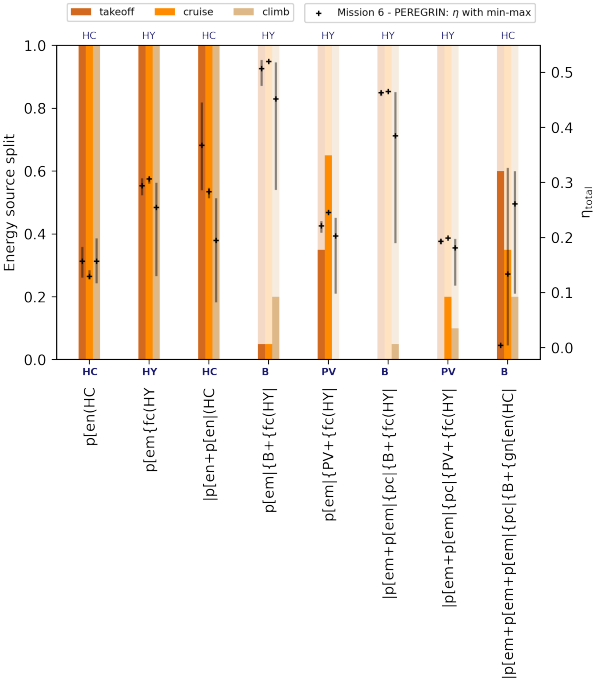

(B) Mission 6 - PEREGRIN test case 1.5b.

FIGURE C.15: Mission 6 - energy source split and efficiency results.

TABLE C.9: Mission 6 - FliTePlat output - optimal thrust and climb angle.

Number	Test string - FliTePlat- Mission 6	Thrust [N]				Climb angle [deg]			
		Takeoff		Cruise	Climb	Takeoff		Cruise	Climb
		Initial	Final	Final	Final	Initial	Final	Final	Final
5	|p[em+p[em|{B	21.57	12.94	10.79	12.94	0	1.95	0	13.25
11	p[em|{B+{PV|	17.26	12.94	10.79	10.79	0	2.9	0	8.75
16	|p[em+p[em|{pc|{B+{PV|	12.94	23.73	15.10	15.10	0	1.95	0	18.5
9	p[em|{B+{gn[en(HC|	15.10	10.79	10.79	12.94	0	1	0	10.25
2	p[en(HC	12.94	10.79	10.79	15.10	0	1	0	9.5
12	p[em|{PV+{gn[en(HC|	17.26	10.79	10.79	15.10	0	1	0	9.5
6	|p[en+p[en|(HC	15.10	12.94	15.10	19.42	0	1	0	8
14	|p[em+p[em|{pc|{B+{gn[en(HC|	15.10	15.10	15.10	19.42	0	1	0	8
17	|p[em+p[em|{pc|{PV+{gn[en(HC|	45.31	19.42	25.89	28.05	0	3.85	0	8.75
13	p[em|{PV+{fc(HY|	25.89	25.89	17.26	45.31	0	3.85	0	10.25
3	p[em{fc(HY	28.05	17.26	15.10	21.57	0	1.95	0	8.75
7	|p[em+p[em|{fc(HY	30.20	15.10	12.94	32.36	0	1.95	0	9.5
15	|p[em+p[em|{pc|{B+{fc(HY|	21.57	15.10	12.94	19.42	0	3.85	0	8.75
18	|p[em+p[em|{pc|{PV+{fc(HY|	25.89	15.10	12.94	19.42	0	1	0	8

TABLE C.10: Mission 6 - PEREGRIN output - optimal thrust and climb angle.

Number	Test string - PEREGRIN- Mission 6	Thrust [N]				Climb angle [deg]			
		Takeoff		Cruise	Climb	Takeoff		Cruise	Climb
		Initial	Final	Final	Final	Initial	Final	Final	Final
10	p[em|{B+{fc(HY|	58.84	49.03	49.03	98.07	0	1	0	8
6	|p[en+p[en|(HC	58.84	49.03	49.03	68.65	0	1	0	8
13	p[em|{PV+{fc(HY|	98.07	49.03	49.03	88.26	0	1	0	8
18	|p[em+p[em|{pc|{PV+{fc(HY|	58.84	49.03	49.03	78.45	0	1	0	9.5
3	p[em{fc(HY	78.45	58.84	49.03	78.45	0	1	0	8.75
15	|p[em+p[em|{pc|{B+{fc(HY|	68.65	49.03	49.03	68.65	0	1	0	8
2	p[en(HC	58.84	49.03	49.03	49.03	0	1	0	8
22	|p[em+p[em+p[em|{pc|{B+{gn[en(HC|	98.07	58.84	49.03	68.65	0	6.7	0	9.5

References

[1] A. Abounada, A. Brahmi, and M. Ramzi. Modelling and simulation of a photovoltaic system. *Modelling, Measurement and Control A*, 81(1-2):29–39, 2008. ISSN: 12595985.

[2] T. J. Adam, G. Liao, J. Petersen, S. Geier, B. Finke, P. Wierach, A. Kwade, and M. Wiedemann. Multifunctional composites for future energy storage in aerospace structures. *Energies*, 11(2):335, feb 2018. DOI: 10.3390/en11020335. ISSN: 19961073.

[3] M. Adamski. Analysis of propulsion systems of unmanned aerial vehicles. *Journal of Marine Engineering and Technology*, 16(4):291–297, feb 2018. DOI: 10.1080/20464177.2017.1383337. ISSN: 20568487.

[4] Airbus. A giant leap towards zero-emission flight. Airbus SE, 2019. [Accessed on: 2023-03-15].

[5] Airbus. Zephyr, 2020. [Accessed on: 2020-08-24].

[6] Airbus. ZEROe, 2023. [Accessed on: 2023-07-12].

[7] Aircraft Electric Propulsion and Power Working Group. Guidelines for Analysis of Hybrid Electric Aircraft System Studies, 2016.

[8] N. M. A. Alrahim Shannan, N. Z. Yahaya, and B. Singh. Single-diode model and two-diode model of PV modules: A comparison. In *Proceedings - 2013 IEEE International Conference on Control System, Computing and Engineering, ICCSCE 2013*, pages 210–214. IEEE, nov 2013. DOI: 10.1109/ICCSCE.2013.6719960. ISBN: 9781479915088.

[9] E. Andrukaitis. Fuel Cells and Other Emerging Manportable Power Technologies for the NATO Warfighter. Technical report, Defense Technical Information Center, 2014.

[10] K. R. Antcliff and F. M. Capristan. Conceptual design of the parallel electric-gas architecture with synergistic utilization scheme (PEGASUS) concept. In *18th AIAA/ISSMO Multidisciplinary Analysis and Optimization Conference, 2017*, pages 1–15, Reston, Virginia, jun 2017. American Institute of Aeronautics and Astronautics. DOI: 10.2514/6.2017-4001. ISBN: 9781624105074.

[11] APC Propellers. Performance Data - APC Propellers, 2014. [Accessed on: 2020-08-25].

[12] H. T. Arat, M. G. Sürer, S. Gökpinar, and K. Aydin. Conceptual design analysis for a lightweight aircraft with a fuel cell hybrid propulsion system. *Energy Sources, Part A: Recovery, Utilization and Environmental Effects*, 45(1):46–60, jun 2023. DOI: 10.1080/15567036.2020.1773966. ISSN: 15567230.

[13] F. Assadian, G. Mohan, and S. Longo. Comparative analysis of forward-facing models vs backward-facing models in powertrain component sizing. In *Hybrid and Electric Vehicles Conference 2013 (HEVC 2013)*, volume HEVC13, pages 1–6. Institution of Engineering and Technology, 2013. DOI: 10.1049/cp.2013.1920. ISBN: 978-1-84919-776-2.

[14] T. Atkinson. *Evolving Graphs by Graph Programming*. PhD thesis, University of York, 2020.

[15] BAE Systems. PHASA-35 First Flight — Newsroom — BAE Systems — International, 2020. [Accessed on: 2022-08-24].

[16] M. Bailey and M. Bower. High Altitude Solar Power Platform. Technical Report April, NASA, 1992.

[17] K. Barnstorff. NASA GL-10, 2015. [Accessed on: 2022-05-27].

[18] Boeing. Phantom Eye UAV, 2022. [Accessed on: 2023-03-14].

[19] E. Botero, A. D. Wendorff, T. MacDonald, A. Variyar, J. M. Vegh, T. Lukaczyk, J. J. Alonso, T. H. Orra, and C. R. Ilario da Silva. SUAVE: An open-source environment for conceptual vehicle design and optimization. In *54th AIAA Aerospace Sciences Meeting*, volume 0, Reston, Virginia, jun 2016. American Institute of Aeronautics and Astronautics. DOI: 10.2514/6.2016-1275. ISBN: 9781624103933.

[20] M. N. Boukoberine, Z. Zhou, and M. Benbouzid. A critical review on unmanned aerial vehicles power supply and energy management: Solutions, strategies, and prospects. *Applied Energy*, 255:113823, dec 2019. DOI: 10.1016/j.apenergy.2019.113823. ISSN: 03062619.

[21] A. Boyal, T. Acarman, and L. Güvenç. Component Sizing in Hybrid Electric Vehicle Design using Optimization and Design of Experiments Techniques. In *3rd AUTOCOM Workshop on Hybrid Electric Vehicle Modeling and Control*, 2007.

[22] J. B. Brandt, R. W. Deters, G. K. Ananda, and M. S. Selig. UIUC Propeller Data Site, 2015. [Accessed on: 2020-09-02].

[23] B. J. Brelje and J. R. Martins. Electric, hybrid, and turboelectric fixed-wing aircraft: A review of concepts, models, and design approaches. *Progress in Aerospace Sciences*, 104(March 2018):1–19, jan 2019. DOI: 10.1016/j.paerosci.2018.06.004. ISSN: 03760421.

[24] N. Brown, B. McKay, F. Gilardoni, and J. Gasteiger. A graph-based genetic algorithm and its application to the multiobjective evolution of median molecules. *Journal of Chemical Information and Computer Sciences*, 44(3):1079–1087, may 2004. DOI: 10.1021/ci034290p. ISSN: 00952338.

[25] K. Bryden, D. Ashlock, S. Corns, and S. Willson. Graph-based evolutionary algorithms. *IEEE Transactions on Evolutionary Computation*, 10(5):550–567, oct 2006. DOI: 10.1109/TEVC.2005.863128. ISSN: 1089-778X.

[26] D. Burnett, E. Barbour, and G. P. Harrison. The UK solar energy resource and the impact of climate change. *Renewable Energy*, 71:333–343, nov 2014. DOI: 10.1016/j.renene.2014.05.034. ISSN: 09601481.

[27] M. C. Cameretti, A. Del Pizzo, L. P. Di Noia, M. Ferrara, and C. Pascarella. Modeling and investigation of a turboprop hybrid electric propulsion system. *Aerospace*, 5(4):123, nov 2018. DOI: 10.3390/aerospace5040123. ISSN: 22264310.

[28] H. Chen and A. Khaligh. Hybrid energy storage system for unmanned aerial vehicle (UAV). In *IECON Proceedings (Industrial Electronics Conference)*, pages 2851–2856. IEEE, nov 2010. DOI: 10.1109/IECON.2010.5675076. ISBN: 9781424452262.

[29] M. Chen and G. A. Rincón-Mora. Accurate electrical battery model capable of predicting runtime and I-V performance. *IEEE Transactions on Energy Conversion*, 21(2):504–511, jun 2006. DOI: 10.1109/TEC.2006.874229. ISSN: 08858969.

[30] C. Chin. *Extending the endurance, missions and captabilities of most UAVs using advanced flexible/ridged solar cells and new high power density batteries technology*. PhD thesis, NAVAL POSTGRADUATE SCHOOL, 2011.

[31] L. Cwojdziński and M. Adamski. Power units and power supply systems in UAV. *Aviation*, 18(1):1–8, jan 2014. DOI: 10.3846/16487788.2014.865938. ISSN: 16487788.

[32] H. Çnar, S. Tunçel, I. Kandemir, and T. Gözel. Conceptual design and optimal sizing of a small unmanned aerial vehicle with fuel cell and battery-powered hybrid propulsion system by meta-heuristic algorithms based on energy consumption. *Energy Sources, Part A: Recovery, Utilization and Environmental Effects*, 45(1):140–159, dec 2023. DOI: 10.1080/15567036.2023.2166166. ISSN: 15567230.

[33] J. R. C. da Silva and G. M. Pacheco. An extended methodology for sizing solar unmanned aerial vehicles: Theory and development of a python framework for design assist. *Sensors*, 21(22):7541, nov 2021. DOI: 10.3390/s21227541. ISSN: 14248220.

[34] B. K. Dey, I. Khan, M. N. Abhinav, and A. Bhattacharjee. Mathematical modelling and characteristic analysis of Solar PV Cell. In *7th IEEE Annual Information Technology, Electronics and Mobile Communication Conference, IEEE*

IEMCON 2016, pages 1–5. IEEE, oct 2016. DOI: 10.1109/IEMCON.2016.7746318. ISBN: 9781509009961.

[35] G. Dixon, R. Stobart, and T. Steffen. Unified Backwards Facing and Forwards Facing Simulation of a Hybrid Electric Vehicle using MATLAB Simscape. In *SAE Technical Papers*, volume 2015-April. SAE International, apr 2015. DOI: 10.4271/2015-01-1215.

[36] D. J. Docimo and A. G. Alleyne. Electro-Thermal Graph-Based Modeling for Hierarchical Control with Application to an Electric Vehicle. In *2018 IEEE Conference on Control Technology and Applications, CCTA 2018*, pages 812–819. IEEE, aug 2018. DOI: 10.1109/CCTA.2018.8511390. ISBN: 9781538676981.

[37] T. Donateo, A. Ficarella, and L. Spedicato. Development and validation of a software tool for complex aircraft powertrains. *Advances in Engineering Software*, 96:1–13, jun 2016. DOI: 10.1016/j.advengsoft.2016.01.001. ISSN: 18735339.

[38] T. Donateo, A. Ficarella, and C. L. De Pascalis. Energy management-based design of a Wankel hybrid-electric UAV. *Aircraft Engineering and Aerospace Technology*, 92(5):701–715, may 2020. DOI: 10.1108/AEAT-06-2019-0117. ISSN: 17488842.

[39] T. Donateo, A. Ficarella, and L. Spedicato. A method to analyze and optimize hybrid electric architectures applied to unmanned aerial vehicles. *Aircraft Engineering and Aerospace Technology*, 90(5):828–842, jul 2018. DOI: 10.1108/AEAT-11-2016-0202. ISSN: 17488842.

[40] T. Donateo, A. Ficarella, L. Spedicato, A. Arista, and M. Ferraro. A new approach to calculating endurance in electric flight and comparing fuel cells and batteries. *Applied Energy*, 187:807–819, feb 2017. DOI: 10.1016/j.apenergy.2016.11.100. ISSN: 03062619.

[41] T. Donateo and L. Spedicato. Fuel economy of hybrid electric flight. *Applied Energy*, 206:723–738, nov 2017. DOI: 10.1016/j.apenergy.2017.08.229. ISSN: 03062619.

[42] T. Donateo and R. Totaro. Hybridization of training aircraft with real world flight profiles. *Aircraft Engineering and Aerospace Technology*, 91(2):353–365, feb 2019. DOI: 10.1108/AEAT-01-2018-0036. ISSN: 17488842.

[43] M. Drela. DC Motor / Propeller Matching - Lab 5 Lecture Notes, 2005. [Accessed on: 2020-09-01].

[44] M. Dudek, P. Tomczyk, P. Wygonik, M. Korkosz, P. Bogusz, and B. Lis. Hybrid fuel cell-battery system as a main power unit for small Unmanned Aerial Vehicles (UAV). *International Journal of Electrochemical Science*, 8(6):8442–8463, 2013. DOI: 10.1016/s1452-3981(23)12901-4. ISSN: 14523981.

[45] V. N. Duy and H. M. Kim. Review on the hybrid-electric propulsion system and renewables and energy storage for unmanned aerial vehicles. *International Journal of Electrochemical Science*, 15:5296–5319, jun 2020. DOI: 10.20964/2020.06.13. ISSN: 14523981.

[46] M. A. S. Eqbal, N. Fernando, M. Marino, and G. Wild. Hybrid Propulsion Systems for Remotely Piloted Aircraft Systems. *Aerospace*, 5(2):34, mar 2018. DOI: 10.3390/AEROSPACE5020034. ISSN: 22264310.

[47] Faraday Report. High-energy battery technologies. Technical report, The Faraday Institution, 2020.

[48] D. F. Finger, C. Braun, and C. Bil. An initial sizing methodology for hybrid-electric light aircraft. In *2018 Aviation Technology, Integration, and Operations Conference*, Reston, Virginia, jun 2018. American Institute of Aeronautics and Astronautics. DOI: 10.2514/6.2018-4229. ISBN: 9781624105562.

[49] D. F. Finger, C. Braun, and C. Bil. Comparative assessment of parallel-hybrid-electric propulsion systems for four different aircraft. In *AIAA Scitech 2020 Forum*, volume 1 PartF, Reston, Virginia, jan 2020. American Institute of Aeronautics and Astronautics. DOI: 10.2514/6.2020-1502. ISBN: 9781624105951.

[50] C. Friedrich and P. A. Robertson. Hybrid-electric propulsion for automotive and aviation applications. *CEAS Aeronautical Journal*, 6(2):279–290, jun 2015. DOI: 10.1007/s13272-014-0144-x. ISSN: 18695590.

[51] Fuel Cell Store. Protium 25, 2023. [Accessed on: 2023-01-17].

[52] R. F. Gagg and E. Farrar. Altitude Performance of Aircraft Engines Equipped with Gear-Driven Superchargers. *SAE Transactions*, 29:217–25, 1934.

[53] A. B. Gallo, J. R. Simões-Moreira, H. K. Costa, M. M. Santos, and E. Moutinho dos Santos. Energy storage in the energy transition context: A technology review. *Renewable and Sustainable Energy Reviews*, 65:800–822, nov 2016. DOI: 10.1016/j.rser.2016.07.028. ISSN: 18790690.

[54] Genstattu. Genstattu Batteries, 2023. [Accessed on: 2023-05-09].

[55] R. R. Glassock, J. Y. Hung, L. F. Gonzalez, and R. A. Walker. Multimodal hybrid powerplant for unmanned aerial systems (UAS) Robotics. In: Twenty-Fourth Bristol International Unmanned Air Vehicle Systems Conference. Technical report, Queensland University of Technology, 2009.

[56] A. R. Gnadt, R. L. Speth, J. S. Sabnis, and S. R. Barrett. Technical and environmental assessment of all-electric 180-passenger commercial aircraft. *Progress in Aerospace Sciences*, 105:1–30, feb 2019. DOI: 10.1016/j.paerosci.2018.11.002. ISSN: 03760421.

[57] C. Goering and H. Cho. Engine model for mapping BSFC contours. *Mathematical and Computer Modelling*, 11(C):514–518, jan 1988. DOI: 10.1016/0895-7177(88)90546-8. ISSN: 08957177.

[58] A. Gong and D. Verstraete. Fuel cell propulsion in small fixed-wing unmanned aerial vehicles: Current status and research needs. *International Journal of Hydrogen Energy*, 42(33):21311–21333, aug 2017. DOI: 10.1016/j.ijhydene.2017.06.148. ISSN: 03603199.

[59] O. González-Espasandín, T. J. Leo, and E. Navarro-Arévalo. Fuel Cells: A Real Option for Unmanned Aerial Vehicles Propulsion. *The Scientific World Journal*, 2014:1–12, 2014. DOI: 10.1155/2014/497642. ISSN: 2356-6140.

[60] S. Gudmundsson. The Anatomy of the Propeller. In *General Aviation Aircraft Design*, pages 581–659. Elsevier, jan 2014. DOI: 10.1016/b978-0-12-397308-5.00014-3.

[61] O. Gur and A. Rosen. Optimizing electric propulsion systems for UAV's. In *12th AIAA/ISSMO Multidisciplinary Analysis and Optimization Conference, MAO*, Reston, Virigina, sep 2008. American Institute of Aeronautics and Astronautics. DOI: 10.2514/6.2008-5916. ISBN: 9781563479472.

[62] H2Fly. Maiden flight of emission-free four-seat passenger aircraft HY4, 2016. [Accessed on: 2020-09-10].

[63] A. Harish, J. Gladin, and D. Mavris. Framework for design space exploration of novel propulsion system architectures. In *AIAA Scitech 2020 Forum*, volume 1 PartF, Reston, Virginia, jan 2020. American Institute of Aeronautics and Astronautics. DOI: 10.2514/6.2020-1007. ISBN: 9781624105951.

[64] J. E. Harlow, X. Ma, J. Li, E. Logan, Y. Liu, N. Zhang, L. Ma, S. L. Glazier, M. M. E. Cormier, M. Genovese, S. Buteau, A. Cameron, J. E. Stark, and J. R. Dahn. A Wide Range of Testing Results on an Excellent Lithium-Ion Cell Chemistry to be used as Benchmarks for New Battery Technologies. *Journal of The Electrochemical Society*, 166(13):A3031–A3044, sep 2019. DOI: 10.1149/2.0981913jes. ISSN: 0013-4651.

[65] F. G. Harmon, A. A. Frank, and J. J. Chattot. Conceptual design and simulation of a small hybrid-electric unmanned aerial vehicle. *Journal of Aircraft*, 43(5): 1490–1498, sep 2006. DOI: 10.2514/1.15816. ISSN: 15333868.

[66] R. W. Hascaryo and J. M. Merret. Configuration-independent initial sizing method for uam/evtol vehicles. In *Aiaa Aviation 2020 Forum*, page 16, Reston, Virginia, jun 2020. American Institute of Aeronautics and Astronautics. DOI: 10.2514/6.2020-2630. ISBN: 9781624105982.

[67] G. Hattenberger, A. Drouin, and M. Bronz. Electric Propulsion System Characterization through Experiments. In *International Micro Air Vehicle Conference and Competition*, Beijing, China, 2016. hal-01396980.

[68] C. He, Y. Jia, and D. Ma. Optimization and Analysis of Hybrid Electric System for Distributed Propulsion Tilt-Wing UAV. *IEEE Access*, 8:224654–224667, 2020. DOI: 10.1109/ACCESS.2020.3044449. ISSN: 21693536.

[69] M. Hepperle. Electric Flight-Potential and Limitations. In *AVT-209 Workshop on Energy Efficient Technologies and Concepts Operation*, 2012.

[70] D. Hernandez Lugo, S. Clarke, T. Miller, M. Redifer, and T. Foster. X-57 Maxwell Battery From cell level to system level design and testing. Technical report, NASA, 2018.

[71] C. Honsberg and S. Bowden. Solar Cell Efficiency PVEducation, 2018. ISSN: 0021-9517. [Accessed on: 2020-09-18].

[72] C. E. Howard. Hydrogen fuel-cell technology takes off, powering Hyfish UAV, 2007. [Accessed on: 2023-03-13].

[73] J. Y. Hung and L. F. Gonzalez. On parallel hybrid-electric propulsion system for unmanned aerial vehicles. *Progress in Aerospace Sciences*, 51:1–17, may 2012. DOI: 10.1016/j.paerosci.2011.12.001. ISSN: 03760421.

[74] M. H. Hwang, H. R. Cha, and S. Y. Jung. Practical endurance estimation for minimizing energy consumption of multirotor unmanned aerial vehicles. *Energies*, 11(9):2221, aug 2018. DOI: 10.3390/en11092221. ISSN: 19961073.

[75] Insitu. ScanEagle, 2023. [Accessed on: 2023-03-13].

[76] J. Jalving, Y. Cao, and V. M. Zavala. Graph-based modeling and simulation of complex systems. *Computers and Chemical Engineering*, 125(125):134–154, jun 2019. DOI: 10.1016/j.compchemeng.2019.03.009. ISSN: 00981354.

[77] T. Jarry, F. Lacressonniere, A. Jaafar, C. Turpin, and M. Scohy. Optimal sizing of a passive hybridization fuel cell - Battery. In *International Conference on Electrical,*

Computer, and Energy Technologies, ICECET 2021, pages 1–6. IEEE, dec 2021. DOI: 10.1109/ICECET52533.2021.9698809. ISBN: 9781665442312.

[78] S. Jashnani, T. R. Nada, M. Ishfaq, A. Khamker, and P. Shaholia. Sizing and preliminary hardware testing of solar powered UAV. *Egyptian Journal of Remote Sensing and Space Science*, 16(2):189–198, dec 2013. DOI: 10.1016/j.ejrs.2013.05.002. ISSN: 20902476.

[79] J. H. Jensen. A graph-based genetic algorithm and generative model/Monte Carlo tree search for the exploration of chemical space. *Chemical Science*, 10(12): 3567–3572, 2019. DOI: 10.1039/c8sc05372c. ISSN: 20416539.

[80] J. A. Jervase, H. Bourdoucen, and A. Al-Lawati. Solar cell parameter extraction using genetic algorithms. *Measurement Science and Technology*, 12(11):1922–1925, nov 2001. DOI: 10.1088/0957-0233/12/11/322. ISSN: 09570233.

[81] E. Kabir, P. Kumar, S. Kumar, A. A. Adelodun, and K. H. Kim. Solar energy: Potential and future prospects. *Renewable and Sustainable Energy Reviews*, 82: 894–900, feb 2018. DOI: 10.1016/j.rser.2017.09.094. ISSN: 18790690.

[82] J. Kallo. HyFish- Flying Fuel Cell Demonstrator, 2007. [Accessed on: 2023-03-13].

[83] A. Kerstjens and H. De Winter. LEADD: Lamarckian evolutionary algorithm for de novo drug design. *Journal of Cheminformatics*, 14(1):3, dec 2022. DOI: 10.1186/s13321-022-00582-y. ISSN: 1758-2946.

[84] H. D. Kim, A. T. Perry, and P. J. Ansell. A Review of Distributed Electric Propulsion Concepts for Air Vehicle Technology. In *2018 AIAA/IEEE Electric Aircraft Technologies Symposium, EATS 2018*, Reston, Virginia, jul 2018. American Institute of Aeronautics and Astronautics. DOI: 10.2514/6.2018-4998. ISBN: 9781624105722.

[85] R. D. Kimberlin. *Flight Testing of Fixed Wing Aircraft*. American Institute of Aeronautics and Astronautics, 2000. ISBN: 9781600860560.

[86] J. Koster, C. Humbargar, E. Serani, A. Velazco, D. Hillery, and L. Makepeace. Hybrid Electric Integrated Optimized System (HELIOS) - Design of a Hybrid Propulsion System for Aircraft. In *49th AIAA Aerospace Sciences Meeting including the New Horizons Forum and Aerospace Exposition*, Reston, Virigina, jan 2011. American Institute of Aeronautics and Astronautics. DOI: 10.2514/6.2011-1011. ISBN: 978-1-60086-950-1.

[87] D. Kouzis-Loukas. Scrapy, 2016. [Accessed on: 2021-02-20].

[88] S. Lalouni, D. Rekioua, T. Rekioua, and E. Matagne. Fuzzy logic control of stand-alone photovoltaic system with battery storage. *Journal of Power Sources*, 193(2):899–907, sep 2009. DOI: 10.1016/j.jpowsour.2009.04.016. ISSN: 03787753.

[89] D. Lawhorn, V. Rallabandi, and D. M. Ionel. Scalable graph theory approach for electric aircraft power system optimization. In *AIAA Propulsion and Energy Forum and Exposition, 2019*, pages 1–5, Reston, Virginia, aug 2019. American Institute of Aeronautics and Astronautics. DOI: 10.2514/6.2019-4488. ISBN: 9781624105906.

[90] D. Lawhorn, V. Rallabandi, and D. M. Ionel. A network graph technique for the design of electric aircraft power systems. In *2020 IEEE Transportation Electrification Conference and Expo, ITEC 2020*, pages 809–813. IEEE, jun 2020. DOI: 10.1109/ITEC48692.2020.9161492. ISBN: 9781728146294.

[91] D. Lawhorn, V. Rallabandi, and D. M. Ionel. Multi-Objective Optimization for Aircraft Power Systems Using a Network Graph Representation. *IEEE Transactions on Transportation Electrification*, 7(4):3021–3031, dec 2021. DOI: 10.1109/TTE.2021.3066123. ISSN: 23327782.

[92] B. Lee, P. Park, and C. Kim. Power managements of a hybrid electric propulsion system powered by solar cells, fuel cells, and batteries for uavs. In *Handbook of Unmanned Aerial Vehicles*, pages 495–524. Springer Netherlands, Dordrecht, 2015. DOI: 10.1007/978-90-481-9707-1_115. ISBN: 9789048197071.

[93] B. Lee, P. Park, K. Kim, and S. Kwon. The flight test and power simulations of an UAV powered by solar cells, a fuel cell and batteries. *Journal of Mechanical*

Science and Technology, 28(1):399–405, jan 2014. DOI: 10.1007/s12206-013-0936-7. ISSN: 1738494X.

[94] T. Lei, Z. Yang, Z. Lin, and X. Zhang. State of art on energy management strategy for hybrid-powered unmanned aerial vehicle. *Chinese Journal of Aeronautics*, 32(6):1488–1503, jun 2019. DOI: 10.1016/j.cja.2019.03.013. ISSN: 10009361.

[95] R. Lensen. Series Hybrid Electric Aircraft: Comparing the Well-to-Propeller Efficiency With a Conventional Propeller Aircraft. Technical report, Delft University ofTechnology, 2016.

[96] J. Lieh, E. Spahr, A. Behbahani, and J. Hoying. Design of hybrid propulsion systems for unmanned aerial vehicles. In *47th AIAA/ASME/SAE/ASEE Joint Propulsion Conference and Exhibit 2011*, pages 1–14, Reston, Virigina, jul 2011. American Institute of Aeronautics and Astronautics. DOI: 10.2514/6.2011-6146. ISBN: 9781600869495.

[97] Lycoming. EL-005 Engine, 2020. [Accessed on: 2020-05-20].

[98] H. Maammeur, A. Hamidat, and L. Loukarfi. A numerical resolution of the current-voltage equation for a real photovoltaic cell. *Energy Procedia*, 36: 1212–1221, 2013. DOI: 10.1016/j.egypro.2013.07.137. ISSN: 18766102.

[99] T. MacDonald, E. Botero, J. M. Vegh, A. Variyar, J. J. Alonsoy, T. H. Orra, and C. R. da Silva. SUAVE: An open-source environment enabling unconventional vehicle designs through higher fidelity. In *AIAA SciTech Forum - 55th AIAA Aerospace Sciences Meeting*, Reston, Virginia, jan 2017. American Institute of Aeronautics and Astronautics. DOI: 10.2514/6.2017-0234. ISBN: 9781624104473.

[100] Make Fly Easy. Believer, 2023. [Accessed on: 2023-01-21].

[101] S. A. M. Maleki, H. Hizam, and C. Gomes. Estimation of hourly, daily and monthly global solar radiation on inclined surfaces: Models re-visited. *Energies*, 10(1):134, jan 2017. DOI: 10.3390/en10010134. ISSN: 19961073.

[102] T. Markel, A. Brooker, T. Hendricks, V. Johnson, K. Kelly, B. Kramer, M. O'Keefe, S. Sprik, and K. Wipke. ADVISOR: A systems analysis tool for advanced vehicle modeling. *Journal of Power Sources*, 110(2):255–266, aug 2002. DOI: 10.1016/S0378-7753(02)00189-1. ISSN: 03787753.

[103] A. M. Mazur and R. Domanski. Hybrid energy systems in unmanned aerial vehicles. *Aircraft Engineering and Aerospace Technology*, 91(5):736–746, may 2019. DOI: 10.1108/AEAT-08-2018-0218. ISSN: 17488842.

[104] L. McLay. Open source github for PoETS and its analysis, 2024. [Accessed on: 2024-04-01].

[105] L. McLay, J. Scanlan, and A. Sobester. PoETS: A Proposed Powertrain Topology Encoding Scheme. In *AIAA SCITECH 2023 Forum*, Reston, Virginia, jan 2023. American Institute of Aeronautics and Astronautics. DOI: 10.2514/6.2023-1363. ISBN: 978-1-62410-699-6.

[106] L. McLay, A. Weishaeupl, J. Southern, and P. Wattle. PEREGRIN, 2019. [Accessed on: 2023-08-12].

[107] M. M. Mench. *Fuel Cell Engines*. John Wiley and Sons, Inc., Hoboken, NJ, USA, jan 2008. DOI: 10.1002/9780470209769. ISBN: 9780471689584.

[108] A. Misra. Energy storage for electrified aircraft: The need for better batteries, fuel cells, and supercapacitors. *IEEE Electrification Magazine*, 6(3):54–61, sep 2018. DOI: 10.1109/MELE.2018.2849922. ISSN: 23255889.

[109] S. K. S. Nakka and M. J. Alexander-Ramos. Simultaneous combined optimal design and control formulation for aircraft hybrid-electric propulsion systems. *Journal of Aircraft*, 58(1):53–62, jan 2021. DOI: 10.2514/1.C035678. ISSN: 15333868.

[110] NASA. Past Projects: Pathfinder / Pathfinder Plus Solar-Powered Aircraft, 2010. [Accessed on: 2023-09-10].

[111] NASA. NASA Armstrong Fact Sheet: Altair, 2014. [Accessed on: 2020-08-24].

[112] N. V. Nguyen, J. W. Lee, M. Tyan, and D. Lee. Possibility-based multidisciplinary optimisation for electric-powered unmanned aerial vehicle design. *Aeronautical Journal*, 119(1221):1397–1414, 2015. DOI: 10.1017/S0001924000011313. ISSN: 00019240.

[113] N. M. O'Boyle. Towards a Universal SMILES representation - A standard method to generate canonical SMILES based on the InChI. *Journal of Cheminformatics*, 4(9):22, dec 2012. DOI: 10.1186/1758-2946-4-22. ISSN: 17582946.

[114] N. Omar, M. Daowd, P. van den Bossche, O. Hegazy, J. Smekens, T. Coosemans, and J. van Mierlo. Rechargeable energy storage systems for plug-in hybrid electric vehicles-assessment of electrical characteristics. *Energies*, 5(8):2952–2988, aug 2012. DOI: 10.3390/en5082952. ISSN: 19961073.

[115] Z. F. Pan, L. An, and C. Y. Wen. Recent advances in fuel cells based propulsion systems for unmanned aerial vehicles. *Applied Energy*, 240:473–485, apr 2019. DOI: 10.1016/j.apenergy.2019.02.079. ISSN: 03062619.

[116] E. Papageorgiou. *Development and application of a value driven design assessment framework to an unmanned air system design*. PhD thesis, UNIVERSITY OF SOUTHAMPTON, 2018. DOI: 10.1109/ICASET.2018.8376805.

[117] N. E. M. Pasquini. Hybrid Tiger UAV, 2021. [Accessed on: 2022-05-27].

[118] P. Phlips. SI engine model for vehicle fuel consumption estimation. *FISITA 2014 World Automotive Congress - Proceedings*, 8(2):423–440, 2014. DOI: 10.2307/26273097.

[119] B. G. Pollet, I. Staffell, J. L. Shang, and V. Molkov. Fuel-cell (hydrogen) electric hybrid vehicles. In *Alternative Fuels and Advanced Vehicle Technologies for Improved Environmental Performance: Towards Zero Carbon Transportation*, pages 685–735. Elsevier, jan 2014. DOI: 10.1533/9780857097422.3.685. ISBN: 9780857095220.

[120] S. D. Prior. *Optimizing Small Multi Rotor Unmanned Aircraft - A Practical Design Guide*. Taylor and Francis (CRC), oct 2018. ISBN: 978-1138369887.

[121] W. W. Pulkrabek. Engineering Fundamentals of the Internal Combustion Engine, 2nd Ed. *Journal of Engineering for Gas Turbines and Power*, 126(1):198–198, jan 2004. DOI: 10.1115/1.1669459. ISSN: 0742-4795.

[122] PyGraphviz. PyGraphviz, 2022. [Accessed on: 2022-05-31].

[123] Python Documentation. 9. Classes Python 3.8.5 documentation, 2020. [Accessed on: 2020-09-03].

[124] P. Rajendran and H. Smith. Modelling of solar irradiance and daylight duration for solar-powered UAV sizing. *Energy Exploration and Exploitation*, 34(2):235–243, mar 2016. DOI: 10.1177/0144598716629874. ISSN: 20484054.

[125] R. C. Read. A New System for the Designation of Chemical Compounds. 1. Theoretical Preliminaries and the Coding of Acyclic Compounds. *Journal of Chemical Information and Computer Sciences*, 23(3):135–149, aug 1983. DOI: 10.1021/ci00039a006. ISSN: 00952338.

[126] L. Richardson. Beautiful Soup Documentation, 2016. [Accessed on: 2021-02-20].

[127] G. Rizzoni, L. Guzzella, and B. M. Baumann. Unified modeling of hybrid electric vehicle drivetrains. *IEEE/ASME Transactions on Mechatronics*, 4(3): 246–257, 1999. DOI: 10.1109/3516.789683. ISSN: 10834435.

[128] J. Rohacs and D. Rohacs. Energy coefficients for comparison of aircraft supported by different propulsion systems. *Energy*, 191:116391, jan 2020. DOI: 10.1016/j.energy.2019.116391. ISSN: 03605442.

[129] L. Sai, Z. Wei, and W. Xueren. The Development Status and Key Technologies of Solar Powered Unmanned Air Vehicle. *IOP Conference Series: Materials Science and Engineering*, 187(1):012011, mar 2017. DOI: 10.1088/1757-899X/187/1/012011. ISSN: 1757899X.

[130] G. Saldaña, J. I. S. Martín, I. Zamora, F. J. Asensio, and O. Oñederra. Analysis of the current electric battery models for electric vehicle simulation. *Energies*, 12 (14):2750, jul 2019. DOI: 10.3390/en12142750. ISSN: 19961073.

[131] I. M. Saleh, R. Ali, and H. Zhang. Environmental Impact of High Altitudes on the Operation of PEM Fuel Cell Based UAS. *Energy and Power Engineering*, 10 (03):87–105, 2018. DOI: 10.4236/epe.2018.103007. ISSN: 1949-243X.

[132] O. Schmitz and M. Hornung. Methods for simulation and analysis of hybrid electric propulsion systems. *CEAS Aeronautical Journal*, 6(2):245–256, jun 2015. DOI: 10.1007/s13272-014-0137-9. ISSN: 18695590.

[133] J. Schomann. *Electric Propulsion Systems*. Doctoral thesis, Technical University of Munich, 1935. DOI: 10.1111/j.1559-3584.1935.tb04313.x.

[134] N. J. Schouten, M. A. Salman, and N. A. Kheir. Fuzzy logic control for parallel hybrid vehicles. *IEEE Transactions on Control Systems Technology*, 10(3):460–468, may 2002. DOI: 10.1109/87.998036. ISSN: 10636536.

[135] F. Settele and M. Bittner. Energy-optimal guidance of a battery-electrically driven airplane. *CEAS Aeronautical Journal*, 11(1):111–124, jan 2020. DOI: 10.1007/s13272-019-00398-x. ISSN: 18695590.

[136] J. K. Shiau, D. M. Ma, C. W. Chiu, and J. R. Shie. Optimal sizing and cruise speed determination for a solar-powered airplane. *Journal of Aircraft*, 47(2): 622–629, mar 2010. DOI: 10.2514/1.45908. ISSN: 15333868.

[137] Silicon Solar. What are Standard Test Conditions (STC) — Silicon Solar, 2020. [Accessed on: 2020-09-18].

[138] N. J. Sloane. The on-line encyclopedia of integer sequences, 2013. DOI: 10.2307/j.ctvggx33b.12. ISSN: 17875021. [Accessed on: 2021-07-05].

[139] A. Sóbester. Four suggestions for better parametric geometries. In *10th AIAA Multidisciplinary Design Optimization Specialist Conference*, pages 1–10, Reston, Virginia, jan 2014. American Institute of Aeronautics and Astronautics. DOI: 10.2514/6.2014-1172. ISBN: 978-1-62410-310-0.

[140] M. Sorrentino, F. Mauramati, I. Arsie, A. Cricchio, C. Pianese, and W. Nesci. Application of Willans Line Method for Internal Combustion Engines Scalability

towards the Design and Optimization of Eco-Innovation Solutions. In *SAE Technical Papers*, sep 2015. DOI: 10.4271/2015-24-2397.

[141] Sparkle Tech Limited. Eagle Plus VTOL, 2022. [Accessed on: 2022-05-27].

[142] D. Stinton. *The Design of the Airplane, Second Edition*. American Institute of Aeronautics and Astronautics, Inc., Washington, DC, nov 1983.

[143] R. O. Stroman, M. W. Schuette, K. Swider-Lyons, J. A. Rodgers, and D. J. Edwards. Liquid hydrogen fuel system design and demonstration in a small long endurance air vehicle. *International Journal of Hydrogen Energy*, 39(21): 11279–11290, jul 2014. DOI: 10.1016/j.ijhydene.2014.05.065. ISSN: 03603199.

[144] K. Swider-Lyons, R. Stroman, G. Page, J. Mackrell, J. Rodgers, and M. Schuette. The Ion Tiger Fuel Cell Unmanned Air Vehicle. In *44th Power Sources Conference*, pages 561–563, Las Vegas, NV, 2010.

[145] K. Swider-Lyons, R. O. Stroman, B. D. Gould, J. A. Rodgers, J. Mackrell, M. Schuette, and G. Page. Hydrogen Fuel Cells for Small Unmanned Air Vehicles. *ECS Transactions*, 64(3):963–972, aug 2014. DOI: 10.1149/06403.0963ecst. ISSN: 1938-5862.

[146] TEXTRON Systems. AEROSONDE, 2020. [Accessed on: 2020-05-20].

[147] J. Thauvin, G. Barraud, X. Roboam, B. Sareni, M. Budinger, and D. Leray. Hybrid propulsion for regional aircraft: A comparative analysis based on energy efficiency. In *2016 International Conference on Electrical Systems for Aircraft, Railway, Ship Propulsion and Road Vehicles and International Transportation Electrification Conference, ESARS-ITEC 2016*, pages 1–6, 2016. DOI: 10.1109/ESARS-ITEC.2016.7841392. ISBN: 9781509008148.

[148] S. F. Tie and C. W. Tan. A review of energy sources and energy management system in electric vehicles. *Renewable and Sustainable Energy Reviews*, 20:82–102, apr 2013. DOI: 10.1016/j.rser.2012.11.077. ISSN: 13640321.

[149] S. Toghyani, S. A. Atyabi, and X. Gao. Enhancing the specific power of a pem fuel cell powered uav with a novel bean-shaped flow field. *Energies*, 14(9):2494, apr 2021. DOI: 10.3390/en14092494. ISSN: 19961073.

[150] L. Toscano, S. Stella, and E. Milotti. Using graph theory for automated electric circuit solving. *European Journal of Physics*, 36(3):1–12, may 2015. DOI: 10.1088/0143-0807/36/3/035015. ISSN: 13616404.

[151] J. Tuttle. A comparison of hydrogen and propane fuels, 2011.

[152] Tytorobotics. RCBenchmark Series 1780 (S1780), 2023. [Accessed on: 2023-08-09].

[153] UAVOS. Home - UAVOS - Unmanned Systems Development, Research and Integration, 2020. [Accessed on: 2020-08-06].

[154] H. Ucgun, C. Cicekdemir, and U. Yuzgec. The Comparison of Energy Sources Used in Unmanned Air Vehicles. *International Journal of Scientific and Technological Research*, 5(6):30–38, jun 2019. DOI: 10.7176/jstr/5-6-05.

[155] University of Southampton. RJMitchell Wind Tunnel, 2023. [Accessed on: 2023-03-29].

[156] Unmannedsystemstechnolog. Solar Power Solutions for UAVs, 2019. [Accessed on: 2020-05-19].

[157] I. V. Vasyukov, A. V. Pavlenko, V. S. Puzin, D. V. Batishchev, and I. A. Bolshenko. Mathematical modeling of an electrotechnical complex of a power unit based on hydrogen fuel cells for unmanned aerial vehicles. *Energies*, 14(21):6974, oct 2021. DOI: 10.3390/en14216974. ISSN: 19961073.

[158] J. M. Vegh, E. Botero, M. Clark, J. Smart, and J. J. Alonso. Current capabilities and challenges of ndarc and suave for evtol aircraft design and analysis. In *AIAA Propulsion and Energy Forum and Exposition, 2019*, Reston, Virginia, aug 2019. American Institute of Aeronautics and Astronautics. DOI: 10.2514/6.2019-4505. ISBN: 9781624105906.

[159] D. Verstraete. On the energy efficiency of hydrogen-fuelled transport aircraft. *International Journal of Hydrogen Energy*, 40(23):7388–7394, jun 2015. DOI: 10.1016/j.ijhydene.2015.04.055. ISSN: 03603199.

[160] J. Wang, R. Jia, J. Liang, C. She, and Y. P. Xu. Evaluation of a small drone performance using fuel cell and battery; Constraint and mission analyzes. *Energy Reports*, 7:9108–9121, nov 2021. DOI: 10.1016/j.egyr.2021.11.225. ISSN: 23524847.

[161] D. Weininger. SMILES, a Chemical Language and Information System: 1: Introduction to Methodology and Encoding Rules. *Journal of Chemical Information and Computer Sciences*, 28(1):31–36, feb 1988. DOI: 10.1021/ci00057a005. ISSN: 00952338.

[162] D. Weininger. Smiles. 3. Depict. Graphical Depiction of Chemical Structures. *Journal of Chemical Information and Computer Sciences*, 30(3):237–243, aug 1990. DOI: 10.1021/ci00067a005. ISSN: 00952338.

[163] D. Weininger, A. Weininger, and J. L. Weininger. SMILES. 2. Algorithm for Generation of Unique SMILES Notation. *Journal of Chemical Information and Computer Sciences*, 29(2):97–101, may 1989. DOI: 10.1021/ci00062a008. ISSN: 00952338.

[164] A. Weishäupl, L. McLay, and A. Sóbester. Experimental evaluation of the drag curves of small fixed wing UAVs. *The Aeronautical Journal*, pages 1–30, jul 2023. DOI: 10.1017/aer.2023.61. ISSN: 0001-9240.

[165] A. B. Weishäupl and S. D. Prior. Influence of Propeller Overlap on Large-Scale Tandem UAV Performance. *Unmanned Systems*, 7(4):245–260, oct 2019. DOI: 10.1142/S2301385019500092. ISSN: 23013869.

[166] D. Whitley. A genetic algorithm tutorial. *Statistics and Computing*, 4(2):65–85, 1994. DOI: 10.1007/BF00175354. ISSN: 09603174.

[167] Y. Xie, A. Savvaris, A. Tsourdos, J. Laycock, and A. Farmer. Modelling and control of a hybrid electric propulsion system for unmanned aerial vehicles.

IEEE Aerospace Conference Proceedings, 2018-March:1–13, mar 2018. DOI: 10.1109/AERO.2018.8396436. ISSN: 1095323X.

[168] N. Xue, W. Du, J. R. R. A. Martins, and W. Shyy. Lithium-Ion Batteries: Thermomechanics, Performance, and Design Optimization. In *Handbook of Clean Energy Systems*, pages 1–16. John Wiley and Sons, Ltd, Chichester, UK, jul 2015. DOI: 10.1002/9781118991978.hces225.

[169] X. Yang, J. Zhang, K. Yoshizoe, K. Terayama, and K. Tsuda. ChemTS: an efficient python library for de novo molecular generation. *Science and Technology of Advanced Materials*, 18(1):972–976, dec 2017. DOI: 10.1080/14686996.2017.1401424. ISSN: 1468-6996.

[170] A. Yezeguelian and A. T. Isikveren. Methods to improve UAV performance using hybrid-electric architectures. *Aircraft Engineering and Aerospace Technology*, 92(5):685–700, may 2020. DOI: 10.1108/AEAT-11-2019-0227. ISSN: 17488842.

[171] M. Zhang, Y. Yang, and C. C. Mi. Analytical approach for the power management of blended-mode plug-in hybrid electric vehicles. *IEEE Transactions on Vehicular Technology*, 61(4):1554–1566, may 2012. DOI: 10.1109/TVT.2012.2187318. ISSN: 00189545.

[172] R. Zhang, B. Xia, B. Li, L. Cao, Y. Lai, W. Zheng, H. Wang, W. Wang, and M. Wang. A study on the open circuit voltage and state of charge characterization of high capacity lithium-ion battery under different temperature. *Energies*, 11(9):2408, sep 2018. DOI: 10.3390/en11092408. ISSN: 19961073.

[173] X. Zhang, L. Liu, and Y. Dai. Fuzzy state machine energy management strategy for hybrid electric UAVs with PV/Fuel cell/battery power system. *International Journal of Aerospace Engineering*, 2018:1–16, jul 2018. DOI: 10.1155/2018/2852941. ISSN: 16875974.

[174] X. Zhang, L. Liu, and G. Xu. Energy management strategy of hybrid PEMFC-PV-battery propulsion system for low altitude UAVs. In *52nd AIAA/SAE/ASEE Joint Propulsion Conference, 2016*, Reston, Virginia, jul 2016.

American Institute of Aeronautics and Astronautics. DOI: 10.2514/6.2016-5109. ISBN: 9781624104060.

[175] A. Zimmermann, E. Siira, T. Ghariani, M. Girod-Genet, G. Santos, F. Silva, L. Temal, B. Teixeira, and H. Jarvinen. SEAS Ontology, 2017. [Accessed on: 2020-01-14].

[176] G. Zubi, R. Dufo-López, M. Carvalho, and G. Pasaoglu. The lithium-ion battery: State of the art and future perspectives. *Renewable and Sustainable Energy Reviews*, 89:292–308, jun 2018. DOI: 10.1016/j.rser.2018.03.002. ISSN: 18790690.

[177] B. Zuurendonk. Advanced Fuel Consumption and Emission Modeling using Willans line scaling techniques for engines. Technical report, Technische Universiteit Eindhoven Department Mechanical Engineering Dynamics and Control Technology Group, 2005.